A STUDY OF YTTERBIUM AND EUROPIUM IN THE ALKALI HALIDES

by

Stephen Wilfrid Bland

Submitted for the degree of Doctor of Philosophy

University of Warwick

Physics Department

September, 1985

SUMMARY

Ytterbium and europium have been successfully diffused from the vapour phase into the alkali halides. Both impurities are incorporated in the divalent state and give rise to optical absorption bands in the ultraviolet due to transitions of the type $4f^n - 4f^{n-1}5d$.

Optical absorption spectra for the Yb^{2+} ion in the alkali halides are, with the exception of NaCl, reported for the first time. Generally excellent agreement is obtained between experiment and a theory utilising the J,j-coupling scheme to describe Yb^{2+} in an octahedral crystal field, provided that a correction based on the nephelauxetic effect is taken into account. Certain additional absorption bands are associated with transitions of the type $4f^{14} - 4f^{13}\sigma(A_{1g})$, where $\sigma(A_{1g})$ represents a σ-bonding orbital created between the 6s orbital of the Yb^{2+} ion and a σ orbital of the surrounding octahedrally coordinated anion complex.

Optical absorption spectra are also recorded for the Eu^{2+} ion, of which the spectrum for $KF:Eu^{2+}$ has not been reported previously. Electron spin resonance (ESR) spectra obtained for the Eu^{2+} ion confirm the presence of a cation vacancy along the <110> direction. The ESR spectrum for Eu^{2+} on a conventional orthorhombic site in KF is reported for the first time.

The diffusion of either ytterbium or europium into NaF results in the formation of a separate phase of YbF_2 or EuF_2 respectively. Phases of the type EuX_2 are also observed in thermally aged NaCl and NaBr crystals.

A new coloration technique known as aliovalent coloration is described for the alkali halides. Coloration consists of a number of concentric zones and these are investigated by use of a novel traversing-slit apparatus. New colour centres based on water related defects are observed in KF. A new defect centre is also observed in KCl and KBr. This is attributed to a U-centre perturbed by an impurity-vacancy complex.

To the memory of my mother

CONTENTS

FIGURES

ACKNOWLEDGEMENTS

First and foremost my thanks go to my supervisor Dr M.J.A.Smith for his unbounded enthusiasm and unflagging interest throughout. Were it not for his reassurance and encouragement at one particular stage of this study, this thesis may never have even been started. Many thanks also go to Mr C.F.Randle for his engineering skill and a remarkable ability to transform a rough sketch into a useful piece of apparatus. The success of this project is due in large part to his endeavour and invention. I would also like to take this opportunity to thank the many other students and staff within the Physics Department who contributed either knowingly or unknowingly to this work. In particular, a special mention must go to Dr J.M.Dixon for many helpful discussions during the development of the detailed theoretical aspects. Access to the computer unit's facilities for the many calculations associated with the application of this theory is also much appreciated.

The completion of this thesis became a long and protracted affair and I am indebted to the patience and understanding of family, friends and colleagues during this period. The process was eased to some extent by the assistance of the drawing office at Standard Telecommunication Laboratories Ltd in the preparation of a number of the figures and also ready access at STL to a wordprocessor and printer.

Finally, I would like to thank the Science and Engineering Research Council for financial support.

ACKNOWLEDGEMENTS

First and foremost my thanks go to my supervisor Dr M.J.A.Smith for his unbounded enthusiasm and unflagging interest throughout. Were it not for his reassurance and encouragement at one particular stage of this study, this thesis may never have even been started. Many thanks also go to Mr C.F.Randle for his engineering skill and a remarkable ability to transform a rough sketch into a useful piece of apparatus. The success of this project is due in large part to his endeavour and invention. I would also like to take this opportunity to thank the many other students and staff within the Physics Department who contributed either knowingly or unknowingly to this work. In particular, a special mention must go to Dr J.M.Dixon for many helpful discussions during the development of the detailed theoretical aspects. Access to the computer unit's facilities for the many calculations associated with the application of this theory is also much appreciated.

The completion of this thesis became a long and protracted affair and I am indebted to the patience and understanding of family, friends and colleagues during this period. The process was eased to some extent by the assistance of the drawing office at Standard Telecommunication Laboratories Ltd in the preparation of a number of the figures and also ready access at STL to a wordprocessor and printer.

Finally, I would like to thank the Science and Engineering Research Council for financial support.

1. INTRODUCTION

1.1 General introduction

Considerable effort has been devoted in the past to the study of impurity ions in crystalline solids. Many interesting physical phenomena occur in systems of this type and these are broadly divisible into two distinct areas; the effect that the impurity ion has on the physical properties of the host crystal and, conversely, the influence of the crystalline environment on the properties of the impurity ion. Important categories of the first group are the optical and electrical properties of doped semiconductors [1,2], the mechanical properties of impure crystals [3,4] and the impurity-induced conductivity of ionic crystals [5]. The second group includes the optical properties of ions in crystals [6,7] and the electron spin resonance (ESR) of paramagnetic impurities [8,9]. The study presented here is concerned primarily with this second group and it aims, in particular, to describe how the optical absorption spectrum associated with an impurity ion is dependant on the precise nature of the host crystal. By concentrating on a wide range of structurally similar host crystals a successful correlation is obtained.

The electronic energy level structure of the free ion state has been determined from spectroscopic data for the majority of elements and valence states [10,11]. When the ion is introduced into a crystalline lattice these energy levels are modified by the charge density associated with the neighbouring crystal ions. The energy level structure of the ion is determined qualitatively by the symmetry of its immediate crystalline environment and quantitatively by the specific arrangement, proximity and effective charge of the lattice constituents.

Two different approaches are available to describe the interaction between the crystal and the impurity ion. In an ionic crystal, where the charge densities are localised, it is possible to obtain excellent results

by representing the lattice ions surrounding the impurity ion as an electric field of the appropriate magnitude and symmetry. The resulting energy levels are essentially derived from the free ion states. This method was introduced by Bethe [12] and Becquerel [13] in 1929 and is known as crystal or ligand field theory. When a covalently bonded crystal is involved, the overlap of crystal and impurity wavefunctions is appreciable and the individual charge densities are no longer localised. The resultant energy levels are derived from combined crystal-impurity states. The bonding and antibonding energy levels so produced bear little or no resemblance to the free ion energy levels. This approach is described by the molecular orbital theory [14,15]. Both approaches have achieved a large amount of success in the past, despite the fact that the real situation requires an approach falling somewhere inbetween the two extremes. In practice, it is normally sufficient to select the most appropriate scheme and to consider any deviations in the light of the complementary approach.

An experimental determination of the electronic energy level structure of an impurity ion is obtained by observing the absorption or emission of energy due to the excitation of transitions between levels. In a large number of cases the separation between these energy levels makes them accessible to study by optical absorption/emission techniques. Commercially available spectrophotometers routinely encompass an energy range of approximately 0.05 eV (400 cm^{-1}) to 6.5 eV (52300 cm^{-1}) or alternatively 25 μm to 190 nm (1 eV = 8044.24 cm^{-1}). Optical absorption measurements have received the most comprehensive treatment in the past and form the basis of the study presented here. Phosphorescence and fluorescence are related but, in general, less useful techniques.

Under certain conditions it is possible to observe energy absorption in the microwave region, resulting from an interaction between the system and a d.c. magnetic field. A basic requirement for the occurrence of such

an interaction is that the impurity ion/entity should be paramagnetic. An equivalent condition is that it should possess half integral spin angular momentum. This technique is known as ESR (Electron Spin Resonance) and it is an extremely powerful technique in that it provides detailed information on the symmetry of the crystal site occupied by the paramagnetic impurity ion.

Transitions are not necessarily observed between all of the energy levels of the system due to certain quantum mechanical considerations. Central to a derivation of these selection rules is the mathematical representation theory of groups which enables one to determine whether or not a particular transition is allowed on purely symmetry grounds. An appreciation of this extremely powerful technique is of great importance and therefore chapter 2 is devoted to a discussion of the relevant principles followed by a derivation of the necessary assessment techniques.

In order to illustrate the validity of a model that is proposed to describe the behaviour of a particular system, it is necessary to perform a detailed energy level calculation. A successful comparision is required between the observed transition energies and the energies of the allowed transitions predicted by the theory. Chapter 3 concentrates on a formulation of the required mathematical techniques.

The theoretical techniques which are described in chapters 2 and 3 have been applied successfully to the study of numerous impurity ions in an extensive range of host crystals. For example, the behaviour of ions from the first transition metal series possessing an incompletely filled 3d shell, are well understood [6,7,16]. The second and third transition metal series may be treated in an analagous way with similar success. The situation for the rare earth ions is, however, fundamentally different. In this case the unfilled 4f shell is no longer the outermost level, being situated within, and partially shielded by, two filled shells (5s and 5p). This property leads, in general, to rather more subtle crystal field

effects [17].

The study presented here concentrates on two particular rare earth ions, ytterbium and europium, as impurities in a broad range of alkali halide crystals. Each of the two components, that is the impurity ions and their hosts, are now discussed separately in more detail prior to a consideration of the combined system.

1.2 The rare earths

The rare earths are a group of elements characterised by the progressive filling of the 4f shell. The free atoms possess the general atomic configuration $(Xe)4f^n5s^25p^6s^2$, where (Xe) indicates a closed Xenon configuration and $1 \leq n \leq 14$. A typical charge distribution [18] for the various different atomic shells is shown in figure 1.1. It should be noted that the incomplete 4f shell lies deep within the outer completed shells and it is this feature in particular which leads to the interesting physical and chemical properties of the rare earths.

The absorption of energy by the free ion is accompanied by the promotion of an electron residing in the $4f^n$ shell into one of the unoccupied higher energy orbitals 5d, 6s, 6p etc. The resulting configurations are referred to as $4f^{n-1}5d$, $4f^{n-1}6s$, $4f^{n-1}6p$ etc. The study of the low lying configurations for both doubly and triply ionised ions is essentially complete [17]. The position of the centres of gravity of these elementary configurations are indicated in figure 1.2.

Another class of transitions involves excitations within the $4f^n$ shell. These transitions are not strictly allowed since they do not involve a change in parity and consequently produce only a very weak set of absorption bands. These absorption bands have been widely studied for the trivalent ions in a wide range of host crystals and site symmetries, and are found to resemble very closely the free ion absorption spectrum. This

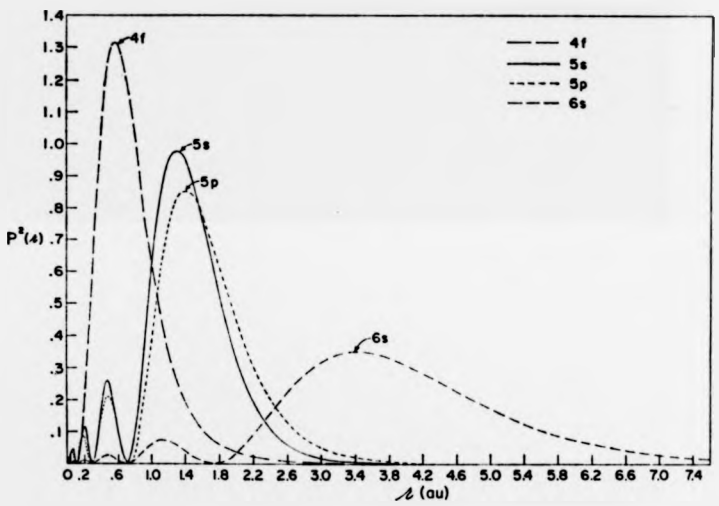

Figure 1.1 Square of the radial wavefunctions for the 4f, 5s, 5p and 6s orbits in Gd^+ showing that the 4f orbits lie well inside the ion (after Freeman and Watson [18]).

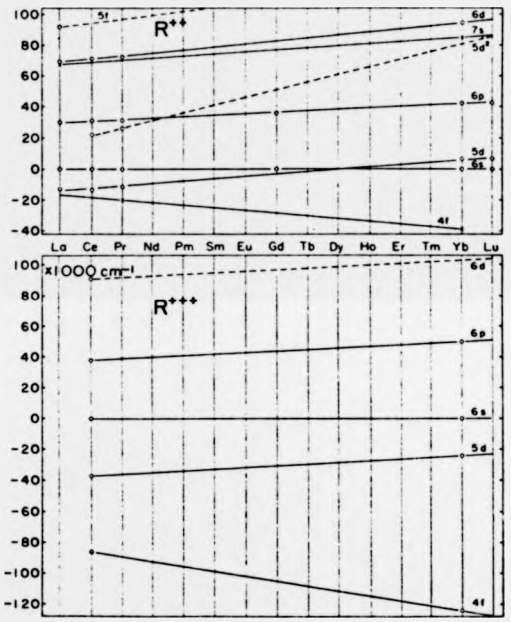

Figure 1.2 Relative positions of the centres of the main configurations of the divalent and trivalent rare earth ions, as derived from empirical data (after Dieke [17]).

property is attributed to the shielding effect provided by the outer filled 5s and 5p shells. Analagous transitions in the divalent ions are normally masked by the much stronger allowed $4f^n - 4f^{n-1}5d$ transitions which occur at a lower energy in this case (see figure 1.2).

The rare earth atoms become ionised on entering a crystal, losing electrons from the 6s and 4f shells. They form chiefly trivalent ions, although there are two notable exceptions. Due to the extra stability gained by the completion of the half filled or completely filled 4f shell it is found that divalent europium (Eu^{2+}, $4f^7 5s^2 5p^6$) and divalent ytterbium (Yb^{2+}, $4f^{14} 5s^2 5p^6$) occur preferentially. Divalent samarium (Sm^{2+}, $4f^6 5s^2 5p^6$) also occurs to a lesser extent.

The rare earths europium and ytterbium are in many respects very similar. The presence of the half filled and filled 4f shell respectively, which is responsible for their stable occurrence in the divalent state, means that both ions possess a spherically symmetric s-like ground state. The most important class of transitions for both ions is from the s-like ground state to levels of the $4f^{n-1}5d$ configuration. These transitions give rise to absorption bands in the accessible near ultraviolet spectral region. Eu^{2+} and Yb^{2+} differ considerably, however, in the detail of their ground and excited state configurations with the situation for Eu^{2+} being considerably more complex than for Yb^{2+} [17,18]. The $4f^7$ ground state configuration of Eu^{2+} consists of a total of 327 levels of which the $^8S_{7/2}$ level is situated at lowest energy. In addition, the excited state configuration $4f^6 5d$ consists of 2725 levels. A direct calculation for the Eu^{2+} ion is unobtainable even in its simplest free ion form and in order to perform a theoretical calculation it is necessary to make certain simplifying assumptions. By way of comparison, the $4f^{14}$ configuration for Yb^{2+} consists of just one level, $^1S_0$, and the excited state contains only 20 levels. It is a relatively simple matter to perform an "exact" calculation of the positions of the 20 levels of Yb^{2+} free ion. Furthermore, it is possible to treat the

effect of the crystal field on the Yb^{2+} levels in a similar direct way, thus providing a clear understanding of the physical situation. Information obtained from the Yb^{2+} case can be used to advantage when choosing a suitable scheme for approximation in the Eu^{2+} case.

The complexity of the optical absorption spectrum of Eu^{2+} and its theoretical intractibility, particularly in a crystalline host, is balanced to some extent by the detailed information obtained from the observation of ESR. A large amount of work has been performed previously on the ESR of Eu^{2+} in many different hosts, including the alkali halides [19-24], the alkaline earth halides [25-27] and the silver halides [28], and it is consequently well characterised. The divalent ytterbium ion is diamagnetic, containing an even number of electrons in the closed 4f shell and does not exhibit ESR. The property of paramagnetism represents the most fundamental difference between Eu^{2+} and Yb^{2+} ions.

The complementary nature of Eu^{2+} and Yb^{2+} ions makes them an interesting system to compare and contrast. It is anticipated that a study of the properties of both ions when introduced into the alkali halides will provide much useful information on the details of their incorporation. The use of a series of host crystals with properties which are in general well characterised is expected to simplify the ensuing analysis. The relevant physical and chemical properties of the alkali halides are outlined in the following section.

1.3 The alkali halides

1.3.1 General

The alkali halides are typical ionic compounds possessing the general form MX, where M denotes a positively charged alkali metal ion (cation) and X denotes a negatively charged halogen ion (anion). The majority of the alkali halides crystallise in the 6-coordinated rocksalt structure ($Fm\bar{3}m$,

or alternatively O_h^5). The cesium halides provide the exception, crystallising in an 8-coordinated structure, but will not concern us here.

Alkali halide crystals are large band gap insulators exhibiting a broad spectral region of optical transparancy extending from the far infrared to the far ultraviolet. Infrared absorption extends from about 0.02 eV to 0.05 eV (60 μm to 25 μm) and is due to interactions between incident photons and the vibrational modes of the lattice (phonons). The ultraviolet absorption corresponds to electronic transitions across the fundamental electronic energy gap. The lower energy limit or fundamental absorption edge for the latter process ranges from about 6 eV to 8 eV (200 nm to 150 nm). This broad range of spectral transparency makes these crystals particularly suitable hosts for the study of optical absorption spectra associated with impurity ions.

1.3.2 The defect structure

At finite temperatures, the crystal deviates from the ideal structure as a result of purely thermodynamic considerations. Point defects are created in order to minimise the free energy of the system [29]. In the alkali halides the predominant defect is the Schottky pair which consists of a vacant cation lattice site V_K' and a vacant anion lattice site $V_{Cl}^{\cdot}$. Cation and anion vacancies are created in equal concentrations to maintain overall charge neutrality.

The defect notation used above and throughout this text is due to Kröger [30]. A letter is used to indicate the primary nature of the defect, such as V for a vacancy, K for a potassium atom or e for a quasi-free electron. A subscript is added to indicate the site that this entity occupies in the crystal, for example the subscript Cl denotes a chlorine anion site or i denotes an interstitial position. Finally a superscript is used to indicate the effective charge of the defect, which

is defined as the difference in the charge of the crystal with the imperfection against the (ideal) crystal without the imperfection. A dot, dash, or cross is used to indicate a positive, negative or zero effective charge respectively. As a specific example, the symbol $Yb_K^{\cdot}$ indicates a divalent ytterbium ion occupying a univalent potassium lattice site and possessing a unit positive effective charge.

The association of two or more defects is indicated by enclosing the assembly in parenthesis. The effective charge for the total combination is indicated in an analagous way. For example, the symbol $(Yb_K^{\cdot}V_K^{'})^{\times}$ denotes a divalent ytterbium-cation vacancy complex of overall charge neutrality.

There are numerous intrinsic point defect centres occuring in the alkali halides based upon the anion and cation vacancies. The most important of these consists of an electron trapped in the potential field of an anion vacancy. The resulting defect centre $V_K^{\times}$ is the well known F-centre. Many other defect centres have been discovered and their properties have been comprehensively studied [31-33]. One of the most important characteristics of these centres is that they introduce new optical absorption bands within the normally transparent region of the crystal. The characteristic coloration attained by the crystal in the presence of such defects gives rise to their collective designation as colour centres. A brief survey is included below to acquaint the reader with the various colour centres that will be encountered later in this study. A more comprehensive treatment can be found in any of the numerous textbooks on this subject [31-33].

The standard model for the F-centre is indicated schematically in figure 1.3 along with its characteristic optical absorption spectrum. Optical absorption results from the excitation of the trapped electron from its s-like ground state into an excited p-type orbital. A transition of this type is strongly allowed with oscillator strengths close to unity (0.8 to 0.9). Strong phonon coupling leads to a broadening of the absorption

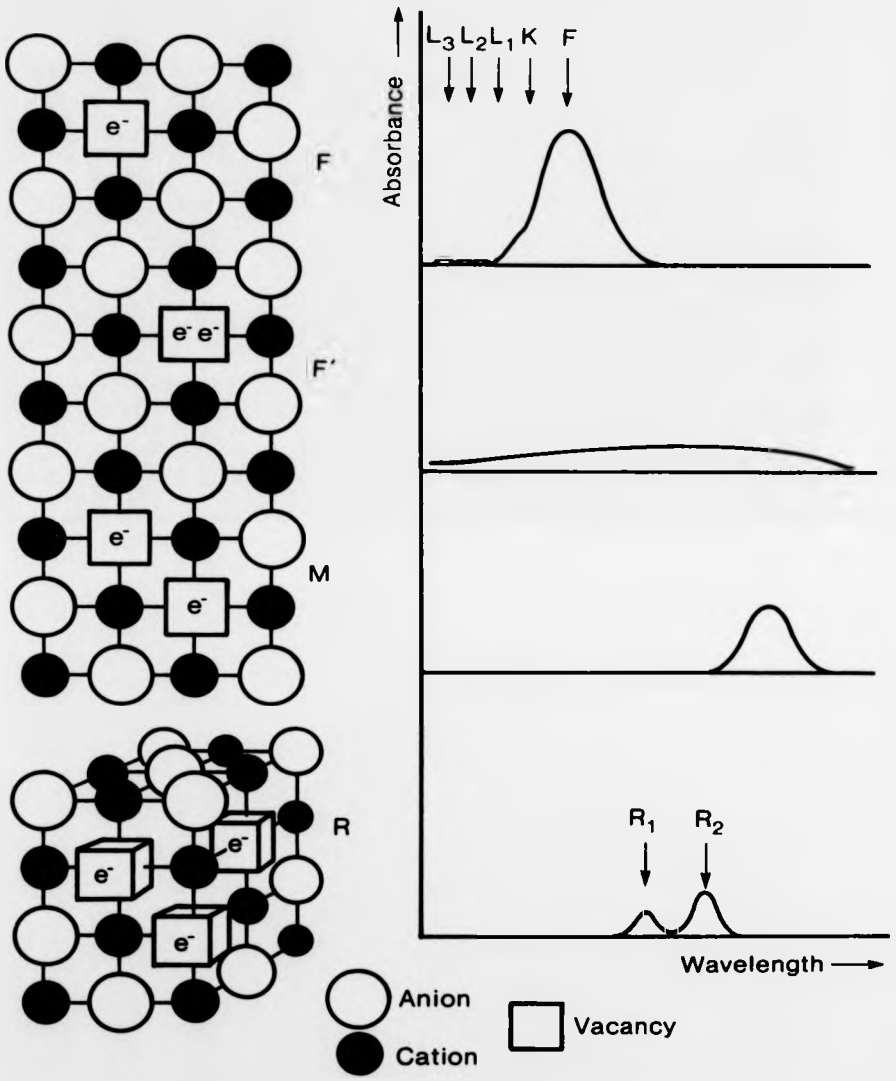

Figure 1.3 A schematic representation of the most important excess electron colour centres, indicating their characteristic optical absorption bands.

into an approximately Gaussian band [34]. The wavelength of the F-band maximum is found to depend monotonically on the host crystal lattice parameter d. An empirical relationship, derived by Mollwo [35] and subsequently improved by Ivy [36], to describe this dependence is given by

$$\lambda_{max} = 703d^{1.84} \qquad 1.1$$

where λ_{max} and d are in Angströms (Å). This is known as the Mollwo-Ivy relation. The much weaker K, L_1, L_2 and L_3 absorption bands, also indicated in figure 1.3, are associated with transitions to progressively higher excited states of the F-centre.

The F-centre is able to trap another electron producing an F'-centre (see figure 1.3). The resulting optical absorption is rather broad and indistinct even at very low temperatures. This second electron is only weakly bound and consequently the F'-centre is unstable at room temperature. However, a significant feature of this defect is that it acts as an important intermediary in many colour centre phenomena, including diffusion and aggregation.

The aggregation of F-centres on nearest neighbour sites $(V_X^{\times})_n$ produces the M, R, N etc centres for n = 2, 3, 4 etc. The F-aggregate centres give rise to absorption bands situated on the long wavelength side of the F-band. The structure and associated absorption of the most important of these are indicated in figure 1.3. Higher order aggregation is characterised by a tendency to form colloidal particles. Absorption bands due to colloidal particles of various sizes are situated at long wavelengths and are identified normally by their insensitvity to temperature variations. The X-band, which is thought to be a small diameter colloid centre, is an interesting exception since it exhibits a dependence on temperature and lattice parameter typical of an atomically dispersed centre.

In addition to the electron excess centres described above, electron deficient or hole excess centres are also encountered and are termed collectively V-centres. The two most important hole centres are indicated in figure 1.4. The simplest of these is the V_K-centre (not to be confused with a potassium vacancy) which is basically a self-trapped hole in the configuration of a halogen ion molecule X_2^- lying along the <110> axes of the crystal. The V_K-centre is stable only at low temperatures. At high temperatures the most important hole excess centre is the V_2-centre $(V_m^x)_2$. The antimorph of the F-centre does not appear to exist. Optical absorption bands associated with the V-centres tend to be situated in the near ultraviolet spectral region.

There are three general methods for producing colour centres in the alkali halides; additive coloration, electrolytic coloration or by exposure to ionising radiation. The first two methods rely on altering the stoichiometry of the crystal. The production of an excess of either the alkali or halogen component requires the incorporation of additional electrons or holes respectively in order to retain overall charge neutrality. These particles subsequently become trapped at suitable lattice sites producing the required colour centres. In the first method the crystal is heated in the vapour of one or other of its constituents. The second method requires the application of an electric field at an elevated temperature. The stoichiometric excess is produced by electrolysis and is accompanied by charge-compensating electron or hole injection. The third method uses X-rays or an electron beam to produce both excess electron and hole centres simultaneously and does not alter the stoichiometry of the crystal.

One advantage of the third method is that it can be used to produce colour centres in a complete range of alkali halide crystals. The first two methods are widely reported to be ineffectual in colouring the alkali fluorides [37-41]. The reasons for this anomalous behaviour are not fully

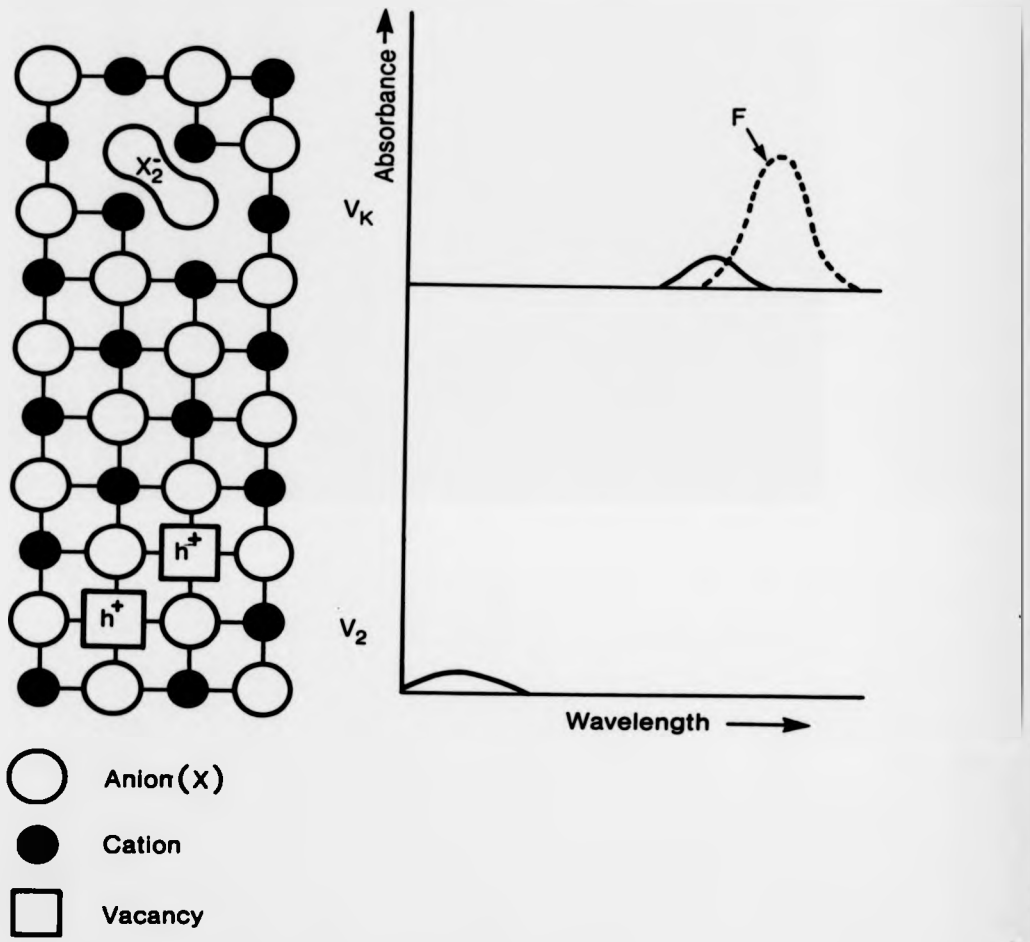

Figure 1.4 A schematic representation of the most important excess hole colour centres, indicating their characteristic optical absorption bands.

understood at present. This aspect will be considered in more detail in chapter 7 in the light of new information contained therein.

1.3.3 Impurities and related defect states

Divalent impurity ions are normally accommodated on substitutional sites in the alkali halides. The additional electric charge is balanced by the formation of an equal number of oppositely charged vacancies. Below a certain temperature, which is dependent on the precise nature of the impurity and the host crystal, the impurity and its charge compensating vacancy occupy nearest neighbour sites forming an impurity-vacancy (I-V) complex.

The local symmetry about the impurity ion is no longer octahedral (O_h) but is reduced by the vacancy lying along the <110> direction to orthorhombic (C_{2v}). This is confirmed by ESR measurements [8,9,19-28] which are particularly sensitive to the local symmetry about the impurity. The occurrence of an I-V complex is further confirmed by workers studying the dielectric loss associated with its dipole moment [42].

The interaction between impurity ions, their associated vacancies and the intrinsic crystal defect centres leads to a secondary set of perturbed colour centres. These are known as F_A-centres when the impurity is univalent and Z-centres when the impurity is divalent. The F_A-centre [44], illustrated schematically in figure 1.5, consists of an isoelectronic impurity ion B situated next to an F-centre along the <100> direction $(V_x^{\cdot}B_h^{\times})^{\times}$. The electric dipole transition from the ground state to the lowest excited state of the F-centre is split into two due to the corresponding reduction in symmetry (C_{4v}). Two distinct cases arise, usually denoted by F_A(I) and F_A(II), depending on whether the most intense transition, which is always the higher energy of the two, is situated at a higher or lower energy respectively than that of the unperturbed F-centre. The F_A(I)

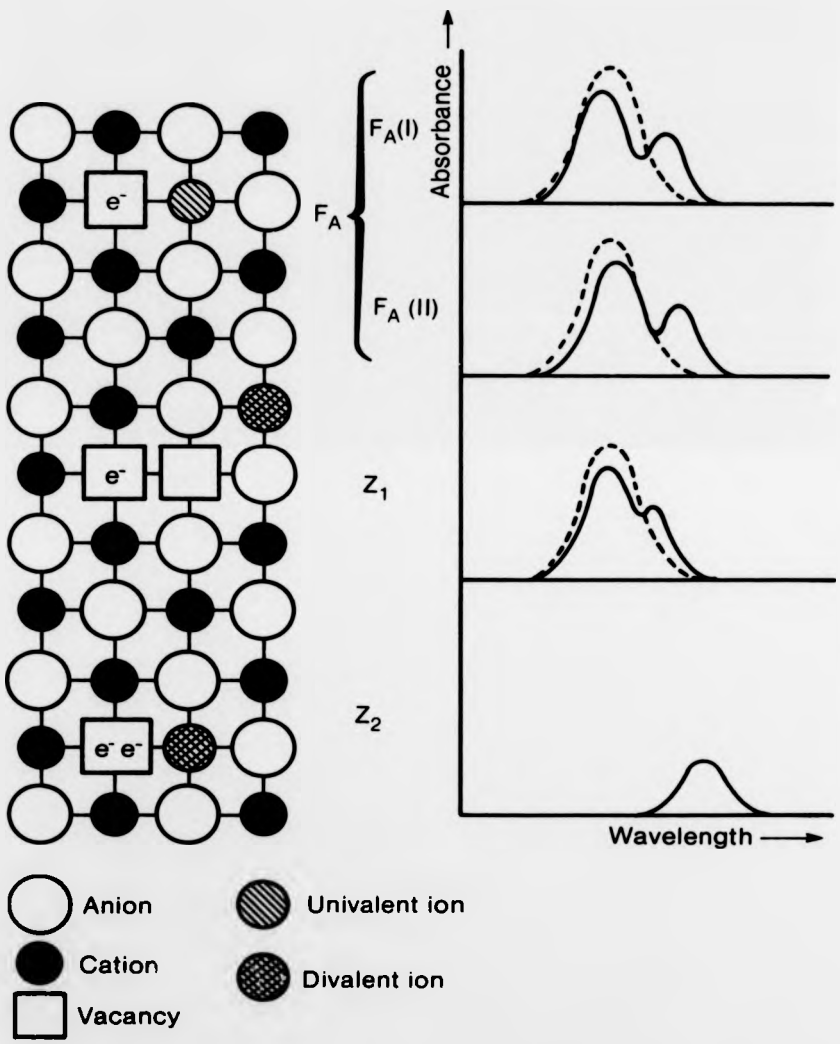

Figure 1.5 A schematic representation of the most important impurity related colour centres, indicating their characteristic optical absorption bands.

type centre dominates in practice.

The Z-centres are more numerous and complex and, consequently, less well understood. At least five different centres have been reported to date and various models have been proposed [30]. The most important are the Z_1- and Z_2-centres whose identities are fairly well established. They are illustrated schematically in figure 1.5. The Z_1-centre consists of a cation vacancy next to an F-centre with the divalent impurity ion D situated nearby (possibly along the <210> direction), that is $(D_M^{\cdot}V_M^{''}V_X^{\times})'$. The Z_2-centre can be envisaged as an F'-centre situated next to the divalent ion, that is $(D_M^{\cdot}V_X^{\cdot})'$, although the real situation is probably more complex [44,45].

Not all divalent ions produce Z-centres. In some cases it appears more favourable for the divalent ion itself to trap an electron and revert to the univalent state. This behaviour seems to be related to the electronegativity of the ion. Trapping of an electron occurs for those ions possessing high electronegativity values such as Zn^{2+}, Cd^{2+}, Mn^{2+} or Pb^{2+} [14,17]; while Ca^{2+}, Ba^{2+}, Sr^{2+} and the divalent rare earth ions give rise to Z-centres.

1.4 References

1. S.M.Sze, "Physics of Semiconductor Devices", Wiley-Interscience, N.Y.(1969)

2. K.Seeger, "Semiconductor Physics", Springer Verlag, Wien (1973)

3. R.Steinbrech et al, Physica Status Solidi A, 46, p107 (1978)

4. D.F.Stein in "International Conference on the Deformation of Crystalline Solids, 1966, Ottawa", Canadian Journal of Physics, 45, (1967) and references therein.

5. A.B.Lidiard, Handbuch der Physik, XX, p246 (1957)

6. D.L.Wood in "Optical Properties of Solids", Ed. Sol Nudelman and S.S.Mitra, Plenum press, N.Y.(1969)

7. D.S.McClure, Solid State Physics, 9, p399 (1959)

8. J.W.Orton, "Electron Paramagnetic Resonance", Iliffe books, London (1968)

9. G.E.Pake and T.L.Estle, "The Physical Principles of Electron Paramagnetic Resonance", 2nd Edition, W.A.Benjamin, Mass (1973)

10. C.E.Moore, "Atomic Energy Levels", Volume I, National Bureau of Standards, Washington (1949); Volume II and III, National Bureau of Standards, Washington (1958)

11. W.C.Martin et al., "Atomic Energy Levels-The Rare Earth Elements", National Bureau of Standards, Washington (1978)

12. H.Bethe, Annalen der Physik Leipzig, 3, p133 (1929)

13. J.Becquerel, Zeitschrift fur Physik, 58, p205 (1929)

14. P.G.Perkins, "Elementary Molecular Bonding Theory", Methuen and Co. Ltd, London (1969)

15. C.A.Coulson, "Valence", Chap. IV, Oxford University Press (1952)

16. J.S.Griffith, "The Theory of Transition Metal Ions", Cambridge University Press (1961)

17. G.H.Dieke, "Spectra and Energy Levels of Rare Earth Ions in Crystals", Ed. H.M.Crosswhite and H.Crosswhite, Interscience, J.Wiley and Sons, N.Y.(1968)

18. A.J.Freeman and R.E.Watson, Physical Review, 127, p2058 (1962)

19. P.G.Nair et al., Journal of Physics and Chemistry of Solids, 29, p2183 (1968)

20. G.Aguilar S. et al., Journal of Chemical Physics, 60, p4665 (1974)

21. J.Rubio O. et al., Journal of Chemical Physics, 61, p5273 (1974)

22. G.Aguilar S. et al., Journal of Chemical Physics, 62, p1197 (1975)

23. E.Munoz P. et al., Journal of Chemical Physics, 62, p3416 (1975)

24. J.Boldu O. et al., Journal of Chemical Physics, 67, p2391 (1977)

25. A.A.Manenkov and A.M.Prokhorov, Soviet Physics Doklady, 1, p196 (1956)

26. J.M.Baker et al., Proceedings of the Royal Society, A247, p141 (1958)

27. V.M.Vinokurov et al., Soviet Physics Solid State, 5, p1415 (1964)

28. S.U.Cheema and M.J.A.Smith, Journal of Physics C, 4, p1231 (1971)

29. N.F.Mott and R.W.Gurney, "Electronic Processes in Ionic Crystals", 2nd. Edition, Dover Publications, N.Y.(1964)

30. F.A.Kröger, "The Chemistry of Imperfect Crystals", 2, 2nd revised Edition, North Holland Publishing Co., Amsterdam (1974)

31. J.H.Schulman and W.D.Compton, "Colour Centres in Solids", Pergamon Press, Oxford (1963)

32. W.B.Fowler Editor, "Physics of Colour Centres", Academic Press, N.Y. and London (1968)

33. J.J.Markham, "F-centres in Alkali Halides", Solid State Physics, Supplement 8, Academic Press, N.Y. and London (1966)

34. D.L.Dexter, Physical review, 133A, p1717 (1964)

35. E.Mollwo, Nachr. Ges. Wissen. Gottingen, p97 (1931)

36. H.Ivey, Physical Review, 72, p341 (1947)

37. P.Gorlich et al., Physica Status Solidi, 3, p1629 (1963)

38. P.Podini, Physica Status Solidi, 9, p737 (1965)

39. C.H.Jirgal et al., American Journal of Physics, 37, p963 (1968)

40. W.C.Collins et al., Applied Physics Letters, 24, p403 (1974)

41. K.I.Jawad and M.J.A.Smith, Philosophical Magazine B, 37, p585 (1978)

42. G.Guemer, Zeitschrift fur Physik, 215, p256 (1968)

43. F.Luty in "Physics of Colour Centres", Ed. W.B.Fowler, Academic Press, N.Y. and London (1968)

44. G.Kenntner and H.J.Paus, Zeitschrift fur Physik B, 25, p219 (1976)

45. H.J.Paus and K.M.Strohm, Zeitschrift fur Physik B, 34, p263 (1979)

2. GROUP THEORY

2.1 Introduction

The following treatment of group theory forgoes the usual mathematical rigour. It is intended to provide the basis for the techniques used later and therefore only those concepts of direct relevance are considered. A more complete treatment can be found in the standard texts (see, for example, references [1],[2] and [3]).

The treatment will concentrate on deriving the symmetry properties of two of the most important symmetry groups; the 3-dimensional rotation-inversion group O(3) and the full octahedral point symmetry group O_h. The former describes the symmetry operations under which a free atom or ion is invariant while the latter describes the point symmetry operations associated with a lattice of the alkali halide type.

2.2 Abstract group theory

2.2.1 Axioms

A group G is a set of distinct elements (E,A,B,C,....) endowed with a law of composition called multiplication such that:

(i) the product of any pair of elements is also an element of G (closure property)

$$AB \in G \qquad \forall A,B \in G \tag{2.1}$$

(ii) the associative law is valid

$$A(BC)=(AB)C \qquad \forall A,B,C \in G \tag{2.2}$$

(iii) the set contains an identity element E

$$\exists E \in G \quad \ni EA = AE = A \quad \forall A \in G \tag{2.3}$$

(iv) for each element of G there exists an inverse element

$$\forall A \in G \quad \exists B \in G \quad \ni AB = BA = E \tag{2.4}$$

The number of elements comprising a group is called the order of the group. Groups are broadly divisible into finite and infinite groups depending on whether they contain a finite or infinite number of elements respectively. An infinite group may have the additional property that its elements are denumerably infinite (discrete group) or non-denumerably infinite (continuous group).

If all of the elements of the group commute, that is $AB = BA \quad \forall A,B \in G$, then the group is said to be commutative or Abelian. The way in which all of the elements combine under multiplication specifies the group.

2.2.2 Conjugate elements

If the following relationship exists between the elements of a group G

$$A^{-1}BA = C \tag{2.5}$$

then we say that B and C are conjugate elements. The set of all such conjugate elements is known as a conjugacy class, or simply a class, of G. Equation 2.5 is said to represent a similarity transformation of B by A.

2.2.3 Subgroups

A set H is a subgroup of a group G if:

(i) the elements of H are contained in G

(ii) H is itself a group under the same law of composition as that of G.

If the subgroup consists of complete classes of the larger group then it is known as a normal subgroup.

2.2.4 Direct product of groups

The direct product of two groups $H = (E, H_2, H_3, \ldots, H_h)$ of order h and $K = (E, K_2, K_3, \ldots, K_k)$ of order k is defined as a group G of order $g = hk$ where

$$\begin{aligned} G = H \otimes K &= (E, H_2, H_3, \ldots, H_h) \otimes (E, K_2, K_3, \ldots, K_k) \\ &= (E, EK_2, EK_3, \ldots, EK_k, H_2K_2, \ldots, H_2K_k, \ldots, H_hK_k) \end{aligned} \qquad 2.6$$

provided that:

(i) each element of H commutes with every element of K

(ii) the only common element is the identity element E.

2.3 Representation theory of finite groups

A group as defined above is essentially an abstract mathematical concept. The representation theory of groups provides the link between this abstract concept and real physical situations. We will now consider the theory as applied to transformations, such as rotation, reflection and inversion (point symmetry operations), under which a physical system is invariant. The set of all such symmetry transformations form a group called the symmetry group of the system.

The elements of a symmetry group of a physical system are interpreted as operators acting upon a 3-dimensional vector space. In order to define

the result of an operation in a 3-dimensional vector space we need to choose a set of 3 orthonormal basis functions (ϕ_1, ϕ_2, ϕ_3). The operation of a group element A on such a set of basis functions can be suitably represented by a square matrix T(A) according to

$$A\phi_i = \sum_{j=1}^{3} \phi_j T_{ji}(A) \qquad 2.7$$

T(A) is referred to as the matrix representation of A with the basis (ϕ_i).

Each element of the group can be represented by a square 3-dimensional matrix in this way. The set of non-singular matrices has the property

$$T(A)T(B) = T(AB) \qquad \forall A, B \in G \qquad 2.8$$

and is said to be a matrix representation of the group. The order of the matrices of the set T is called the dimension of the representation, in this case 3-dimensional. However T is only a group if all of the matrices are distinct.

A convenient set of orthonormal basis functions in a 3-dimensional vector space is $\underline{e}_1, \underline{e}_2, \underline{e}_3$ defining the three cartesian axes x,y,z. The types of transformation that we shall be concerned with possess the important property of preserving the Euclidean properties of the vector spaces (norms and scalar products). Such an operation results in a new set of orthonormal basis functions and the matrix representations are unitary.

The choice of basis functions is not unique and therefore the form of the matrix representing an operator depends on the particular choice made. In general a matrix representation T(A) may be reduced via a similarity or unitary transformation into a component set of irreducible representations $\Gamma_i(A)$.

$$T(A) = \sum_i a_i \Gamma_i(A) = a_1\Gamma_1(A) \oplus a_2\Gamma_2(A) \oplus \ldots \qquad 2.9$$

where the summation refers to a direct sum addition of matrices (see appendix 1).

It is important to realise that, although the form of the matrix changes under a similarity transformation, the trace is an invariant. The trace suitably characterises the representation irrespective of the choice of basis functions. The trace of the matrix representation Γ is defined as the character X, that is

$$X(A) = \sum_k (\Gamma(A))_{kk} \qquad \forall A \in G \qquad 2.10$$

If we now take the trace of both sides of equation 2.9 we obtain

$$X(A) = \sum_i a_i X_i(A) \qquad 2.11$$

which provides a more convenient method of determining the expansion coefficients a_i.

On reconsidering equation 2.5 it is apparant that conjugate elements are defined as being connected via a similarity transformation. Therefore it follows that elements of a class have the same character and belong to the same irreducible representation. This observation implies that the maximum number of distinct irreducible representations of a group cannot exceed the number of classes. In fact it can be shown that these two quantities are equivalent [1,2,3].

Two additional properties of irreducible representations required later are now simply quoted. Derivations may be found in references [1], [2] or [3].

(i) The dimension l_i of an irreducible representation Γ_i is

related to the order g of the group G by

$$\sum_{i=1}^{c} (l_i)^2 = g \qquad 2.12$$

where c is the number of classes of G.

(ii) The great orthogonality theorem states that

$$\sum_{A \in G} (\Gamma_i(A))_{km} (\Gamma_j^*(A))_{sn} = (g/l_i)\delta(i,j)\delta(k,s)\delta(m,n) \qquad 2.13$$

where $(\Gamma_i(A))_{km}$ represents the (k,m) element of the irreducible representation $\Gamma_i(A)$; similarly for $(\Gamma_j(A))_{sn}$. The asterisk denotes the complex conjugate.

By choosing k = m and s = n in equation 2.13 and summing over k and s, the equation simplifies to give

$$\sum_{A \in G} \Gamma_i(A)\Gamma_j^*(A) = (g/l_i)\delta(i,j)l_i = g\delta(i,j) \qquad 2.14$$

or taking the trace of both sides

$$\sum_{A \in G} X_i(A)X_j^*(A) = g\delta(i,j) \qquad 2.15$$

2.4 The octahedral symmetry group O_h

There are 32 crystallographic point symmetry groups in a 3 dimensional space of which the full octahedral group O_h has the highest symmetry. The point group O_h is the full symmetry group of the cube and has 48 elements. These can be decomposed into 24 proper rotations and 24 improper rotations (rotation plus inversion). Since the inversion operation J commutes with all other operations and forms a two element inversion group (E,J) we have

$$O_h = O \otimes (E,J) \qquad 2.16$$

where O is a normal subgroup of O_h called the octahedral group of proper rotations. A study of the smaller group O will suffice here since it is a trivial matter to include the inversion operation later.

The 24 elements of O are set out below with reference to figure 2.1.

(i) The identity element E (1 element).

(ii) A rotation through 90 degrees about a 4-fold axis C_4^1 (3 elements).

(iii) A rotation through 270 degrees about a 4-fold axis C_4^3 (3 elements).

(iv) A rotation through 180 degrees about a 4-fold axis C_4^2 (3 elements).

(v) A rotation through 180 degrees about a 2-fold axis C_2^1 (6 elements).

(vi) A rotation through 120 degrees about a 3-fold axis C_3^1 (8 elements).

C_n^m denotes a rotation through an angle $2\pi m/n$ about an n-fold axis.

The elements fall into 5 classes (C_4^1 and C_4^3 constitute a single class, denoted by C_4) and so there are 5 irreducible representations $\Gamma_1,\Gamma_2,\ldots,\Gamma_5$. According to equation 2.12 the dimensions l_i of the representations Γ_i satisfy the condition

$$(l_1)^2 + (l_2)^2 + (l_3)^2 + (l_4)^2 + (l_5)^2 = 24 \qquad 2.17$$

The only possible solution gives the dimensions of the irreducible representations as 1, 1, 2, 3 and 3. A commonly encountered labelling scheme for the irreducible representations is A_1, A_2, E, T_1 and T_2 respectively, suitably reflecting these dimensions.

In order to completely define the symmetry properties of a group it is sufficient to tabulate the characters of the individual irreducible representations for each class. This is known as a character table and is given for the group O in figure 2.2. A convenient set of basis functions for the irreducible representations is also indicated in this figure. It is instructive to present the basis functions in a graphical form as

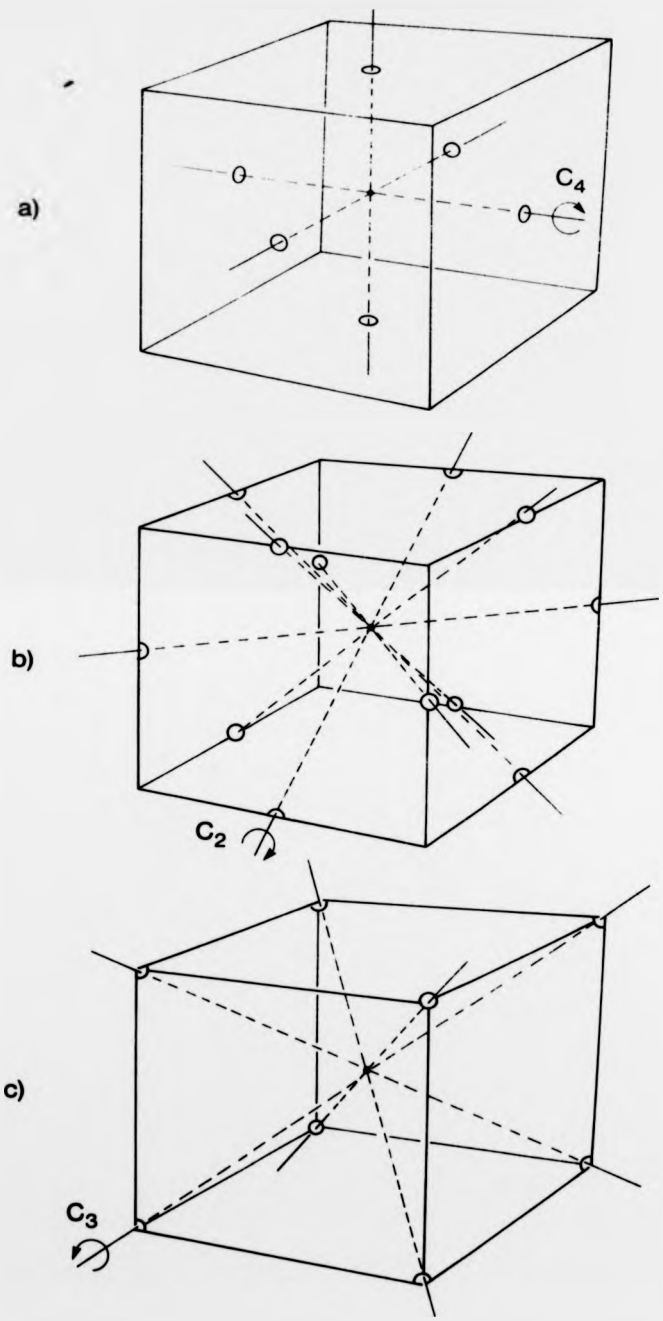

Figure 2.1 The symmetry operations of a cube; (a) 4-fold rotation axes, (b) 2-fold rotation axes and (c) 3-fold rotation axes.

Irreducible representations	E	$6C_4$	$3C_4^2$	$6C_2$	$8C_3$	Basis functions (Classes)
Γ_1	1	1	1	1	1	$x^n+y^n+z^n$; n even
Γ_2	1	-1	1	-1	1	xyz
Γ_3	2	0	2	0	-1	$\{x^2-y^2, 2z^2-x^2-y^2\}$
Γ_4	3	1	-1	-1	0	$\{x, y, z\}$
Γ_5	3	-1	-1	1	0	$\{xy, yz, zx\}$

Figure 2.2 Character table for the point symmetry group O.

illustrated in figure 2.3.

The character table of a symmetry group is constructed using the following basic rules:

(i) $X_i(E) = l_i$, since the representation of the identity element is just the unit matrix.

(ii) $X_1(A) = 1 \quad \forall A \in G$. Here Γ_1 is chosen to be the identity representation.

(iii) For 1 dimensional representations the characters and representations are the same.

(iv) The orthogonality relation between characters (columns) and representations (rows) is invoked to obtain the remaining characters (equations 2.14 and 2.15).

In order to extend these results to the full octahedral symmetry group O_h it is necessary to indicate whether or not the representation changes sign under inversion, that is whether it is of odd or even parity. It is common practice to use the subscripts g or u which are derived from the German words gerade (even) and ungerade (odd). Typical examples are A_{1g}, T_{1u} and Γ_{5u}.

2.5 The 3-dimensional rotation-inversion group O(3)

The group of all rotations and inversions in free space is a simple example of an infinite continuous group. Although the techniques that have been developed so far are specifically applicable to finite groups, it is a simple matter to extend them to embrace simple infinite groups of this kind. By analogy with the treatment already presented for the full octahedral group O_h, it is only necessary to consider the subgroup of O(3) consisting of all proper rotations of the coordinate system SO(3). The relation between the two is

$$O(3) = SO(3) \otimes (E,J) \qquad 2.18$$

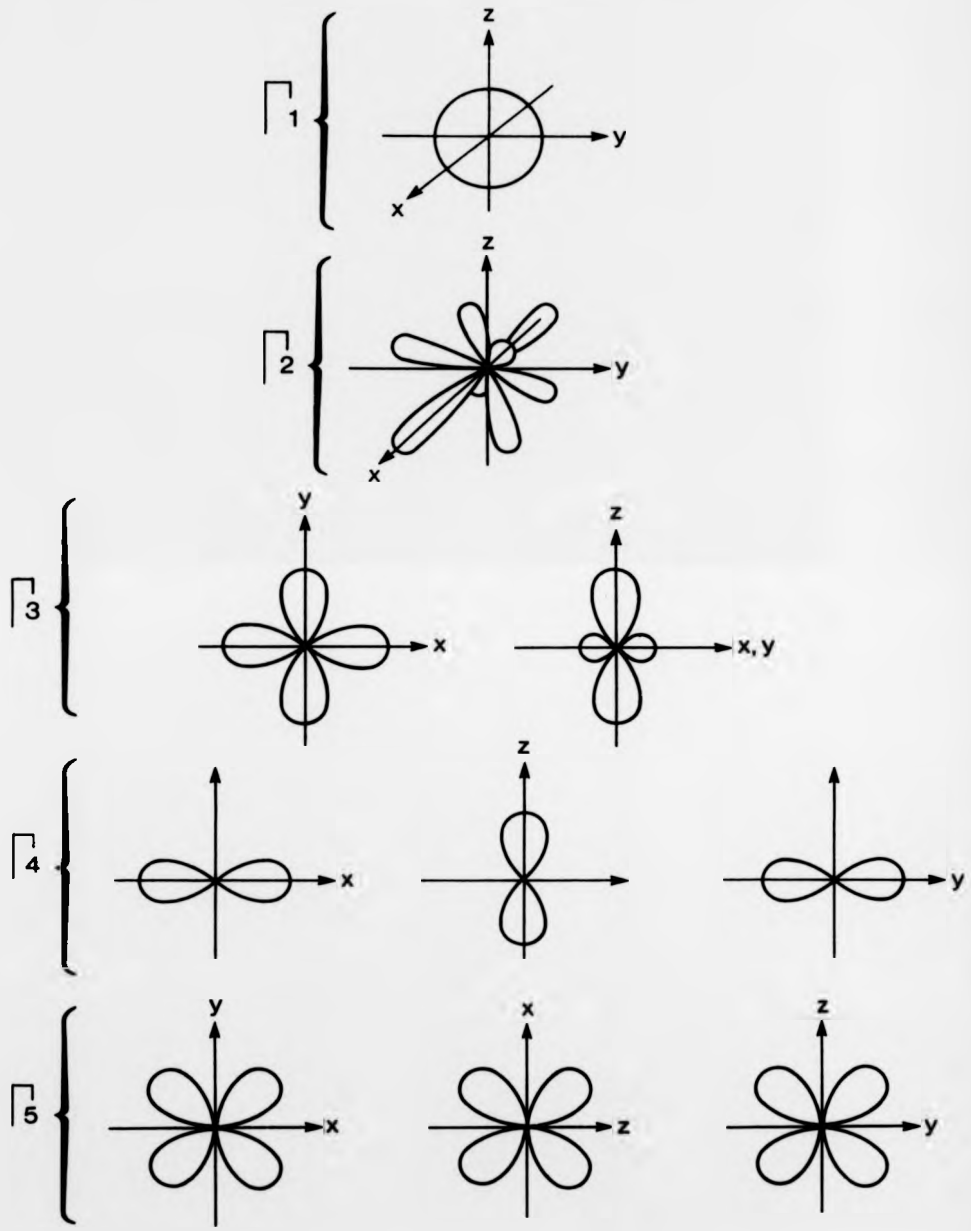

Figure 2.3 A graphical interpretation of the basis functions for the octahedral symmetry group O.

In order to discuss rotations in 3 dimensions, a suitable method is required for expressing a rotation with respect to a cartesian coordinate system (x,y,z). One possibility would be to use the polar coordinates (θ,ϕ,Ψ) to describe a rotation through an angle Ψ about an axis fixed by the parameters θ and ϕ (see figure 2.4(a)). However the most convenient method is to express the rotation in terms of the Euler angle (α,β,γ) (see figure 2.4(b)). A rotation $R(\alpha,\beta,\gamma)$ is defined as consisting of three succesive rotations:

(i) a rotation through an angle α about the z axis $R_z(\alpha)$

(ii) a rotation through an angle β about the new y axis $R_y(\beta)$

(iii) a rotation through an angle γ about the transformed z axis $R_z(\gamma)$

that is

$$R(\alpha,\beta,\gamma) = R_z(\gamma)R_y(\beta)R_z(\alpha) \qquad 2.19$$

The transformation matrix for a general element is obtained by taking the product of transformation matrices for the individual elements according to equation 2.19 yielding

$$R(\alpha,\beta,\gamma) = \begin{pmatrix} \cos\alpha\cos\beta\cos\gamma-\sin\alpha\sin\gamma & \sin\alpha\cos\beta\cos\gamma+\cos\alpha\sin\gamma & \sin\beta\cos\gamma \\ -\cos\alpha\cos\beta\sin\gamma-\sin\alpha\cos\gamma & -\sin\alpha\cos\beta\sin\gamma+\cos\alpha\cos\gamma & -\sin\beta\sin\alpha \\ -\cos\alpha\sin\beta & -\sin\alpha\sin\beta & -\cos\beta \end{pmatrix} \qquad 2.20$$

This is an orthogonal matrix with determinant +1 (unitary matrix).

A suitable set of basis functions for a representation is simply the set of $(2l+1)$ spherical harmonics $Y_l^m(\theta,\phi)$ which transform under rotations into linear combinations of themselves. They are given by

$$Y_l^m(\theta,\phi) = (-1)^m\left(\frac{(2l+1)(l-m)!}{4\pi(l+m)!}\right)^{1/2} P_l^m(\cos\theta)e^{im\phi} \qquad 2.21$$

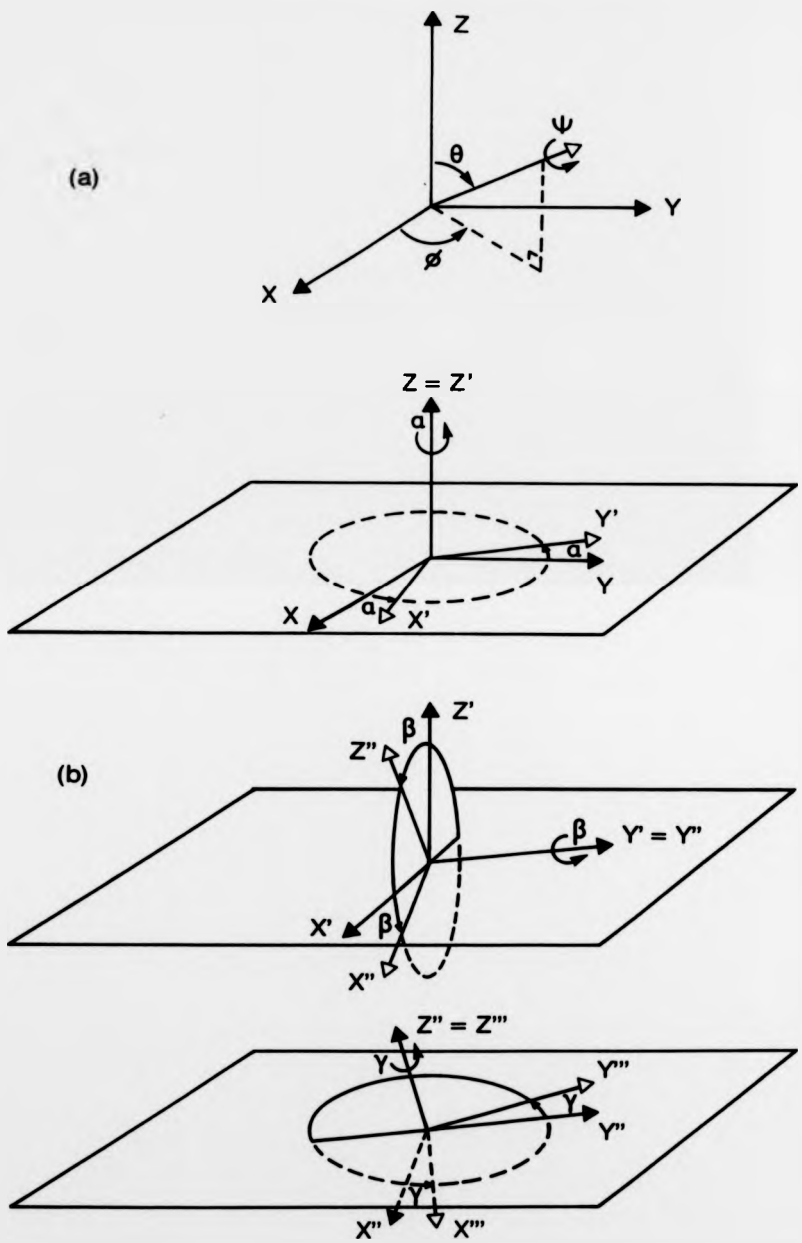

Figure 2.4 Two alternative schemes for expressing a rotation in a 3-dimentional space; (a) Polar co-ordinates and (b) Euler angles. Refer to the accompanying text for an explanation.

with $$P_l^m(x) = \frac{(1-x^2)^{m/2}}{2^l l!} \frac{d^{l+m}}{dx^{l+m}}(x^2-1)^l \qquad 2.22$$

and $$l = 0, 1, 2, \ldots \qquad -l \leq m \leq l$$

The class structure of SO(3) is particularly simple. All rotations through a given angle about all axes belong to a class. The characters of the elements of SO(3) depend therefore on the angle of rotation alone. To determine the character common to all elements of a class corresponding to rotations through an angle α, it is sufficient to choose, with complete generality, a particular axis say z. The action of this rotation $R_z(\alpha)$ on the basis functions is described by

$$\begin{aligned} R_z(\alpha)Y_l^m(\theta,\phi) &= Y_l^m(\theta,\phi-\alpha) \\ &= \exp^{-im\alpha} Y_l^m(\theta,\phi) \end{aligned} \qquad 2.23$$

The matrix representing $R_z(\alpha)$ is therefore diagonal, with a character $X_l(\alpha)$ given by the sum of all such elements for $-l \leq m \leq l$

$$\begin{aligned} X^{(l)}(\alpha) &= \sum_{m=-l}^{l} e^{-im\alpha} = \sum_{m=-l}^{l} e^{im\alpha} \\ &= e^{il\alpha}(1 + e^{i\alpha} + e^{2i\alpha} + \ldots + e^{2il\alpha}) \\ &= \frac{e^{i(l+1/2)\alpha} - e^{-i(l+1/2)\alpha}}{e^{i\alpha/2} - e^{-i\alpha/2}} \end{aligned}$$

giving $$X^{(l)}(\alpha) = \frac{\sin(l+1/2)\alpha}{\sin(\alpha/2)} \qquad 2.24$$

The representations $D^{(l)}$ in this basis are irreducible and are given in the general case by (equation 2.7)

$$R(\alpha,\beta,\gamma)Y_l^m(\theta,\phi) = \sum_{m'=-l}^{l} Y_l^{m'}(\theta,\phi)D_{m'm}^{(l)}(\alpha,\beta,\gamma) \qquad 2.25$$

The extension to O(3) requires the use of four parameters $(\alpha,\beta,\gamma,\delta)$,

where δ indicates the parity of the representation under inversion. This additional parameter is added as a suffix in the form of a plus or minus sign (for example $D^{(1,+)}(\alpha,\beta,\gamma)$).

2.6 Direct product of representations

The direct product (see appendix 1) of two matrix representations Γ_i and Γ_j of a group G is also a representation Γ_k of G. In general Γ_k is reducible giving

$$\Gamma_i \otimes \Gamma_j = \Gamma_k \qquad 2.26$$

with $$\Gamma_k = \sum_n a_n^{ij}\, \Gamma_n \qquad 2.27$$

The direct product of characters is obtained by taking the trace of both sides of equation 2.26

$$X_i X_j = \sum_n a_n^{ij}\, X_n \qquad 2.28$$

If the basis functions for Γ_i are $(\phi_1,\phi_2,\ldots\phi_{l_i})$ and for Γ_j are $(\theta_1,\theta_2,\ldots\theta_{l_j})$, then the direct product representation has the basis functions $\Psi_{mn} = \phi_m\theta_n$ $(1 \leq m \leq l_i;\ 1 \leq n \leq l_j)$.

As an example, consider the direct product of Γ_5 and Γ_4 of the group O. The character table for the group O is given in figure 2.2 and according to this table $\Gamma_5 = [3,-1,-1,1,0]$ and $\Gamma_4 = [3,1,-1,-1,0]$ giving $\Gamma_5 \otimes \Gamma_4 = [9,-1,1,-1,0]$. By inspection of the character table it can be determined that the direct product decomposes into $X_5 + X_4 + X_3 + X_2$, that is

$$\Gamma_5 \otimes \Gamma_4 = \Gamma_5 \oplus \Gamma_4 \oplus \Gamma_3 \oplus \Gamma_2 \qquad 2.29$$

If irreducible representations of O(3) are considered then decomposition is described by the Clebsh-Gordon series (see for example Joshi [1])

$$D^{(j,\sigma)} \otimes D^{(j',\sigma')} = \sum_{j=|j-j'|}^{j+j'} D^{(j,\sigma\sigma')} \qquad 2.30$$

Physically, the importance of direct products of representations arises when the system under consideration consists of a number of identical particles whose individual wavefunctions transform according to representations of the same symmetry group. The combined system then transforms according to the direct product representations of the group. In the case of a number of distinguishable particles with wavefunctions transforming according to representations of different symmetry groups, the system transforms according to representations of the direct product group (described in section 2.2.4).

2.7 Double groups

It is well known from quantum physics that the wavefunction of a system consisting of an odd number of electrons is antisymmetric with respect to rotations through an angle of 2π. In general this situation arises whenever the total angular momentum of a system is a half integral multiple of $\hbar$ and this is likely to occur whenever we consider a number of particles which have spin angular momentum. The groups considered so far are unable to describe this situation since they are invariant under a rotation through 2π. In this case the symmetry of the wavefunctions is governed by the irreducible representations of the corresponding double group.

The double group of G is denoted G' and contains a new element $\bar{E}$ defining a rotation through 2π about a general axis. G' then consists of all of the elements of G plus the elements of G combined with the element

$\bar{E}$, denoted by $A\bar{E} = \bar{E}A = \bar{A}$ $\forall A \in G$. Although the order of G' is double that of G, in general the number of classes is not doubled. E and $\bar{E}$ belong to different classes and, in order to determine whether or not the general elements A and $\bar{A}$ belong to the same class, a set of rules have been formulated by Opechowski [4].

The double group O' of order 48 has 8 classes; $3C_4^2$ and $3\bar{C}_4^2$ constitute a class and $6C_2$ and $6\bar{C}_2$ constitute another class. The 3 additional irreducible representations are denoted by Γ_6, Γ_7 and Γ_8 having dimensions given by $(l_6)^2 + (l_7)^2 + (l_8)^2 = 24$, that is $l_6 = l_7 = 2$ and $l_8 = 4$. The full character table for O' is given in figure 2.5. It is determined as follows:

(i) $X(\bar{E}) = \pm X(E)$, where the positive sign applies for the single valued representation of O (Γ_1 to Γ_5) and the negative sign applies for the double valued representations (Γ_6 to Γ_8)

(ii) similarly for a general element $X(\bar{A}) = \pm X(A)$

(iii) when A and $\bar{A}$ belong to the same class $X(\bar{A}) = +X(A)$ and hence, for Γ_6 to Γ_8, $X(\bar{A}) = -X(A) = 0$

(iv) the orthogonality conditions are used to complete the table.

The double group SO'(3) consists of double-valued representations of SO(3) obtained when j is half-integral. The characters of SO'(3) are also given by equation 2.24.

2.8 References

1. A.Joshi, "Elements of Group Theory for Physicists" 2nd Ed, New Dehli, Wiley Eastern (1977)

2. G.Ya.Lyubarskii, "The Application of Group Theory in Physics", Pergammon press, Oxford (1960)

3. B.L.van der Waerden, "Group Theory and Quantum Mechanics", Springer verlag, Berlin (1974)

Classes

Irreducible representations	E	$\bar{E}$	$6C_4$	$\overline{6C_4}$	$(3C_4^2, \overline{3C_4^2})$	$(6C_2\overline{6C_2})$	$8C_3$	$\overline{8C_3}$
Γ_1	1	1	1	1	1	1	1	1
Γ_2	1	1	−1	−1	1	−1	1	1
Γ_3	2	2	0	0	2	0	−1	−1
Γ_4	3	3	1	1	−1	−1	0	0
Γ_5	3	3	−1	−1	−1	1	0	0
Γ_6	2	−2	$\sqrt{2}$	$-\sqrt{2}$	0	0	1	−1
Γ_7	2	−2	$-\sqrt{2}$	$\sqrt{2}$	0	0	1	−1
Γ_8	4	−4	0	0	0	0	−1	1

Figure 2.5 Character table for the octahedral double group O′.

4. W.Opechowski, Physica, 7, p552 (1941)

3. ENERGY LEVEL CALCULATIONS

3.1 Introduction

The object of this chapter is to present the basic theoretical groundwork necessary to enable the energy level structure of an atom or ion to be calculated. The emphasis throughout is placed on appreciating and exploiting the rotational symmetry associated with the system. For example, the intimate relationship between rotational symmetry and angular momentum operators is discussed. The use of angular momentum operators is central to a description and classification of atomic spectra.

Probably the most important utilisation of the rotational symmetry of the system has been in the derivation of spherical (or irreducible) tensor operator algebra by Racah [1-4]. This classic series of papers, starting in 1942, represented the most significant advance in the theory of complex spectra since the publication in 1935 of the standard text on this subject by Condon and Shortly [5]. The application of tensor operator techniques to the theory of atomic spectroscopy is described below and includes a derivation of the system Hamiltonian in tensor operator form. The number of matrix elements and the overall complexity of the calculation can be significantly reduced using these methods.

Initially, the basic problem of calculating the free atomic energy states will be considered. The effect on these states of introducing the atom or ion into a crystalline environment is described later.

3.2 Atomic structure calculations

The Hamiltonian describing a free atom or ion consists of a contribution due to the nucleus and a contribution due to the electrons. Because we are only interested in the electronic states of the atom and transitions between these states we employ the Born-Oppenheimer or

adiabatic approximation to separate out these two contributions. In this scheme the electrons are regarded as moving in a fixed potential field provided by the effectively stationary nucleus. The non-relativistic Hamiltonian of such a system is, for an N electron atom, given by

$$H = \sum_{i}^{N} (-(\hbar^2\nabla^2/2m) - (Ze^2/r_i)) + \sum_{i>j}^{N} e^2/r_{ij} \qquad 3.1$$

where r_i is the distance of the i^{th} electron from the nucleus and r_{ij} is its distance from the j^{th} electron. The symbol m represents the mass of an electron and the charge on the nucleus is given by -Ze.

A direct solution of the Schrödinger equation $H\Psi = E\Psi$ requires a further simplification to the Hamiltonian since the second term in equation 3.1 prevents a separation of the variables. This is achieved by considering each electron as moving in a central potential $-U(r_i)/e$ which is provided by the nucleus plus a potential energy term due to the interaction of each electron with all the others. The zeroth-order Hamiltonian H_o is therefore given by

$$H_o = \sum_{i}^{N} (-(\hbar^2\nabla^2/2m) + U(r_i)) \qquad 3.2$$

and the interaction between electrons can now be added as a perturbation V

$$H = H_o + V \qquad 3.3$$

where $$V = \sum_{i}^{N} (-(Ze^2/r_i) - U(r_i)) + \sum_{i>j}^{N} e^2/r_{ij} \qquad 3.4$$

The non-relativistic nature of the Hamiltonian can be relieved by a further contribution to the perturbation potential. This additional term represents the motion of the magnetic moment of the electron in the electric field of the nucleus and the other electrons according to Dirac's equation

[6,7]. The most important term to be considered is given by

$$V' = \sum_{i}^{N} \xi(r_i)\underline{s}_i \cdot \underline{l}_i \qquad 3.5$$

$$\text{with} \quad \xi(r) = (\hbar^2/2m^2c^2r)dU/dr \qquad 3.6$$

where $\underline{s}_i$ and $\underline{l}_i$ are the spin and orbital angular momenta of the i^{th} electron respectively.

In practice it is found that for free atoms the two perturbations V and V' dominate. The complete perturbation V_T is then finally

$$V_T = \sum_{i} (-(Ze^2/r_i) - U(r_i)) + \sum_{i>j} e^2/r_{ij} + \sum_{i} \xi(r_i)\underline{s}_i \cdot \underline{l}_i \qquad 3.7$$

The effect of H_o alone is to produce a series of degenerate energy levels called configurations which are labelled by the principal quantum number n (n = 1, 2, 3, ...) and the total orbital angular momentum l expressed as a spectral term s, p, d, f, etc. corresponding to l = 0, 1, 2, 3, etc. The total number of electrons resident within the configuration is denoted by the addition of a superscript. For example $4f^2$ indicates a configuration with n = 4, l = 3 and containing 2 electrons. The addition of the perturbatio V_T leads to a partial removal of this degeneracy. The first term in V_T leads to a shift in energy of the whole configuration and is often neglected since only the structure within a configuration is generally of interest. The second term represents the Coulombic or electrostatic interaction and the third term is the spin-orbit interaction. These latter terms will be refered to as H_1 and H_2 respectively. A study of these terms and their relative importance for different atoms forms the basis of atomic spectroscopy.

While the two terms described above are indeed dominant it should not be forgotten that other interactions do exist. Probably the most important occurs between nearby configurations and is referred to as configurational

interaction. This interaction occurs only between configurations of opposite parity and its magnitude depends inversely on the energy separation between them. It has been shown that the addition of configurational interaction for certain systems satisfying these requirements is able to yield a significant improvement in the correspondance between theory and experiment [8-10].

A full derivation of the atomic energy level structure is achieved by calculating the matrix elements of the various interaction terms between some convenient basis functions and diagonalising the resulting matrices. This process will now be discussed in more detail starting with a treatment of angular momentum operators and tensor operators.

3.3 Angular momentum operators [11]

Classically the rotational properties of a system are described by a quantity known as the angular momentum. This quantity is a constant of the motion (it is conserved) if the classical Hamiltonian is invariant under rotations. In quantum mechanical systems, physical observables are represented by angular momentum operators. If a physical observable is invariant under rotations then the corresponding angular momentum operator will commute with the Hamiltonian. A study of the algebra of angular momentum operators is central to the description of a rotationally invariant system such as a free atom.

An angular momentum operator $\underline{J}$ has 3 components J_x, J_y, J_z each of which is an angular momentum operator corresponding to a physical observable. The operator $\underline{J}$ determines, and conversely may be determined from, the transformation properties of the system under rotations of the coordinate system. If the wavefunction describing the system is Ψ, and $R_{\underline{n}}(\theta)$ denotes a rotation through an angle θ about an axis of rotation $\underline{n}$, then $\underline{J}$ is defined according to

$$R_n(\theta)\Psi = e^{-i\theta(\underline{n}\cdot\underline{J})}\Psi \qquad 3.8$$

An equivalent method of defining $\underline{J}$ is in terms of its commutation relations, namely

$$\underline{J} \times \underline{J} = i\underline{J} \qquad 3.9$$

or $$[J_x,J_y] = iJ_z,\ [J_y,J_z] = iJ_x,\ [J_z,J_x] = iJ_y$$

The non-commutation of components implies that it is only possible to precisely define one component of $\underline{J}$, say J_z, at a time. This observation is equivalent to stating that in any representation only one component of $\underline{J}$ may be diagonalised at any one time. However, the square of the angular momentum operator $\underline{J}^2 = (J_x)^2 + (J_y)^2 + (J_z)^2$ commutes with each component of $\underline{J}$. This means that the basis functions for the representation can be chosen to be simultaneous eigenfunctions of both $\underline{J}^2$ and J_z with complete generality. Such a basis is denoted by $|jm\rangle$ and is refered to as the standard representation of angular momentum. The eigenvalues of $\underline{J}^2$ and J_z in this basis are

$$\begin{aligned} \underline{J}^2\,|jm\rangle &= j(j+1)\,|jm\rangle \\ J_z\,|jm\rangle &= m\,|jm\rangle \end{aligned} \qquad 3.10$$

where j is the angular momentum quantum number in units of $\hbar$ and $m = -j, -j+1, \ldots, j-1, j$. Alternatively the matrix elements are given by

$$\begin{aligned} \langle jm|\,\underline{J}^2\,|j'm'\rangle &= j(j+1)\,\delta(j,j')\delta(m,m') \\ \langle jm|\,J_z\,|j'm'\rangle &= m\,\delta(j,j')\delta(m,m') \end{aligned} \qquad 3.11$$

readily demonstrating the diagonality of the operators $\underline{J}^2$ and J_z in the chosen basis. J_x and J_y are not diagonal in this basis and therefore

$$\langle jm| J_{\pm} |j'm'\rangle = [(j \mp m')(j \pm m' + 1)]^{1/2} \delta(j,j')\delta(m,m'\pm 1) \quad 3.12$$

The operators $J_{\pm} = J_x \pm iJ_y$ are also known as the raising and lowering operators due to their effect on the value of m.

3.4 The addition of angular momenta

3.4.1 Introduction

In a general system it is necessary to consider more than one angular momentum operator. The total angular momentum is obtained by coupling together the separate angular momenta vectorially provided that the individual components commute. The coupling of up to four angular momenta is considered here.

3.4.2 Two angular momenta

The total angular momentum $\underline{J}$ is obtained by coupling together the two angular momenta $\underline{J}_1$ and $\underline{J}_2$, that is $\underline{J} = \underline{J}_1 + \underline{J}_2$. The basis $|jm\rangle$ on which $\underline{J}$ operates is obtained by taking a linear combination of the individual products of the basis functions $|j_1m_1\rangle$ and $|j_2m_2\rangle$, corresponding to $\underline{J}_1$ and $\underline{J}_2$ respectively. That is

$$|jm\rangle = \sum_{m_1 m_2} |j_1m_1, j_2m_2\rangle \langle j_1m_1, j_2m_2|jm\rangle \quad 3.13$$

where the expansion coefficients $\langle j_1m_1, j_2m_2|jm\rangle$ are known as the Clebsh-Gordon or Wigner coefficients. An expansion of this type possesses the required property, namely

$$\underline{J}^2 \,|jm\rangle = j(j+1)\,|jm\rangle$$

$$J_z \,|jm\rangle = m\,|jm\rangle \qquad 3.14$$

and $$J_i^2 \,|jm\rangle = j_i(j_i+1)\,|jm\rangle \qquad \text{for } i = 1, 2$$

It is more convenient to express the Clebsh-Gordon coefficient in terms of a 3-j symbol as follows

$$\langle j_1 m_1, j_2 m_2 | jm \rangle = (-1)^{j_1 - j_2 - m} [j]^{1/2} \begin{pmatrix} j_1 & j_2 & j \\ m_1 & m_2 & -m \end{pmatrix} \qquad 3.15$$

where the symbol [j] represents the quantity (2j+1). The 3-j symbols are more widely tabulated [12,13] and illustrate graphically the symmetrical nature of the coefficients. These properties are summarised below:

(i) An even permutation of the columns leaves the numerical value unaltered

$$\begin{pmatrix} j_1 & j_2 & j_3 \\ m_1 & m_2 & m_3 \end{pmatrix} = \begin{pmatrix} j_2 & j_3 & j_1 \\ m_2 & m_3 & m_1 \end{pmatrix} = \begin{pmatrix} j_3 & j_1 & j_2 \\ m_3 & m_1 & m_2 \end{pmatrix} \qquad 3.16$$

(ii) An odd permutation of the columns introduces the phase factor $(-1)^s$, where $s = j_1 + j_2 + j_3$

$$\begin{pmatrix} j_1 & j_2 & j_3 \\ m_1 & m_2 & m_3 \end{pmatrix} = (-1)^s \begin{pmatrix} j_2 & j_1 & j_3 \\ m_2 & m_1 & m_3 \end{pmatrix} \qquad 3.17$$

(iii) Reversal of the sign of the arguments introduces the phase factor $(-1)^s$

$$\begin{pmatrix} j_1 & j_2 & j_3 \\ m_1 & m_2 & m_3 \end{pmatrix} = (-1)^s \begin{pmatrix} j_1 & j_2 & j_3 \\ -m_1 & -m_2 & -m_3 \end{pmatrix} \qquad 3.18$$

(iv) The 3-j symbol $\begin{pmatrix} j_1 & j_2 & j_3 \\ m_1 & m_2 & m_3 \end{pmatrix}$ vanishes unless $m_1 + m_2 + m_3 = 0$

3.4.3 Three angular momenta

When dealing with more than two angular momenta then the order in which they are coupled is no longer unique. Similarly the basis functions are dependent on this choice although they are linked via an unitary transformation For the case of three angular momenta $\underline{J}_1$, $\underline{J}_2$ and $\underline{J}_3$ with basis functions $|j_1m_1\rangle$, $|j_2m_2\rangle$ and $|j_3m_3\rangle$ respectively, it is possible to first couple two of these, for example $\underline{J}_1 + \underline{J}_2 = \underline{J}_{12}$, and then couple the third to the partial sum to obtain the total angular momentum $\underline{J} = \underline{J}_{12} + \underline{J}_3$. Since any two angular momenta may be coupled to form the partial sum there are three distinct coupling possibilities. For the order described above, the coupled state is expressed in terms of the uncoupled states in an analagous way to equation 3.13 giving

$$|(j_1j_2)j_{12},j_3|jm\rangle = \sum_{m} |j_1m_1,j_2m_2,j_3m_3\rangle\langle j_1m_1,j_2m_2,j_3m_3|j_{12},j,m\rangle \qquad 3.19$$

where $$\langle j_1m_1,j_2m_2,j_3m_3|j_{12},j,m\rangle = \sum_{m_{12}} \langle j_1m_1,j_2m_2|j_{12}m_{12}\rangle\langle j_{12}m_{12},j_3m_3|jm\rangle$$

The different coupling schemes derived according to the partial sums j_{12} and j_{23} are related by

$$|(j_1j_2)j_{12},j_3|jm\rangle = \sum_{j_{23}} |j_1,(j_2j_3)j_{23}|jm\rangle\langle(j_1j_2)j_{12},j_3,j|j_1,(j_2j_3)j_{23},j\rangle \qquad 3.20$$

where the recoupling coefficients are related to the 6-j symbols by

$$\langle(j_1j_2)j_{12},j_3,j|j_1,(j_2j_3)j_{23},j\rangle = (-1)^{j_1+j_2+j_3}([j_{12}][j_{23}])^{1/2}\begin{Bmatrix} j & j_3 & j_{12} \\ j_2 & j_1 & j_{23} \end{Bmatrix} \qquad 3.21$$

The 6-j symbol is extensively tabulated [12,14] and is invariant under the following operations:

(i) Any permutation of the columns

$$\begin{Bmatrix} j_1 & j_2 & j_3 \\ l_1 & l_2 & l_3 \end{Bmatrix} = \begin{Bmatrix} j_2 & j_1 & j_3 \\ l_2 & l_1 & l_3 \end{Bmatrix} = \begin{Bmatrix} j_3 & j_1 & j_2 \\ l_3 & l_1 & l_2 \end{Bmatrix} \qquad 3.22$$

(ii) The interchange of the upper and lower arguments in each of any two columns

$$\begin{Bmatrix} j_1 & j_2 & j_3 \\ l_1 & l_2 & l_3 \end{Bmatrix} = \begin{Bmatrix} l_1 & l_2 & j_3 \\ j_1 & j_2 & l_3 \end{Bmatrix} = \begin{Bmatrix} l_1 & j_2 & l_3 \\ j_1 & l_2 & j_3 \end{Bmatrix} \qquad 3.23$$

3.4.4 Four angular momenta

The case of four angular momenta is in principle a trivial extension of the preceeding ideas. Here the total angular momentum $\underline{J}$ is obtained by summing together two partial sums. As an example consider $\underline{J} = \underline{J}_{12} + \underline{J}_{34}$, where $\underline{J}_{12}$ and $\underline{J}_{34}$ are defined as above, giving for the basis

$$|(j_1 j_2) j_{12}, (j_3 j_4) j_{34}, jm\rangle$$
$$= \sum_{\text{all}} |j_1 m_1, j_2 m_2, j_3 m_3, j_4 m_4\rangle \langle j_1 m_1, j_2 m_2, j_3 m_3, j_4 m_4 | j_{12}, j_{34}, j, m\rangle \qquad 3.24$$

where

$$\langle j_1 m_1, j_2 m_2, j_3 m_3, j_4 m_4 | j_{12}, j_{34}, j, m\rangle$$
$$= \sum_{m_1 \cdots m_4} \langle j_1 m_1, j_2 m_2 | j_{12} m_{12}\rangle \langle j_3 m_3, j_4 m_4 | j_{34} m_{34}\rangle \langle j_{12} m_{12}, j_{34} m_{34} | jm\rangle$$

Alternatively it is permissible to couple together the partial sums $\underline{J}_{13}$ and $\underline{J}_{24}$ in an entirely analagous way. The transformation between these two different coupling schemes is given by

$$|j_{12},j_{34},j\rangle = \sum |j_{13},j_{24},j\rangle\langle j_{13},j_{24},j|j_{12},j_{34},j\rangle \qquad 3.25$$

where $$\langle j_{13},j_{24},j|j_{12},j_{24},j\rangle = ([j_{12}][j_{34}][j_{13}][j_{24}])^{1/2} \begin{Bmatrix} j_1 & j_2 & j_{12} \\ j_3 & j_4 & j_{34} \\ j_{13} & j_{24} & j \end{Bmatrix}$$

This relation serves also to define the 9-j symbol which has the following symmetry properties:

(i) An even permutation of the rows or columns leaves it invariant

$$\begin{Bmatrix} j_1 & j_2 & j_{12} \\ j_3 & j_4 & j_{34} \\ j_{13} & j_{24} & j \end{Bmatrix} = \begin{Bmatrix} j_2 & j_{12} & j_1 \\ j_4 & j_{34} & j_3 \\ j_{24} & j & j_{13} \end{Bmatrix} = \begin{Bmatrix} j_{24} & j & j_{13} \\ j_2 & j_{12} & j_1 \\ j_4 & j_{34} & j_3 \end{Bmatrix} \qquad 3.26$$

(ii) An odd permutation of the rows or columns introduces the phase factor $(-1)^s$, where $s = j_1 + j_2 + j_3 + j_4 + j_{12} + j_{34} + j_{13} + j_{24} + j$

$$\begin{Bmatrix} j_1 & j_2 & j_{12} \\ j_3 & j_4 & j_{34} \\ j_{13} & j_{24} & j \end{Bmatrix} = (-1)^s \begin{Bmatrix} j_3 & j_4 & j_{34} \\ j_1 & j_2 & j_{12} \\ j_{13} & j_{24} & j \end{Bmatrix} \qquad 3.27$$

(iii) A reflection of the symbol in either of the two diagonals leaves it invariant

$$\begin{Bmatrix} j_1 & j_2 & j_{12} \\ j_3 & j_4 & j_{34} \\ j_{12} & j_{24} & j \end{Bmatrix} = \begin{Bmatrix} j_1 & j_3 & j_{13} \\ j_2 & j_4 & j_{24} \\ j_{12} & j_{34} & j \end{Bmatrix} \qquad 3.28$$

The 9-j symbols have also been tabulated [15]

3.5 Atomic coupling schemes

In the free atom it is necessary to consider a number of electrons each of which possesses both spin and orbital angular momenta. The way in which these are coupled together in order to obtain the total angular momentum for the free atom is of the utmost importance. The two most important coupling schemes are known as LS-coupling (also known as Russel-Saunders coupling)

and jj-coupling.

In the LS-coupling scheme the orbital and spin angular momenta for the complete system are coupled separately to obtain the total orbital angular momentum $\underline{L} = \sum_i \underline{l}_i$ and the total spin angular momentum $\underline{S} = \sum_i \underline{s}_i$. The total angular momentum $\underline{J}$ is then obtained by coupling together these two partial sums ($\underline{J} = \underline{L} + \underline{S}$).

In the jj-coupling scheme the orbital and spin angular momenta are coupled for each electron separately ($\underline{j}_i = \underline{l}_i + \underline{s}_i$). The sum of all such angular momenta for all of the electrons in the system gives the total angular momentum $\underline{J} = \sum_i \underline{j}_i$. For configurations of the type $f^n l$ which are usually encountered for the rare earths, the outer l electron is generally coupled with the f^n core in $J_1 j$-coupling. $J_1 j$-coupling is the natural generalisation of jj-coupling.

The importance of the LS-coupling scheme is that both $\underline{L}$ and $\underline{S}$ commute with the electrostatic interaction Hamiltonian H_1. The resulting states or terms can therefore be labelled by the set of quantum numbers α,S,L (where α denotes any additional quantum numbers necessary to ensure a unique description). Each term is $(2\alpha+1)(2S+1)(2L+1)$-fold degenerate and is conventionally written as a capital letter denoting the value of L, according to the spectroscopic series, accompanied by a raised prefix giving the spin multiplicity (2S+1). For example the term ^3G denotes a state with L = 4 and S = 1.

For the spin-orbit interaction it is found that neither $\underline{L}$ nor $\underline{S}$ commute separately with the Hamiltonian H_2. The resultant $\underline{J} = \underline{L} + \underline{S}$ does however commute with H_2. In this case the resulting states are correctly described in a jj-coupling scheme. Each term is now denoted by the set αnlj for each electron (for example $2p_{1/2}3d_{3/2}$).

In an earlier section it was stated that it is the relative importance of the two interactions H_1 and H_2 which to a large extent determines the properties of the free atom. Clearly since both interactions are present

simultaneously neither of the two coupling extremes discussed above is entirely applicable. For an accurate analysis it is necessary to employ some intermediate coupling scheme. This ideal solution is normally unattainable for anything but the very simplest configurations. This is due to the complexity of the calculations involved. Fortunately for a large number of configurations either H_1 or H_2 dominates and it is possible to approximate to one or other of the coupling schemes. Each term in this zeroth-order scheme can then be treated using perturbation theory to obtain an approximate solution.

For most atomic configurations the electrostatic interaction dominates and the LS-coupling scheme is best able to describe the resulting states. However for heavier ions, higher ionisation states and higher lying excited state configurations, the spin-orbit interaction becomes increasingly important. For the rare-earth ions, the spin-orbit interaction certainly cannot be neglected and towards the end of the series it becomes the dominant interaction. This aspect will become clear later when divalent ytterbium is considered.

3.6 The algebra of tensor operators

3.6.1 Introduction

As already discussed, the rotational properties of an operator are determined by its commutator with the total angular momentum operator $\underline{J}$. For the case of a scalar operator A, which is by definition invariant under all rotations, the commutator is given by $[\underline{J},A] = 0$. A vector operator $\underline{V}$ can be expressed in terms of its cartesian components V_x, V_y and V_z. However, since most systems of interest possess spherical symmetry, it is more convenient to work with the spherical components defined by

$$V_1 = -(V_x + iV_y)(2)^{-1/2}$$
$$V_0 = V_z \qquad 3.29$$
$$V_{-1} = (V_x - iV_y)(2)^{-1/2}$$

The commutation relations which define the rotational properties of a vector operator are given by

$$[J_\pm, V_q] = (2 - q(q \pm 1))^{1/2} V_{q\pm1}$$
$$[J_z, V_q] = qV_q \qquad q = 1, 0, -1 \qquad 3.30$$

A vector operator transforms under rotations according to the irreducible representation $D^{(1)}$ of SO(3). This follows from equation 2.25 where the spherical components of the vector $\underline{V}$ correspond to the $l = 1$ ($m = -1, 0, 1$) components of the spherical harmonics. When the extension is made to the rotation-inversion group O(3) it becomes necessary to distinguish between vector operators which transform differently under the inversion operation. A polar vector operator transforms according to $D^{(1,-)}$, changing sign under inversion, while an axial vector operator transforms according to $D^{(1,+)}$. The electric dipole moment operator is an example of a polar vector operator and the orbital and spin angular momenta operators are examples of axial vector operators.

The importance of choosing the components of an operator to simplify its representations in the scheme of use becomes more important when considering tensor operators in general. The more usual cartesian tensor operators generally appear in a reducible form when dealing with rotationally invariant systems. For example, consider two vector operators $\underline{U}$ and $\underline{V}$ transforming separately under rotations according to equation 2.17 with $l = 1$. The second rank tensor operator $\underline{UV}$ is the direct product of $\underline{U}$ and $\underline{V}$, a general component of which transforms under rotations according to

$$R(\alpha,\beta,\gamma)U_iV_j = \sum_{n,m=-1}^{1} U_nV_m\ D^{(1)}_{ni}(\alpha,\beta,\gamma)\ D^{(1)}_{mj}(\alpha,\beta,\gamma) \qquad 3.31$$

The tensor $\underline{UV}$ consists of nine components and these generate the direct product representation $D^{(1)} \otimes D^{(1)}$ of SO(3). According to equation 2.30 this is reducible into the following irreducible representations

$$D^{(1)} \otimes D^{(1)} = D^{(0)} \oplus D^{(1)} \oplus D^{(2)} \qquad 3.32$$

Therefore it is possible to decompose $\underline{UV}$ into three irreducible tensor operators $\underline{T}^{(0)}$, $\underline{T}^{(1)}$ and $\underline{T}^{(2)}$ which transform as spherical harmonics of degree zero, one and two respectively.

In general an irreducible tensor operator (or spherical tensor operator) $\underline{T}^{(k)}$ of degree k, where k = 0, 1/2, 1, 3/2, ..., is defined as an operator having 2k+1 components $T^{(k)}_q$, with q = -k, -k+1, ..., k, called the spherical or standard components which transform under rotations according to

$$R(\alpha,\beta,\gamma)T^{(k)}_q = \sum_{m=-k}^{k} T^{(k)}_m\ D^{(k)}_{mq}(\alpha,\beta,\gamma) \qquad 3.33$$

Only integral values of k occur in physical problems and therefore the components of an irreducible tensor operator have the same commutation relations with the components of the total angular momentum operator J as the spherical harmonics

$$\begin{aligned} [J_\pm, T^{(k)}_q] &= (k(k+1) - q(q\pm1))^{1/2}\ T^{(k)}_{q\pm1} \\ [J_z, T^{(k)}_q] &= q\ T^{(k)}_q \end{aligned} \qquad 3.34$$

These relations provided the starting point for the derivation of irreducible tensor operator algebra by Racah [2].

3.6.2 The Wigner-Eckart theorem

The importance of irreducible tensor operators becomes apparent when considering the matrix elements of the components of such operators. The dependence of the matrix element of $T_q^{(k)}$ on m in the $|jm\rangle$ scheme is given by the Wigner-Eckart theorem [16]

$$\langle jm| T_q^{(k)} |j'm'\rangle = (-1)^{j-m} \begin{pmatrix} j & k & j' \\ -m & q & m' \end{pmatrix} \langle j\| T^{(k)} \|j'\rangle \qquad 3.35$$

where $\langle j\| T^{(k)} \|j'\rangle$ is known as the reduced matrix element. The dependence on m is contained totally within the 3-j symbol and phase factor which are both easily calculable. Consideration of the 3-j symbol alone indicates that the matrix element is zero unless $m = m' + q$.

3.6.3 Matrix elements of mixed tensor operators

The scalar product of two tensor operators $\underline{T}^{(k)}$ and $\underline{U}^{(k)}$ is defined by

$$\underline{T}^{(k)}.\underline{U}^{(k)} = \sum_q (-1)^q T_q^{(k)} U_{-q}^{(k)} \qquad 3.36$$

with its matrix element given by [16]

$$\langle \alpha jm| (\underline{T}^{(k)}.\underline{U}^{(k)}) |\alpha' j'm'\rangle = \sum_{\alpha'',j''} (-1)^{j-j''} \langle \alpha j\| T^{(k)} \|\alpha'' j''\rangle \langle \alpha'' j''\| U^{(k)} \|\alpha' j'\rangle \times \delta(j,j')\delta(m,m')/[j] \qquad 3.37$$

The symbol α stands for any additional quantum numbers necessary to define the state uniquely.

Consider a system containing two angular momenta j_1 and j_2. If $\underline{T}^{(k)}$ and $\underline{U}^{(k)}$ are of such a form that they act on different parts of the system with basis functions $|j_1 m_1\rangle$ and $|j_2 m_2\rangle$ respectively, then the matrix elements between the basis functions $|j_1 j_2 JM\rangle$ of the combined system are

$$\langle \alpha j_1 j_2 JM | \; (\underline{T}^{(k)}.\underline{U}^{(k)}) \; | \alpha' j_1' j_2' J' M' \rangle$$

$$= (-1)^{j_1'+j_2+J} \begin{Bmatrix} j_1' & j_2' & J \\ j_2 & j_1 & k \end{Bmatrix} \delta(J,J')\delta(M,M')$$

$$\times \sum_{\alpha''} \langle \alpha j_1 \| \, T^{(k)} \, \| \alpha'' j_1' \rangle \langle \alpha'' j_2' \| \, U^{(k)} \, \| \alpha' j_2' \rangle \qquad 3.38$$

Two special cases arise from a consideration of equation 3.38:

(i) For an operator $T^{(k_1)}$ acting on part 1 only and which commutes with j_2 it can be shown that

$$\langle \alpha j_1 j_2 J | \; T^{(k_1)} \; | \alpha' j_1' j_2' J' \rangle$$

$$= (-1)^{j_1+j_2+J'+k_1} \begin{Bmatrix} J & k_1 & J' \\ j_1' & j_2 & j_1 \end{Bmatrix} \delta(j_2,j_2')([J][J'])^{1/2}$$

$$\times \langle \alpha j_1 \| \, T^{(k_1)} \, \| \alpha' j_1' \rangle \qquad 3.39$$

(ii) For an operator $U^{(k_2)}$ acting on part 2 only and which commutes with j_1 it can be shown that

$$\langle \alpha j_1 j_2 J | \; U^{(k_2)} \; | \alpha' j_1' j_2' J' \rangle$$

$$= (-1)^{j_1+j_2'+J+k_2} \begin{Bmatrix} J & k_2 & J' \\ j_2' & j_1 & j_2 \end{Bmatrix} \delta(j_1,j_1')([J][J'])^{1/2}$$

$$\times \langle \alpha j_2 \| \, U^{(k_2)} \, \| \alpha' j_2' \rangle \qquad 3.40$$

The problem of calculating matrix elements of tensor operators ultimately becomes one of calculating the reduced matrix elements. The methods that are employed to obtain these reduced matrix elements will be discussed later in relation to some specific examples.

3.7 The application of tensor operator techniques in atomic spectroscopy

3.7.1 Introduction

The use of tensor operator techniques in a determination of the matrix elements of the Hamiltonian of an atomic system involves the separation of

the Hamiltonian into its angular and radial components. The angular component is expressed in terms of tensor operators and its matrix elements are calculated using the techniques developed in the previous section. Matrix elements of the radial component result in various radial integrals which are in theory calculable provided accurate wavefunctions are available. In practice the radial dependencies of these wavefunctions are not known accurately enough and the results of such calculations are unreliable. The radial integrals are therefore normally regarded as variable parameters to be determined by fitting the theoretically derived energy levels to those observed experimentally.

The two major contributions, H_1 and H_2, to the atomic Hamiltonian are now derived in a tensor operator form and their matrix elements calculated. In this detailed analysis only the two electron configuration will be considered. The extension to a many electron atom is discussed in a later section.

3.7.2 The electrostatic interaction H_1

The electrostatic or Coulombic interaction between two electrons is given by (equation 3.3)

$$H_1 = \sum_{i>j} e^2/r_{ij}$$

$$= \frac{e^2}{((r_i)^2 + (r_j)^2 - 2r_ir_j\cos(w))^{1/2}} \qquad 3.41$$

where w is the angle between the radii vectors r_i and r_j of the two electrons. Alternatively the denominator in equation 3.41 can be expanded as a series of Legendre polynomials P_w [17]

$$((r_i)^2 + (r_j)^2 - 2r_ir_j\cos(w))^{-1/2} = \Sigma\ (r_<^k/r_>^{k+1})P_k\cos(w) \qquad 3.42$$

where $r_<$ is the lesser and $r_>$ is the greater of r_i and r_j. Furthermore the spherical harmonics addition theorem [5] states that

$$P_k\cos(w) = (4\pi/[k]) \sum_q Y_k^{q*}(\theta_i,\phi_i)Y_k^q(\theta_j,\phi_j)$$

$$= \sum_q (-1)^q (C_{-q}^{(k)})_i (C_q^{(k)})_j$$

giving $$P_k\cos(w) = (\underline{C}_i^{(k)}.\underline{C}_j^{(k)}) \qquad 3.43$$

where the tensor operator $\underline{C}^{(k)}$ is defined by

$$C_q^{(k)} = (4\pi/[k])^{1/2} Y_k^q(\theta,\phi) \qquad 3.44$$

The subscript to $\underline{C}^{(k)}$ in equation 3.43 indicates that it is a function of the coordinates of a particular electron. The electrostatic interaction is therefore expressed in the tensor operator form as

$$H_1 = e^2 \sum_k (r_<^k/r_>^{k+1})(\underline{C}_i^{(k)}.\underline{C}_j^{(k)}) \qquad 3.45$$

The matrix elements of H_1 are most easily calculated for an LS-coupling scheme where the matrix is diagonal. Considering the angular component initially, the general matrix element is given by

$$\langle(s_1s_2)S,(l_1l_2)L,J,M|\ \underline{C}_1^{(k)}.\underline{C}_2^{(k)}\ |(s_1s_2)S',(l_1l_2)L',J',M'\rangle \qquad 3.46$$

A simplification is afforded by the fact that for a two electron system it is only possible to have S = 0 or 1. This gives rise to two sets of terms called singlet and triplet terms respectively. Each term is given by (equation 3.38)

$$\langle l_1,l_2,L|\ \underline{C}_1^{(k)}.\underline{C}_2^{(k)}\ |l_1,l_2,L'\rangle$$

$$= (-1)^{l_1+l_2+L}\begin{Bmatrix} l_1 & l_2 & L \\ l_2 & l_1 & k \end{Bmatrix}\delta(L,L')\langle l_1\| C_1^{(k)} \|l_1\rangle\langle l_2\| C_2^{(k)} \|l_2\rangle$$

$$= f_k \quad \text{say} \tag{3.47}$$

The reduced matrix elements are given in general by [16]

$$\langle l\| C^{(k)} \|l'\rangle = (-1)^l([l][l'])^{1/2}\begin{pmatrix} l & k & l' \\ 0 & 0 & 0 \end{pmatrix} \tag{3.48}$$

so that $$f_k = (-1)^L\delta(L,L')\begin{Bmatrix} l_1 & l_2 & L \\ l_2 & l_1 & k \end{Bmatrix}[l_1][l_2]\begin{pmatrix} l_1 & k & l_1 \\ 0 & 0 & 0 \end{pmatrix}\begin{pmatrix} l_2 & k & l_2 \\ 0 & 0 & 0 \end{pmatrix} \tag{3.49}$$

The 3-j symbols of the type $\begin{pmatrix} j_1 & j_2 & j_3 \\ 0 & 0 & 0 \end{pmatrix}$ have the property that they are zero if the sum $j_1 + j_2 + j_3$ is odd. If the sum is even then the 3-j symbol can be evaluated according to the following algebraic formula [16]

$$\begin{pmatrix} j_1 & j_2 & j_3 \\ 0 & 0 & 0 \end{pmatrix} = (-1)^{J/2}\left[\frac{(J-2j_1)!\,(J-2j_2)!\,(J-2j_3)!}{(J+1)!}\right]^{1/2}\frac{(J/2)!}{(J/2-j_1)!\,(J/2-j_2)!\,(J/2-j_3)!} \tag{3.50}$$

where $J = j_1 + j_2 + j_3$. The total number of k values necessary for the description of a particular configuration is limited by the specific form of the 3-j symbols. This is also known as the triangular condition and states that the matrix element is zero unless the sum $l + k + l$ is even and $k \leq 2l$. Therefore all k values are even and $k_{max} = 2l_{min}$.

The radial component is normally left in the form of a radial integral designated by F^k

$$F^k = e^2\int_0^\infty\int_0^\infty (r_<^k/r_>^{k+1})(R_{n_1l_1}(r_1)R_{n_2l_2}(r_2))^2\,dr_1dr_2 \tag{3.51}$$

where $R_{nl}(r)$ is the radial function for the state with quantum numbers n,l. F^k is known as the direct Slater integral.

While the above calculation would suffice for two equivalent electrons, that is $n_1 = n_2$ and $l_1 = l_2$, a more general case would involve electrons in different atomic shells. In this case it is necessary to consider the

quantum mechanical exchange term in addition to the direct term evaluated above. The exchange interaction involves the general matrix element

$$\langle l_1, l_2, L | \underline{C}_1^{(k)} . \underline{C}_2^{(k)} | l_2, l_1, L' \rangle = g_k \qquad 3.52$$

and has a sign which is dependent on the way in which the electron spins are coupled. If both electrons have their spin vectors parallel giving S = 1 (triplet state), then the exchange term is negative. If the spins are antiparallel giving a singlet state with S = 0 then it is positive. To distinguish between these two possibilities we introduce the factor $-(1/2 + 2(\underline{s}_1 . \underline{s}_2))$. The matrix element is therefore given by

$$\begin{aligned} g_k &= -(1/2 + 2(\underline{s}_1 . \underline{s}_2))(-1)^{l_1 + l_2 + L}\, \delta(L, L')\, \langle l_1 \| C^{(k)} \| l_2 \rangle^2 \begin{Bmatrix} l_1 & l_1 & L \\ l_2 & l_2 & k \end{Bmatrix} \\ &= -(1/2 + 2(\underline{s}_1 . \underline{s}_2))(-1)^L [l_1][l_2] \begin{Bmatrix} l_1 & l_2 & L \\ l_1 & l_2 & k \end{Bmatrix} \begin{pmatrix} l_1 & k & l_2 \\ 0 & 0 & 0 \end{pmatrix}^2 \end{aligned} \qquad 3.53$$

The radial integral G^k, also known as the indirect Slater integral, is similarly

$$G^k = e^2 \int_0^\infty \int_0^\infty (r_<^k / r_>^{k+1})\, (R_{n_1 l_1}(r_1) R_{n_1 l_1}(r_2) R_{n_2 l_2}(r_1) R_{n_2 l_2}(r_2))\, dr_1 dr_2 \qquad 3.54$$

Once again only certain values of k satisfying the relations $l_1 + k + l_2$ = even and $k \leq l_1 + l_2$ need be considered. However in this case k may be either even or odd.

When the term energies for a given configuration have been determined it is observed that they involve a commonly repeated denominator D_k. In order to simplify the presentation of these terms the Slater-Condon parameters F_k and G_k are introduced. These parameters are related to the radial integrals F^k and G^k by

$$F_k = F^k/D_k$$
$$G_k = G^k/D_k \qquad 3.55$$

It is these corrected parameters which are quoted in most experimental studies.

A determination of the matrix elements of H_1 in a jj-coupling scheme is more complicated. Probably the easiest method is to take the terms as calculated in the LS-coupling scheme and then transform them into the jj-coupling scheme using the recoupling equation (equation 3.25). The complete transformation is given by

$$\langle (s_1 l_1) j_1, (s_2 l_2) j_2, J | H | (s_1 l_1) j_1', (s_2 l_2) j_2', J' \rangle$$
$$= \delta(J,J') ([j_1][j_2][j_1'][j_2'])^{1/2} \sum_{S,L} [S][L] \begin{Bmatrix} s_1 & s_2 & S \\ l_1 & l_2 & L \\ j_1 & j_2 & J \end{Bmatrix} \begin{Bmatrix} s_1 & s_2 & S \\ l_1 & l_2 & L \\ j_1' & j_2' & J \end{Bmatrix}$$
$$\times \langle (s_1 s_2) S, (l_1 l_2) L, J | H | (s_1 s_2) S', (l_1 l_2) L', J' \rangle \qquad 3.56$$

3.7.3 The spin-orbit interaction H_2

The spin-orbit interaction H_2 given by (equation 3.4)

$$H_2 = \sum_i \xi(r_i) \underline{s}_i . \underline{l}_i \qquad 3.57$$

is already in tensor operator form. In this instance it is the scalar product of two tensor operators of degree one. As already discussed, S and L are no longer good quantum numbers and it is necessary to consider the total angular momentum $\underline{J}$. This means that H_2 is diagonal in the jj-coupling scheme. For simplicity the matrix elements of H_2 are determined initially between states of this type giving

$$\langle j_1, j_2, J, M | H_2 | j_1', j_2', J', M' \rangle$$
$$= \delta(J,J')\delta(M,M') \left[\langle s_1 l_1 j_1 m_1 | \xi(r_1) \underline{s}_1 . \underline{l}_1 | s_1 l_1 j_1' m_1' \rangle \right.$$
$$\left. + \langle s_2 l_2 j_2 m_2 | \xi(r_2) \underline{s}_2 . \underline{l}_2 | s_2 l_2 j_2' m_2' \rangle \right] \qquad 3.58$$

Each individual term is easily calculated

$$\langle slj|m|\ \underline{s}.\underline{l}\ |slj'm'\rangle = (-1)^{s+l+j}\begin{Bmatrix} s & l & j \\ l & s & 1 \end{Bmatrix}\delta(j,j')\delta(m,m')\ \langle s\|\ s\ \|s\rangle\langle l\|\ l\ \|l\rangle \qquad 3.59$$

where the reduced matrix elements are simply [16]

$$\begin{aligned}\langle l\|\ l\ \|l\rangle &= [l(l+1)(2l+1)]^{1/2} \\ \langle s\|\ s\ \|s\rangle &= [s(s+1)(2s+1)]^{1/2}\end{aligned} \qquad 3.60$$

The 6-j symbol is given algebraically by [16]

$$\begin{Bmatrix} s & l & j \\ l & s & 1 \end{Bmatrix} = (-1)^{s+l+j}\frac{2[j(j+1) - s(s+1) - l(l+1)]}{[2s(2s+1)(2s+2)2l(2l+1)(2l+2)]^{1/2}} \qquad 3.61$$

Therefore

$$\langle slj|\ \underline{s}.\underline{l}\ |slj'\rangle = \delta(j,j')[j(j+1) - s(s+1) - l(l+1)]/2 \qquad 3.62$$

The radial component of the spin-orbit Hamiltonian is represented by the radial integral

$$\xi_{nl} = \int_0^\infty R_{nl}(r)\xi(r)R_{nl}(r)dr \qquad 3.63$$

The matrix elements of H_2 may also be expressed in an LS-coupling scheme although the equations in this case are more complex. The general matrix element is now

$$\langle S,L,J,M|\ \underline{s}_i.\underline{l}_i\ |S',L',J',M'\rangle = \delta(J,J')\delta(M,M')(-1)^{M'+L+J}\begin{Bmatrix} S & S' & 1 \\ L' & L & J \end{Bmatrix}\sum_i \langle S\|\ s_i\ \|S'\rangle\langle L\|\ l_i\ \|L'\rangle \qquad 3.64$$

where

$$\langle l_1 l_2 L \| \, l_1 \, \| l_1 l_2 L' \rangle$$

$$= (-1)^{l_1+l_2+L'+1} ([L][L'])^{1/2} \begin{Bmatrix} L & 1 & L' \\ l_1 & l_2 & l_1 \end{Bmatrix} \langle l_1 \| \, l_1 \, \| l_1 \rangle$$

$$= (-1)^{l_1+l_2+L'+1} ([L][L'][l_1]l_1(l_1+1))^{1/2} \begin{Bmatrix} L & 1 & L' \\ l_1 & l_2 & l_1 \end{Bmatrix} \qquad 3.65$$

Similarly

$$\langle l_1 l_2 L \| \, l_2 \, \| l_1 l_2 L' \rangle$$

$$= (-1)^{l_1+l_2+L+1} ([L][L'][l_2]l_2(l_2+1))^{1/2} \begin{Bmatrix} L & 1 & L' \\ l_2 & l_1 & l_2 \end{Bmatrix} \qquad 3.66$$

The reduced matrix elements of the spin angular momentum operator $\underline{s}$ are obtained in a completely analagous way.

3.7.4 Configurations containing almost closed shells

Upon consideration of electrons in an orbital shell l which is 2(2l+1) = m fold degenerate, it is observed that striking similarities exist between a configuration containing n electrons (l^n) and a configuration containing (m-n) electrons (l^{m-n}). These are called conjugate configurations and simple relationships exist between them [2]. In particular, the reduced matrix elements for conjugate states are the same up to a sign factor

$$\langle \alpha SLJ \| \, U^k_{m-n} \, \| \alpha' S' L' J' \rangle = (-1)^k \langle \alpha SLJ \| \, U^k_n \, \| \alpha' S' L' J' \rangle \qquad 3.67$$

The coefficients of F^k, the direct Slater integrals, are simply related between conjugate configurations. In this case the parameter k takes only even values and therefore

$$(f_k)_{m-n} = - (f_k)_n \qquad 3.68$$

Similarly the coefficients of ζ_{nl}, the spin-orbit interaction parameter, involve matrix elements of a scalar product of two operators. Therefore

k = 0 and symbolically

$$(g_{n1})_{m-n} = -(g_{n1})_n \qquad 3.69$$

The situation for the coefficients of G^k is more complex. In this case k can take both odd and even values. For a two electron configuration however the following result holds [2]

$$(g_k)_{m-n} = (1 - 4(\underline{s}_1.\underline{s}_2))\delta(L,K)([l_1][l_2]/[k])\begin{pmatrix} l_1 & k & l_2 \\ 0 & 0 & 0 \end{pmatrix}^2 \qquad 3.70$$

Therefore only singlet states can involve terms in G^k and of these only a limited number simultaneously satisfy the delta product.

3.8 Crystal field theory

3.8.1 Introduction

When an ion is placed into a crystal it is perturbed by the electric field due to the neighbouring ions comprising the crystal lattice. The actual interactions involved are very complex but a large amount of success has been achieved using the simplified crystal field theory first developed in 1929 by Bethe [18] and Becquerel [19].

Crystal field theory is based on the following assumptions:

(i) The central ion is considered to be in a static electric field produced by the neighbouring ions.

(ii) The electric field can be modelled by considering the neighbouring ions as fixed electrostatic charges.

(iii) All dynamic interactions with the lattice or with individual ions are neglected.

The crystal field approach is most appropriate for ionic crystals where there is little or no overlap between the impurity ion wavefunction and the

neighbouring ion wavefunctions. For a covalent crystal the opposite is normally true and in this case the resulting states are better described using molecular orbital theory [20,21].

The use of elementary group theory allows one to determine qualitatively how the free ion energy levels will be affected by the imposition of a crystal field of a particular symmetry. The wavefunctions or eigenfunctions Ψ^{α} of the free ion form into l_{α} degenerate sets corresponding to each eigenvalue E_{α}. The set of eigenfunctions $(\Psi_1^{\alpha},\Psi_2^{\alpha},\ldots,\Psi_{l}^{\alpha})$ clearly form a basis for the irreducible representation $D^{(\alpha,\sigma)}$ of the 3-dimensional rotation-inversion group O(3). The parity is fixed for a given configuration so it is only necessary to consider irreducible representations $D^{(\alpha)}$ of the subgroup SO(3).

When the ion is placed into a crystal, the symmetry of the system is reduced to the point symmetry group P associated with the lattice site. The group P will be a subgroup of SO(3) and the degenerate set of eigenfunctions (Ψ_i^{α}) now generate a representation of P which is in general reducible. A set of eigenfunctions forming a basis for an irreducible representation of P may be constructed from subsets of the set of eigenfunctions (Ψ_i^{α}). Each subset is associated with a different eigenvalue, hence a normally degenerate level in the free ion may 'split' under the influence of the crystal field.

As an example consider an ion experiencing a crystal field of cubic symmetry (octahedral point symmetry group O). The electronic states in the free ion are invariant under infinitesimal rotations, however in the crystal they become invariants under only two-fold C_2, three-fold C_3 and four-fold C_4 rotations. The characters of these elements in the representation $D^{(\alpha)}$ of SO(3) can be calculated using equation 2.24. These characters are shown in figure 3.1 for integral values of α in the range $0 \leq \alpha \leq 6$. By comparing these characters to those of the group O (figure 2.2) it is found that the decomposition of the irreducible

	E	$3C_4^2$	$6C_4$	$6C_2$	$8C_3$
$D^{(0)}$	1	1	1	1	1
$D^{(1)}$	3	-1	1	-1	0
$D^{(2)}$	5	1	-1	1	-1
$D^{(3)}$	7	-1	-1	-1	1
$D^{(4)}$	9	1	1	1	0
$D^{(5)}$	11	-1	1	-1	-1
$D^{(6)}$	13	1	-1	1	1

Figure 3.1 Characters of the elements of the symmetry group O in the irreducible representations of SO(3).

representations $D^{(a)}$ is given by

$$
\begin{aligned}
D^{(0)} &= \Gamma_1 \\
D^{(1)} &= \Gamma_4 \\
D^{(2)} &= \Gamma_3 \oplus \Gamma_5 \\
D^{(3)} &= \Gamma_2 \oplus \Gamma_4 \oplus \Gamma_5 \\
D^{(4)} &= \Gamma_1 \oplus \Gamma_3 \oplus \Gamma_4 \oplus \Gamma_5 \\
D^{(5)} &= \Gamma_3 \oplus 2\Gamma_4 \oplus \Gamma_5 \\
D^{(6)} &= \Gamma_1 \oplus \Gamma_2 \oplus \Gamma_3 \oplus \Gamma_4 \oplus 2\Gamma_5
\end{aligned}
\qquad 3.71
$$

These relations indicate that levels with total angular momentum J = 0 or 1 are unsplit by an octahedral field. The J = 2 level splits into a doubly degenerate level and a triply degenerate level transforming according to the irreducible representations Γ_3 and Γ_5 of O respectively. This relation illustrates the well known example of the splitting of a d-type level ($D^{(2)}$) into two levels (e_g and t_{2g}) by a cubic crystalline field. All levels of higher J value are split by the field.

When J is half odd integral then by an analagous process

$$
\begin{aligned}
D^{(1/2)} &= \Gamma_6 \\
D^{(3/2)} &= \Gamma_8 \\
D^{(5/2)} &= \Gamma_7 \oplus \Gamma_8 \\
D^{(7/2)} &= \Gamma_6 \oplus \Gamma_7 \oplus \Gamma_8
\end{aligned}
\qquad 3.72
$$

where the decomposition is in terms of the double-valued representations of O.

3.8.2 The crystal field Hamiltonian H_3

The electric potential $V(r,\theta,\phi)$ produced at a central ion by an array of fixed electrostatic charges can be expanded in a series of spherical harmonics

$$V(r,\theta,\phi) = \sum_{k,q} A_k^q r^k Y_k^q(\theta,\phi) \qquad 3.73$$

The crystal field Hamiltonian H_{cf} is a sum of these potentials for each electron in the configuration and is conventionaly written in terms of the Steven's potentials V_k^q [22]

$$H_{cf} = -e \sum_i \sum_{k,q} A_k^q \langle r^k \rangle V_k^q$$

$$= -e \sum_i \sum_{k,q} B_k^q V_k^q \qquad 3.74$$

In practice it is only necessary to consider a limited number of k values depending on the symmetry of the array of charges. The higher the symmetry, the lower the number of terms required. For the highly symmetric case of a rare earth ion at a site of cubic symmetry then it is sufficient to consider the k = 4 and k = 6 terms with q = 0 and q = 4 [23]. In addition due to the triangular condition only k = 4 is permitted for d electrons and k = 4 and 6 for f electrons.

For the two electron configurations considered in the present analysis, it is a simple matter to separate the Hamiltonian into two terms; one due to the crystal field at the f electron $H_{cf}(f)$ and the other due to the crystal field at the d electron $H_{cf}(d)$. The crystal field has no effect on the s electron. The two Hamiltonians are given by

$$H_{cf}(f) = B_4^0 V_4^0 + B_4^4 V_4^4 + B_6^0 V_6^0 + B_6^4 V_6^4 \qquad 3.75$$

$$H_{cf}(d) = B_4^0 V_4^0 + B_4^4 V_4^4 \qquad 3.76$$

The coefficients $B_k^q = A_k^q \langle r^k \rangle$ are normally regarded as empirical parameters. The presence of a radial integral $\langle r^k \rangle$ precludes a reliable calculation although the parameters A_k^q may be obtained in principle when the crystal structure is known. For the important case of a crystalline field

of octahedral symmetry there are two distinct possibilities for the arrangement of the crystal ions. The ionic charges may be positioned at the corners of a cube giving rise to 8-fold coordination of the central ion. This arrangement is shown schematically in figure 3.2(a). Alternatively the charges may be positioned at the centre of each face giving 6-fold coordination. This arrangement is shown in figure 3.2(b). These two cases will be distinguished subsequently by the terms cubic crystal field and octahedral crystal field respectively.

For a central ion with charge -Ze surrounded by ions with charge -e at a distance R then the point ion model gives [24,25]

$$B_4^* = A_4^*\langle r^4\rangle = -(7/18)Ze^2\langle r^4\rangle/R^5 \qquad \text{(cubic)} \qquad 3.77$$

$$= (7/16)Ze^2\langle r^4\rangle/R^5 \qquad \text{(octahedral)} \qquad 3.78$$

$$B_6^* = A_6^*\langle r^6\rangle = (1/9)Ze^2\langle r^6\rangle/R^7 \qquad \text{(cubic)} \qquad 3.79$$

$$= (3/64)Ze^2\langle r^6\rangle/R^7 \qquad \text{(octahedral)} \qquad 3.80$$

Furthermore the parameters B_k^* for different values of q are related in the cubic case by $B_4^* = 5B_4^*$ and $B_6^* = -21B_6^*$. The relationships between the cubic parameters $(B_k^*)_{cub}$ and the octahedral parameters $(B_k^*)_{oct}$ are therefore independent of q and are given by

$$\begin{aligned}(B_4^*)_{oct} &= -(9/8)(B_4^*)_{cub}\\ (B_6^*)_{oct} &= 3(3/8)^2(B_6^*)_{cub}\end{aligned} \qquad 3.81$$

Similar relationships exist for the d electron system although in this case it is conventional to employ the parameter Dq defined by [24,25]

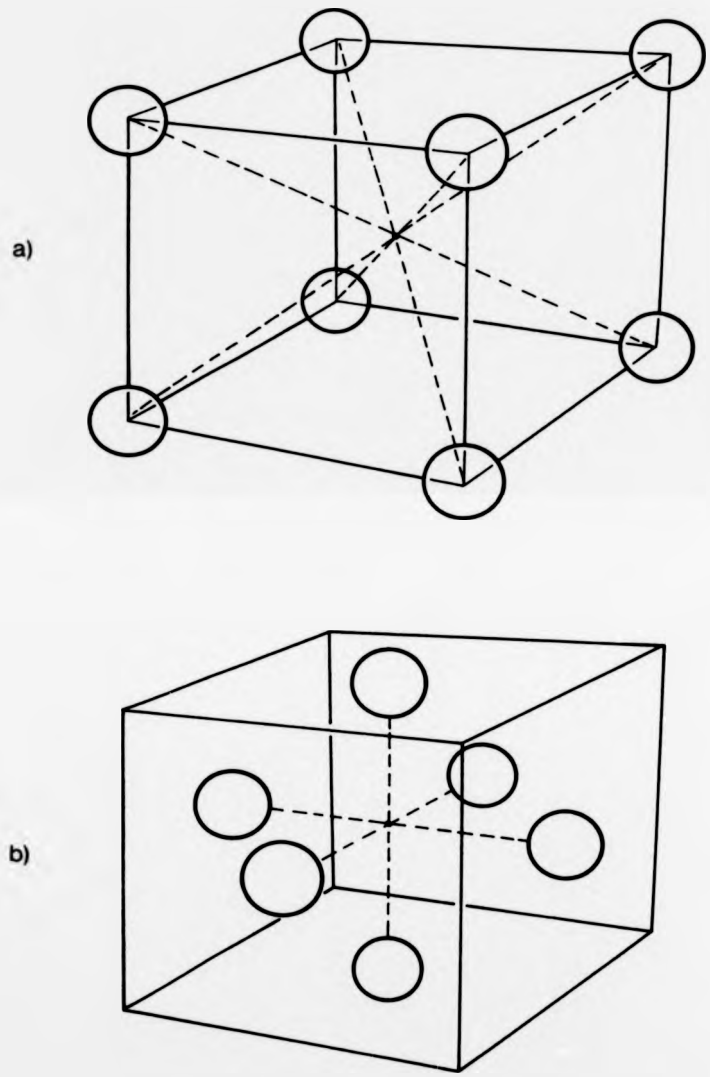

Figure 3.2 Two different atomic arrangements belonging to the symmetry group 0; a) 8-fold co-ordination or cubic and b) 6-fold co-ordination or octahedral.

$$Dq = -(4/27)Ze^2\langle r^4\rangle/R^5 \qquad \text{(cubic)} \qquad 3.82$$

$$= (1/6)Ze^2\langle r^4\rangle/R^5 \qquad \text{(octahedral)} \qquad 3.83$$

giving $$Dq = (8/21)B_4^4 \qquad 3.84$$

and therefore $$(Dq)_{oct} = -(9/8)(Dq)_{cub} \qquad 3.85$$

In order to apply the tensor operator techniques developed earlier, the above Hamiltonians must be expressed in terms of irreducible tensor operators. In this respect it is convenient to introduce the irreducible tensor operator $U^k_{q,l}$ acting on electrons belonging to the orbital shell labelled by l. The following convention applies to $U^k_{q,l}$

$$\langle l' \| U^k_{q,l} \| l' \rangle = \delta(l,l') \qquad 3.86$$

This means that d electrons and f electrons are treated differently. According to Dieke [23] the conversion factors between Steven's potentials V^q_k and the irreducible tensor operators U^k_q for these two cases are given by (the subscript l is removed since the orbital shell is specified)

(i) f electrons (l = 3)

$$\begin{aligned} V^4_4 &= 8(14/11)^{1/2}\, U^4_4 \\ V^4_2 &= 8(55)^{-1/2}\,[U^4_4 + U^4_{-4}] \\ V^4_0 &= -160(7/429)^{1/2}\, U^4_0 \\ V^4_{-2} &= -(80/3)(2/429)^{1/2}\,[U^4_4 + U^4_{-4}] \end{aligned} \qquad 3.87$$

(ii) d electrons (l = 2)

$$\begin{aligned} V^4_4 &= 8(10/7)^{1/2}\, U^4_4 \\ V^4_2 &= (8/7)\,[U^4_4 + U^4_{-4}] \end{aligned} \qquad 3.88$$

The irreducible tensor operator form for the cubic crystal field Hamiltonian follows simply

$$H_3(d) = B_4^0(V_4^0 + 5V_4^4)$$
$$= -(21/8)Dq[8(10/7)^{1/2} U_0^0 + (40/7)(U_4^0 + U_{-4}^0)]$$
$$= -6(30)^{1/2}Dq[(7/12)^{1/2} U_0^0 + (5/24)^{1/2}(U_4^0 + U_{-4}^0)]$$

giving finally $H_3(d) = -6(30)^{1/2}\,\theta_\Gamma^0\,Dq$ 3.89

where $\theta_\Gamma^0 = (7/12)^{1/2} U_0^0 + (5/24)^{1/2}(U_4^0 + U_{-4}^0)$ 3.90

Similarly for the f electron terms

$$H_3(f) = B_4^0(V_4^0 + 5V_4^4) + B_6^0(V_6^0 - 21V_6^4)$$
$$= 16(6/11)^{1/2}\,\theta_\Gamma^0\,B_4^0 + 320(14/429)^{1/2}\,\theta_\Gamma^0\,B_6^0 \quad 3.91$$

where θ_Γ^0 is as given above and

$$\theta_\Gamma^6 = -(1/8)^{1/2} U_0^0 + (7/16)^{1/2}(U_4^0 + U_{-4}^0) \quad 3.92$$

The quantities θ_Γ^k have been introduced in accordance with the work of Druzhinin [26]. They suitably reflect the inherent symmetry of the crystal field which transforms according to Γ_1 of the group O. The Hamiltonian is therefore expressed as a linear combination of irreducible tensor operators transforming in a similar way.

The wavefunctions of the system under the crystal field interaction can no longer be labelled uniquely by their value of J. This is because each state with a particular J value reduces to a direct sum of irreducible representations of the point symmetry group of the crystal. A suitable label for these states is provided by the irreducible representations of the relevant point symmetry group. Such a wavefunction in jj-coupling is

written as $|(s_1l_1)j_1,(s_2l_2)j_2,J\ ^{\alpha}\Gamma_i\rangle$, where α is an index necessary to distinguish between representations of the same type with the same J value.

A determination of the matrix elements of H_3 between basis functions of the type given above involves calculations of the form

$$\langle j_1,j_2,J\ ^{\alpha}\Gamma_i|\ \theta^k_{\Gamma}\ |j_1',j_2',J'\ ^{\beta}\Gamma_j\rangle$$

$$= (k\Gamma_1,J'\ ^{\beta}\Gamma_j|J\ ^{\alpha}\Gamma_i)\ \langle j_1,j_2,J\|\ U^k\ \|j_1',j_2',J'\rangle \qquad 3.93$$

where $(k\Gamma_1,J'\ ^{\beta}\Gamma_j|J\ ^{\alpha}\Gamma_i)$

$$= \sum_{M_J,M_J',q} (-1)^{J-M_J}(kq|k\Gamma_1)(J\ ^{\alpha}\Gamma_i|JM_J)(J'M_J'|J'\ ^{\beta}\Gamma_j)\begin{pmatrix} J & k & J' \\ -M_J & q & M_J' \end{pmatrix} \qquad 3.94$$

The coefficients $(k\Gamma_1,J'\ ^{\beta}\Gamma_j|J\ ^{\alpha}\Gamma_i)$ have been tabulated for J = 0 to J = 6 [27,28] and J = 1/2 to J = 15/2 [29]. The reduced matrix elements are calculated using equations 3.39 and 3.40 in conjunction with the following relations derived by Racah for a two electron system [2]

$$\langle l,1/2,j=l\pm1/2\|\ C^{(k)}\ \|l',1/2,j'=l'\pm1/2\rangle$$

$$= (-1)^{(j'+k-j)/2}\ [(j+j'-k)!\ (j+k-j')!\ (j'+k-j)!\ /(j+j'+k+1)!\ ]^{1/2}$$

$$\times\ [(j+j'+k+1)!!/(j+j'-k-1)!!\ (j+k-j')!!\ (j'+k-j)!!\ ] \qquad 3.95$$

$$\langle l,1/2,j=l\pm1/2\|\ C^{(k)}\ \|l',1/2,j'=l'\mp1/2\rangle$$

$$= (-1)^{(j'+k-j-1)/2}\ [(j+j'-k)!\ (j+k-j')!\ (j'+k-j)!\ /(j+j'+k+1)!\ ]^{1/2}$$

$$\times\ [(j+j'+k)!!/(j+j'-k)!!\ (j+k-j'-1)!!\ (j'+k-j-1)!!\ ] \qquad 3.96$$

where $(2n+1)!! = 1.3.5.....(2n+1)$ and $(2n)!! = 2.4.6.....(2n)$. The irreducible tensor operator $U^{(k)}_q$ is related to the tensor operator $C^{(k)}_q$ by

$$U^{(k)}_q = C^{(k)}_q/\langle l\|\ C^{(k)}\ \|l'\rangle \qquad 3.97$$

giving specifically for the f electrons

$$U^{\uparrow}_{q} = (11/14)^{1/2}\, C^{\uparrow}_{q}$$
$$U^{\downarrow}_{q} = -(1/10)(429/7)^{1/2}\, C^{\downarrow}_{q} \qquad 3.98$$

and for d electrons

$$U^{\uparrow}_{q} = (7/10)^{1/2}\, C^{\uparrow}_{q} \qquad 3.99$$

3.9 Selection rules

The application of a perturbation of lower symmetry is not only capable of producing a splitting of the energy levels but also creates the possibility of inducing transitions between different eigenvalues of the unperturbed Hamiltonian H_o. The use of group theory enables forbidden transitions to be predicted purely from a basic consideration of the symmetry of the eigenfunctions and the perturbation.

Consider two eigenvalues E^{i}_{α} and E^{f}_{β} of H_o with eigenfunctions Ψ^{i}_{α} and Ψ^{f}_{β} which belong to the irreducible representations Γ_α and Γ_β of a group G (the symmetry group of the unperturbed Hamiltonian). If a perturbation V is now applied to the system then the possibility arises that, if the system initially has an eigenvalue E^{i}_{α}, it may be found afterwards with some eigenvalue E^{f}_{β}. The transition probability between these two states is proportional to the matrix element

$$\langle \Psi^{i}_{\alpha} |\, V \,| \Psi^{f}_{\beta} \rangle = (\Psi^{i}_{\alpha},\, V\Psi^{f}_{\beta}) \qquad 3.100$$

The function $V\Psi^{f}_{\beta}$ is not an eigenfunction of H_o (unless V commutes with H_o) and therefore it generates in general a reducible representation of G. If V generates the representation Γ_ν of G, then the function $V\Psi^{f}_{\beta}$ generates the direct product representation $\Gamma_\nu \otimes \Gamma_\beta = \sum_{\gamma} a_\gamma \Gamma_\gamma$. If the decomposition into irreducible representations of G does not contain the irreducible

representation Γ_α, then the matrix element vanishes.

For example let the perturbation take the form of the electric dipole moment operator $\underline{\mu} = e\underline{r}$. This is a polar vector operator with the components e(x,y,z) which generates the representation $D^{(1,-)}$ of O(3). Electric dipole transitions within the free ion from a state transforming according to $D^{(J,\sigma)}$ to a state $D^{(J',\sigma')}$ are allowed if $D^{(1,-)} \times D^{(J',\sigma')}$ contains $D^{(J,\sigma)}$. That is, using equation 2.30

$$D^{(1,-)} \otimes D^{(J',\sigma')} = \begin{cases} D^{(J'+1,-\sigma')} \oplus D^{(J',-\sigma')} \oplus D^{(J'-1,-\sigma')} & \text{for } J' \neq 0 \\ D^{(1,-\sigma')} & \text{for } J' = 0 \end{cases} \qquad 3.101$$

Therefore the representation $D^{(J,\sigma)}$ appears only if

$$J = \begin{cases} J', J'\pm 1 & (J' \neq 0) \\ 1 & (J' = 0) \end{cases} \qquad 3.102$$

and $\sigma = -\sigma'$

The condition on parity is also known as the Laporte selection rule.

When the ion is introduced into a crystal field of lower symmetry then the selection rules above are altered considerably. Consider a crystal field possessing octahedral symmetry O_h, the three components of $\underline{\mu}$ now transform according to the irreducible representation Γ_{4u}. Transitions from a state Γ_α to a state Γ_β are allowed if $\Gamma_4 \otimes \Gamma_\beta$ contains Γ_α along with the necessary change in parity. The direct product decomposition table for the group O is given in figure 3.3. From this table it is a simple matter to discover which transitions are allowed and which are not. Finally it should be noted that group theory serves only as a guide in the prediction of allowed transitions. Such transitions may in fact be forbidden due to other considerations. The true strength of this technique arises from its ability to rigorously predict those transitions that are forbidden.

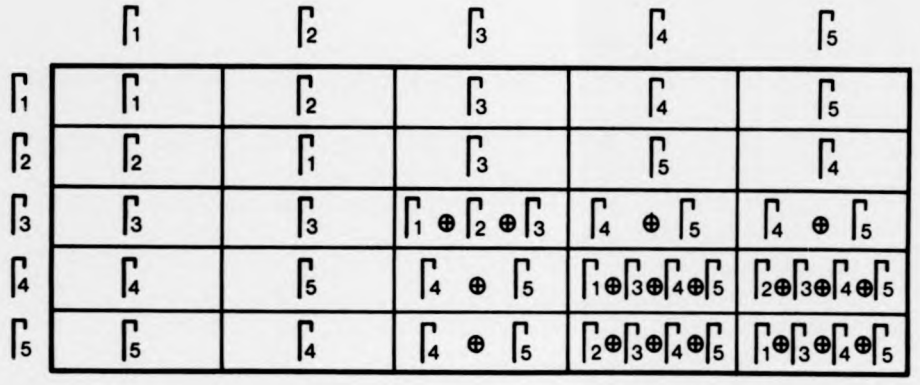

Figure 3.3 The direct product decomposition table for irreducible representations of the symmetry group O.

3.10 References

1. G.Racah, Physical Review, 61, p186 (1942)

2. G.Racah, Physical Review, 62, p438 (1942)

3. G.Racah, Physical Review, 63, p367 (1943)

4. G.Racah, Physical Review, 76, p1352 (1949)

5. E.U.Condon and G.H.Shortly, "The Theory of Atomic Spectra", Cambridge University Press (1935)

6. P.A.M.Dirac, "The Principles of Quantum Mechanics", Oxford University Press (1947)

7. H.A.Bethe and E.E.Salpeter, "Quantum Mechanics of One- and Two-electron Atoms", Springer-Verlag OHG, Berlin (1957)

8. R.F.Bacher, Physical Review, 43, p264 (1933)

9. R.E.Trees, Physical Review, 83, p756 (1951)

10. J.N.P.Hume and M.F.Crawford, Physical Review, 84, p486 (1951)

11. M.E.Rose, "Elementary Theory of Angular Momentum", John Wiley and Sons, N.Y. (1957)

12. M.Rotenberg et al., "The 3j and 6j Symbols", Technology Press, Cambridge, Mass. (1959)

13. P.E.Bryant, "Tables of Wigner 3-j Symbols", University of Southampton Research Report, 60-1, Southampton (1960)

14. K.M.Howell, "Revised Tables of 6j-symbols", University of Southampton Research Report, 59-1, Southampton (1959)

15. H.Matsunobu and H.Takebe, Progress in Theoretical Physics, 14, p589 (1955)

16. B.R.Judd, "Operator Techniques in Atomic Spectroscopy", McGraw-Hill, N.Y. (1963)

17. T.M.MacRobert, "Spherical Harmonics", Pergamon Press, Oxford (1967)

18. H.Bethe, Annalen der Physik Leipzig, 3, p133 (1929)

19. J.Becquerel, Zeitschrift fur Physik, 58, p205 (1929)

20. P.G.Perkins, "Elementary Molecular Bonding Theory", Methuen and Co. Ltd., London (1969)

21. C.J.Ballhausen, "Introduction to Ligand Field Theory", McGraw-Hill, N.Y. (1962)

22. K.W.H.Stevens, Proceedings of the Physical Society A, 65, p209 (1952)

23. G.H.Dieke, "Spectra and Energy Levels of Rare Earth Ions in Crystals", Ed. H.M.Crosswhite and H.Crosswhite, Interscience, J.Wiley and Sons, N.Y. (1968)

24. M.T.Hutchings, Solid State Physics, 16, p227 (1964)

25. N.S.Altshuler, Soviet Physics Solid State, 7, p2023 (1966)

26. V.V.Druzhinin, Optics and Spectroscopy, 22, p496 (1967)

27. V.V.Druzhinin, Optics and Spectroscopy, 22, p446 (1967)

28. M.V.Eremin, Optics and Spectroscopy, 29, p53 (1970)

29. N.S.Altshuler et al., Soviet Physics Solid State, 11, p2921 (1969)

4. EXPERIMENTAL METHOD

4.1 Materials and handling

The alkali halides used in this work were obtained from The Harshaw Chemical Company in the form of single crystals. Europium metal (99.99% purity) and ytterbium metal (99.9% purity) were supplied in ingot form by Koch-Light Laboratories Ltd. Ytterbium was obtained from the same source in the form of a thin (0.25 mm) metal foil (99.9% purity).

All materials were stored and handled prior to diffusion in a glove box containing a dry nitrogen atmosphere. This treatment was particularly important for europium metal which is highly reactive and liable, in finely divided form, to spontaneous ignition in air. It also enabled the controlled handling and cleaving of strongly deliquescent crystals such as KF, NaI and NaBr.

Both europium and ytterbium metals are soft and the removal of a small sliver for use in the diffusion process was easily achieved using a scalpel blade.

4.2 Specimen preparation

A number of the more important physicochemical properties of the rare earth metals [1-4] are indicated in figure 4.1. Certain interesting features are in evidence concerning the behaviour of europium and ytterbium. They are significantly more volatile than the remainder of the rare earth metals, excepting erbium and thulium. In addition, along with cerium, they possess the lowest melting points. However, the property that is probably of greater significance in the present study is that, for the range of temperatures just below the melting points of the alkali halides (about 660°C to 990°C), ytterbium and europium possess the highest vapour pressures [5]. This behaviour is illustrated in figure 4.2. The

ELEMENT	ATOMIC WEIGHT	MELTING POINT (°C)	BOILING POINT (°C)	LATENT HEAT OF VAPORIZATION ($kcal\,mole^{-1}$)	DENSITY (25°C) (gcm^{-3})	VAPOUR PRESSURE AT MELTING POINT (Nm^{-2})
Lanthanum	138.9	921	3457	96	6.145	1.33×10^{-7}
Cerium	140.1	799	3426	95	6.657	—
Praseodymium	140.9	931	3512	79	(α) 6.773 (β) 6.74	—
Neodymium	144.2	1021	3068	69	6.80 7.007	6.03×10^{-3}
Promethium	(145)	1168±6	2460	—	7.22 ± 0.02	—
Samarium	150.4	1077±5	1791	46	(α) 7.52 (β) 7.40	5.63×10^{2}
Europium	152.0	822	1597	42	5.243	1.44×10^{2}
Gadolinium	157.3	1313±1	3266	72	7.9004	2.44×10^{4}
Terbium	158.9	1356	3123	70	8.229	—
Dysprosium	162.5	1412	2562	67	8.550	—
Holmium	164.9	1474	2695	67	8.795	—
Erbium	167.3	1497	2863	67	9.066	—
Thulium	168.9	1545±5	1947	59	9.321	4.90×10^{-3}
Ytterbium	173.0	819	1194	38	(α) 6.965 (β) 6.54	3.95×10^{2}
Lutetium	175.0	1663	3395	99	9.840	2.46×10^{3}

Figure 4.1 Some physicochemical properties of the rare earths. [1, 2]

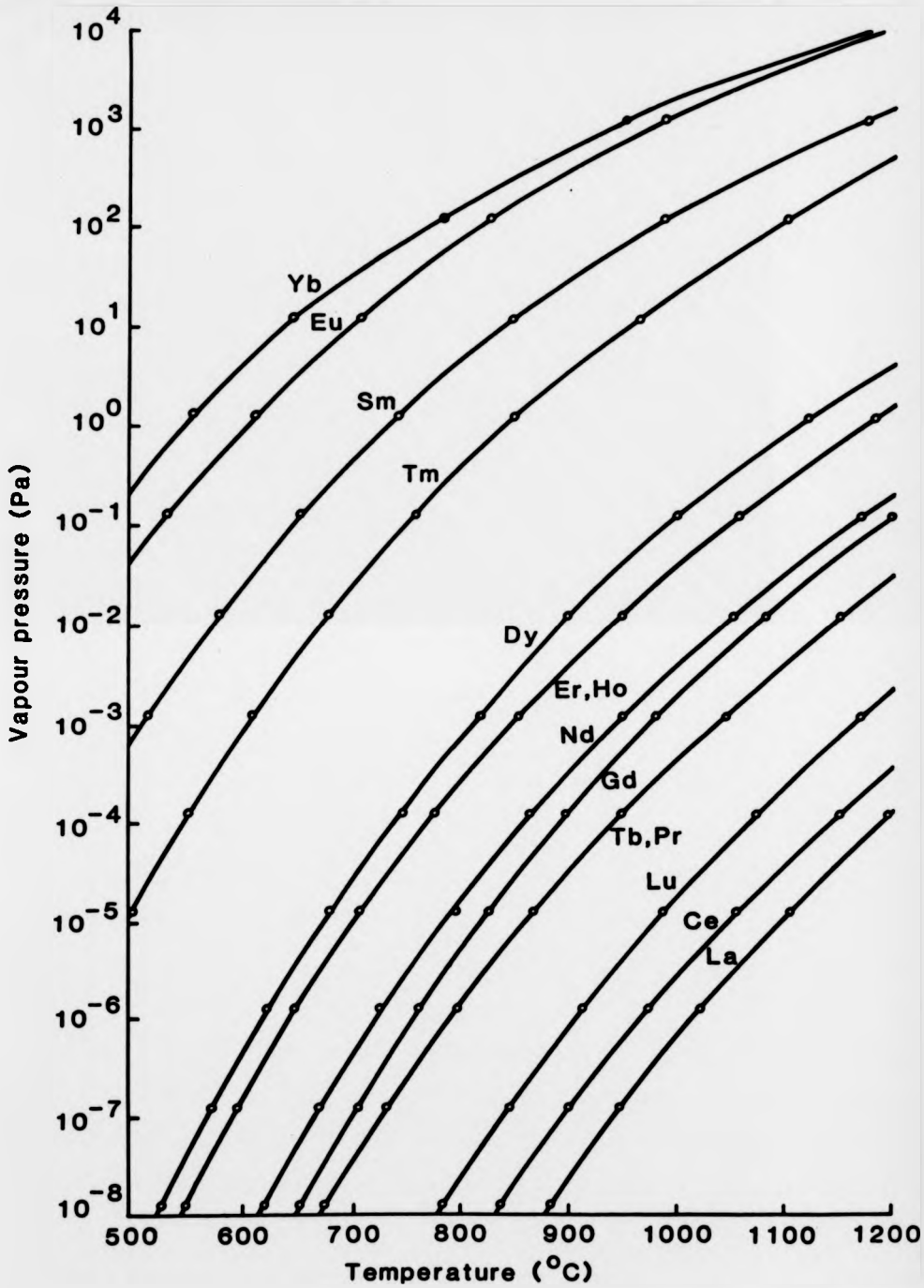

Fig.4.2 Vapour pressures of the rare earth metals as a function of temperature (after Hultgren et al [5])

relatively high vapour pressures observed for both ytterbium and europium offers the possibility of sample preparation by vapour phase diffusion. Such a method has been adopted in the present study.

In the past europium- and ytterbium-doped alkali halide crystals have normally been prepared by direct incorporation of the impurity in the alkali halide melt. Various crystal growing methods have been employed, the most popular being the Bridgman, Czochralski and Kyropolous techniques [6-10]. The author is only aware of one previous reference to doping by diffusion from the vapour phase. This is described by Radhakrishna and Chowdari [11] who have used the method in conjunction with the Bridgman and Kyropolous techniques to produce ytterbium-doped crystals of KCl, NaCl and KBr. It is interesting to note that the optical absorption spectra obtained by these workers bear no obvious resemblance to the spectra to be presented here. There is therefore some doubt that their particular application of the technique was successful.

Vapour phase diffusion was carried out in the evacuated stainless steel ampoule shown in figure 4.3. The use of a silica ampoule was also investigated but proved unsatisfactory due to the strong reactivity of the dopants, europium in particular, with the SiO_2 lattice. Such behaviour is analagous to that encountered for the alkali metals. Freshly cleaved crystals of approximate dimensions 8 mm x 5 mm x 2 mm were placed along with a small sliver (approximately 15 mg) of the appropriate metal in the primary diffusion ampoule. A separate ampoule was employed for each dopant. After each diffusion the internal surfaces were carefully cleaned by bead-blasting, followed by a wash in Decon 90 solution and a deionised water rinse.

The primary diffusion ampoule is illustrated schematically in figure 4.4. The most important feature is the finely machined dry conical joint which provides an excellent seal at the high diffusion temperatures encountered (up to about 850°C). This design necessitated the use of a

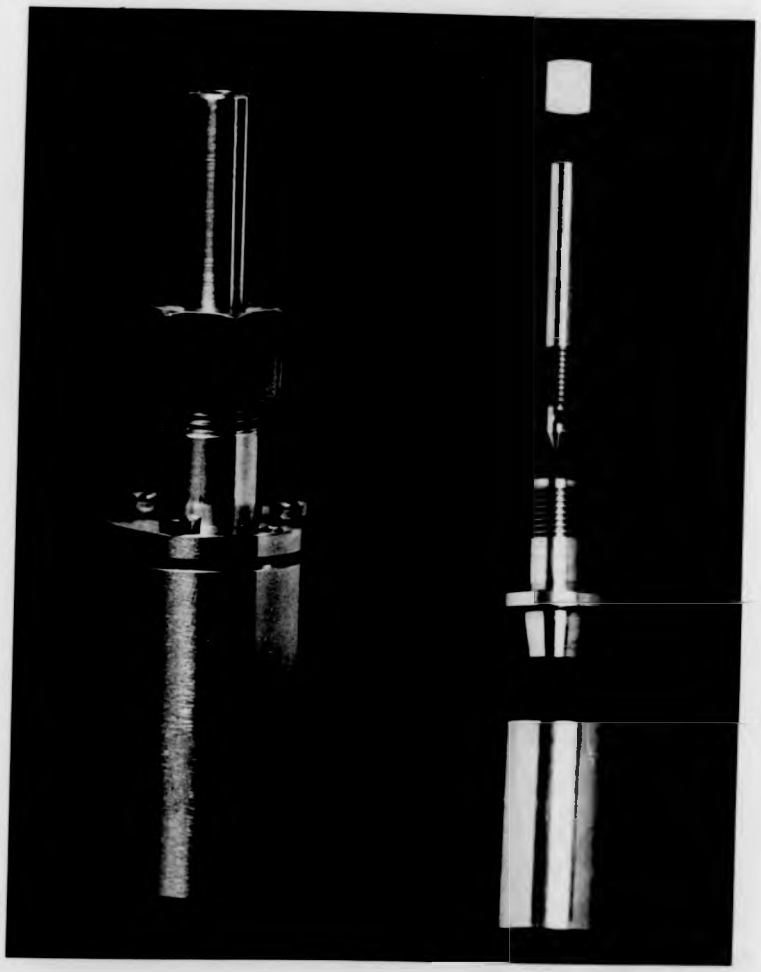

Figure 4·3 The primary diffusion ampoule

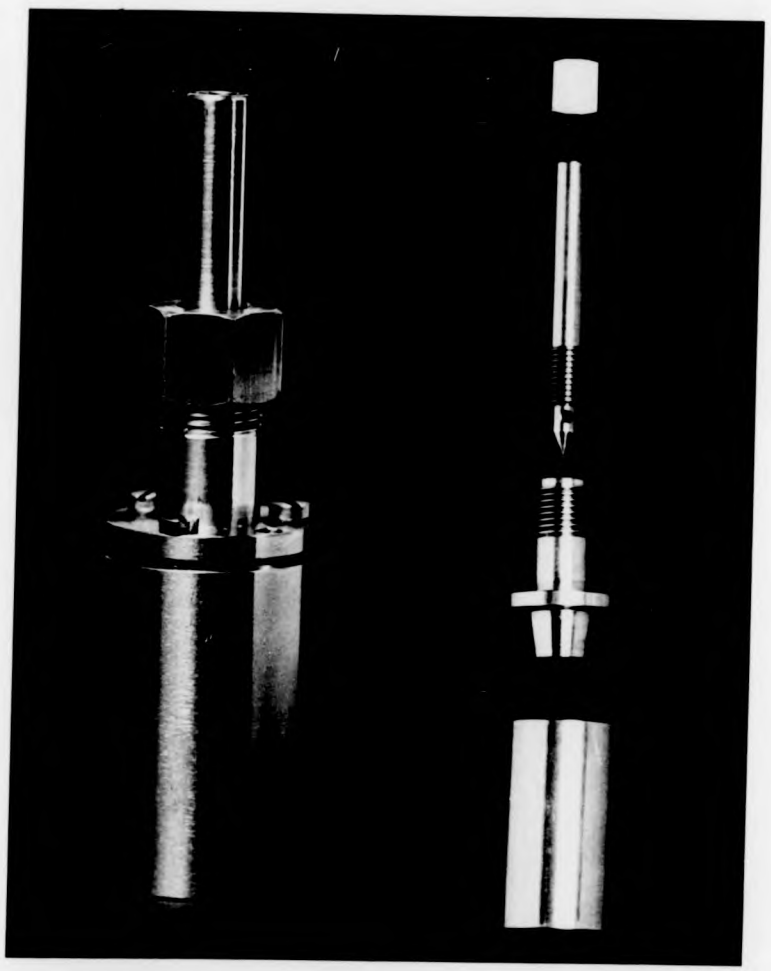

Figure 4·3 The primary diffusion ampoule

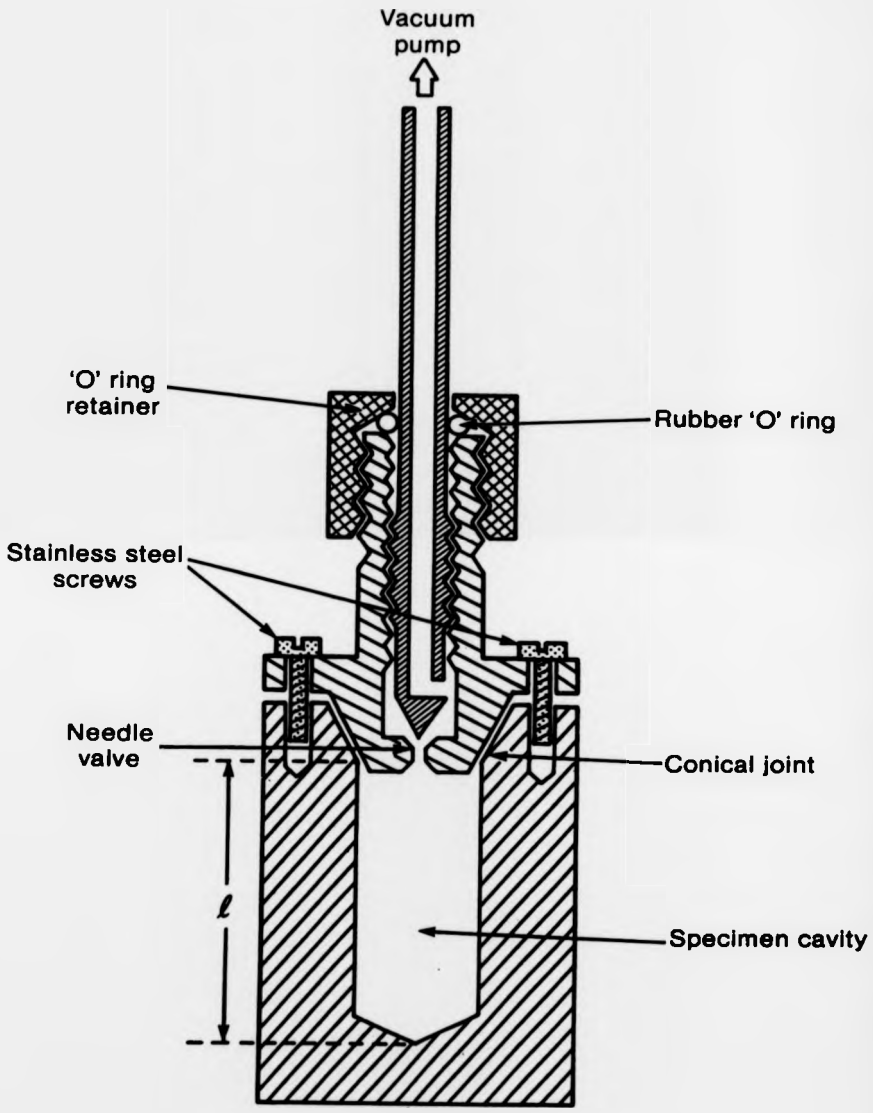

Figure 4.4 The primary diffusion ampoule in cross-section. The diagram depicts the situation during evacuation of the cavity. When the needle valve is closed the rubber 'O' ring and its retainer may be removed.

special formulation of stainless steel called Immaculate V (Chromium 25%, Nickel 20%) which is capable of sustained periods of exposure up to temperatures of 1100°C without degradation. The effectiveness of the conical joint was maintained by regular lapping with a fine abrasive.

A needle valve arrangement provided pumping access to the cavity (approximate volume 4.4 cm^3). Subsequently the cavity could be closed off by screwing the valve down tightly. A rubber 'O' ring prevented leakage via the coarse (3/8" Whitworth) thread while evacuation took place, and was easily removed once the needle valve had been closed off. The crystals were supported in a molybdenum boat and separated from the dopant by a thin section of molybdenum foil.

After evacuation, the primary ampoule was placed inside a secondary ampoule. The secondary ampoule is constructed from standard composition stainless steel and consists of two main parts: a long cylindrical main body equipped with a water cooling jacket below the pumping access point, and a plug sealed with an 'O' ring. Figure 4.5 shows the two component parts of the secondary ampoule along with the primary ampoule for comparison. A thermocouple is included as an integral part of the secondary ampoule plug. It passes via a glass-to-metal seal in the plug and rests in a hole provided in the base of the primary ampoule with the junction situated as close as possible to the specimen.

The combined assembly of primary and secondary ampoule was lowered into an upright tube furnace capable of operating up to about 1000°C. The temperature was stabilised to within about ± 5°C by a commercial controller (Ether 'Mini' 17-90B). The assembly was evacuated continuously throughout the diffusion process via the pumping access point situated on the secondary ampoule. Quenching of the sample after diffusion was achieved by removing the primary ampoule from inside the heated secondary ampoule and lowering it into liquid nitrogen. It took approximately 3 minutes to quench the sample from around 700°C to room temperature.

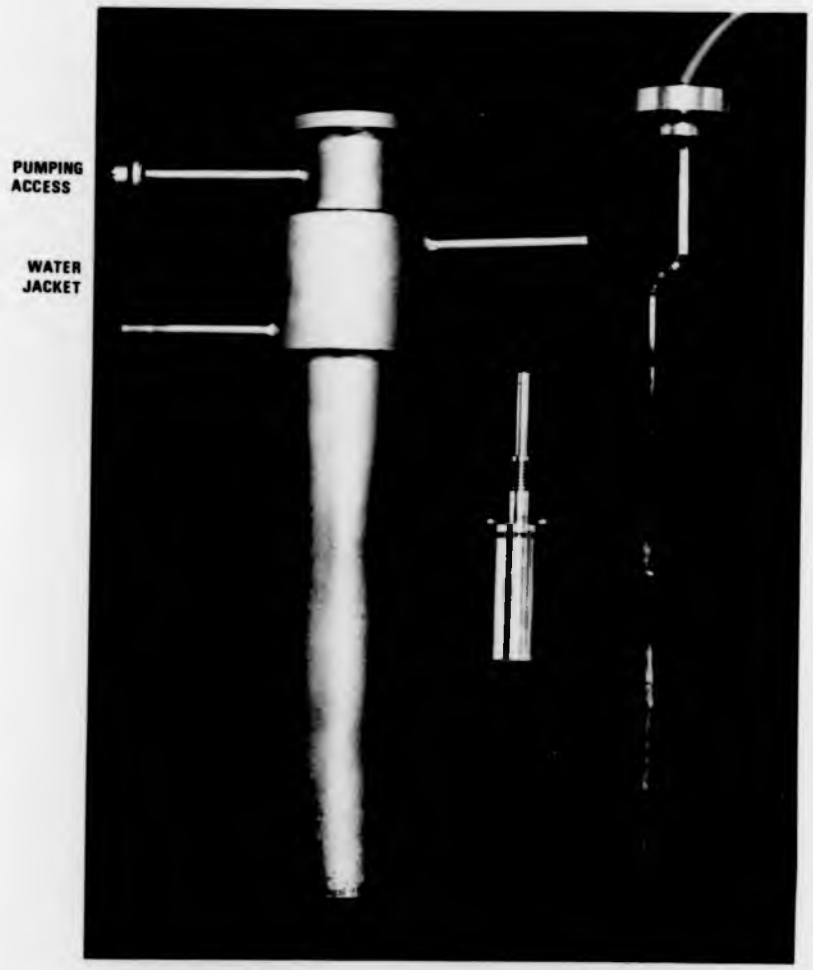

Figure 4-5 The secondary diffusion ampoule. The primary diffusion ampoule is included for comparison.

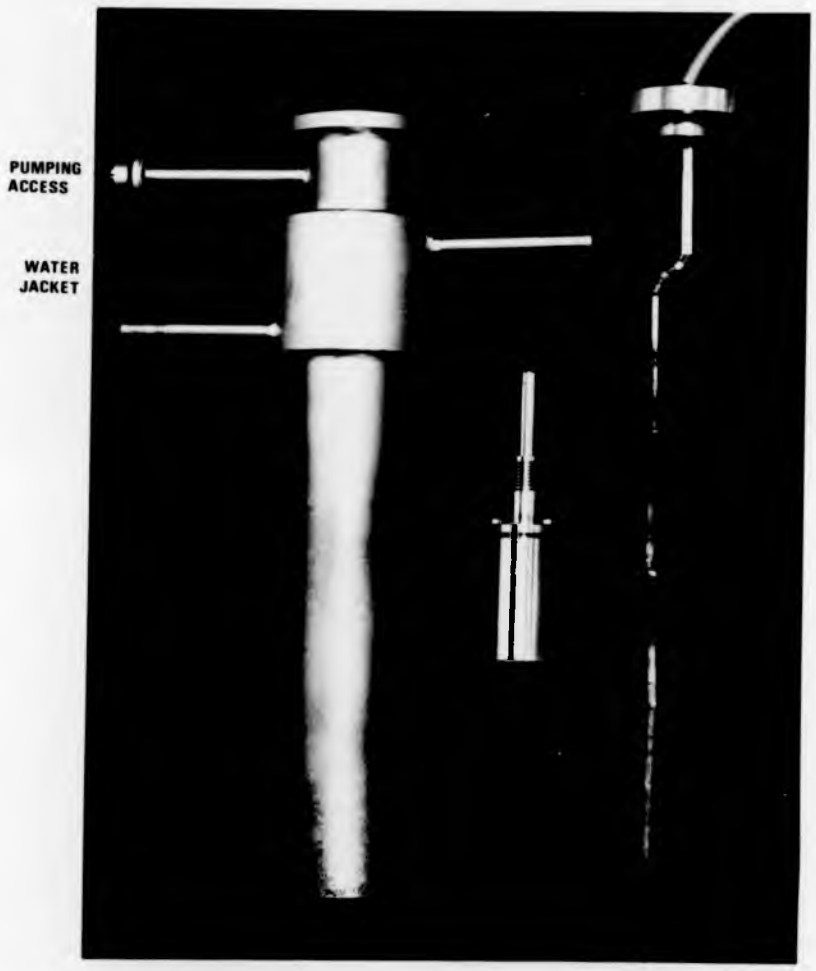

Figure 4·5 The secondary diffusion ampoule. The primary diffusion ampoule is included for comparison.

The diffusion temperature was normally chosen to be about 50°C below the melting point of the respective alkali halide crystal. Diffusion times were relatively short, ranging from about 30 minutes to 3 hours. It was found that prolonged diffusion at these temperatures tended to result in a certain amount of melting at the doped crystal face. The use of a higher temperature exaggerated this effect. It appears that the dopant, when present in a sufficiently high concentration, depresses the intrinsic melting point of the crystal.

The use of short diffusion times resulted in an inhomogeneous impurity distribution. In general the impurity extended to a depth of approximately 0.2 mm into each crystal face. This situation was found to be desireable in view of certain interesting phenomena which arose. This aspect, which relates to the formation of colour centres in the central undoped crystal regions, is discussed in chapter 7. In addition, additional absorption bands which are associated with impurities already present in the 'nominally pure' crystals could be identified by a direct comparison between the outer and inner crystal regions.

All subsequent heat treatments of the specimens were carried out in a second stabilised furnace based on a silica cross-tube arrangement. The specimen, contained in a separate silica sample tube, was introduced through one arm of the assembly while the secondary arm at right angles allowed direct visual access. The sample tube could be either filled with gas (normally dry nitrogen) or evacuated. Quenching to room temperature was accomplished by dropping the specimen onto a copper block. When dealing with deliquescent crystals the block was enclosed in a vessel containing silica gel.

The diffusion temperature was normally chosen to be about 50°C below the melting point of the respective alkali halide crystal. Diffusion times were relatively short, ranging from about 30 minutes to 3 hours. It was found that prolonged diffusion at these temperatures tended to result in a certain amount of melting at the doped crystal face. The use of a higher temperature exaggerated this effect. It appears that the dopant, when present in a sufficiently high concentration, depresses the intrinsic melting point of the crystal.

The use of short diffusion times resulted in an inhomogeneous impurity distribution. In general the impurity extended to a depth of approximately 0.2 mm into each crystal face. This situation was found to be desireable in view of certain interesting phenomena which arose. This aspect, which relates to the formation of colour centres in the central undoped crystal regions, is discussed in chapter 7. In addition, additional absorption bands which are associated with impurities already present in the 'nominally pure' crystals could be identified by a direct comparison between the outer and inner crystal regions.

All subsequent heat treatments of the specimens were carried out in a second stabilised furnace based on a silica cross-tube arrangement. The specimen, contained in a separate silica sample tube, was introduced through one arm of the assembly while the secondary arm at right angles allowed direct visual access. The sample tube could be either filled with gas (normally dry nitrogen) or evacuated. Quenching to room temperature was accomplished by dropping the specimen onto a copper block. When dealing with deliquescent crystals the block was enclosed in a vessel containing silica gel.

4.3 Measurement techniques

4.3.1 General

All optical absorption spectra were recorded using a Varian DMS-90 UV-VIS Spectrophotometer covering the wavelength range 190 nm to 900 nm. Measurements at liquid nitrogen temperature (LNT) were made using a standard optical cryostat.

Optical bleaching was performed using a Hanovia 250 W projector in conjunction with a set of Balzer interference filters (50 nm bandwidth). The ultraviolet spectral region was covered using a high pressure mercury lamp.

ESR spectra for the europium-doped alkali halides were obtained at room temperature using a Decca XI Spectrometer operating at X-band (9278 MHz) with 100kHz field modulation. Calibration of the magnetic field was achieved using a $(Cr(NH_3)_5Cl)Cl_2$ sample following the procedure outlined by Andriessen [12].

4.3.2 The traversing-slit attachment

The traversing-slit (TS) attachment (figure 4.6(a)) was designed to be used in conjunction with the spectrophotometer in order to resolve the spacial inhomogeneities arising in the diffused crystals. The intention was to develop a technique for studying the distribution of defect centres through their characteristic optical absorption bands. Once this information had been obtained it would serve as the basis for a description of the physical processes occuring during diffusion.

The profiling technique involved recording the optical absorption spectrum from a thin region of the crystal selected by a very narrow aperture. By systematically incrementing the position of the crystal behind the aperture, the complete crystal area could be sampled. In figure 4.6(b) the TS assembly is shown in its dismantled form. The crystal is

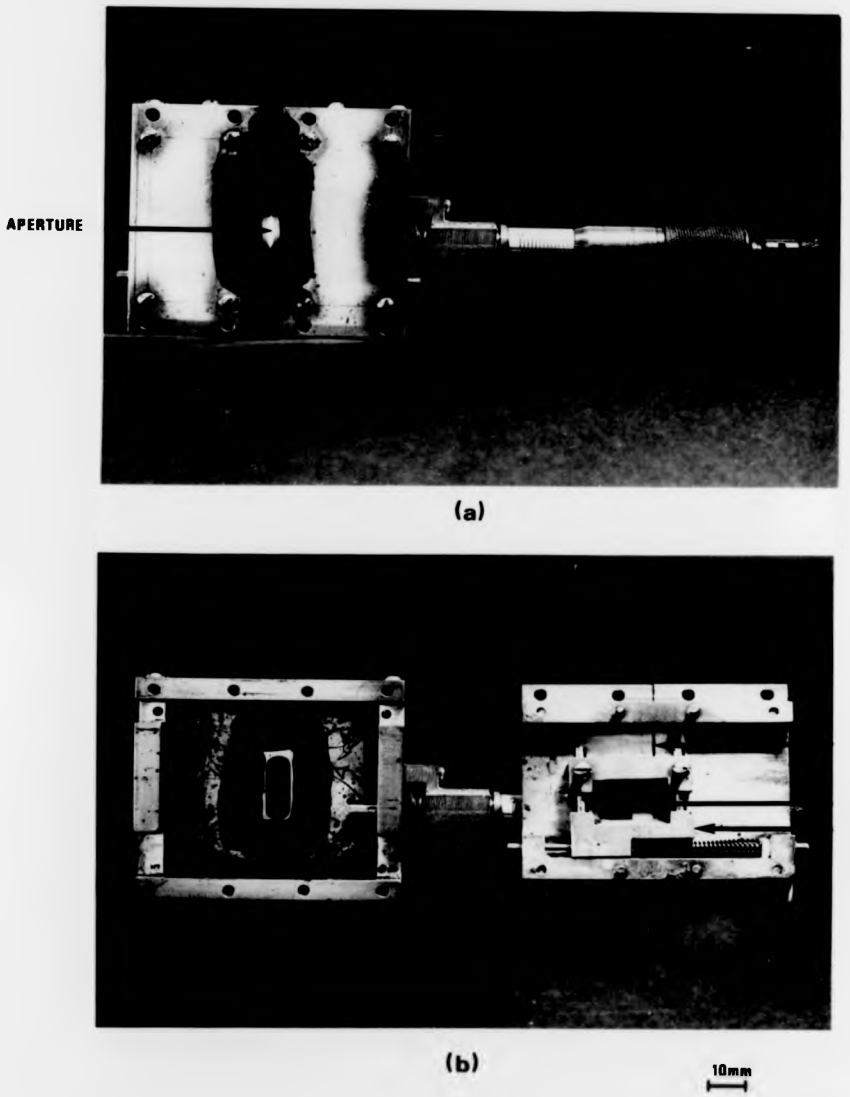

Figure 4·6 The traversing slit attachment
(a) Complete
(b) Dismantled to illustrate its method of operation

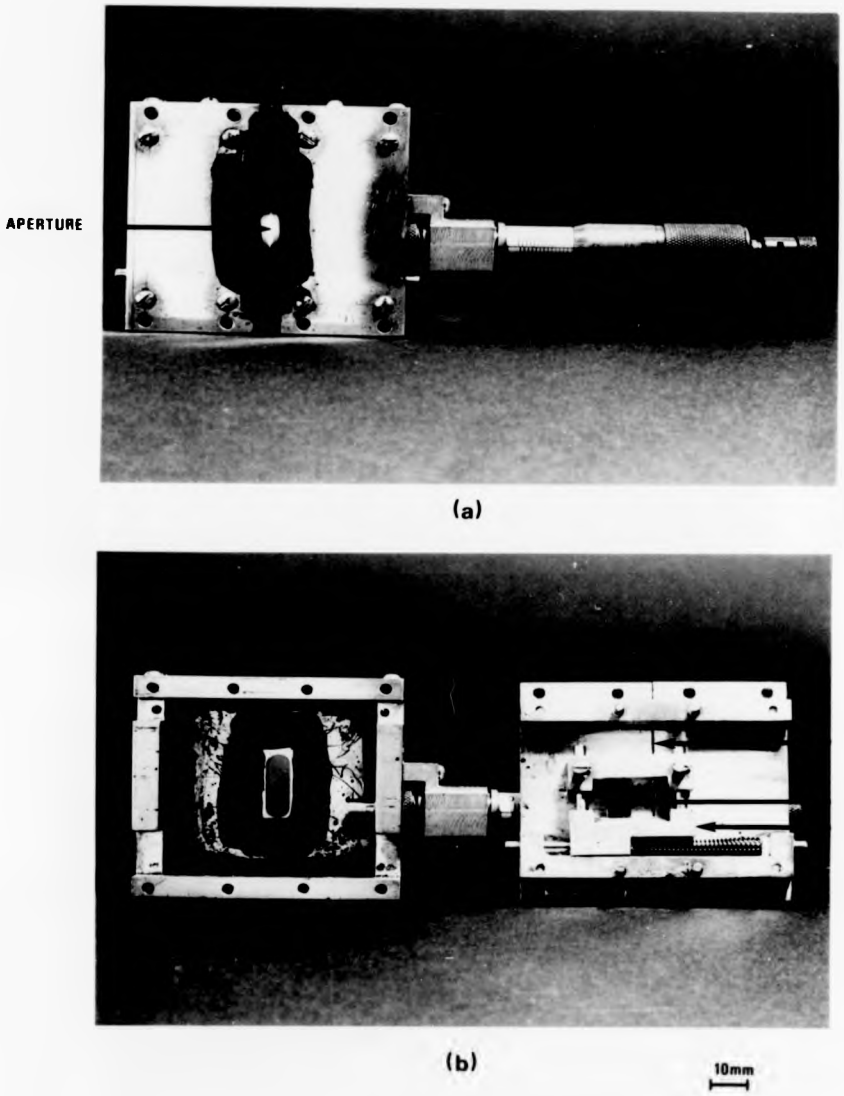

Figure 4·6 The traversing slit attachment
(a) Complete
(b) Dismantled to illustrate its method of operation

mounted in an upright postion clamped between the horizontally arranged upper and lower sharp-edged blinds. The blinds form part of a carriage which is moved relative to the aperture by means of an external micrometer screw thread. Spectrosil quartz windows cover the front and rear apertures in order to provide an atmospheric seal. A dry nitrogen atmosphere, necessary while studying deliquescent crystals, could be introduced through a nozzle to the rear of the assembly.

Analysis of the curves obtained using the TS assembly is based on the assumption that the concentration of a particular defect centre is proportional to the maximum absorption coefficient of its associated absorption band. This is equivalent to assuming that Beer's law is obeyed [6]. Generally the information is presented as a graph displaying the maximum absorbance (proportional to the maximum absorption coefficient for a fixed crystal thickness) associated with each defect centre versus distance into the crystal. It should be noted that these absorbance values need to be corrected for the characteristic background absorption associated with an identically dimensioned piece of nominally pure material. This procedure is particularly important for measurements obtained where the crystal edge is contained within the aperture. A typical plot of background absorbance versus distance into an undoped crystal is shown in figure 4.7. The passage of the crystal edge across the aperture produces a rise in the absorbance level. As the edge region moves out of the sampled area, the absorbance drops to a constant level characteristic of the pure crystal alone. The point at which this occurs provides a measure of the total aperture width.

The choice of aperture width was necessarily a compromise between obtaining high spatial resolution and high signal-to-noise ratio. An aperture width of 0.36 ± .01 mm was used for all early work, representing as it did a good compromise. Some of the later work used an aperture of 0.25 ± .01 to provide better spatial resolution but at the expense of

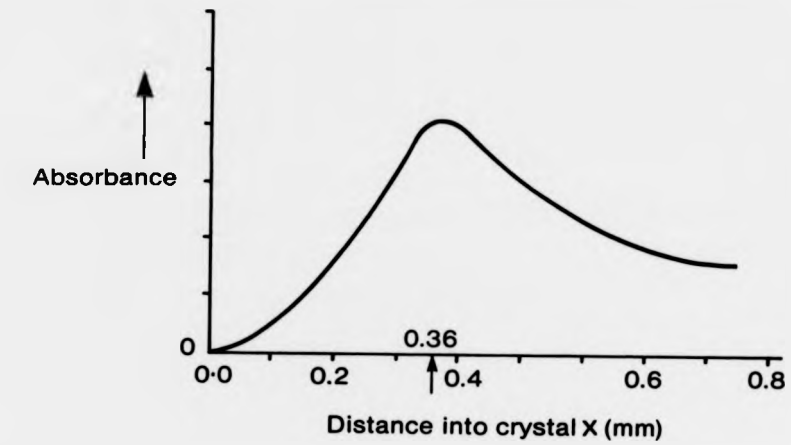

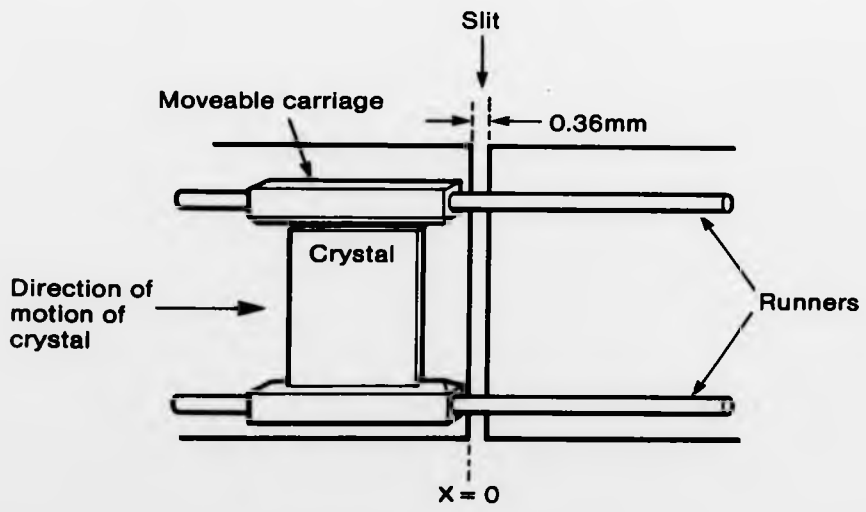

Figure 4.7 The background absorption as a function of the distance measured into the crystal. A schematic diagram describing the movement of the crystal over the slit is also included.

increased signal noise. Since the aperture is of a comparable width to the various crystal regions under measurement, an averaged absorbance/concentration profile is observed. Some examples of how the experimental absorbance profile relates to the actual concentration profile are given in figure 4.8.

4.4 Computational method

All computational work was performed in the Algol progamming language using a Burroughs B6700 digital computer. Use was made of the Burroughs B6700 implementation of the Numerical Algorithms Group (NAG) Algol 60 library Mark 6.

The problem was essentially that of diagonalising the matrices obtained in the energy level calculations. The matrix elements were calculated by hand using the methods described earlier and entered in surd form into the program. Only the lower triangle is required since all of the matrices are real and symmetric. The total matrix was formed by summing the individual matrices and finally, all of the eigenvalues and eigenfunctions were determined using the F02ABA algorithm (NAGALIB: 996/20: Mk5: Nov '75).

4.5 References

1. F.H.Spedding and A.H.Daane, "The Rare Earths", John-Wiley and sons, N.Y. (1961)

2. R.C.Weast Editor, "CRC Handbook of Chemistry and Physics", 62nd Edition, CRC Press Inc., Florida (1981-1982)

3. G.V.Samsonov Editor, "Handbook of the Physicochemical Properties of the Elements", Oldbourne, London (1968)

4. An.N.Nesmayanov, "Vapour Pressures of the Chemical Elements", R.Gary

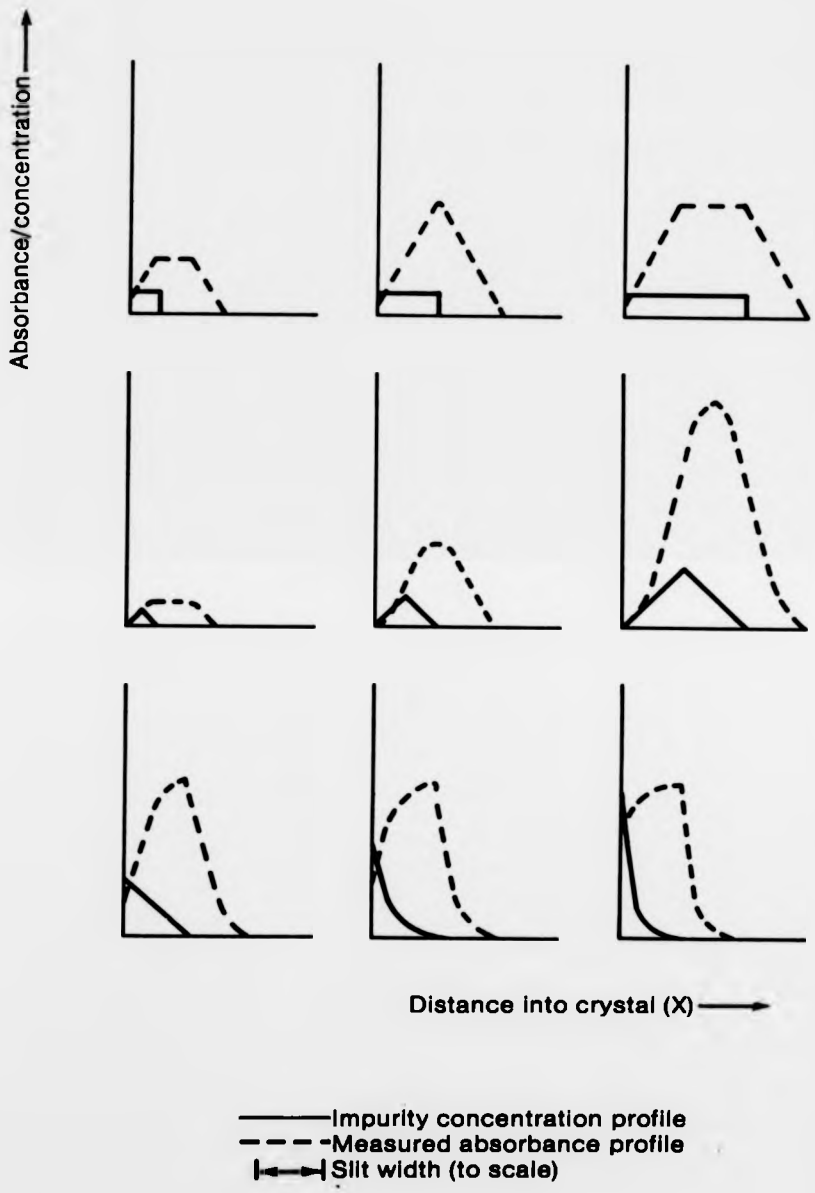

Figure 4.8 The relationship between the actual impurity concentration profile and the measured optical absorbance profile using the TS assembly.

Ed., Elsevier Publ. Co., Amsterdam and N.Y. (1963)

5. P.Hultgren et al., "Selected Values of the Thermodynamic properties of the Elements", American Society for Metals, Ohio (1973)

6. Z.K.Kun et al., Journal of the Physics and Chemistry of Solids, 29, p895 (1968)

7. B.S.Gorobets et al., Soviet Physics Doklady, 13, p519 (1968)

8. B.V.R.Chowdari, Solid State Communications, 9, p1659 (1971)

9. B.V.R.Chowdari and N.Itoh, Physica Status Solidi (b), 44, p549 (1971)

10. J.Boldu O et al., Journal of Chemical Physics, 67, p2391 (1977)

11. S.Radhakrishna and B.V.R.Chowdari, Physica Status Solidi (a), 12, p557 (1972)

12. W.T.M.Andriessen, Journal of Magnetic Resonance, 23, p339 (1976)

5. DIVALENT YTTERBIUM

5.1 Introduction

In this chapter the results derived in chapters 2 and 3 are used to discuss the atomic energy level structure of Yb^{2+} and, in particular, the effect on these levels of an applied octahedral (O_h) crystal field. The energy level structure is investigated by considering the energies of the allowable electric dipole transitions. A detailed theoretical treatment is presented followed by the description of a comprehensive set of experimental results obtained for Yb^{2+} in a range of alkali halide crystals. The theoretical and experimental results are compared in some detail.

It is well known that the site symmetry of a divalent ion in the alkali halides is orthorhombic (C_{2v}) due to the presence of a charge-compensating cation vacancy. The following theoretical treatment assumes that the situation may be represented to a good approximation by an octahedral site symmetry. The charge-compensating cation vacancy responsible for the lowering of symmetry effectively confines the orthorhombic distortion to the cation sublattice. The major contribution to the crystal field however arises from the surrounding nearest-neighbour anions of opposite charge. Unless there is a marked relaxation of the lattice in the vicinity of the cation vacancy, the anion sublattice will remain relatively unaffected. Consequently, the crystal field will be of predominantly octahedral symmetry. This approximation is widely used with generally excellent results, particularly for computations made of the optical dipole transition energies [1].

5.2 The free ion spectrum of Yb^{2+}

5.2.1 Introduction

Yb^{2+}, or alternatively Yb(III), possesses the electronic configuration $(Xe)4f^{14}5s^25p^6$. The completely filled 4f shell leads to a very simple $^1S_0$ ground state. The most important excited state configurations are, in order of increasing energy (figure 1.2), $4f^{13}5d$, $4f^{13}6s$ and $4f^{13}6p$. According to the arguments presented in section (3.6.4), it is possible to regard each of these states as a two electron configuration. As a result the analysis is comparatively straightforward.

Consider the relative importance of each of these configurations with respect to electric dipole transitions from the ground state. The $4f^{13}6p$ configuration is of little consequence for the following reasons. Firstly, transitions of the type $4f^{14} - 4f^{13}6p$ are Laporte (parity) forbidden and any resulting absorption bands will be at best very weak. Secondly, assuming that the relative energy positions shown in figure 1.2 are only slighty altered on placing Yb^{2+} into a crystal, such transitions will occur in the vacuum ultraviolet and are either masked by the very strong intrinsic band to band transitions of the host crystal or occur outside the range of the spectrophotometer. Both the $4f^{13}5d$ and $4f^{13}6s$ configurations possess the correct parity although as will be seen later, transitions to the $4f^{13}6s$ configuration are disallowed for other reasons.

The electron (hole) in the 4f shell transforms according to the direct product representation $D^{(3,-)} \otimes D^{(1/2,+)}$ of the group O(3). Similarly, electrons in the 6s and 5d shells transform as $D^{(0,+)} \otimes D^{(1/2,+)}$ and $D^{(2,+)} \otimes D^{(1/2,+)}$ respectively. It follows that the combined system wavefunction for the $4f^{13}6s$ configuration transforms according to the direct product

$$(D^{(3,-)} \otimes D^{(1/2,+)}) \otimes (D^{(0,+)} \otimes D^{(1/2,+)}) = D^{(4,-)} \oplus D^{(3,-)} \oplus D^{(2,-)} \qquad 5.1$$

Similarly for the $4f^{13}5d$ configuration

$$(D^{(3,-)} \otimes D^{(1/2,+)}) \otimes (D^{(2,+)} \otimes D^{(1/2,+)})$$
$$= D^{(4,-)} \oplus 3D^{(3,-)} \oplus 4D^{(4,-)} \oplus 4D^{(3,-)}$$
$$\oplus 4D^{(2,-)} \oplus 3D^{(1,-)} \oplus D^{(0,-)} \qquad 5.2$$

An electric dipole transition ($D^{(1,-)}$) from an initial state $^1S_0$ ($D^{(0,+)}$) is only allowed if the final state transforms according to $D^{(1,-)}$ (see section (3.8)). There are only three such states occuring in the decompositions above, all of which belong to the $4f^{13}5d$ configuration.

Based on the above, albeit elementary, analysis it would be quite reasonable to dismiss entirely the $4f^{13}6s$ configuration. We will nevertheless consider it further since a complete analysis of its energy level structure is quite simple and, moreover, the similarity of the principles involved will allow much of the detail to be omitted from the calculation of the more complex $4f^{13}5d$ configuration. Furthermore, an understanding of the $4f^{13}6s$ configuration is required later in connection with certain details of the Yb^{2+} spectrum in the alkali halides.

5.2.2 The $4f^{13}6s$ configuration

The $4f^{13}6s$ configuration consists of a total of four states (equation 5.1). All states possess odd parity and are described by their total angular momenta J = 4, 3, 3 and 2. In an LS-coupling scheme, L = 3 and S = 0 or 1 giving rise to two terms ^1F and ^3F with energies given by

$$^3F = -\sum_k f_k F^k$$
$$^1F = -\sum_k f_k F^k + g_3 \zeta^3 \qquad 5.3$$

Using equation 3.49 and putting $l_1 = 3$ and $l_2 = 0$ gives

$$f_k = (-1)^3 \begin{Bmatrix} 3 & 0 & 3 \\ 0 & 3 & k \end{Bmatrix} [3][0] \begin{pmatrix} 3 & k & 3 \\ 0 & 0 & 0 \end{pmatrix} \begin{pmatrix} 0 & k & 0 \\ 0 & 0 & 0 \end{pmatrix} \qquad 5.4$$

The second of the 3-j symbols has the effect of limiting the available values of k to k = 0. Therefore the only permissible value is $f_0 = 1$

The coefficient g_3 for this configuration is given by

$$g_3 = (1 - 4(\underline{s}_1.\underline{s}_2))([3][0]/[3]) \begin{pmatrix} 3 & 3 & 0 \\ 0 & 0 & 0 \end{pmatrix}^2 = 2/7 \qquad 5.5$$

Hence, using the fact that $D_3 = 7$ for the fs configuration [2], the LS-coupled term energies become finally

$$\begin{aligned} {}^3F &= -F_0 \\ {}^1F &= -F_0 + 2G_3 \end{aligned} \qquad 5.6$$

The next stage is to transform the above LS-coupling term energies into their equivalent form in a J_1j-coupling scheme by using repeatedly the recoupling relation (equation 3.56) for each matrix element. For example, consider the following matrix element

$$\langle j_1=5/2, j_2=1/2, J=3 | H_1 | j_1'=7/2, j_2'=1/2, J=3 \rangle$$

$$= (192)^{1/2} \left[7 \begin{Bmatrix} 1/2 & 1/2 & 0 \\ 3 & 0 & 3 \\ 5/2 & 1/2 & 3 \end{Bmatrix} \begin{Bmatrix} 1/2 & 1/2 & 0 \\ 3 & 0 & 3 \\ 7/2 & 1/2 & 3 \end{Bmatrix} \langle 0,3,3 | H_1 | 0,3,3 \rangle \right.$$

$$\left. + 21 \begin{Bmatrix} 1/2 & 1/2 & 1 \\ 3 & 0 & 3 \\ 5/2 & 1/2 & 3 \end{Bmatrix} \begin{Bmatrix} 1/2 & 1/2 & 1 \\ 3 & 0 & 3 \\ 7/2 & 1/2 & 3 \end{Bmatrix} \langle 1,3,3 | H_1 | 1,3,3 \rangle \right]$$

$$= 8(3)^{1/2} \left[\frac{(-F_0 + 2G_3)}{28} - \frac{(-F_0)}{28} \right]$$

$$= \frac{4(3)^{1/2}}{7} G_3 \qquad 5.7$$

All possible matrix elements are evaluated in this way and the completed matrix is shown in figure 5.1.

The spin-orbit interaction H_2 is diagonal in a J,j-coupling scheme. It's matrix elements are determined very simply by using equations 3.58 and 3.62 giving

$$\begin{aligned}
&\langle (1/2,3)j,(1/2,0)1/2,J|\ H_2\ |(1/2,3)j',(1/2,0)1/2,J'\rangle \\
&\quad = (-\zeta_{4f})[j(j+1) - 1/2(1/2+1) - 3(3+1)]/2\ \delta(J,J')\delta(j,j') \\
&\quad = -\zeta_{4f}[j(j+1) - 51/4]/2 \\
&\quad = -(3/2)\zeta_{4f} \qquad \text{for } j = 7/2 \\
&\quad = 2\zeta_{4f} \qquad \text{for } j = 5/2
\end{aligned} \tag{5.8}$$

The principal quantum number, n = 4, has been dropped in this case since there can be no confusion as to which shell the spin-orbit parameter refers. The completed matrix is given in figure 5.2.

The complete system energies (eigenvalues) and wavefunctions (eigenfunctions) are obtained by combining the electrostatic and spin-orbit interactions. This is achieved by summing the two matrices obtained above and then diagonalizing the resultant matrix. The procedure is equivalent to solving the secular determinant

$$\det \begin{vmatrix} -F_0-3\zeta_{4f}/2-\epsilon_4 & 0 & 0 & 0 \\ 0 & -F_0+8G_3/7-3\zeta_{4f}/2-\epsilon_3 & (3)^{1/2}4G_3/7 & 0 \\ 0 & (3)^{1/2}4G_3/7 & -F_0+8G_3/7+2\zeta_{4f}-\epsilon_3 & 0 \\ 0 & 0 & 0 & -F_0+2\zeta_{4f}-\epsilon_2 \end{vmatrix} = 0 \tag{5.9}$$

where ϵ_J denotes the energy of a state with total angular momentum J. The solution of equation 5.9 is straightforward yielding the following energies

		$^2F_{7/2}\ S_{1/2}$		$^2F_{5/2}\ S_{1/2}$	
		4	3	3	2
$^2F_{7/2}\ S_{1/2}$	4	$-F_0$	0	0	0
	3	0	$-F_0 + {}^{8}/_{7}\,G_3$	$\frac{4(3)^{1/2}}{7}\,G_3$	0
$^2F_{5/2}\ S_{1/2}$	3	0	$\frac{4(3)^{1/2}}{7}\,G_3$	$-F_0 + {}^{6}/_{7}\,G_3$	0
	2	0	0	0	$-F_0$

Figure 5.1 The electrostatic interaction matrix for the $4f^{13}6s$ configuration in a J_1j-coupling scheme.

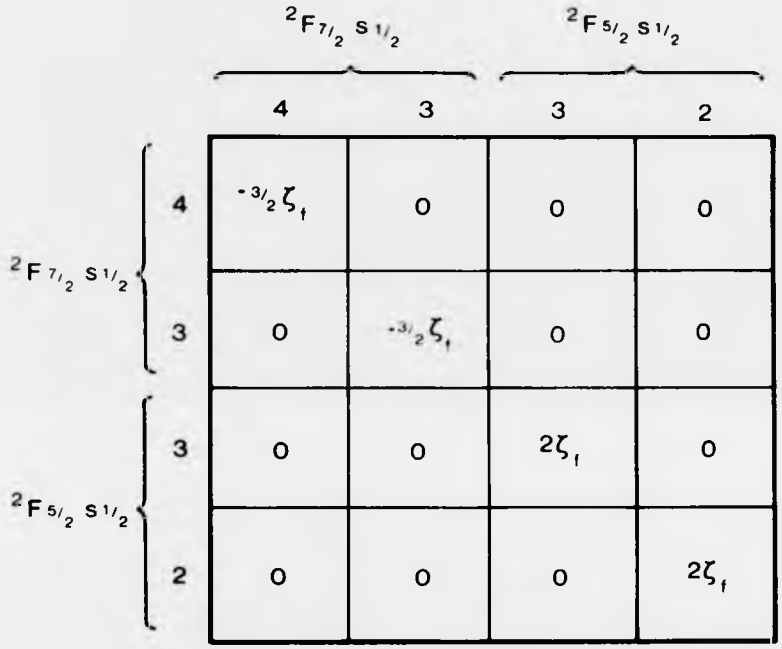

Figure 5.2 The spin-orbit interaction matrix for the $4f^{13}6s$ configuration in a $J_l j$-coupling scheme.

$$\epsilon_2 = -F_0 + 2\zeta_d$$

$$\epsilon_3 = -F_0 + G_3 + \zeta_d \pm [(G_3 + 7\zeta_d/4)^2 - 4G_3\zeta_d]^{1/2} \qquad 5.10$$

$$\epsilon_4 = -F_0 - 3\zeta_d/2$$

The positive sign in the expression for ϵ_3 refers to the $^2F_{5/2}s_{1/2}$ term.

The actual coupling scheme on which the total system energy levels are based is intermediate between that of pure LS-coupling (electrostatic interaction alone) and pure J_1j-coupling (spin-orbit interaction alone). The precise composition depends on the relative importance of the two interactions. It is instructive to determine the manner in which the system evolves between the two coupling extremes. For this purpose it is convenient to choose coordinates for the axes such that both extremes are represented on the same graph with unity overall splitting. This condition is satisfied by plotting a normalised energy η_J for each state of total angular momentum J against a dimensionless parameter ξ given by

$$\xi = X/(1 + X) \qquad 5.11$$

where $$X = 7\zeta_d/4G_3 \qquad 5.12$$

The relationship for η_J is given by

$$\eta_J = \epsilon_J/[(2G_3)^2 + (7\zeta_d/2)^2]^{1/2}$$

$$= \epsilon_J/[(7\zeta_d/2)(1 + 1/X^2)^{1/2}] \qquad 5.13$$

In the LS-coupling limit $\zeta_d \to 0$ and consequently $\xi \to 0$; in the J_1j-coupling limit $G_3 \to 0$ and $\xi \to 1$.

Using equations 5.10 and 5.13 the following relationships for the individual η_J are obtained

$$\epsilon_2 = -F_0 + 2\zeta_p$$

$$\epsilon_3 = -F_0 + G_3 + \zeta_p \pm [(G_3 + 7\zeta_p/4)^2 - 4G_3\zeta_p]^{1/2} \qquad 5.10$$

$$\epsilon_4 = -F_0 - 3\zeta_p/2$$

The positive sign in the expression for ϵ_3 refers to the $^2F_{5/2}s_{1/2}$ term.

The actual coupling scheme on which the total system energy levels are based is intermediate between that of pure LS-coupling (electrostatic interaction alone) and pure J,j-coupling (spin-orbit interaction alone). The precise composition depends on the relative importance of the two interactions. It is instructive to determine the manner in which the system evolves between the two coupling extremes. For this purpose it is convenient to choose coordinates for the axes such that both extremes are represented on the same graph with unity overall splitting. This condition is satisfied by plotting a normalised energy η_J for each state of total angular momentum J against a dimensionless parameter ξ given by

$$\xi = X/(1 + X) \qquad 5.11$$

where $$X = 7\zeta_p/4G_3 \qquad 5.12$$

The relationship for η_J is given by

$$\eta_J = \epsilon_J/[(2G_3)^2 + (7\zeta_p/2)^2]^{1/2}$$

$$= \epsilon_J/[(7\zeta_p/2)(1 + 1/X^2)^{1/2}] \qquad 5.13$$

In the LS-coupling limit $\zeta_p \to 0$ and consequently $\xi \to 0$; in the J,j-coupling limit $G_3 \to 0$ and $\xi \to 1$.

Using equations 5.10 and 5.13 the following relationships for the individual η_J are obtained

$$\eta_2 = (4/7)(1 + 1/X^2)^{-1/2}$$

$$\eta_3 = \frac{((1/X) + (1/7)) \pm [(1/X^2) - (2/7X) + 1]^{1/2}}{2(1 + 1/X^2)^{1/2}} \qquad 5.14$$

$$\eta_4 = -(3/7)(1 + 1/X^2)^{-1/2}$$

These normalised energy levels are plotted in figure 5.3. The dashed line at $\zeta = 0.938$ indicates the position of the free ion levels as determined by Bryant [3]. The closeness of the free ion levels to the J,j-coupling limit fully justifies the earlier decision to label the final states in this way. Such labels correspond very closely with the real situation.

Bryant's least squares analysis of the experimentally observed energy levels at 34656, 34991, 44854 and 45208 cm^{-1} yields the following values for the parameters G_3 and ζ_f

$G_3 = 336.6\ cm^{-1}$

$\zeta_f = 2913.6\ cm^{-1}$

The value given for F_0 in his paper is, however, incorrectly attributed. The value quoted is in fact equal to the common energy addition to the $4f^{13}6s$ configuration compared with the ground state. According to the complete system Hamiltonian described in section 3.2, the true value of F_0 is expected to provide only a small and negative contribution to these diagonal terms. In addition, the parameters relating to the electrostatic interaction have been incorrectly defined. It is not sufficient to take the term energies associated with the fs configuration and merely invert them to give $^1F = F_0 + G_3$ and $^3F = F_0 - G_3$ for the $f^{13}s$ configuration. Although such a choice of parameter definition produces no difference in the value for G_3 (the total splitting in both cases is $2G_3$), it makes the value for F_0 totally meaningless. To avoid this confusion it is more appropriate to use the parameter Δ to represent the total common contribution to the energy levels of the excited state configuration with

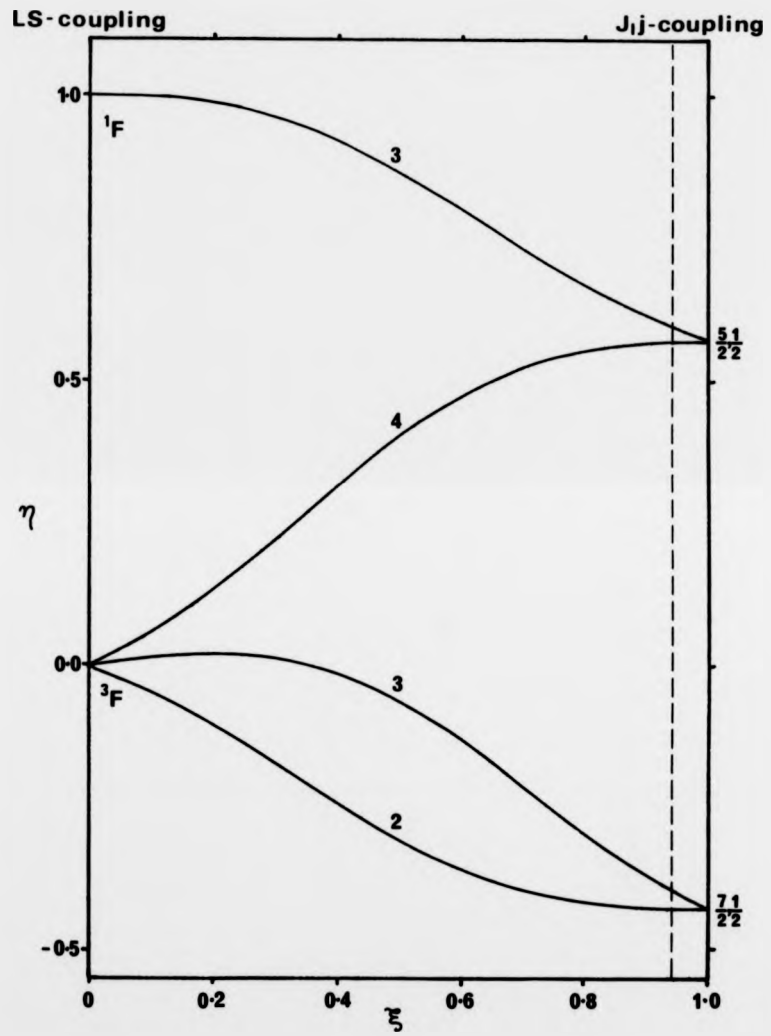

Figure 5.3 Evolution of the normalised $4f^{13}6s$ configuration energy levels between the LS– and J_1j–coupling limits. The dashed line at $\xi = 0.938$ indicates the position of the free ion levels.

respect to the ground state. That is

$$\Delta = \langle f^{13}s| H_o |f^{13}s\rangle + \langle f^{13}s| \Sigma(-Ze^2/r_i - U(r_i))|f^{13}s\rangle - F_o - \langle f^{14}| H |f^{14}\rangle \qquad 5.15$$

Using the values obtained in Bryant's paper, a value of $\Delta = 39303\ cm^{-1}$ is obtained.

5.2.3 The $4f^{13}5d$ configuration

The $4f^{13}5d$ configuration consists of a total of 20 states all of which possess odd parity (equation 5.2). These states are subdivided according to their total angular momentum J = 6, 5, 4, 3, 2, 1 and 0. A calculation of the energy level structure proceeds in the same way as for the $4f^{13}6s$ configuration. However, due to the increased number of states involved, the resulting matrices are more cumbersome.

In an LS-coupling scheme L = 5, 4, 3, 2, 1 and S = 0, 1 giving rise to the terms $^{1,3}H$, $^{1,3}G$, $^{1,3}F$, $^{1,3}D$ and $^{1,3}P$. The coefficients f_k of the direct Slater integrals contain 3-j symbols of the form $\begin{pmatrix}2 & k & 2\\ 0 & 0 & 0\end{pmatrix}\begin{pmatrix}3 & k & 3\\ 0 & 0 & 0\end{pmatrix}$ which limits the possible values of k to k = 0, 2 and 4. The coefficients g_k are dependant on a 3-j symbol of the type $\begin{pmatrix}2 & k & 3\\ 0 & 0 & 0\end{pmatrix}$, limiting the values of k in this case to k = 1, 3 and 5. Note that it is only the singlet terms with L = k which actually contain an exchange part, namely the ^1P, ^1F and ^1H terms. The following expressions for the term energies are readily obtained

$$^3H = -F_o - 10F_2 - 3F_4$$

$$^1H = -F_o - 10F_2 - 3F_4 + 420G_5$$

$$^3G = -F_o + 15F_2 + 22F_4$$

$$^1G = -F_o + 15F_2 + 22F_4$$

$$^3F = -F_o + 11F_2 - 66F_4$$

$$^1F = -F_0 + 11F_2 - 66F_4 + 1206_3 \qquad 5.16$$

$$^3D = -F_0 - 6F_2 + 99F_4$$

$$^1D = -F_0 - 6F_2 + 99F_4$$

$$^3P = -F_0 - 24F_2 - 66F_4$$

$$^1P = -F_0 - 24F_2 - 66F_4 + 706_1$$

with [2] $F_2 = F^2/105$

$F_4 = F^4/693$

$G_1 = G^1/35$

$G_3 = G^3/315$

$G_5 = G^5/1524.6$

The transformation from LS-coupling to J,j-coupling is achieved using equation 3.56 and the resulting matrix is shown in figure 5.4.

The matrix elements of H_2 in a J,j-coupling scheme are easily obtained using equations 3.58 and 3.62. They are given by

$$^2F_{7/2}d_{5/2} = -3\xi_f/2 + \xi_d$$

$$^2F_{7/2}d_{3/2} = -3\xi_f/2 - 3\xi_d/2 \qquad 5.17$$

$$^2F_{5/2}d_{5/2} = 2\xi_f + \xi_d$$

$$^2F_{5/2}d_{3/2} = 2\xi_f - 3\xi_d/2$$

Note that the sign of the spin-orbit parameter ξ_f is reversed since it refers to a hole in the 4f shell ($4f^{13}$) not to an electron ($4f^1$). The complete H_2 matrix is reproduced in figure 5.5 in the same form as the H_1 matrix.

An exact analytical solution of the secular determinant for $H_1 + H_2$ in this case requires the evaluation of three quartics and two cubics. In practice the best that can be achieved is to obtain numerical solutions for various combinations of values using a computer. This method has been used previously by Bryant [3] to compare theory with experiment for the Yb^{2+} free ion. He obtained the following values for the various

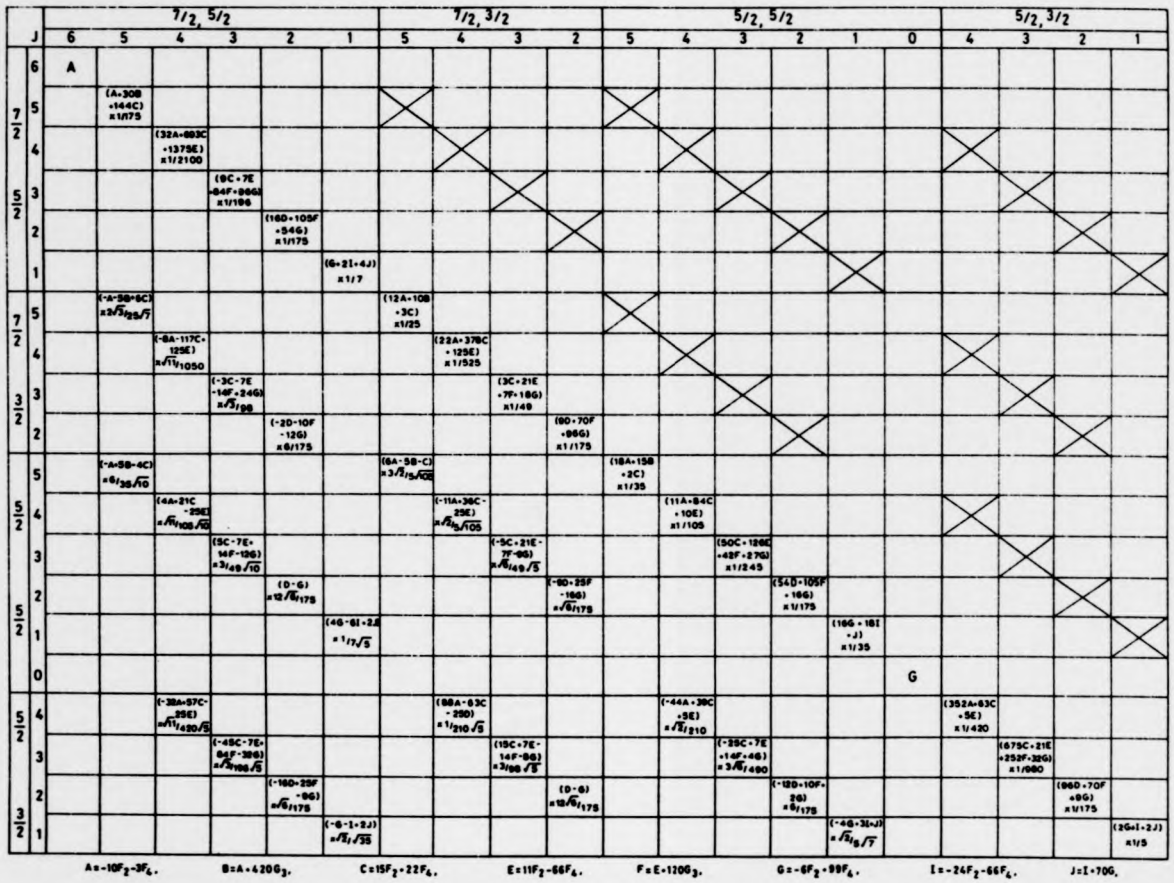

Fig.5.4 The electrostatic interaction matrix for the $4f^{13}5d$ configuration in a Jᵢⱼ–coupling scheme. The matrix is symmetric

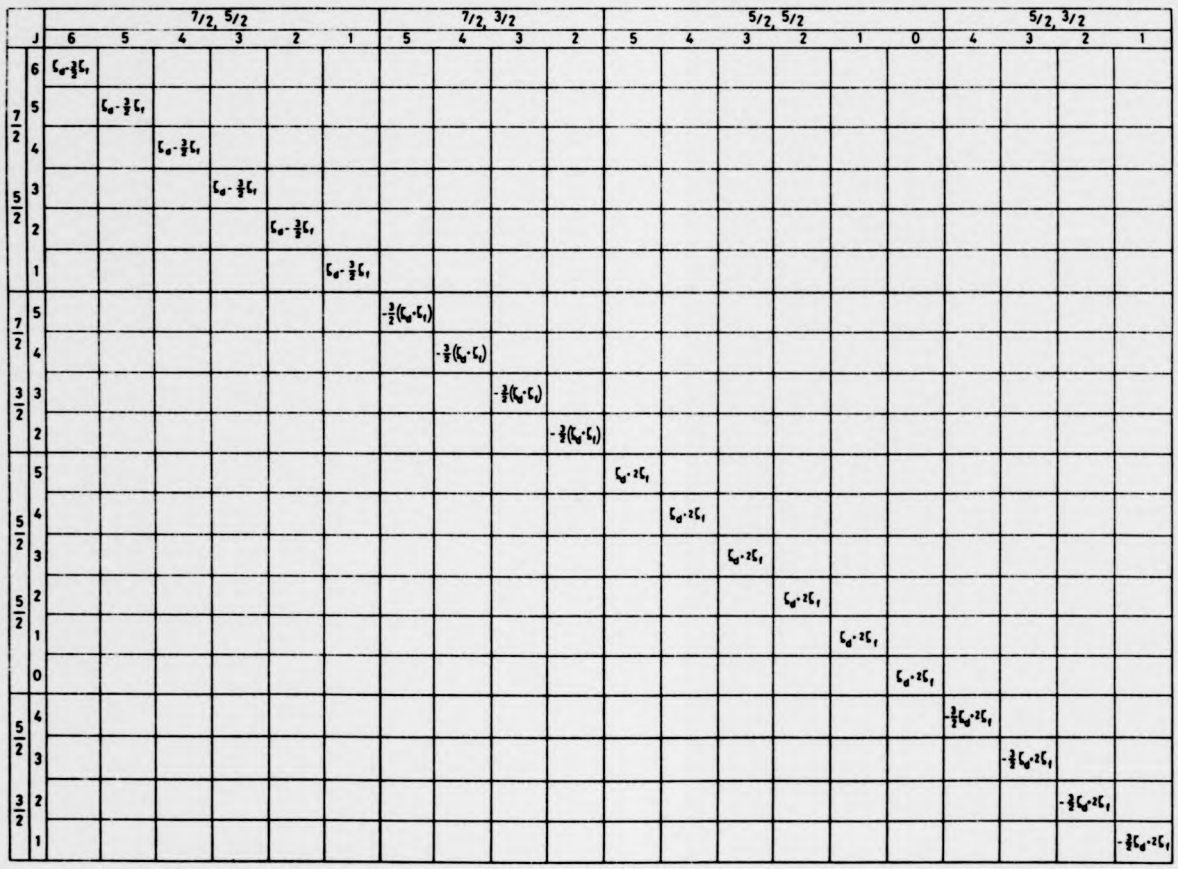

Fig.5.5 The spin-orbit interaction matrix for the $4f^{13}5d$ configuration in a Jlj-coupling scheme

parameters using a least squares analysis

F_2 = 186.8 cm^{-1}

F_4 = 14.4 cm^{-1}

G_1 = 193.2 cm^{-1}

G_3 = 24.62 cm^{-1}

G_5 = 4.11 cm^{-1}

ζ_f = 2950.2 cm^{-1}

ζ_d = 1211.0 cm^{-1}

Δ = 44073 cm^{-1}

The parameter Δ replaces the parameter F_0 incorrectly used by Bryant. The reasons for this are the same as those discussed earlier in connection with the $4f^{13}6s$ configuration.

The spin-orbit parameters appear to be the most influencial for the $4f^{13}5d$ configuration. This situation is equivalent to the observation made earlier for the $4f^{13}6s$ configuration. Unfortunately, since in this case only a numerical solution is obtainable, it is not possible to derive a quality factor equivalent to ξ. Certain evidence to support the greater importance of J_1j-coupling is nevertheless provided by a comparison of figures 5.6 and 5.7. Figure 5.6 illustrates the manner in which the free ion levels evolve from the LS-coupling limit; figure 5.7 shows their evolution from the J_1j-coupling limit. The levels exhibit considerably less divergence in the latter case.

5.2.4 Transition intensities

As discussed earlier, electric dipole transitions from the $4f^{14}$ ground state are allowed only to a state which transforms according to $D^{(1,-)}$. The $4f^{13}5d$ configuration possesses three such states and, therefore, three

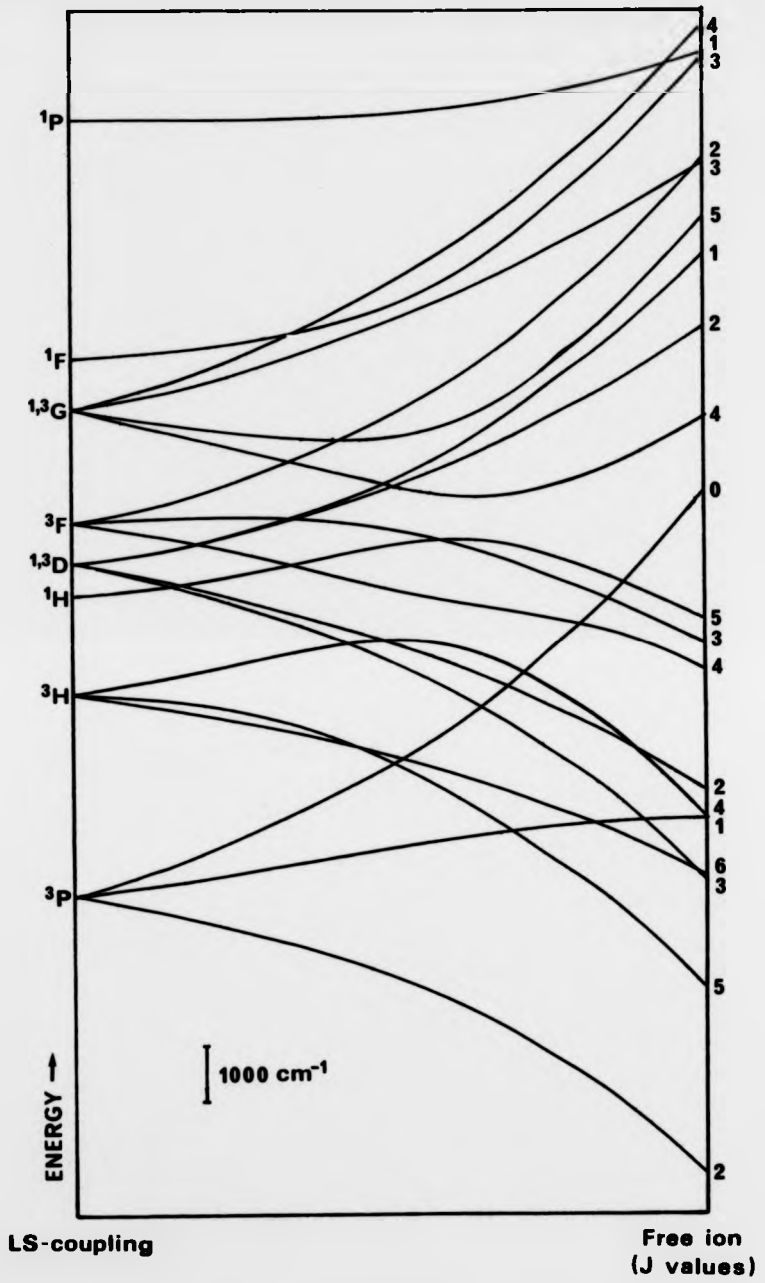

Figure 5.6 Evolution of the free ion energy levels of the $4f^{13}5d$ configuration of Yb^{2+} from the LS–coupling limit.

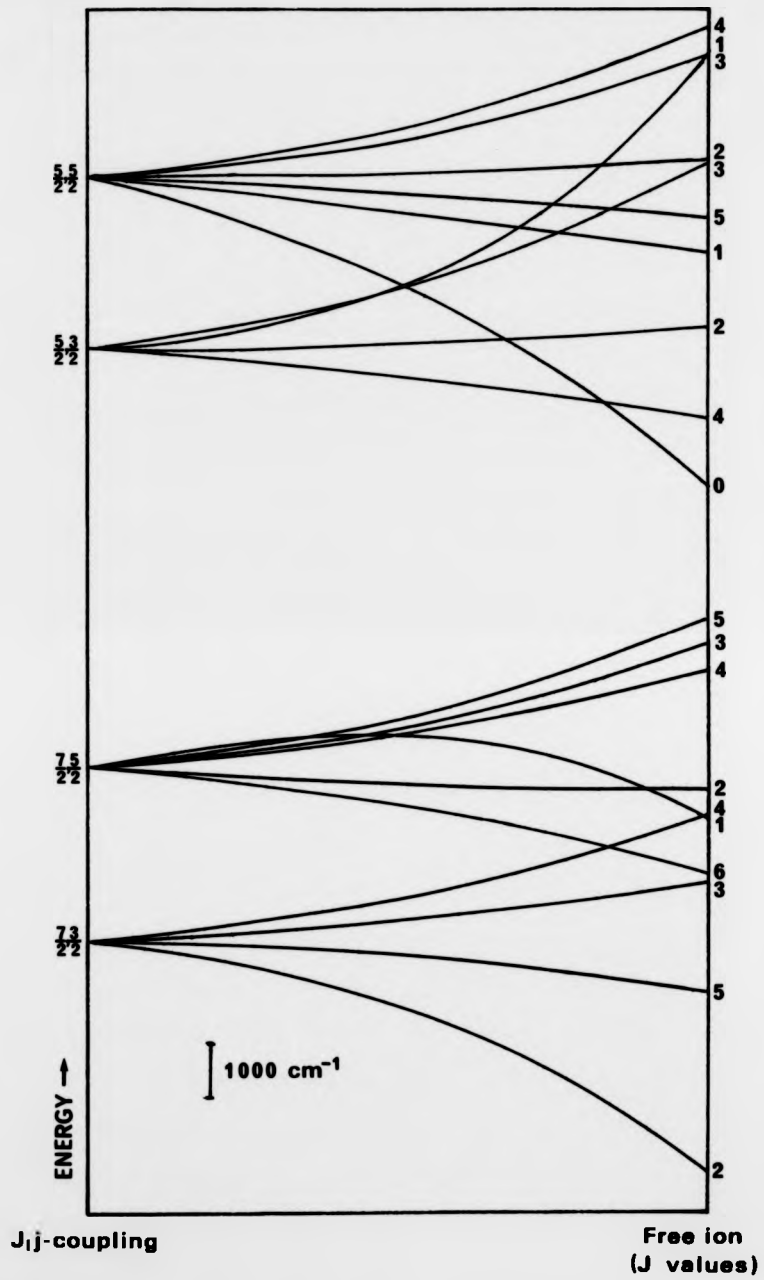

Figure 5.7 Evolution of the free ion energy levels of the $4f^{13}5d$ configuration of Yb^{2+} from the J_1j–coupling limit.

transitions are expected although not necessarily of the same intensity. If pure LS-coupling were applicable, then the three states of interest would be denoted by the terms $^1P_1$, $^3P_1$ and $^3D_1$. Since the electric dipole operator does not act on the spin angular momentum, the only allowed transition will be to the singlet state $^1P_1$. The effect of the spin-orbit interaction is to mix the three states with J = 1 resulting in a redistribution of the available intensity. The transition intensity for will be directly proportional to $(a_i)^2$, where a_i is the coefficient of $^1P_1$ wavefunction (i.e. $a_i|0,1,1\rangle$) contained in the i^{th} state.

Since the above analysis has been presented in the more appropriate J,j-coupling scheme, it is necessary to express the LS-coupled $|0,1,1\rangle$ wavefunction in terms of J,j-coupled wavefunctions. This is accomplished using equation 3.18 giving

$$|0,1,1\rangle = 2(1/7)^{1/2}\,|7/2,5/2,1\rangle + (1/35)^{1/2}\,|5/2,5/2,1\rangle + (2/5)^{1/2}\,|5/2,3/2,1\rangle \qquad 5.18$$

The computer program was able to determine both the eigenvalues and the eigenfunctions of the $4f^{13}5d$ configuration. The coefficients of the J,j-coupled eigenfunctions were used directly with equation 5.18 to obtain the transition intensity of each state. The individual coefficients are reproduced in figure 5.8 along with the calculated coefficients of $|0,1,1\rangle$ and the corresponding overall intensities. The coefficients of $|0,1,1\rangle$ are the same as those given by Bryant [3]. It should be noted that 90 percent of the available intensity is concentrated in transitions to the $(^2F_{5/2}d_{5/2})_1$ level.

Designation of state	Coefficients				Intensity
	$\|^{7}/_{2}, ^{5}/_{2}, 1\rangle$	$\|^{5}/_{2}, ^{5}/_{2}, 1\rangle$	$\|^{5}/_{2}, ^{3}/_{2}, 1\rangle$	$\|0, 1, 1\rangle$	
$(^2F_{5/2}\, d_{3/2})_1$	-0.5154	-0.1745	-0.8390	-0.9497	0.902
$(^2F_{5/2}\, d_{5/2})_1$	0.2176	0.9203	-0.3251	0.1145	0.013
$(^2F_{7/2}\, d_{5/2})_1$	0.8288	-0.3500	-0.4363	0.2916	0.085

Figure 5.8 The relationship between LS-coupled and J_1j-coupled wavefunctions and the intensities of the three allowed transitions of the type $4f^{14} \rightarrow 4f^{13}5d$ for the Yb^{2+} free ion.

5.3 The optical absorption spectrum of Yb^{2+} in an octahedral crystal field

5.3.1 Preliminary treatment

In this section the problem of determining how the Yb^{2+} free ion levels decompose under the influence of an octahedral/cubic crystal field is discussed. Initially the approach will be qualitative, based on group theoretical arguments, although later the groundwork for a more quantitative analysis will be described in some detail. The importance of this preliminary consideration of the underlying symmetry arguments becomes apparent when an attempt is made to classify the resultant states. The only meaningful classification is shown to be in terms of irreducible representations of the octahedral point symmetry group O_h. In addition, the insight provided by such a treatment can often indicate the existence of a simplifying trend which may subsequently be of benefit in reducing the complexity of the quantitative calculations.

The decomposition of energy levels transforming according to irreducible representations of the group O(3) under the influence of an octahedral crystal field is described by equation 3.71. For example the ground state of Yb^{2+}, which transforms according to $D^{(0,+)}$ in the O(3) symmetry situation, is found to transform according to Γ_{1g} in a field of O_h symmetry. The situation for the various states of the $4f^{13}5d$ configuration is rather less trivial. According to equation 5.2 the free ion states are described by the decomposition

$$D^{(4,-)} \oplus 3D^{(3,-)} \oplus 4D^{(4,-)} \oplus 4D^{(3,-)} \oplus 4D^{(2,-)} \oplus 3D^{(1,-)} \oplus D^{(0,-)}$$

In an octahedral symmetry these states decompose to give

$$6\Gamma_{1u} \oplus 5\Gamma_{2u} \oplus 12\Gamma_{3u} \oplus 18\Gamma_{4u} \oplus 17\Gamma_{5u} \qquad 5.19$$

Therefore, the 20 levels of the free ion configuration decompose into 58 levels under the influence of an octahedral crystal field.

Electric dipole transitions from the Γ_{1g} ground state are only allowed to levels transforming according to Γ_{4u}. There are 18 such levels appearing in the decomposition above, resulting in at most 18 transitions. Thus the initial problem of considering a total of 58 levels, requiring the manipulation of 58x58 matrices, has been reduced quite rigorously to one of considering only 18x18 matrices. A significant simplification based purely on symmetry arguments.

5.3.2 The $4f^{13}5d$ configuration in an octahedral crystal field

The Hamiltonian H describing the complete system comprises the following terms

$$H = H_0 + H_1 + H_2 + H_3(d) + H_3(f) \qquad 5.20$$

The methods derived in chapter 3 with $\Gamma_1 = \Gamma_6$ are used to obtain the matrix elements for each of these interactions separately in a common J_1j-coupling scheme. The resulting matrices are summed and the total matrix is diagonalised by computer to yield the complete system eigenvalues and eigenfunctions. The H_0 term has no effect on the relative separation of the levels within the configuration and is normally neglected.

A similar approach has been published previously by Piper et al [4] and by Eremin [5]. In both cases, however, the system was described in terms of LS-coupled states. The ambiguity involved in labelling the free ion states in this way is apparent in the discrepancies between figure 3 of reference [4] and figure 1 of reference [5]. These are the only theoretical calculations published to date for the $4f^{13}5d$ configuration in a crystal

field, although an earlier paper by Eremin [6] describes a different but incorrect approach.

The matrix elements of the free ion Hamiltonians H_1 and H_2 have already been calculated (see section 5.2.3). Only those states with J = 1, 3, 4, 5 and 6 need be included since states with J = 0 and 2 contain no part transforming according to Γ_4. The state with J = 5 is included twice because it contains two separate parts transforming in this way. The system wavefunction is written as

$$|(s_1=1/2,l_1=3)j_1,\ (s_2=1/2,l_2=2)j_2,\ J\ \alpha\Gamma_4\rangle$$

where the index α is used to distinguish between the two J = 5 states.

The matrix elements of the crystal field Hamiltonians $H_3(d)$ and $H_3(f)$ are calculated using the results of section (3.8.2). Both a fourth and a sixth order crystal field operator arise for the f electron Hamiltonian and the resulting matrices are referred to respectively as the B_4^* and B_6^* matrices. The d electron matrix is referred to as the Dq matrix. All three matrices are reproduced in appendix 2. In order to obtain the complete system matrix it is necessary to sum together the modified H_1 and H_2 matrices with the matrices given in appendix 2, each individually multiplied by the relevant adjustable radial parameter(s). The complete system matrix is next diagonalised to yield the required eigenvalues and eigenfunctions.

Each of the three crystal field matrices was checked in the following way. The adjustable parameter associated with the matrix under scrutiny was set equal to unity with all other parameters set equal to zero. The total system matrix was then diagonalised. Only values of 6 and -4 should be obtained for Dq = 1, B_4^* = 0 and B_6^* = 0. For Dq = 0, B_4^* = 1 and B_6^* = 0, the values obtained should be 1.45454545, -0.48484848 and -2.90909090 [5]. For Dq = 0, B_4^* = 0 and B_6^* = 1, the corresponding values should be 8.95104895, 3.72960373 and -6.71328671 [5]. This procedure provides a very accurate check of the

correctness of all of the matrix elements.

In total there are 10 adjustable parameters to be considered, namely F_2, F_4, G_1, G_3, G_5, ζ_d, ζ_f, Dq, B_4^4 and B_6^4. Certain simplifying assumptions are required since to allow each and every parameter to vary independently would produce a hopelessly complicated state of affairs. It is not unreasonable as a starting approximation to employ the free ion values for the direct and exchange electrostatic parameters and the spin-orbit parameters. The effect of varying each of the crystal field parameters in turn can then be investigated.

The evolution of the crystal field levels from the free ion levels due to variations in Dq, B_4^4 and B_6^4 are presented in figures 5.9, 5.10 and 5.11 respectively. A number has been added to each energy level in order to indicate its relative transition strength. The transition strength has been calculated for each level as $(50a_i)^2$, where a_i is the coefficient of $|0,1,i\rangle$ for the i^{th} level. Dq is varied over both positive and negative values corresponding to octahedral and cubic crystal fields respectively. In each case the range over which the adjustable parameter is allowed to vary is chosen to be representative for systems of this type. A further calculation is presented in figure 5.12 where B_4^4 and B_6^4 are allowed to vary while Dq is set equal to a mid range value of 1000 cm^{-1}. Both B_4^4 and B_6^4 are seen to have a comparatively negligible effect on the energy level positions and transition strengths. It is apparant that the overall effect of an applied crystal field is a redistribution of the total transition intensity in a complex manner over the 18 available levels.

The general behaviour of the levels as Dq is increased (figure 5.9) is rather interesting. At high crystal fields , that is Dq greater than 1400 cm^{-1}, the 18 levels segregate into 4 distinct groups. Furthermore, these 4 groups can be arranged into a pair (separation of order 10000 cm^{-1}) tending towards lower energies and a pair (separation similarly of order 10000 cm^{-1}) tending towards higher energies. The slope $\partial E/\partial Dq$ of each pair of levels at

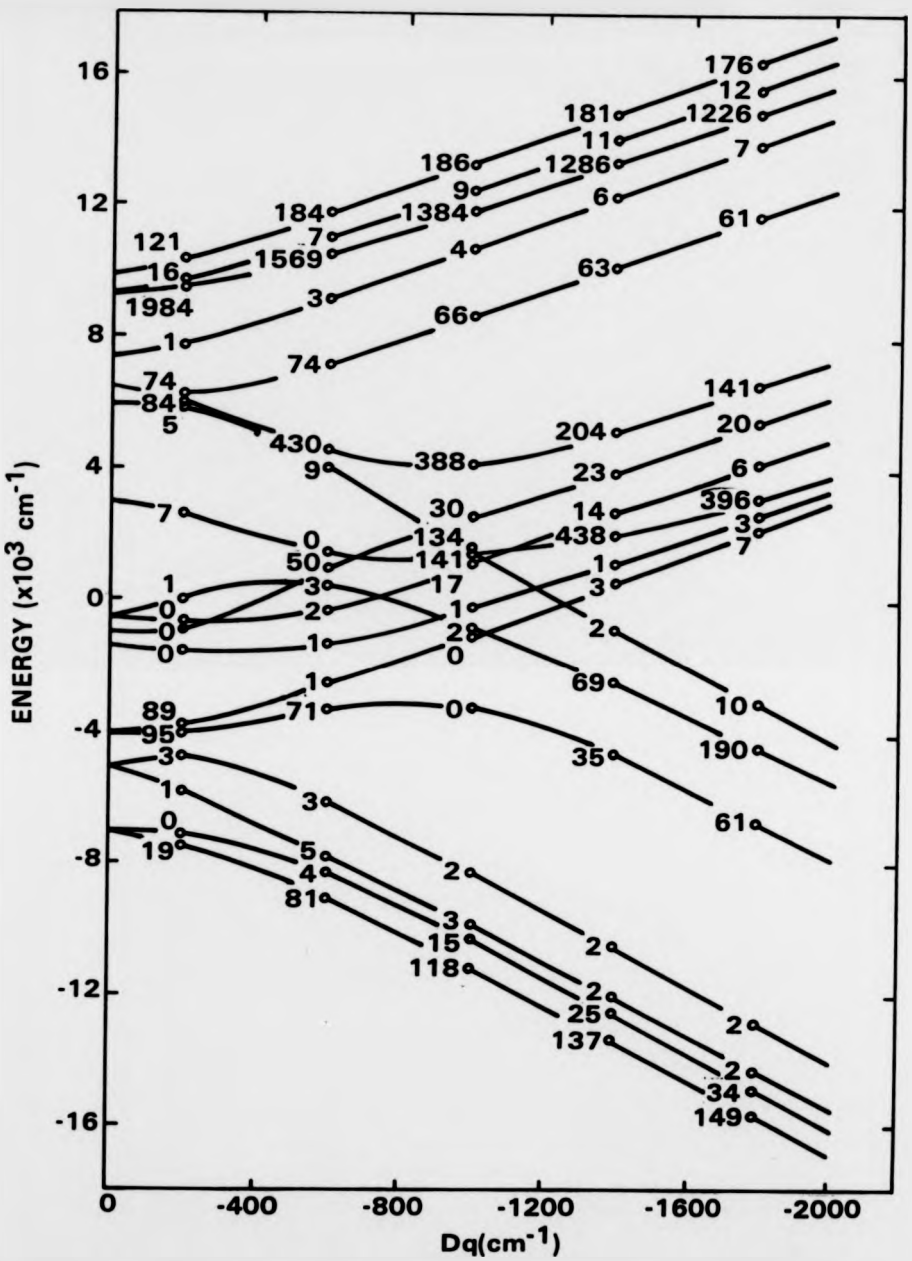

Fig. 5.9 **The effect of variations in the parameter Dq on the free ion energy level structure for the $4f^{13}5d$ configuration. The numbers indicate relative transition intensities.**
(b) Cubic crystal field.

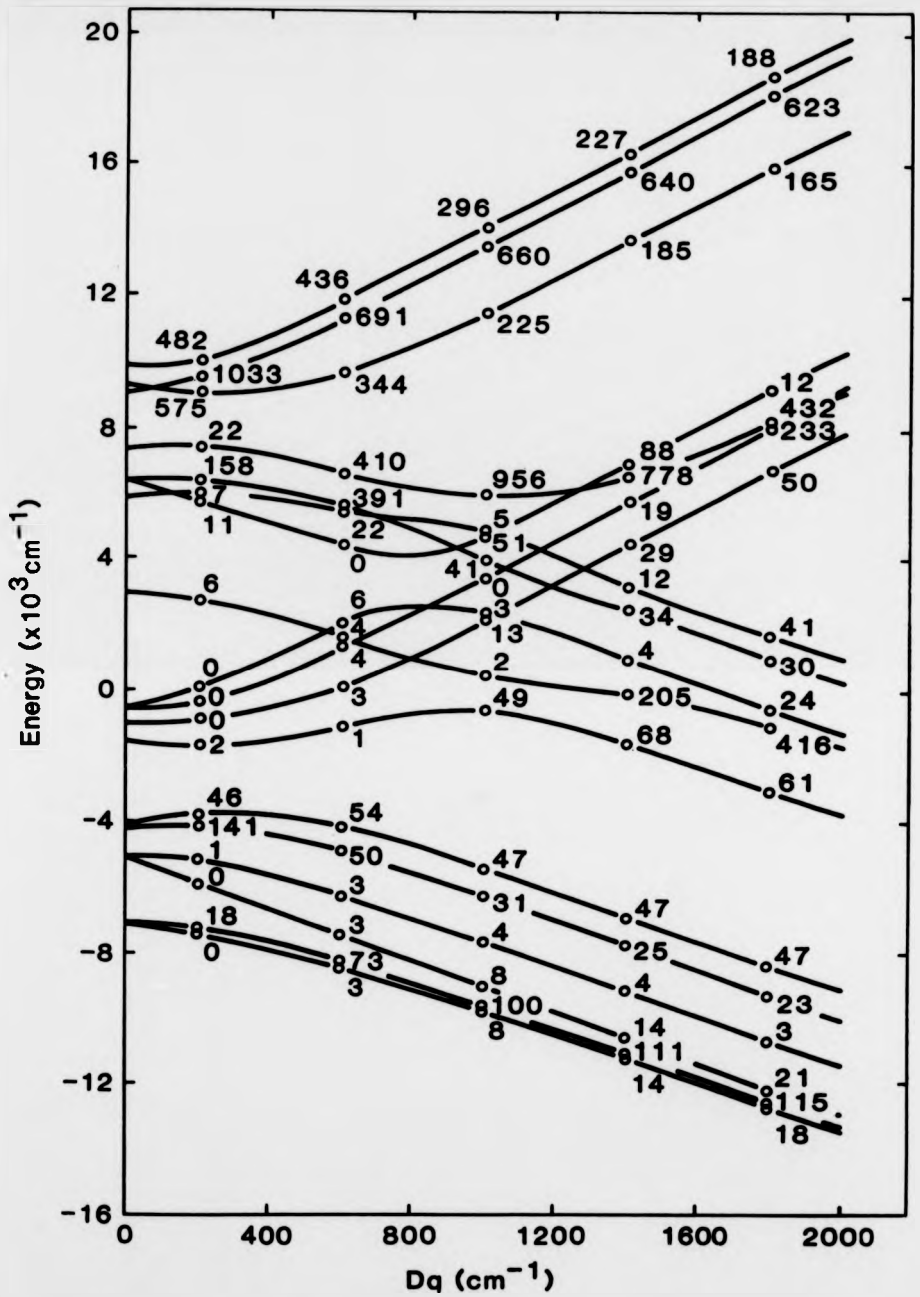

Fig. 5.9 The effect of variations in the parameter Dq on the free ion energy level structure for the $4f^{13}5d$ configuration. The numbers indicate relative transition intensities.
(a) Octahedral crystal field

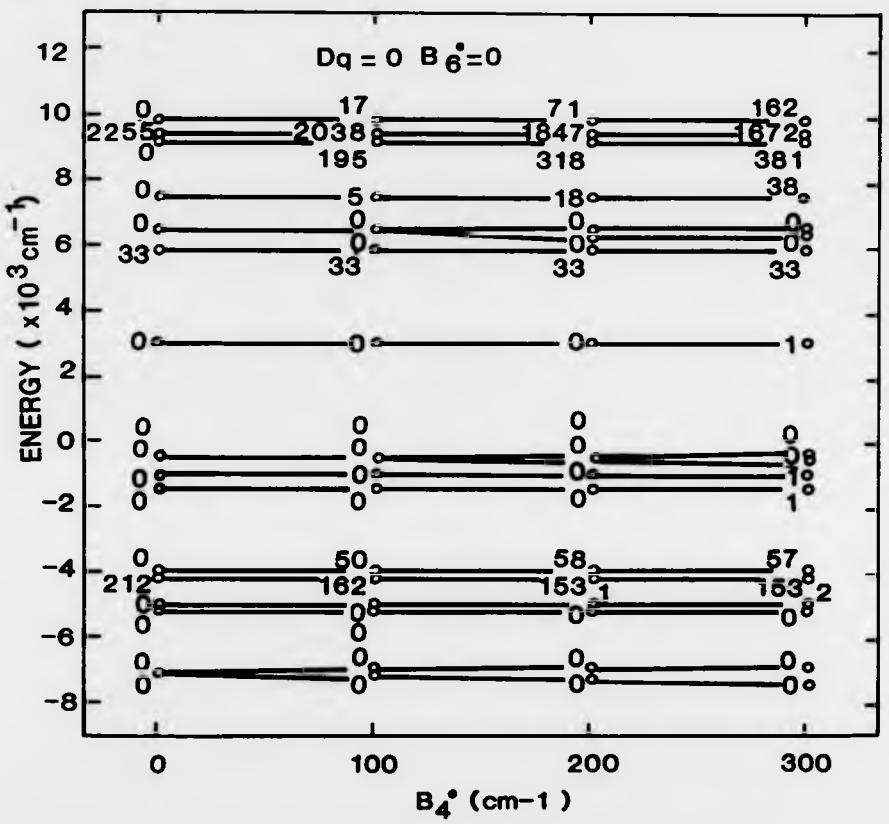

Fig 5.10 The effect of variations in the parameter B_4° on the free ion energy level structure for the $4f^{13}5d$ configuration The numbers indicate relative transition intensities.

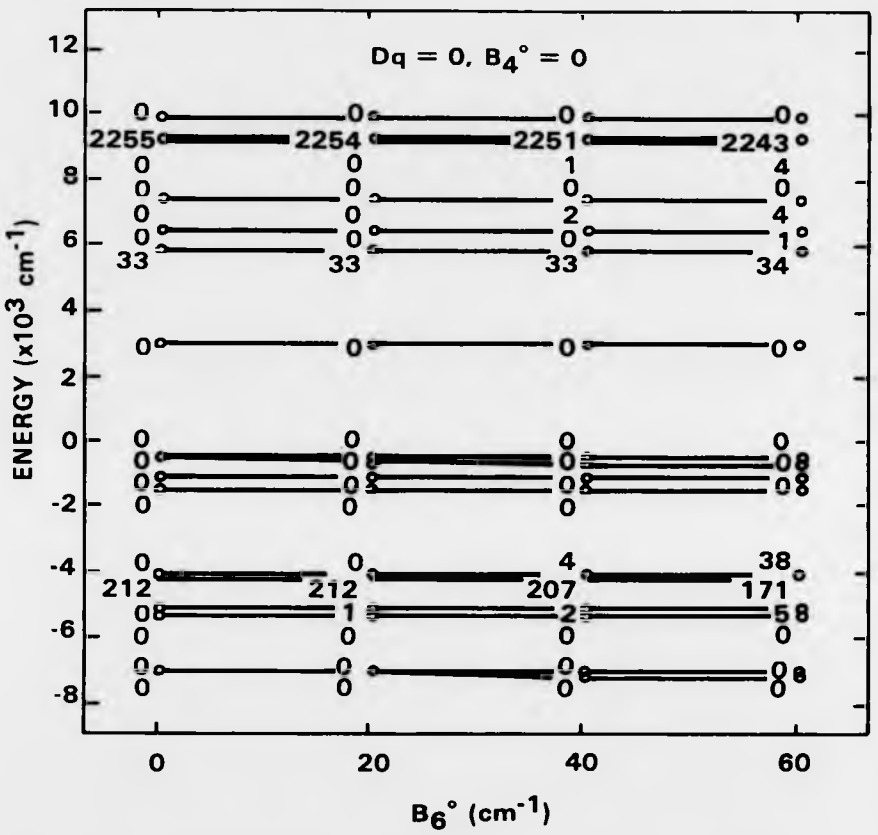

Fig. 5.11 The effect of variations in the parameter B_6° on the free ion energy level structure for the $4f^{13}5d$ configuration. The numbers indicate relative transition intensities.

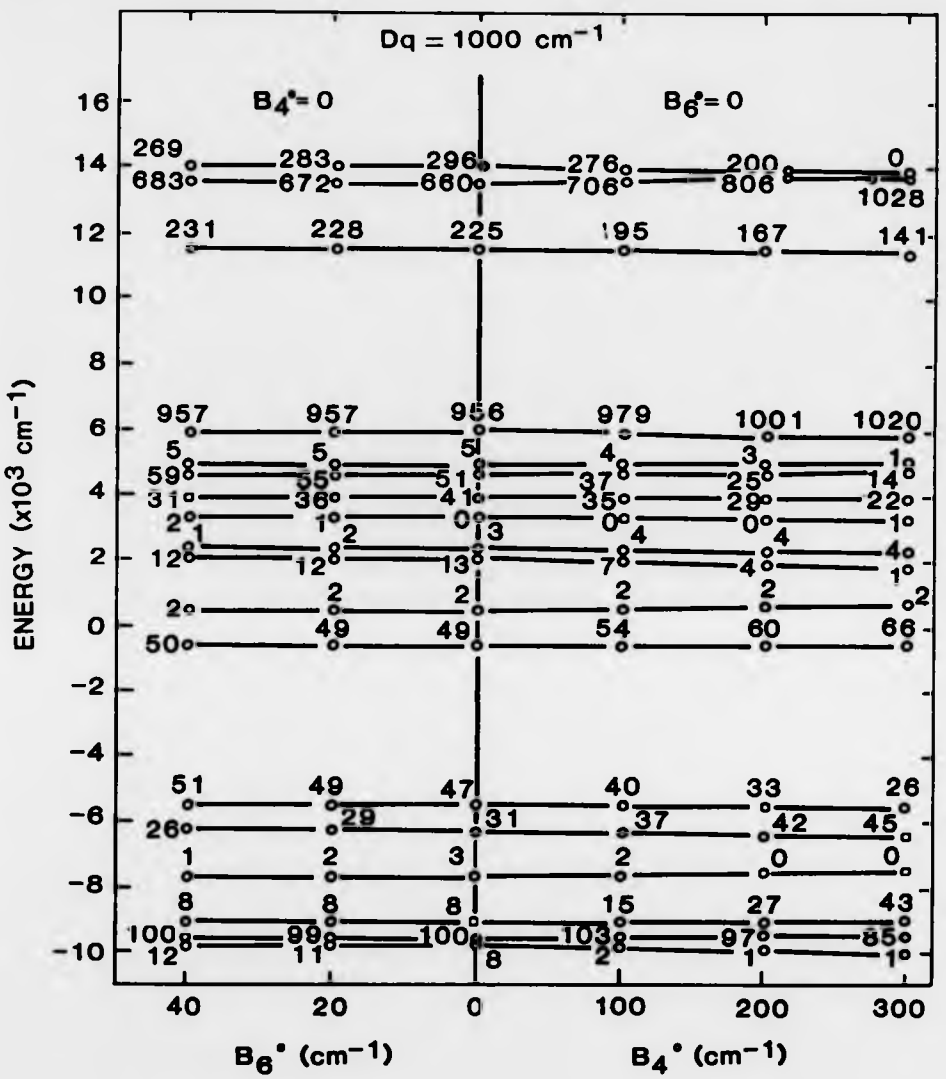

Fig. 5.12 The effect of variations in the parameters B_4° and B_6° on the energy level structure for the $4f^{13}5d$ configuration in an octahedral crystal field (Dq = 1000 cm $^{-1}$). The numbers indicate relative transition intensities.

Dq = 1800 cm^{-1} in an octahedral field is 5.83 ± 0.06 and -3.88 ± 0.05 respectively. For a cubic field the slopes are 3.90 ± 0.06 and -5.82 ± 0.06. These values compare very closely with the values expected for a single d electron, namely 6 and -4 for the octahedral case and 4 and -6 for the cubic case. The relatively constant separation between the groups of levels reflects very well the spin-orbit splitting of the $4f^{13}$ state. This splitting is given by equation 5.8 as $7\zeta_{4f}/2$ which, on substitution of the free ion value for ζ_{4f}, is equal to 10325.7 cm^{-1}.

The observations made above for the Yb^{2+} ion in a crystal field can be described qualitatively by a relatively simple model. The model consists of a $4f^{13}$ core state, which is relatively unaffected by the field, coupled to a crystal-field-split 5d electron state. The situation is illustrated schematically in figure 5.13. The model predicts that each group of levels at high fields is characterised by a pair of terms referring to the $4f^{13}$ core states ($^2F_{7/2}$ or $^2F_{5/2}$) and to the d electron states ($d_{5/2}$ or $d_{3/2}$). It is a relatively simple matter to predict the number of levels within each of these groups. For example, the set of levels characterised by $^2F_{7/2}d_{3/2}$ transform according to the direct product representation $D^{(7/2)} \otimes D^{(3/2)}$ of SO(3) (neglecting parity). In an octahedral crystal field this product decomposes into

$$(\Gamma_4 \oplus \Gamma_7 \oplus \Gamma_8) \otimes \Gamma_8 = \Gamma_1 \oplus \Gamma_2 \oplus 3\Gamma_3 \oplus 4\Gamma_4 \oplus 4\Gamma_5 \qquad 5.21$$

predicting a total of 4 individual levels transforming according to Γ_4. Similarly, the groups of levels characterised by $^2F_{5/2}d_{3/2}$, $^2F_{7/2}d_{5/2}$ and $^2F_{5/2}d_{5/2}$ consist of 4,6 and 5 individual levels respectively in complete agreement with figure 5.9.

The dependence of the energy levels on B_4^4 and B_6^4 is much weaker than for Dq. This behaviour is not unexpected since the inner 4f electrons are

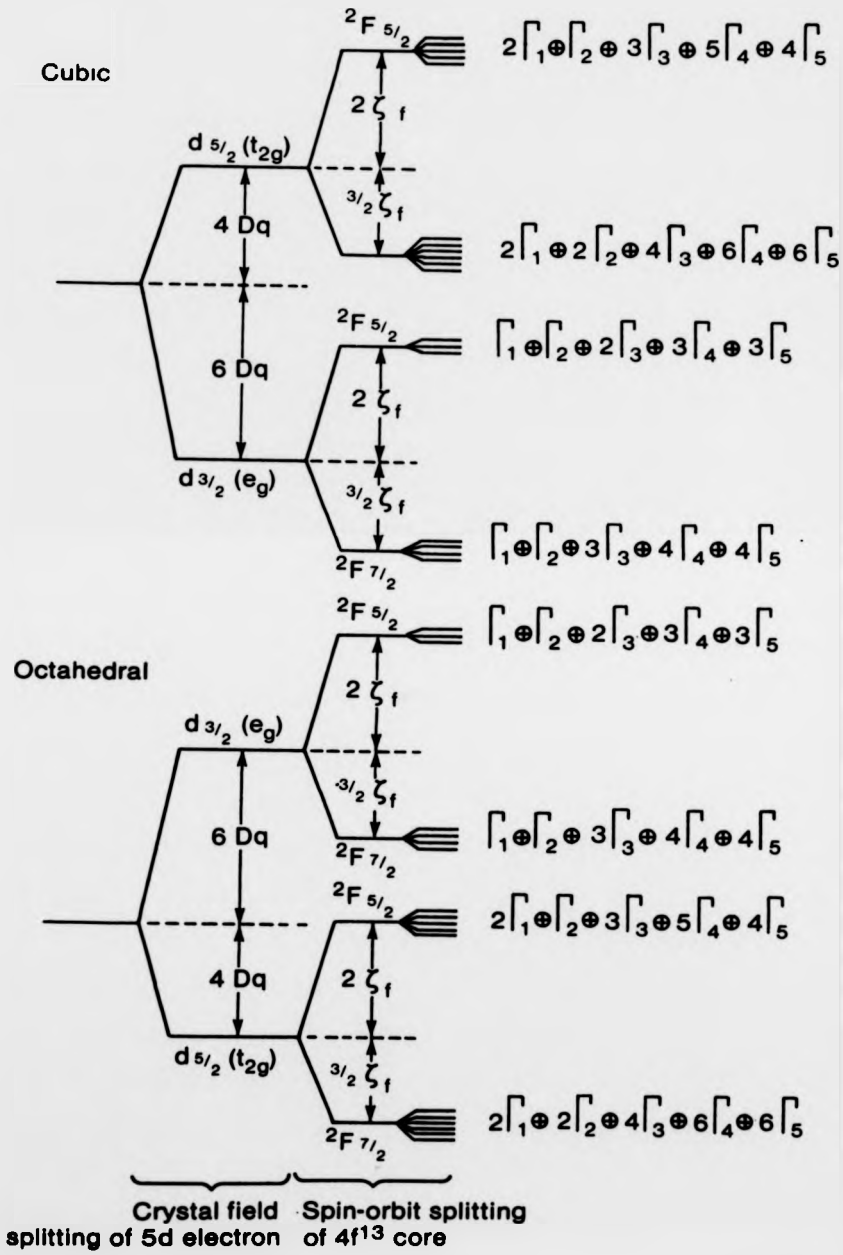

Figure 5.13 Schematic representation of a spin-orbit split $4f^{13}$ core state coupled to a crystal field split 5d electron.

shielded from the crystal field to a large extent by the filled 5s and 5p atomic shells. However, even though adjusting B_4^0 and B_6^0 generally leads to only a small variation in the relative energy level positions (eigenvalues), it does have a more marked effect on the transition strengths (eigenfunctions) Such extreme sensitivity of the eigenfunctions compared with the eigenvalues to changes in the adjustable parameters is a well known characteristic of systems of this type. Often, in an approximate treatment, B_4^0 and B_6^0 are neglected (see for example [4,5]) thereby leading to reasonable energy levels but poor intensities.

In the present study it was felt important to retain all of the crystal field parameters although certain assumptions as to their interrelation were made based on a survey of existing published experimental results. On a simplistic level it is expected that Dq, B_4^0 and B_6^0 will all increase in magnitude with decreasing impurity ion-anion(ligand) distance R. According to the point ion model both Dq and B_4^0 are proportional to R^{-5} while B_6^0 is proportional to R^{-7}. Experimentally the dependance for B_4^0 is observed to be more like R^{-2} [7]. Another interesting fact to emerge from the published experimental results is that, for a particular ion, the ratio B_6^0/B_4^0 remains relatively constant for a wide range of host crystals [7,8]. Even for different rare earth ions the ratio varies only slightly. For the Ho^{2+} ion ($4f^{11}$) in CaF_2 the ratio is found to be equal to -0.18 [8]. The ratio becomes -0.19 for Tm^{2+} ($4f^{13}$) in the same host [9]. Extrapolating from this slight but general trend and anticipating that the extra d electron for the $4f^{13}5d$ configuration will improve the shielding slightly, a reasonable value for the Yb^{2+} ion is

$$(B_6^0/B_4^0)_{cub} = -0.20 \qquad 5.22$$

The equivalent value corresponding to a crystal field of octahedral symmetry is, according to equations 3.81, given by

$$(B_2^0/B_4^0)_{oct} = -0.075 \qquad 5.23$$

It is more difficult to justify connecting Dq and B_4^0 via a simple relationship of this type. The 5d electron is strongly influenced by the surrounding lattice ions whereas the deeper 4f electrons are well shielded and only weakly influenced. Nevertheless, by considering the dependence of B_4^0 on host crystal for the Dy^{3+} ion in a range of alkaline earth fluorides [10,11] and on assuming typical values for Dq from results obtained elsewhere [5], it is possible to derive a linear relationship of the form

$$B_4^0 = -(a + b|Dq|) \qquad 5.24$$

where B_4^0 and Dq are in units of cm^{-1} and the absolute value of Dq is indicated. The best fit is provided when the parameters a and b take the values 150 cm^{-1} and 0.067 respectively.

When a divalent ion is considered in the same alkaline earth flouride system, it is found that the absolute value of B_4^0 is considerably smaller. For example, Dy^{3+} in CaF_2 yields a value $B_4^0 = -257.2\ cm^{-1}$ [11] consistent with equation 5.24, whilst $B_4^0 = -180\ cm^{-1}$ [9] or $-189\ cm^{-1}$ [12] for the isoelectronic divalent ion Tm^{2+} in the same host. Similarly for $CaF_2{:}Dy^{2+}$ a value of $B_4^0 = -188\ cm^{-1}$ is obtained [7]. It is assumed that a functional dependence similar to equation 5.24 connects B_4^0 and the magnitude of Dq for divalent ions. A direct scaling of the coefficients gives

$$(B_4^0)_{cub} = -(100 + 0.05|Dq|) \qquad 5.25$$

for the Yb^{2+} ion in a cubic field. This relationship is used in the present study along with the corresponding form relating to octahedral symmetry given by

$$(B_4^*)_{oct} = 100 + 0.05|Dq| \qquad 5.26$$

In figure 5.14 the energy levels and their associated transition strengths are plotted against the crystal field strength Dq. The relations derived above (equations 5.22, 5.23, 5.25 and 5.26) have been used to obtain reasonable values for B_4^* and B_2^*. A comparison with figure 5.9 shows that, while the inclusion of B_4^* and B_2^* significantly alters the transition strengths the energy level positions differ only slightly.

5.4 The optical absorption spectrum of Yb^{2+} in the alkali halides

5.4.1 Experimental results

The optical absorption spectra associated with Yb^{2+} in KI, NaI, KBr, NaBr, KCl, NaCl, KF and NaF obtained at both room temperature (RT) and liquid nitrogen temperature (LNT), and with Yb^{2+} in LiF obtained at RT, are shown in figures 5.15 to 5.23 respectively. It is noted that the spectrum for NaCl:Yb^{2+} agrees well with that reported by Tsuboi et al [13]. All crystals, except for NaF and LiF, were annealed at approximately 100°C below their respective melting points in a dry nitrogen atmosphere until no further shifts were observed in their optical absorption band positions. This procedure was adopted in order to eliminate the effects of stress and strain within the crystal. The spectra shown for NaF and LiF were obtained immediately after quenching following the diffusion of Yb^{2+}. Annealing of these particular crystals resulted in other more subtle effects which will be discussed later.

A number of common features characterise the absorption band structure for Yb^{2+} in KI, NaI, KBr, NaBr, KCl, NaCl and KF. In all cases absorption starts at around 25000 cm^{-1} (400 nm) with two distinct bands, designated A1 and A2, of approximately constant separation and

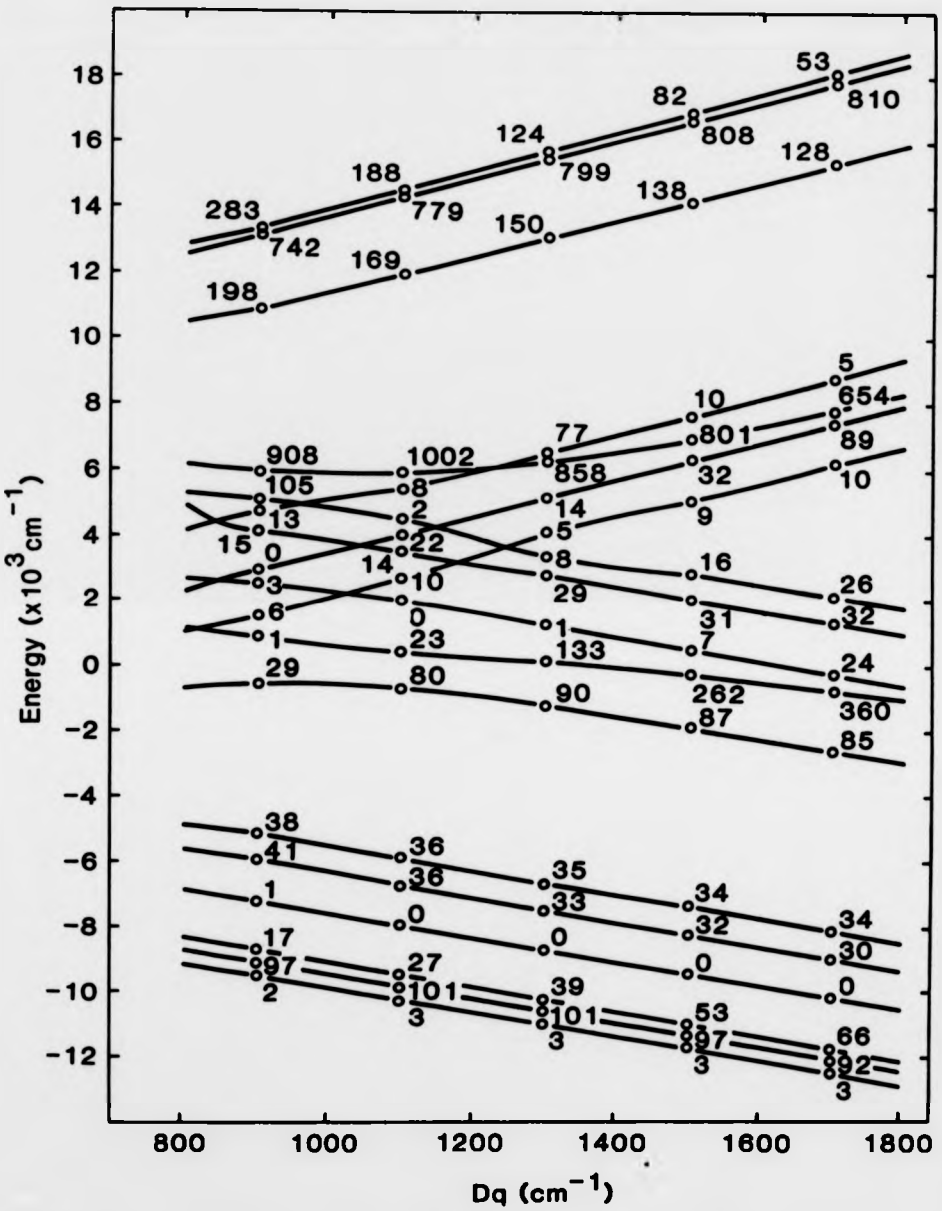

Fig. 5.14 **Energy level positions and relative transition intensities for the $4f^{13}5d$ configuration in a varying crystal field (B_4^* and B_6^* are included – see text)**
(a) octahedral

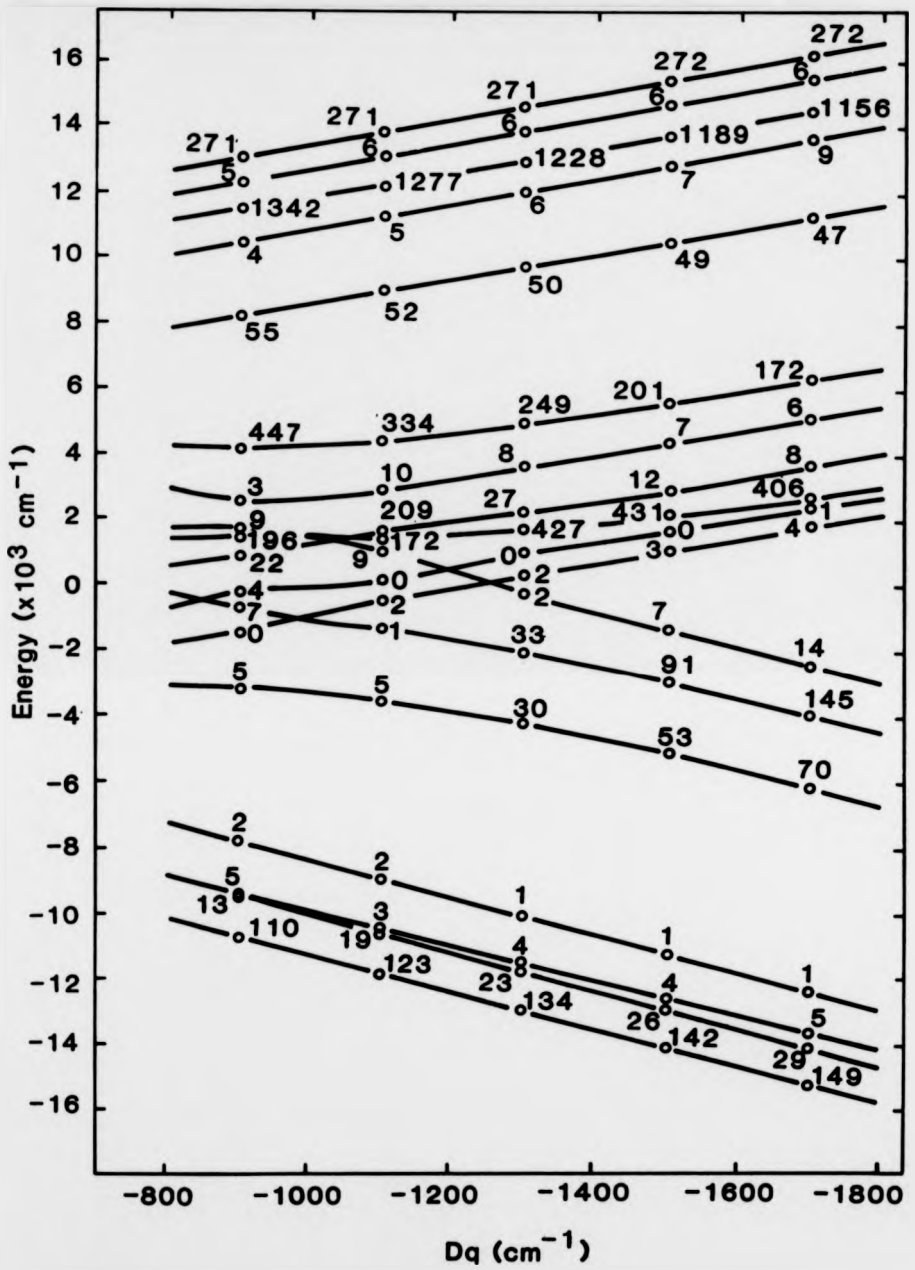

Fig. 5.14 Energy level positions and relative transition intensities for the $4f^{13}5d$ configuration in a varying crystal field (B_4^* and B_6^* are included – see text) (b) cubic

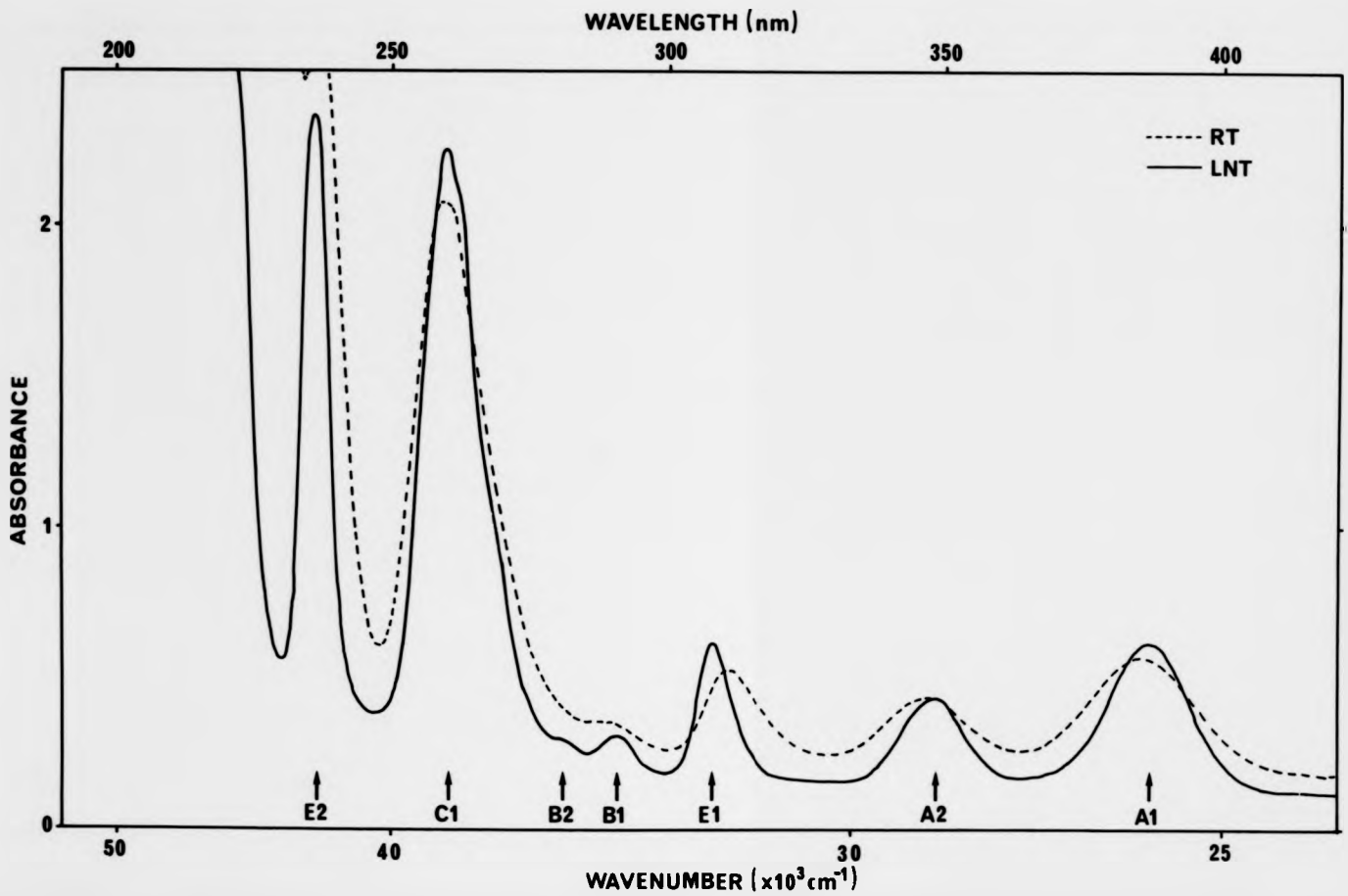

Figure 5.15 The optical absorption spectrum of Yb^{2+} in KI at RT and LNT.

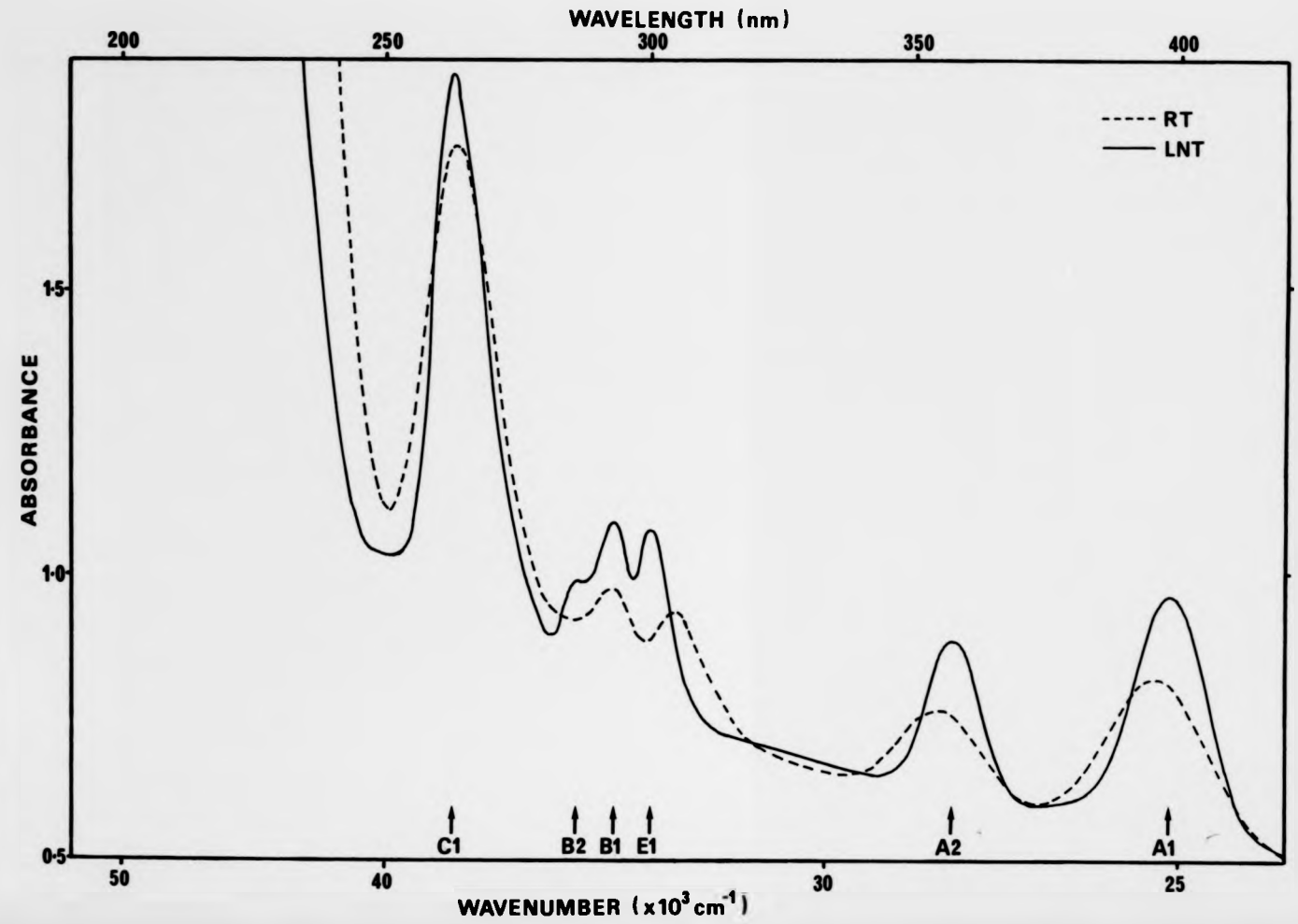

Figure 5.16 The optical absorption spectrum of Yb^{2+} in NaI at RT and LNT.

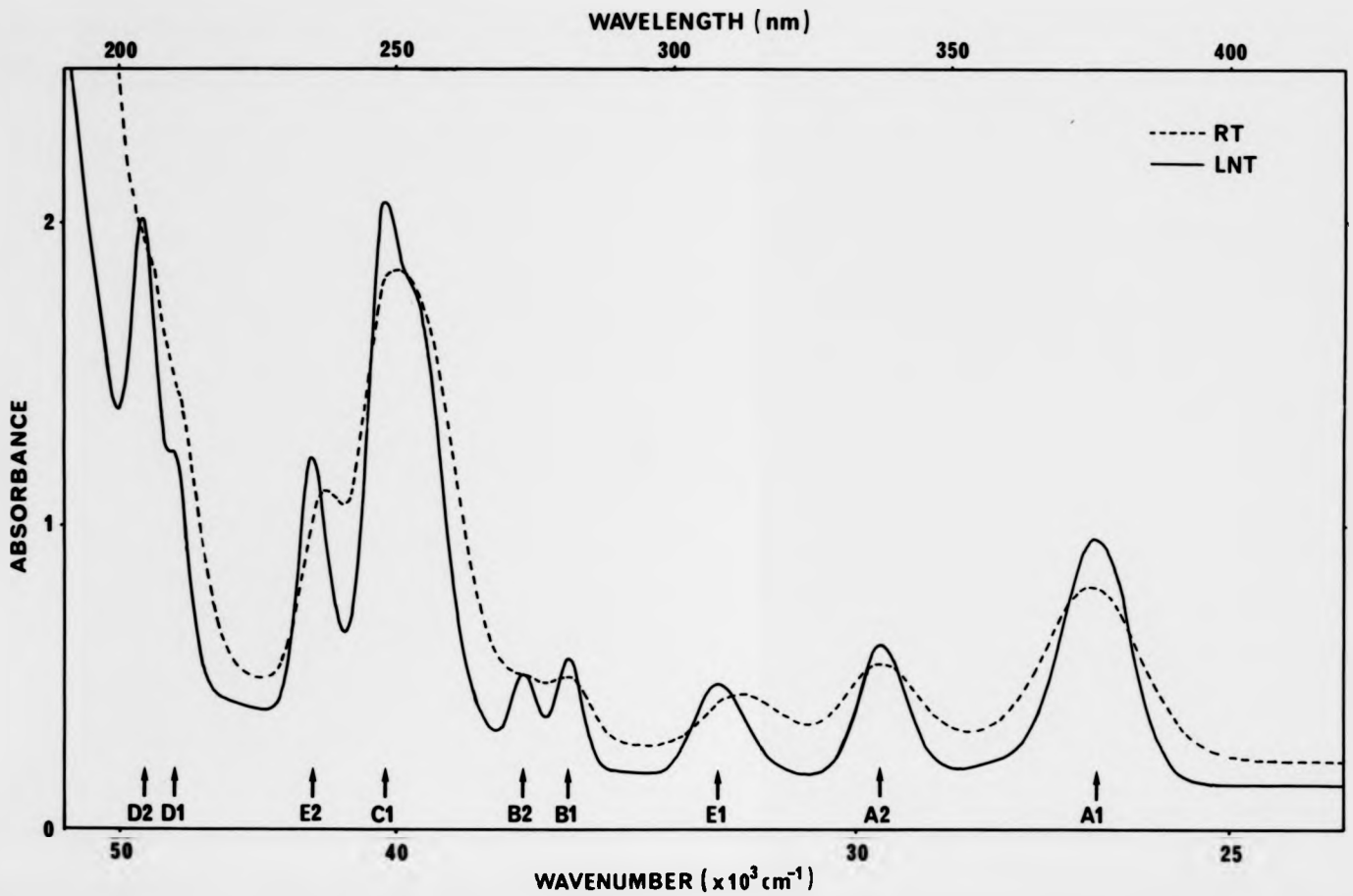

Figure 5.17 The optical absorption spectrum of Yb^{2+} in KBr at RT and LNT.

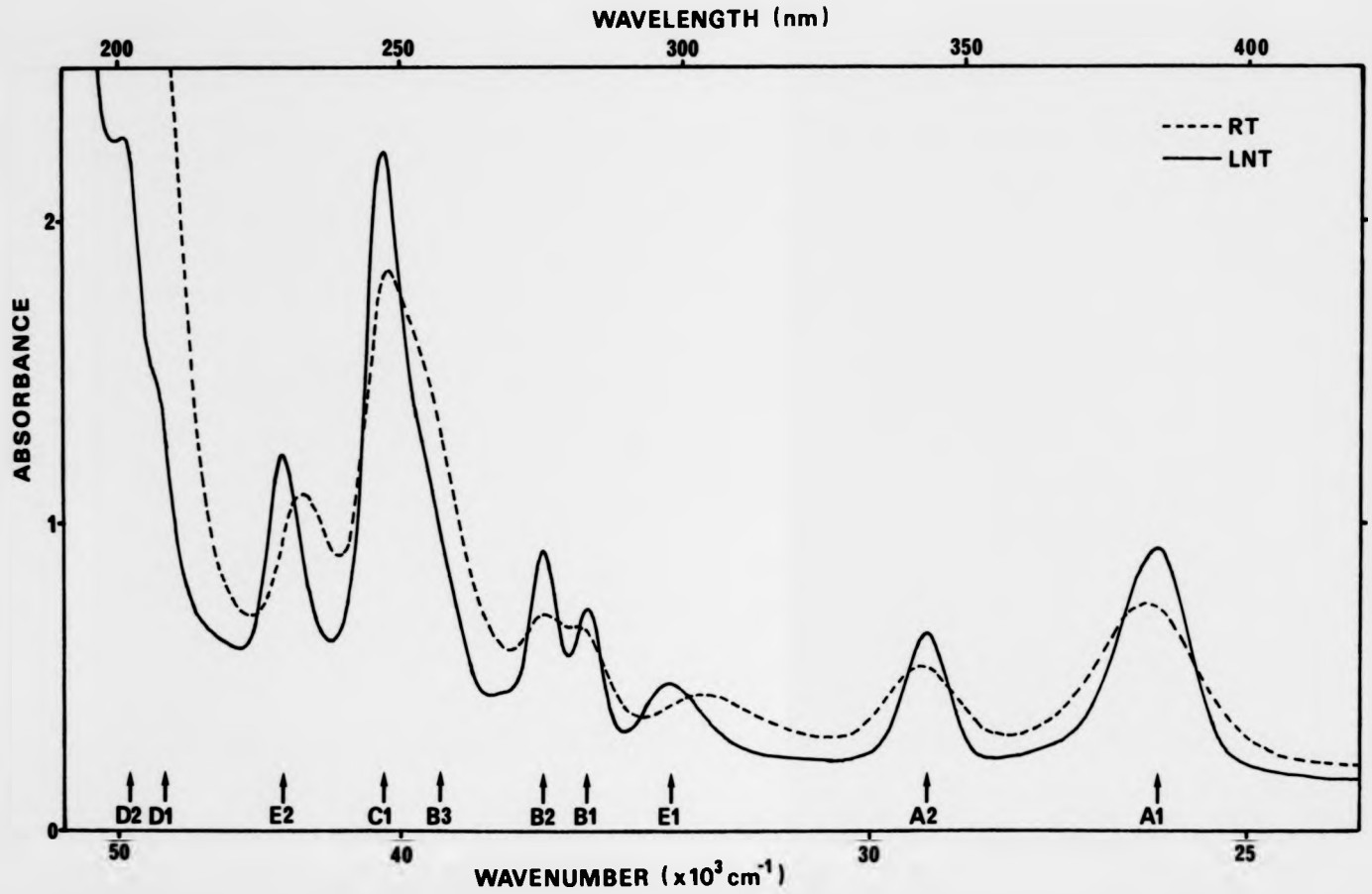

Figure 5.18 The optical absorption spectrum of Yb^{2+} in NaBr at RT and LNT.

Figure 5.19 The optical absorption spectrum of Yb^{2+} in KCl at RT and LNT.

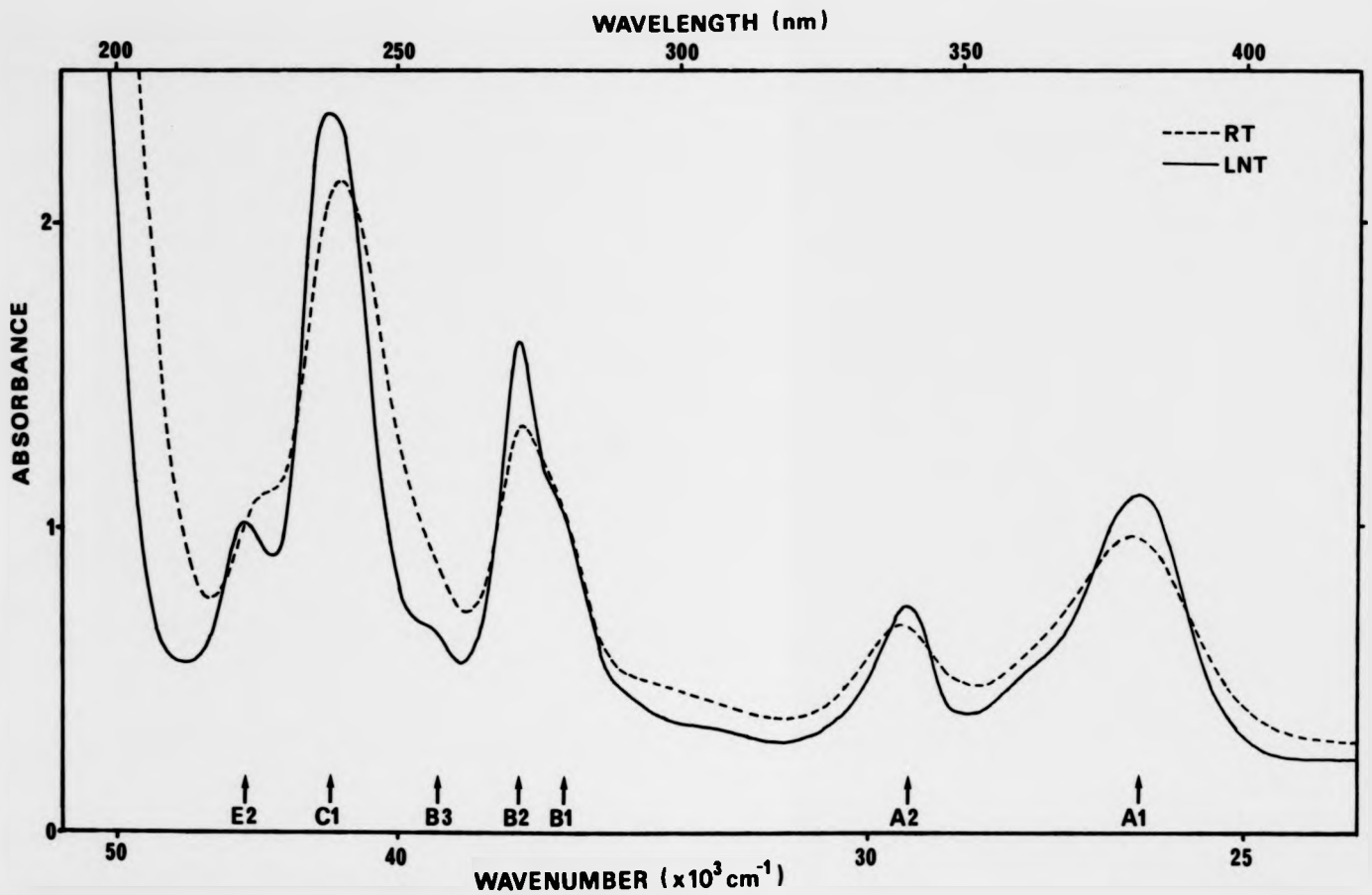

Figure 5.20 The optical absorption spectrum of Yb^{2+} in NaCl at RT and LNT.

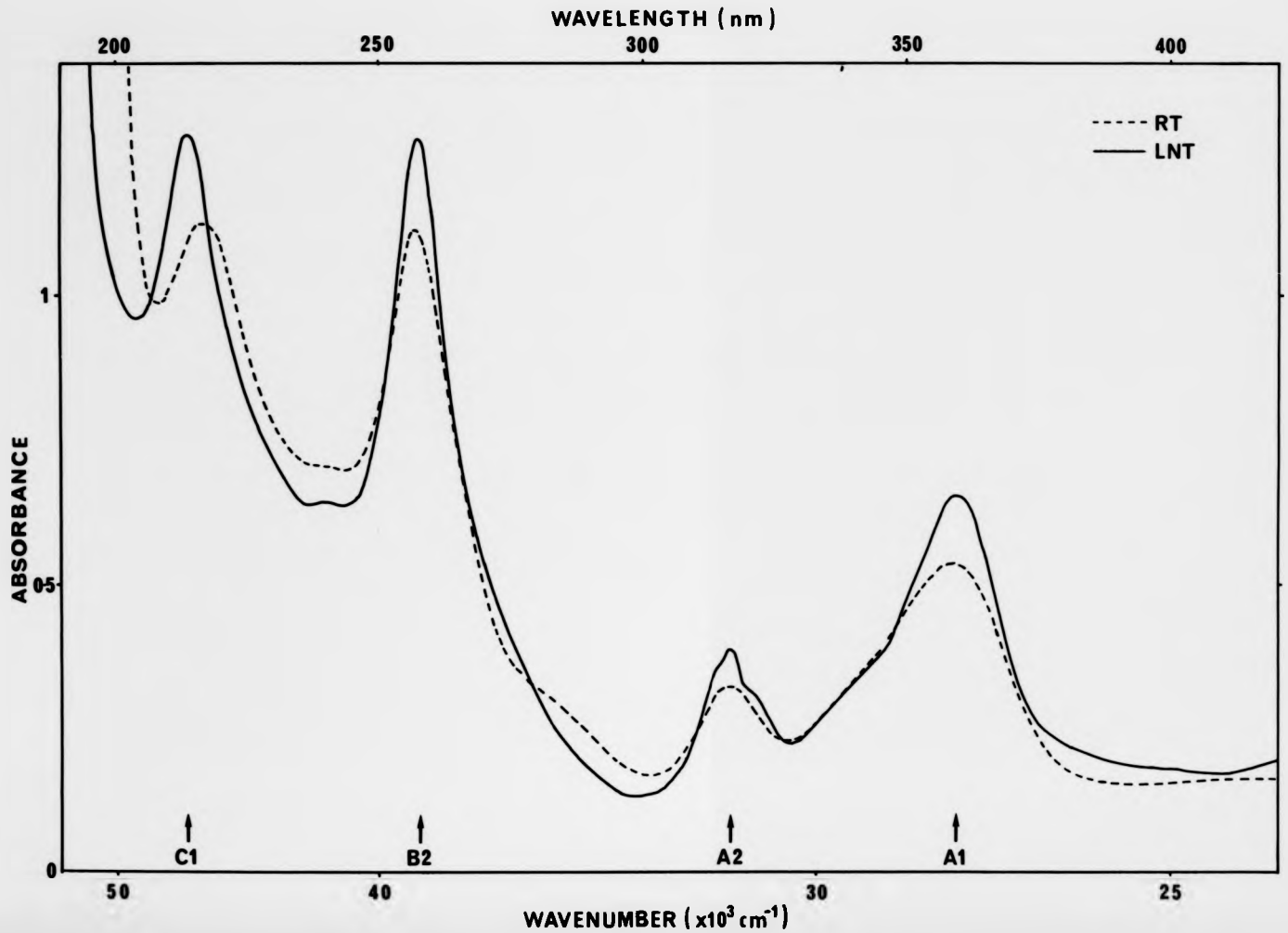

Figure 5.21 The optical absorption spectrum of Yb^{2+} in KF at RT and LNT.

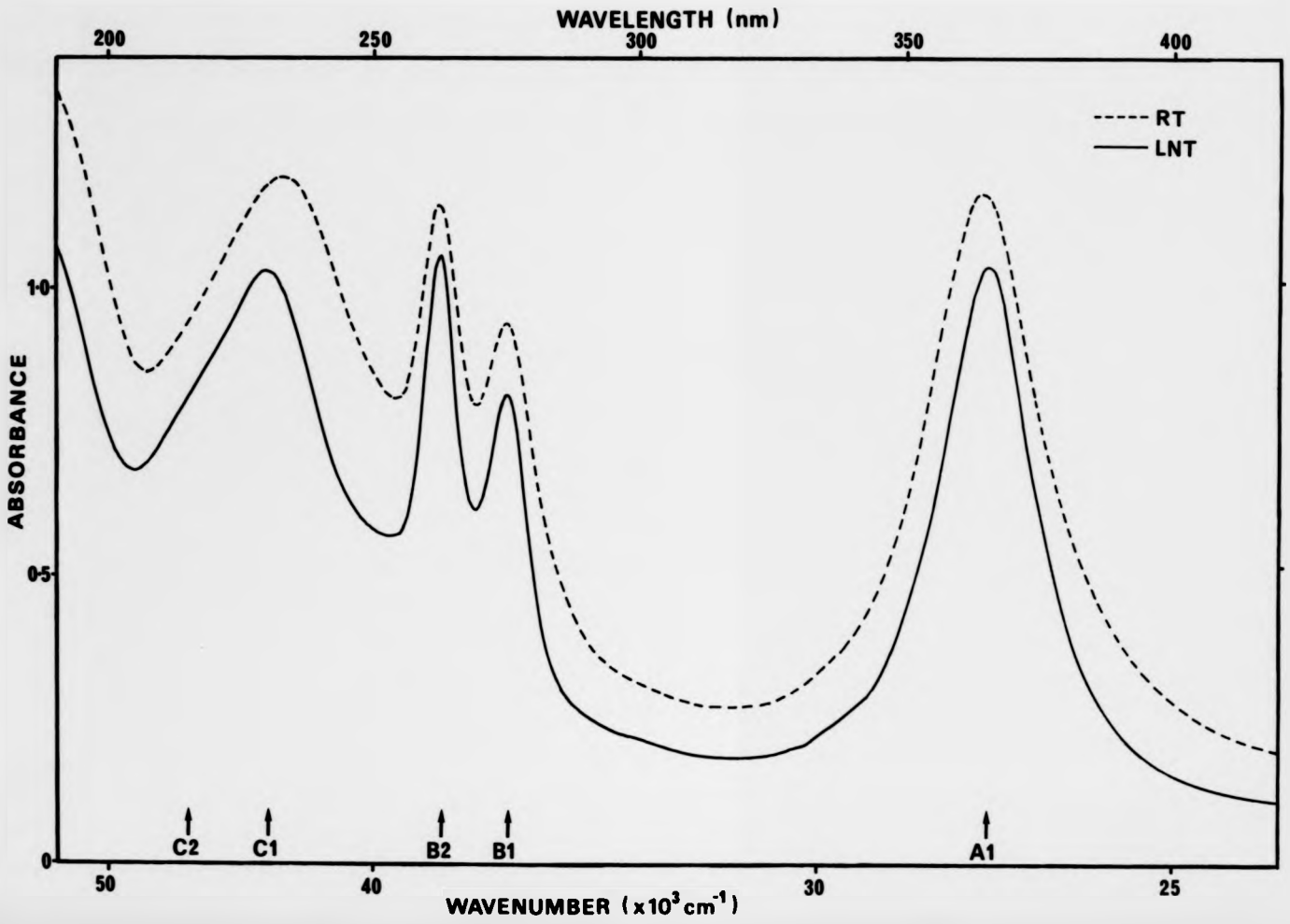

Figure 5.22 The optical absorption spectrum of Yb^{2+} in NaF at RT and LNT.

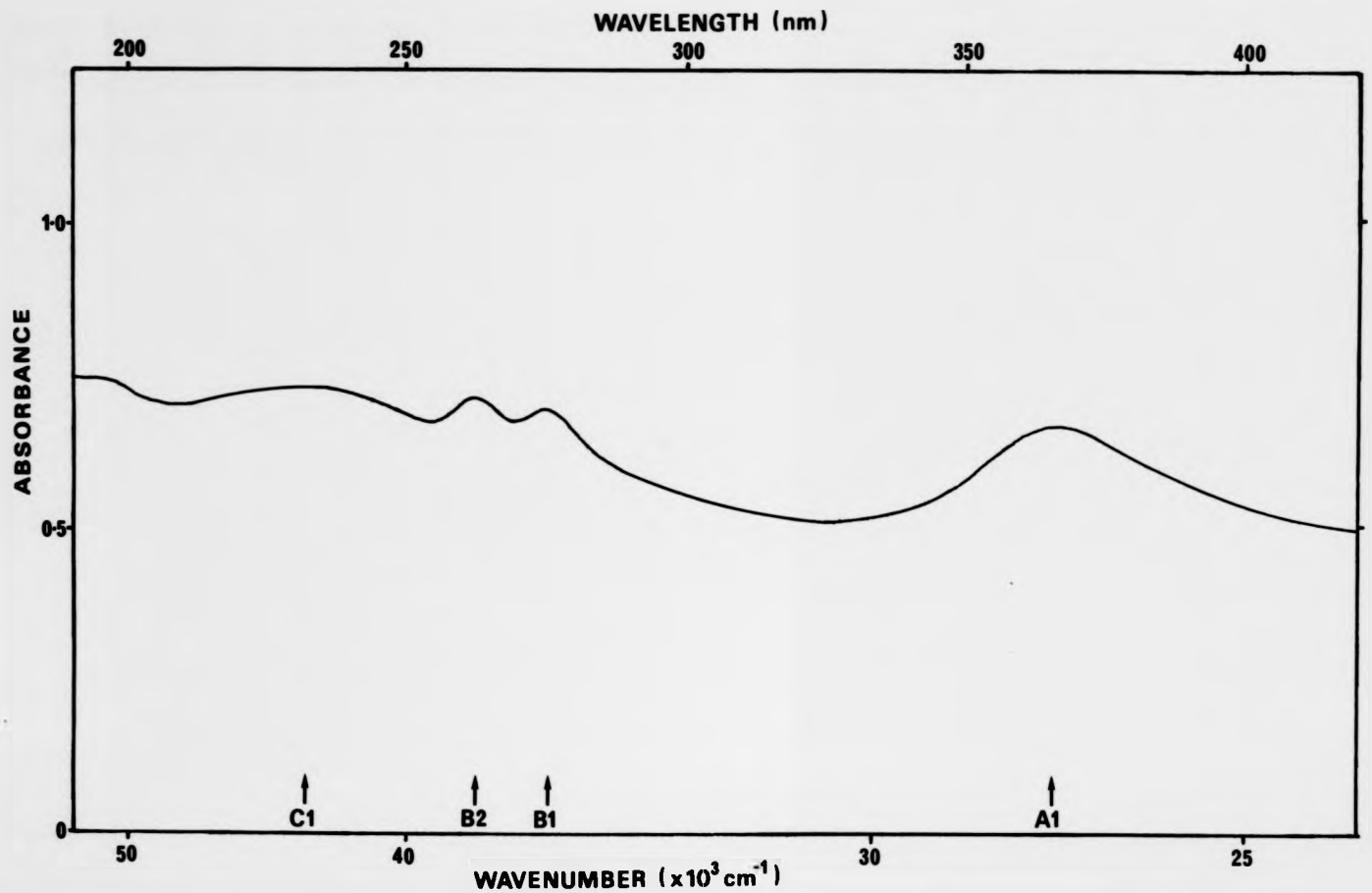

Figure 5.23 The optical absorption spectrum of Yb^{2+} in LiF at RT.

relative intensity. A strong absorption band C1 occurs at around 38000 to 42000 cm^{-1} (263 to 213 nm) preceded in energy by a pair of weaker bands designated B1 and B2. A third band B3 is also observed in this region for crystals of NaBr, KCl and NaCl. At higher energies some fairly strong bands designated D1 and D2 are observed in a number of the crystals (KBr, NaBr and KCl). In the other crystals, corresponding bands are either obscured by the onset of a strong absorption associated with the nominally-pure host (impurities or intrinsic band edge), or else presumably lay outside the range of the spectrophotometer. Each of the sets of bands A, B, C and D sharpen slightly on cooling and normally exhibit a small shift in position either to higher or lower energy. There is no apparant change in the total area under these absorption bands and, hence, in their transition strengths assuming that Smakula's equation [14] is applicable. This and their overall intensity implies that the spectra are to be associated with allowed transitions.

The two bands designated E1 and E2 behave differently from the bands A, B, C and D with respect to changes in temperature. They both sharpen quite appreciably on cooling and simultaneously exhibit a quite pronounced shift in position, always to higher energy. Their overall combined integrated absorption intensity appears to be strongly dependent on the host crystal, although it remains fixed relative to the bands A to D in each case. This behaviour suggests that the bands E1 and E2 are associated with the same defect centre as bands A to D, that is with the Yb^{2+} ion. In particular, their strong dependence on host crystal appears to be a function of the anion constituent. Transition intensities are most strong in the alkali iodides and progressively less so in the alkali bromides and the alkali chlorides. In KF no such bands can be observed. In a later section (section 5.6) the probable identity of these bands is discussed.

For both NaF and LiF containing Yb^{2+} the absorption band structure

differs slightly from the general format described earlier for the majority of the alkali halides. The most striking difference is that the band corresponding to A2 is completely absent. In addition, the two bands which at first glance correspond to B1 and B2 have a separation and overall relative intensity which is much greater than is observed for the remaining alkali halides. The spectrum obtained for LiF was always very much weaker than that obtained for NaF although its structure is identical.

In the following section the bands A to D are considered in more detail and are shown to be associated with transitions from the ground state of Yb^{2+} to states of the $4f^{13}5d$ configuration in an octahedral crystal field. This situation applies for the majority of the alkali halides. For NaF and LiF it is necessary to interpret the spectra in terms of a cubic crystal field (section 5.5).

5.4.2 The optical absorption bands A, B, C and D

Figure 5.24 shows the experimental energy level positions of the most intense absorption bands at LNT as a function of crystal field strength Dq described by d^{-5}, where d is the lattice parameter. For the alkali halides d represents the cation-anion separation which is assumed equal to the Yb^{2+}-anion separation R. Absolute configuration energies have been chosen arbitrarily. A transition strength has been indicated for each absorption band. Each band is assumed to be Gaussian in shape and the transition intensity is then directly proportional to the product of the peak absorbance multiplied by the halfwidth [14]. The transition strengths have been given relative to a normalised value of 100 for the band A1. There is excellent qualitative agreement between figure 5.24 and figure 5.14 which depicts the theoretically derived energy level dependence for the $4f^{13}5d$ configuration. In fact most of the trends predicted by the theory are observed. An example is the behaviour of B1 and B2. At low

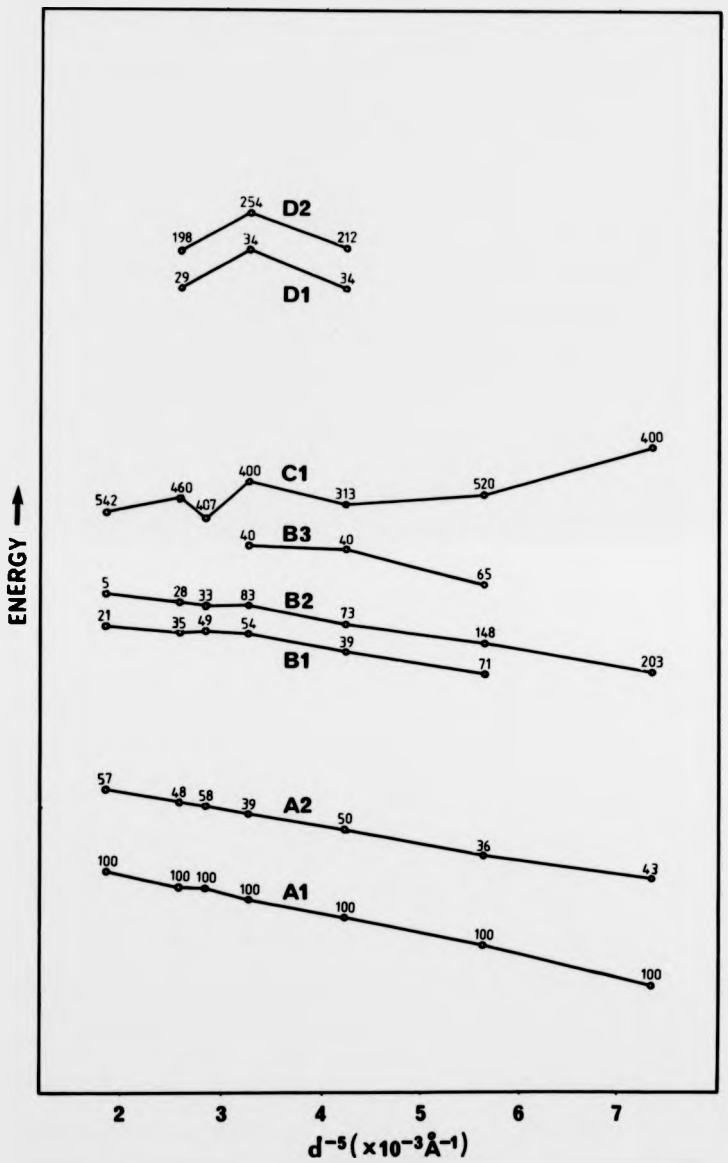

Figure 5.24 Experimental energy level positions and intensities (numbers normalised to A1 = 100) of the most intense absorption bands at LNT as a function of d^{-5}. Absolute configuration energies have been adjusted to illustrate qualitative agreement with figure 5.14(a).

crystal fields the B1 band dominates. As the crystal field increases, the B2 band begins to increase in intensity with respect to B1. Eventually, at high crystal fields, the B2 band dominates. Another interesting area of agreement is the gradual "splitting-off" of the band B3 from the very strong C1 band with increasing crystal field.

The labeling scheme employed here to distinguish between individual bands is based on the following considerations. According to the theory, the individual energy levels form into four distinct groups at high crystal field strengths. Each group is assigned a letter from A to D in order of increasing energy. Thus, for the case of an octahedral crystal field, the bands belonging to the groups A, B, C and D correspond to the overall states $^2F_{7/2}d_{5/2}$, $^2F_{5/2}d_{5/2}$, $^2F_{7/2}d_{3/2}$ and $^2F_{5/2}d_{3/2}$ respectively. A number is added in order to distinguish individual bands within a group.

Evidence to support the proposed classification of the experimentally determined absorption bands is provided by observing the effect of changes in temperature. On cooling, the crystal lattice contracts slightly leading to an increase in the value for Dq (this is certainly true of the alkali halides). According to the theory, bands belonging to group A will shift to lower energy and bands in group D will shift to higher energy. For bands in groups B and C the behaviour is more complex. In general there are two cases to consider. Below Dq = 1000 cm^{-1}, the bands C1 and B2 will both shift toward lower energies while B1 will shift toward higher energy. Above Dq = 1000 cm^{-1}, C1 will shift toward higher energy while both B1 and B2 will shift toward lower energies. These trends are found to be reproduced perfectly in the spectra shown in figures 5.15 to 5.21. Note that for KI:Yb^{2+}, the band C1 exhibits a shift to lower energy on cooling thereby establishing a value for Dq of less than 1000 cm^{-1}. This is consistent with values obtained elsewhere [15].

Although satisfactory qualitative agreement has been achieved, some serious discrepancies exist to prevent a satisfactory quantitative

analysis. Theoretically the minimum separation between the bands B1 and C1 is 6400 cm^{-1} at Dq = 950 cm^{-1}, while for $KI:Yb^{2+}$ and $NaI:Yb^{2+}$ the observed separations are 4027 cm^{-1} and 3980 cm^{-1} respectively. Indeed, it is only for $KF:Yb^{2+}$ that a single value for Dq (= 1650 cm^{-1}) can be found which reasonably satisfies all the energy separations simultaneously. It would appear that the free-ion values employed for the various radial parameters in the theoretical treatment are at best only meaningful for $KF:Yb^{2+}$. For the iodides in particular the values are totally unsuitable. The use of free-ion values will now be reviewed in the light of this observation.

5.4.3 The nephelauxetic effect

The model which has been adopted in the analysis presented thus far assumes localised charge distributions and purely electrostatic forces. In particular, the excited state configuration of the impurity ion in a crystal field was treated as being highly localised spatially. The limitations of the point-ion approach are well known and have been discussed by Jørgensen [16,17]. A more realistic approach should consider the excited 5d electron orbital as extending to a certain degree over the surrounding anions rather than being totally localised on the impurity ion. One particular consequence of overlap is a transfer of charge from the anion to the impurity ion, with the impurity ion behaving as if it possessed an effective ionic charge below its oxidation number. This effect is referred to as central-field covalency. A second effect, known as symmetry-restricted covalency, relates to the formation of molecular orbitals from the anion and impurity-ion orbitals. Electron delocalisation into the molecular orbitals results in a lowering of the charge density close to the impurity ion. The outcome of these overlap effects is an expansion of the outer orbitals for which the mean extension appears to increase as the electronegativity of the anion decreases (polarisability

increases). Behaviour involving orbital expansion is usually refered to as the nephelauxetic (from the Greek for "cloud expanding") effect [18].

A consequence of an effective orbital expansion is a reduction in the magnitude of the radial integrals below their free ion values which, in turn, leads to a reduction in the associated Slater-Condon, or equivalent Racah, and spin-orbit parameters. The extent to which the nephelauxetic effect is significant is rather more difficult to establish. Jørgensen has derived an empirical series reflecting the ability of a number of different anions (ligands) to produce a reduction in the Racah parameters B (= $F_2 - 5F_4$) and C (= $35F_4$) for a particular transition metal ion. This nephelauxetic series takes the form $O^{2-} > I^- > Br^- > Cl^- >> F^-$ for the commonest anions. The ordering reflects the polarisability of the anion to which the degree of covalence might well be related. The nephelauxetic ratio $\beta = B'/B$, where B' is the reduced value of the Racah parameter B, is often used to quantify the observed reduction. Examples of such usage are common in the literature [19] with β often taking a value between 0.6 and 0.9.

Treatments of this nature are much less common for the rare earth ions. Alig [20] has studied Tm^{2+} in $SrCl_2$ and found it necessary to use a reduced value for the electrostatic interaction ($\beta \simeq 0.6$). Similar, though much weaker, effects have been observed for some trivalent rare earth ions in a series of crystals of the type $LaCl_3$. Wong and Richman [21], Wong et al [22] and McLaughlin and Conway [23] have studied Pr^{3+} in a number of such hosts and have discovered a small change in the Slater integrals. They all attribute the effect to a small change in the covalence of the bonds, that is an increase in orbital overlap. Wong and Richman [24] have also determined that Nd^{3+} behaves in an identical, if less marked, manner in the same hosts.

In all of the above cases the optical transitions studied are weak, being of the parity disallowed type $4f^n - 4f^n$. Only the direct Slater-Condon parameters are involved together with one type of spin-orbit parameter. The

changes observed are of the order of 1 to 2 percent which is to be expected for the inner, well shielded, 4f shell. In the present work, which concerns the divalent rare earth ions, the problem encountered is more complex. Allowed transitions to the outer, less localised, 5d orbital are involved. Consequently the overlap effects are expected to be more important. In addition, there are now not only the direct Slater-Condon parameters to consider, but also the exchange and two types of spin-orbit parameter. In total there are eight adjustable parameters, F_2, F_4, G_1, G_3, G_5, ζ_d, ζ_f and Dq. The effect of a reduction of each of these parameters separately on the energy level structure will first be investigated. The intention is to establish the relative importance of each of the parameters as a precursor to the formulation of a suitable scheme for approximation.

In figures 5.25 to 5.29 the crystal field parameter Dq has been held fixed at 1000 cm^{-1} and each of the five Slater-Condon parameters have in turn been reduced by up to 50%. In general the SO parameters depend less on the radial integrals than do the electrostatic parameters [7]. This is particularly true of the parameter ζ_f since the 4f wavefunction is less sensitive to the surrounding anions than the unshielded 5d wavefunction. Figure 5.30 shows the effect of reductions in the spin-orbit parameters by up to 10%.

The energy level structure is found to be most sensitive to reductions in F_2 and G_1. The other parameters, with the possible exception of F_4, have a comparitively negligible effect on the energy level positions. Therefore the most important features of the crystal field spectrum will be quite sucessfully reproduced by altering only these two parameters. Based on the premise that similar classes of parameter (direct, indirect or spin-orbit) produce energy level variations in the same direction, it was decided to link these similar types in a specific way. In the following analysis the ratios F_4/F_2, G_3/G_1, G_5/G_1 and ζ_f/ζ_d have been held fixed at their free ion values. As a result of the approximations described above, an analysis based on eight

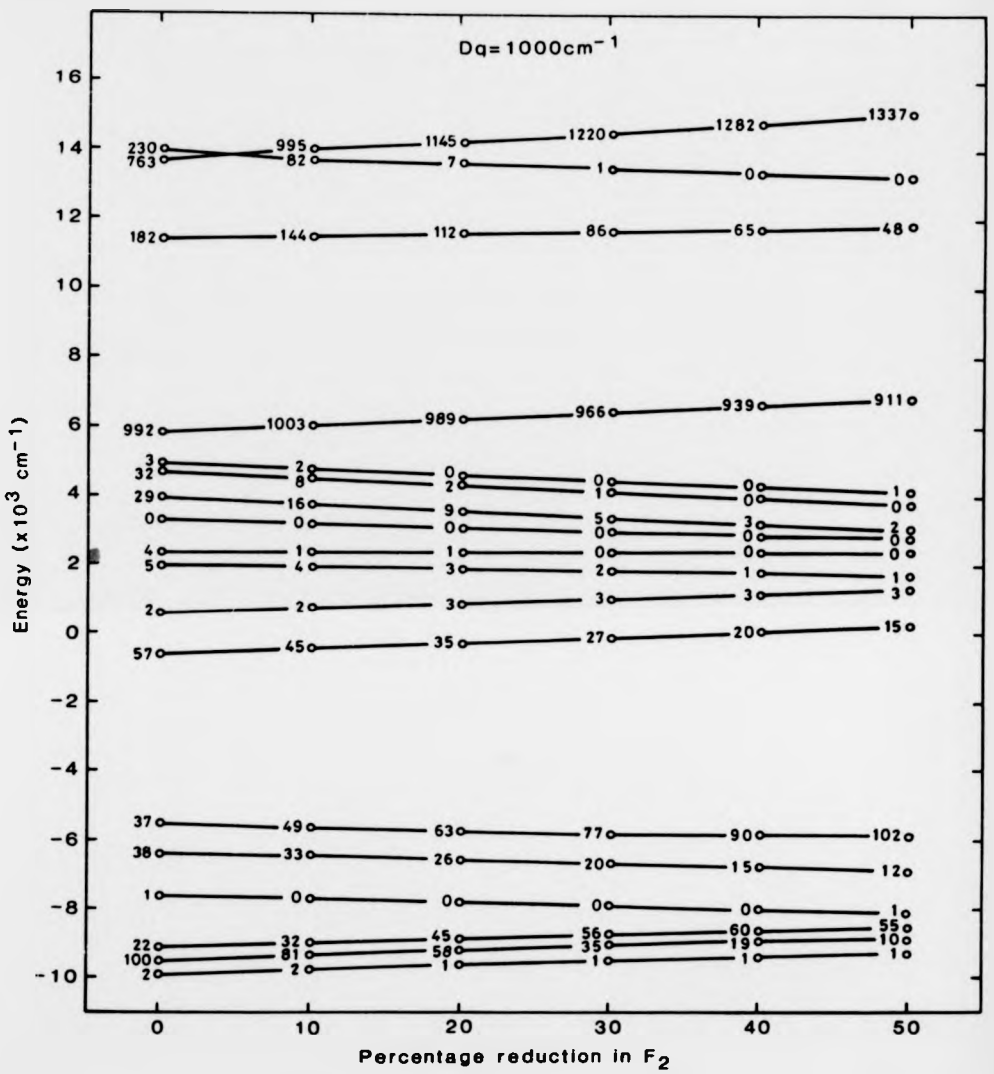

Fig.5.25 The effect of reductions in the parameter F_2 on the energy level structure. The numbers indicate relative transition intensities (a) Octahedral crystal field (Dq = 1000 cm^{-1})

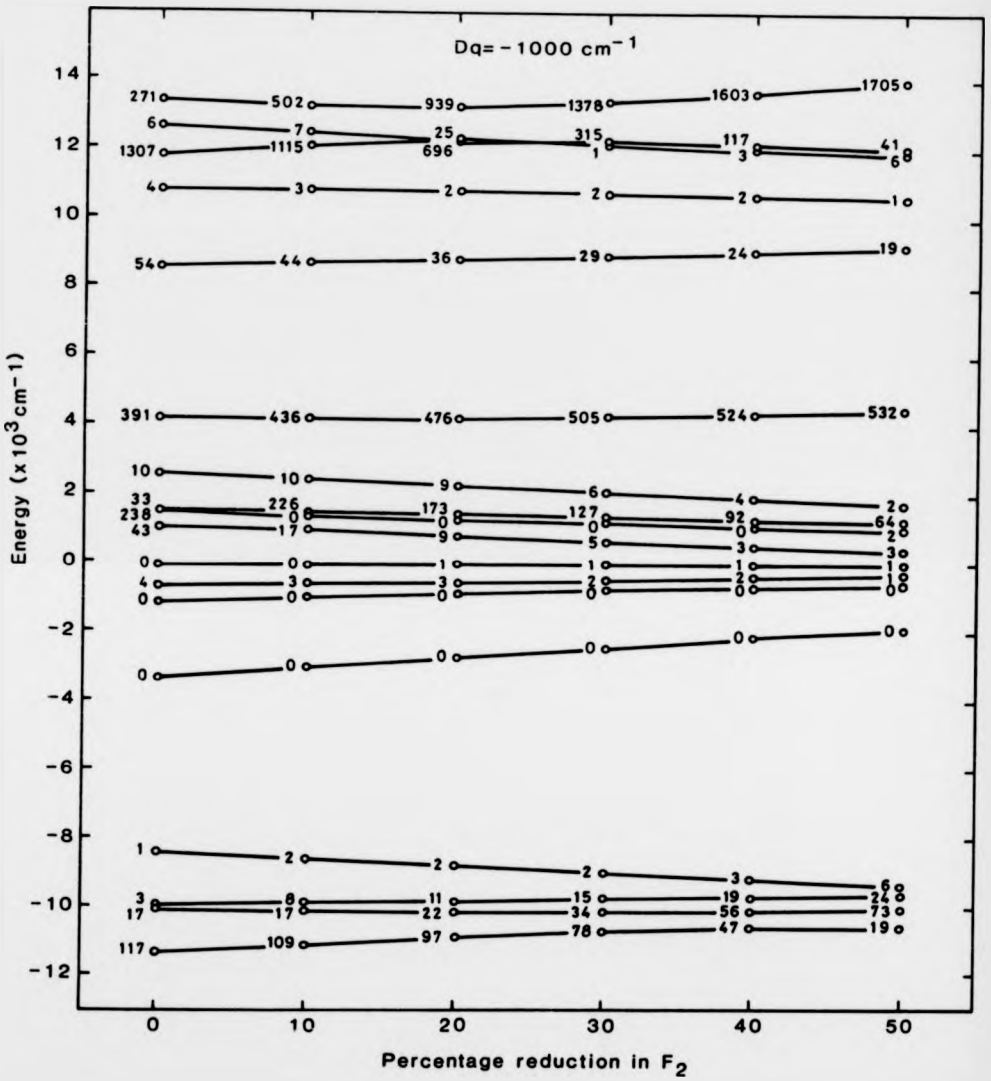

Fig.5.25 (b) Cubic crystal field (Dq = −1000 cm^{-1})

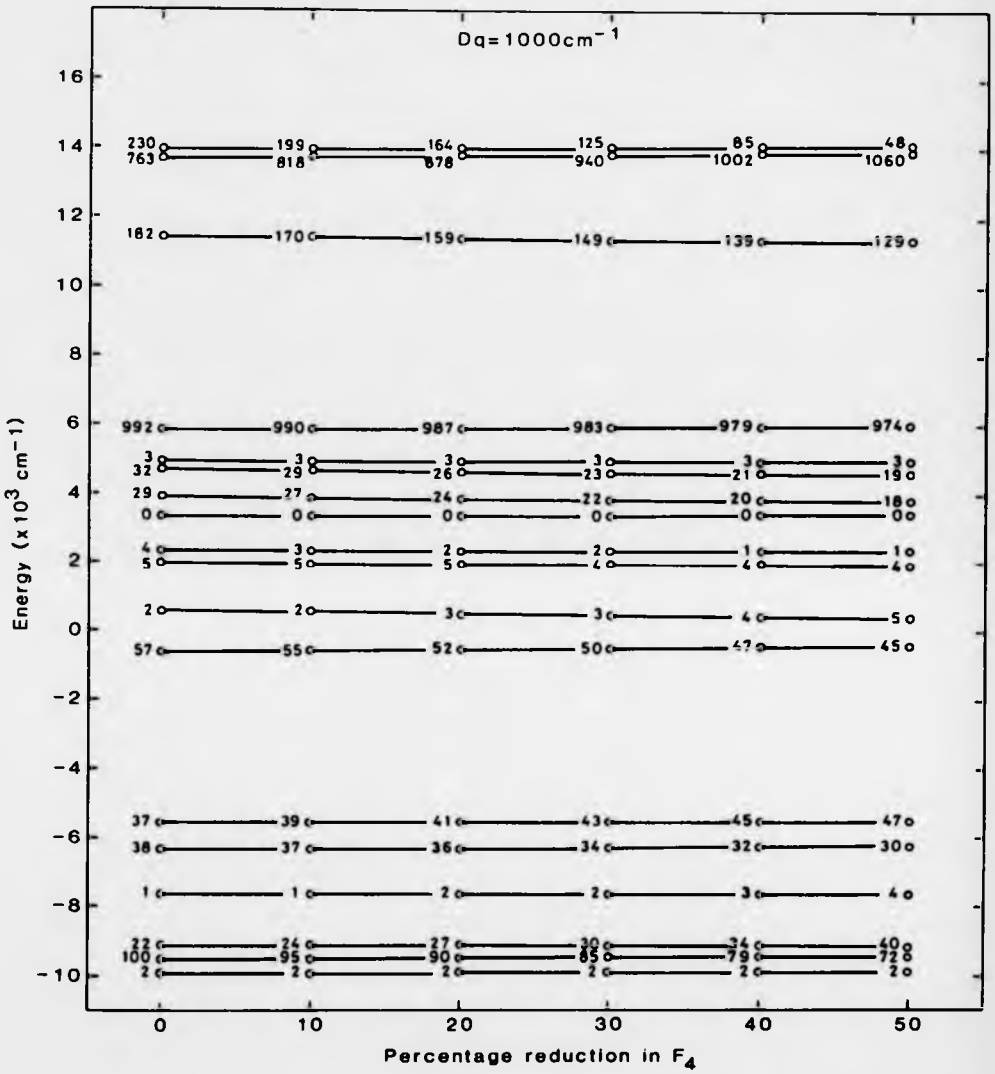

Fig.5.26 The effect of reductions in the parameter F_4 on the energy level structure. The numbers indicate relative transition intensities (a) Octahedral crystal field (Dq = 1000 cm^{-1})

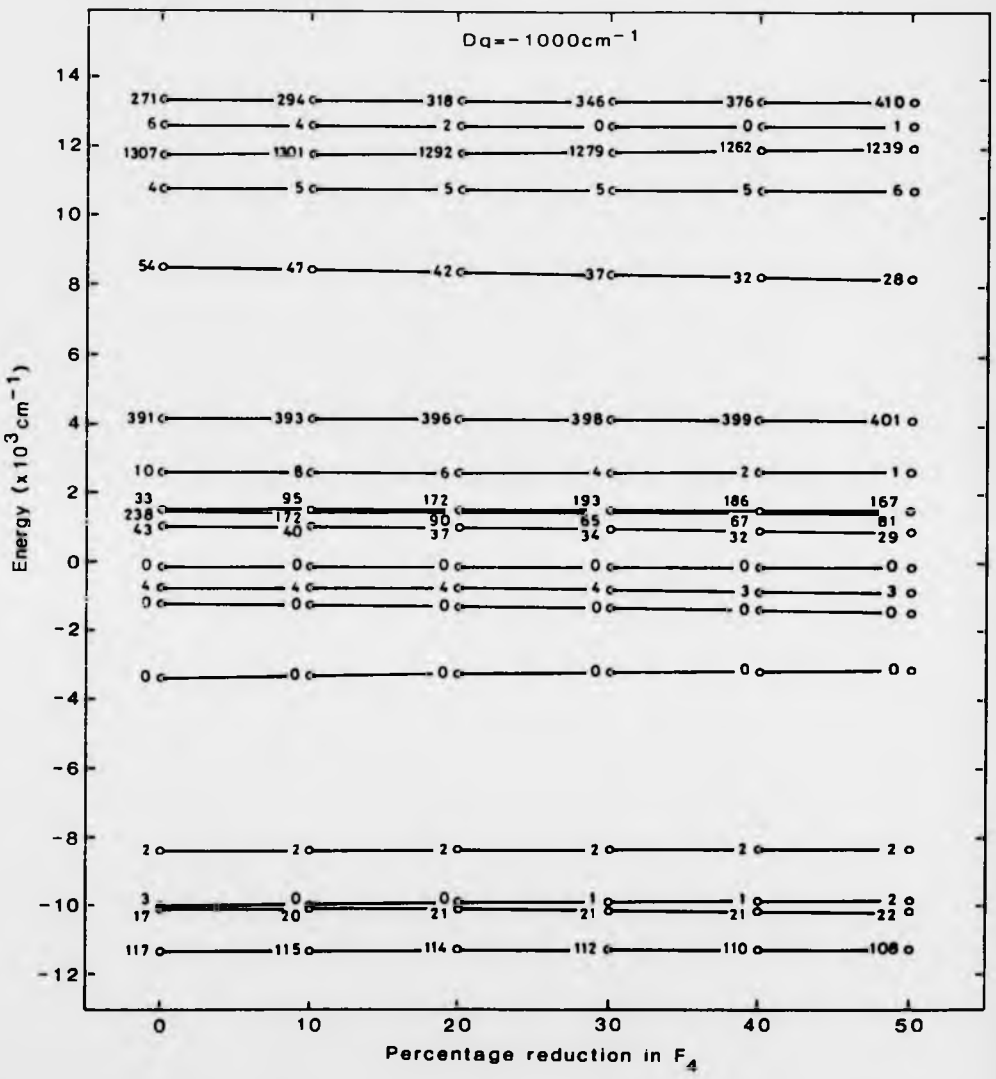

Fig.5.26 (b) Cubic crystal field (Dq= −1000 cm^{-1})

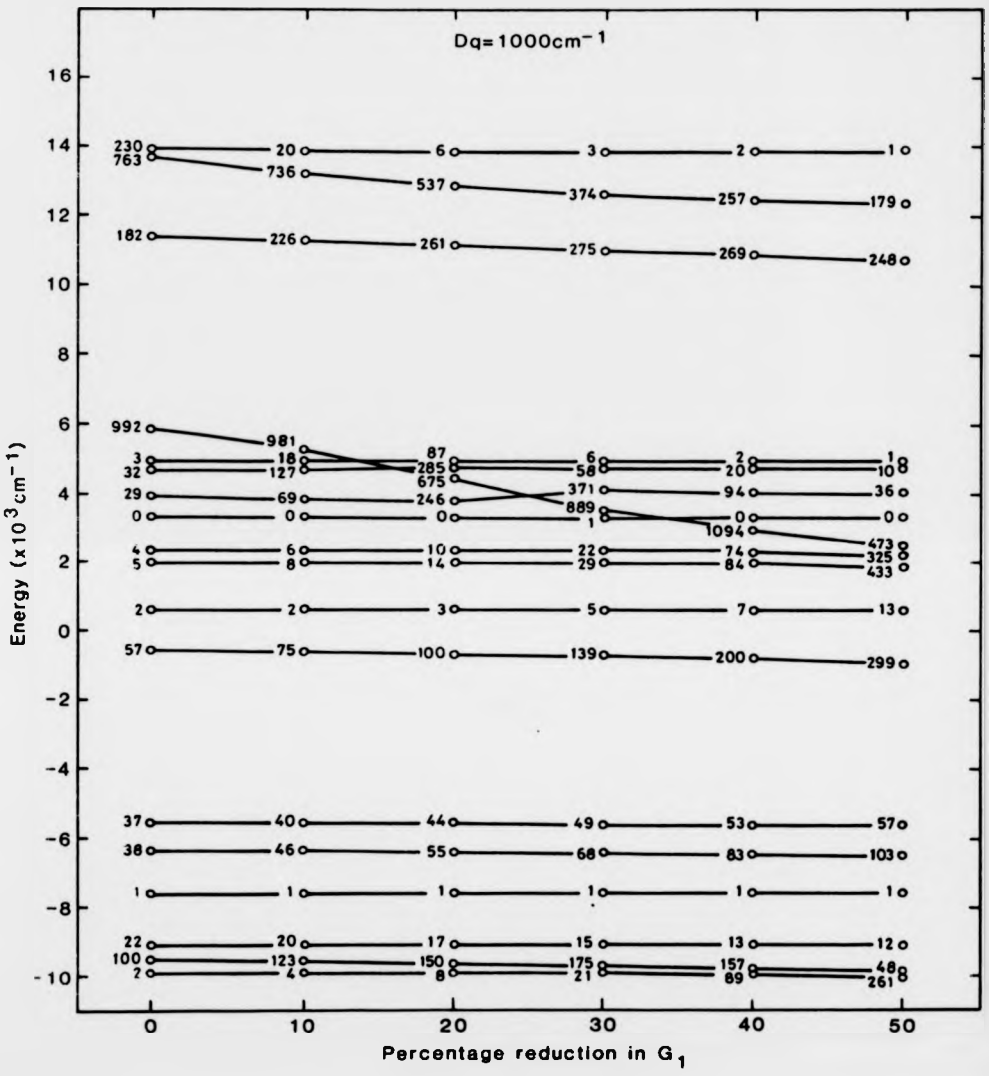

Fig. 5.27 The effect of reductions in the parameter G_1 on the energy level structure. The numbers indicate relative transition intensities (a) Octahedral crystal field (Dq = 1000 cm^{-1})

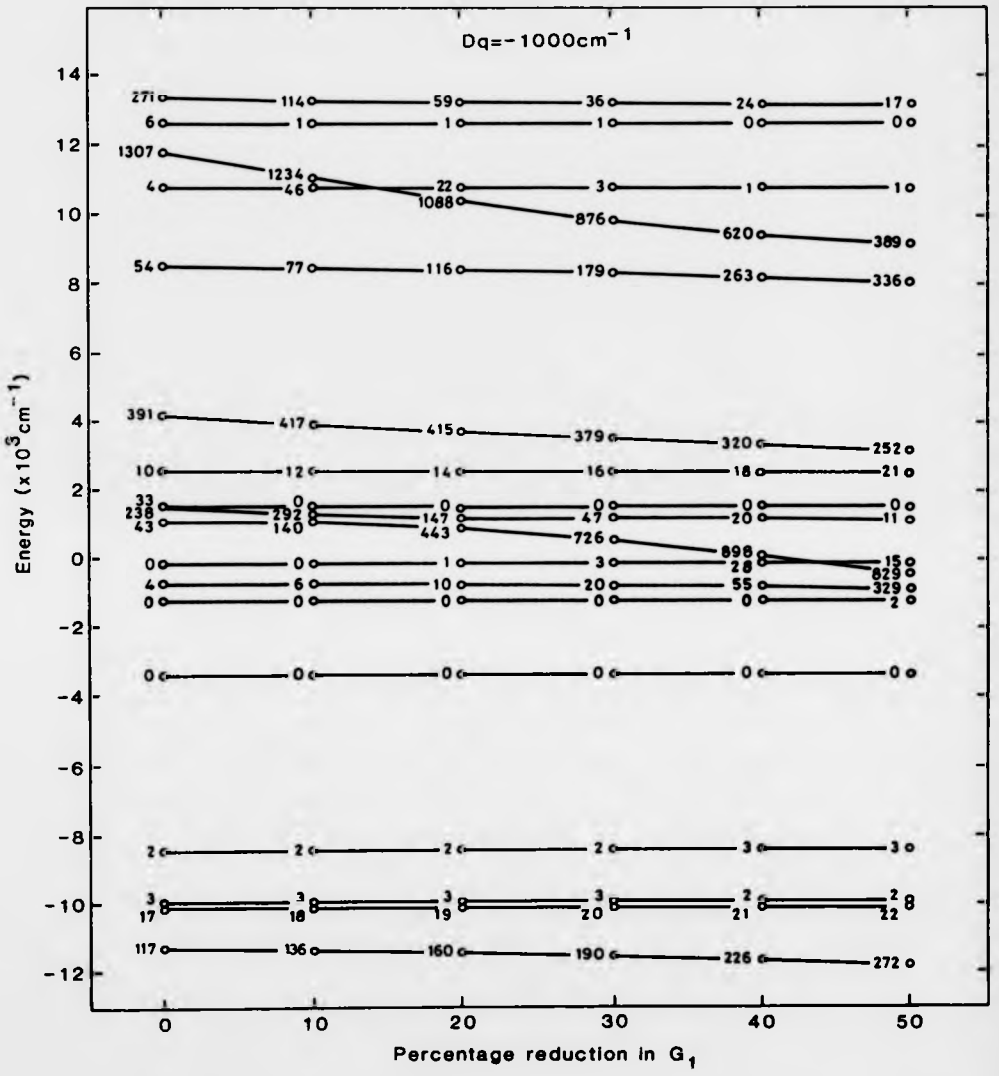

Fig.5.27 (b) Cubic crystal field (Dq = −1000 cm^{-1})

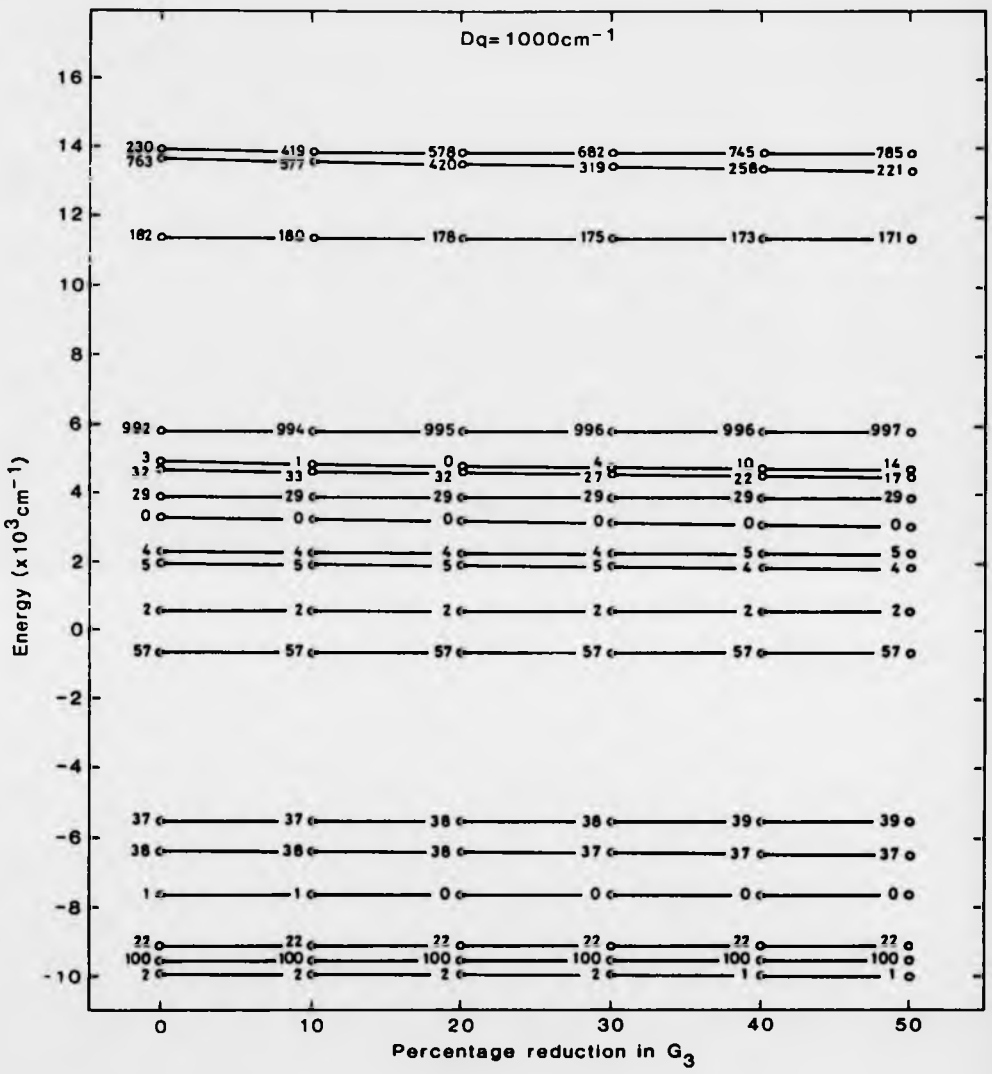

Fig.5.28 The effect of reductions in the parameter G_3 on the energy level structure. The numbers indicate relative transition intensities (a) Octahedral crystal field (Dq=1000 cm^{-1})

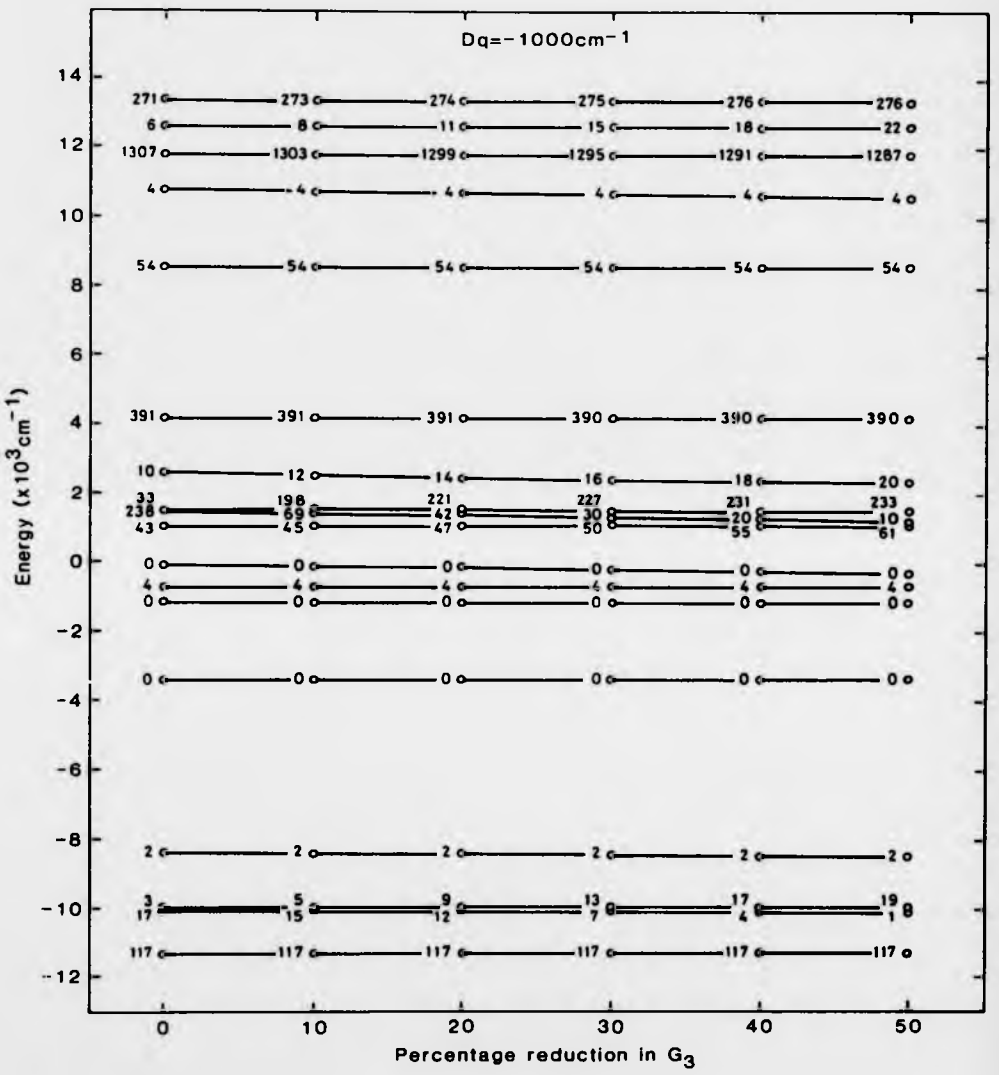

Fig.5.28 (b) Cubic crystal field (Dq = −1000 cm^{-1})

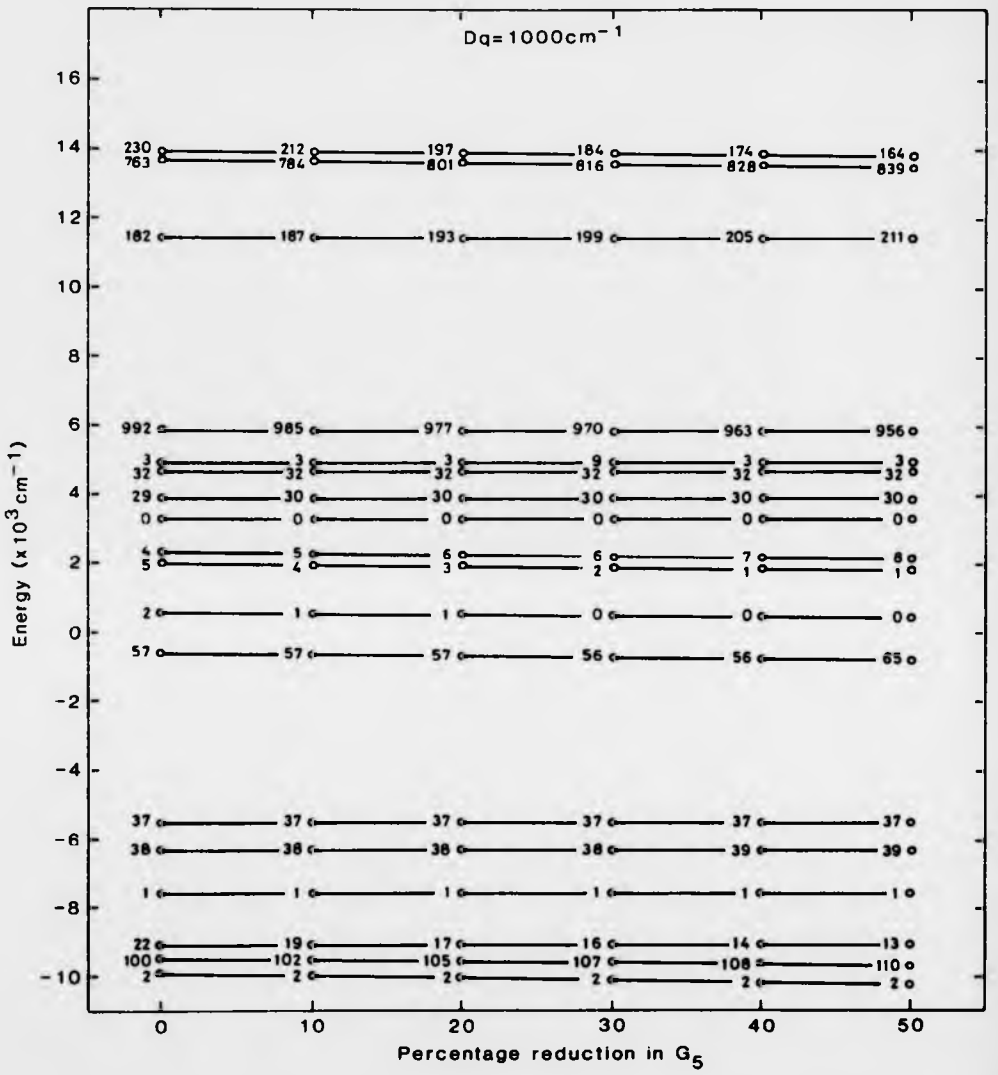

Fig.5.29 The effect of reductions in the parameter G_5 on the energy level structure. The numbers indicate relative transition intensities (a) Octahedral crystal field (Dq = 1000cm^{-1})

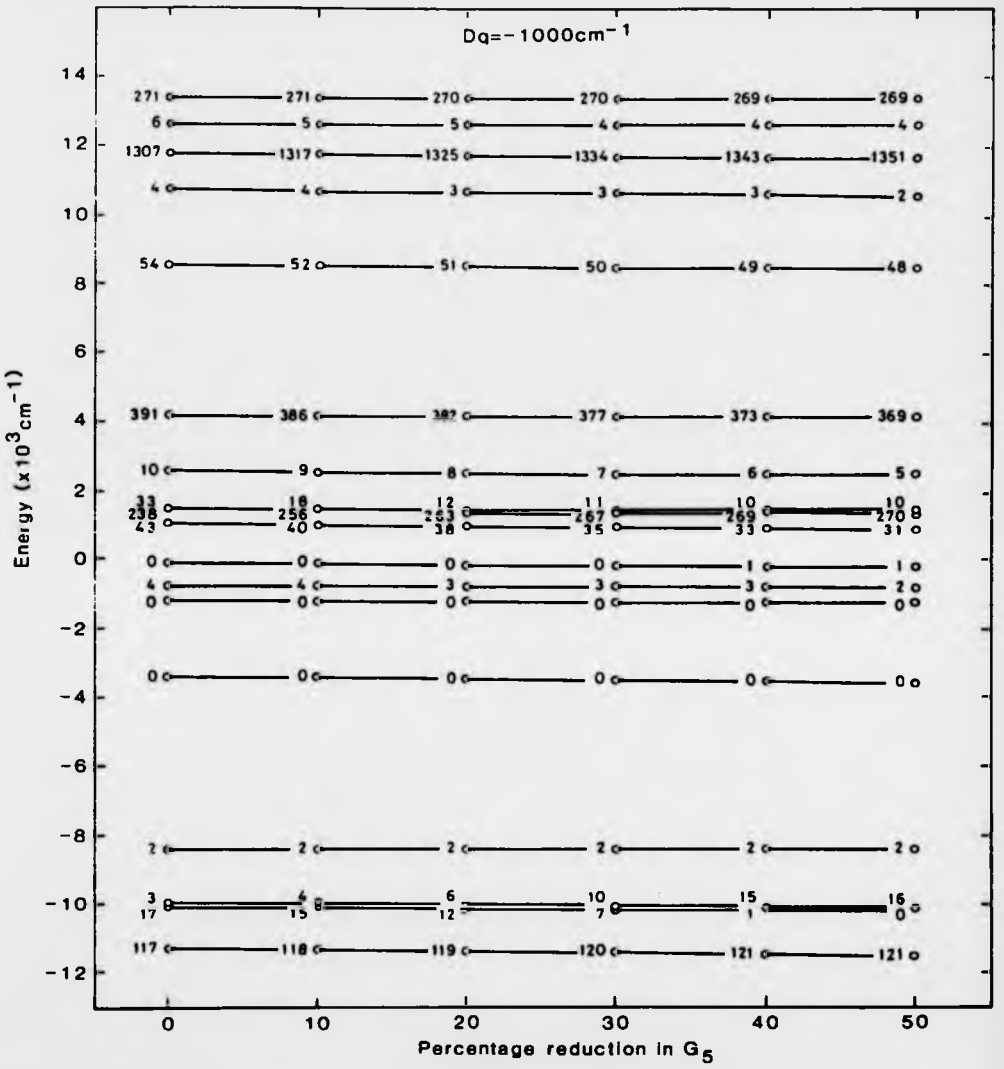

Fig.5.29 (b) Cubic crystal field (Dq = 1000 cm^{-1})

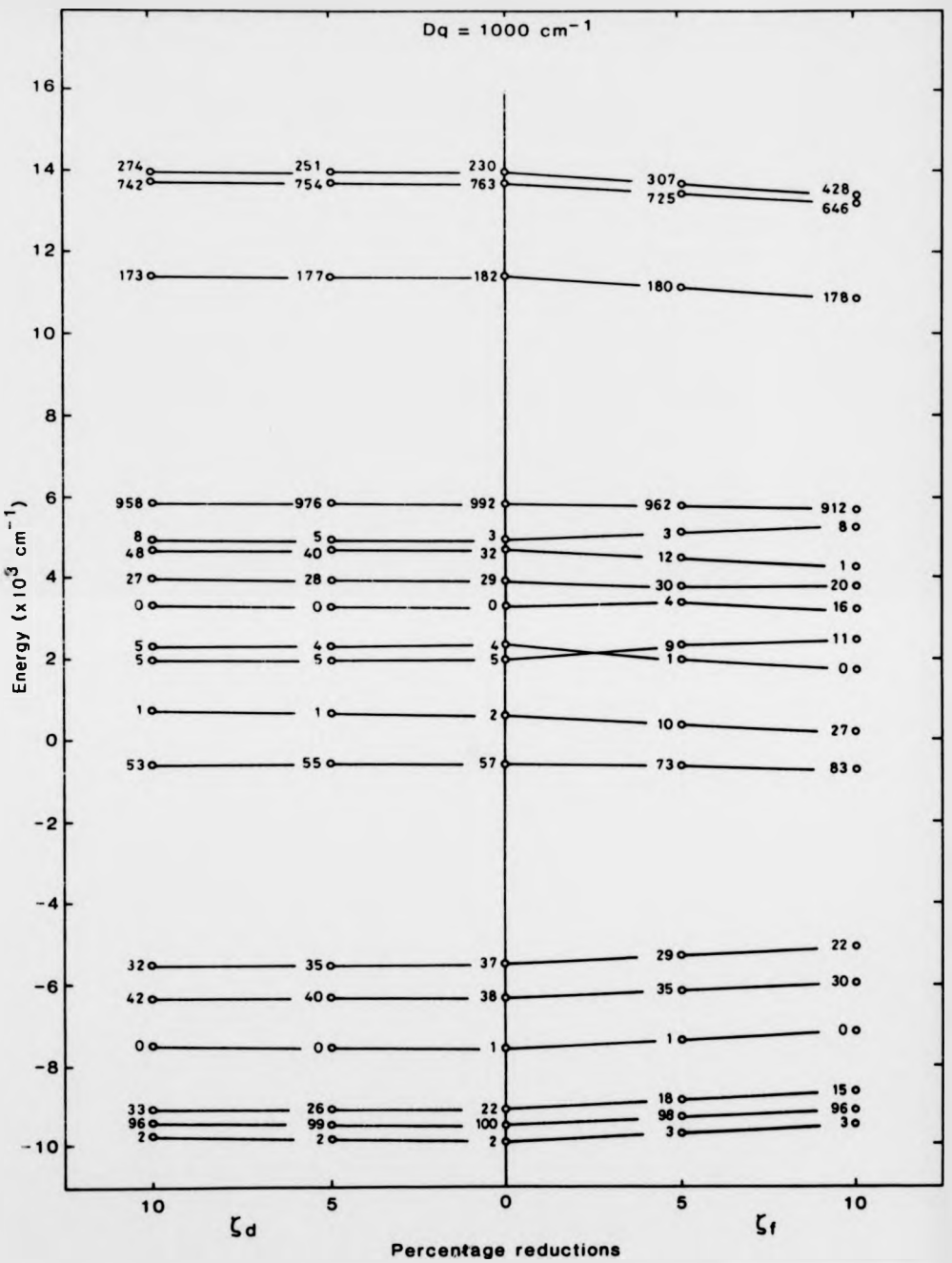

Fig.5.30 The effect of independent reductions in the parameters ζ_d and ζ_f on the energy level structure. The numbers indicate relative transition intensities (a) Octahedral crystal field (Dq = 1000 cm^{-1})

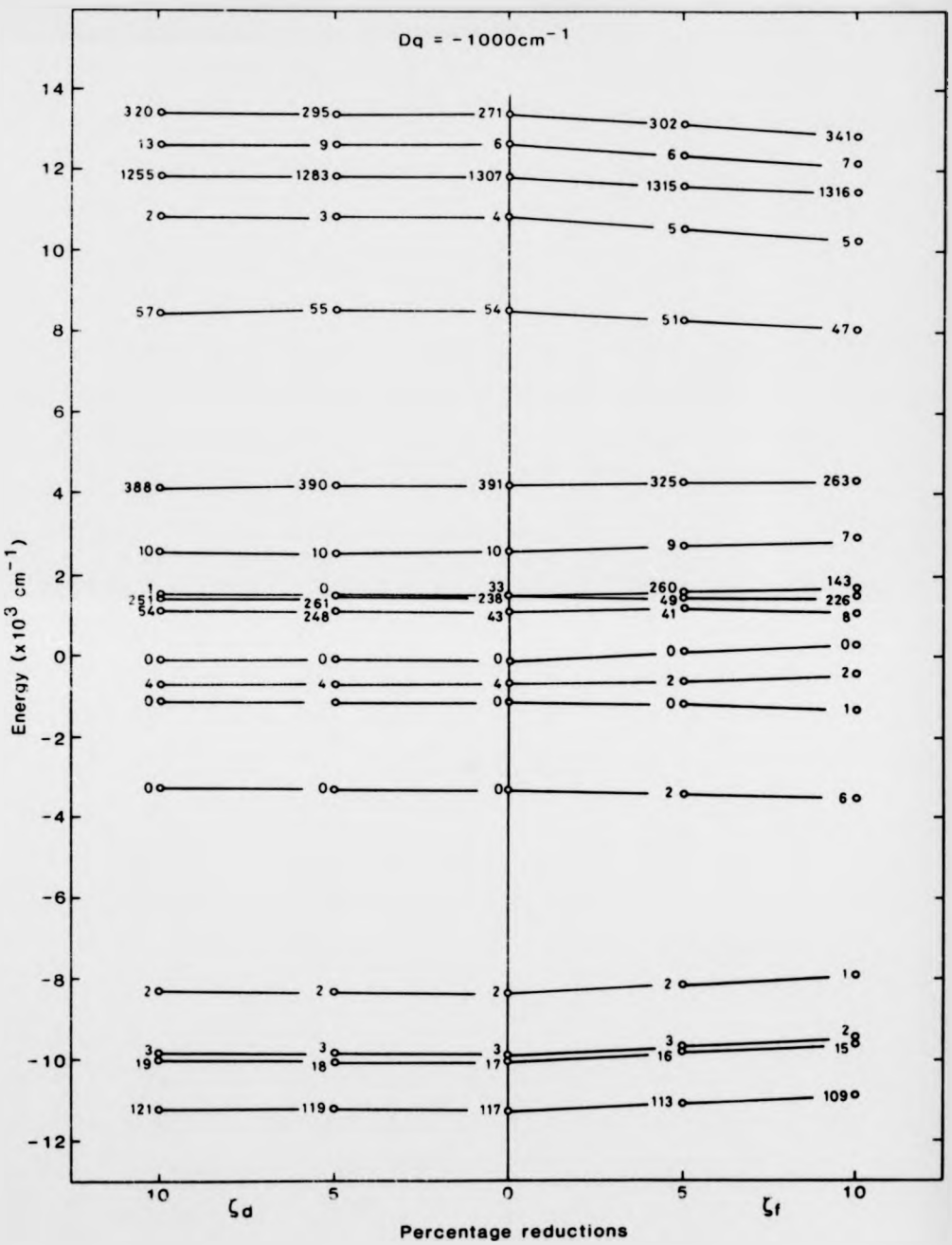

Fig.5.30 (b) Cubic crystal field (Dq = -1000 cm^{-1})

adjustable parameters has been reduced to the more manageable situation of only four i.e. F (= F_2), G (= G_1), ζ (= ζ_{4f}) and Dq. It should be remembered that even small variations in any one of the original parameters has a significant effect on the transition probabilities so that, while the simplifications noted above should lead to reasonably accurate energy level positions, the actual intensities are expected to be less well represented.

The energy separations between the dominant bands A1, A2, B1, B2, C1, D1 and D2 are selective in their dependence on re-defined parameter values. For example, the separations between A1 and A2 and between B1 and B2 are determined principally by F. The separations A1 to C1 and B1 to C1 are determined by G. The parameter ζ affects both the A1 to B1 and the A1 to D1 separations but the latter only weakly so. F and G control the D1 to D2 separation. Based on these dependencies the following iterative procedure was devised to fit the theoretical energy levels to the experimental levels. Initially, an approximate value of Dq is chosen by reference to figure 5.14 in order to satisfy the experimental separation between A1 and B1 and, if available, the separation between A1 and D1. The parameter G is next adjusted until the relative separations between the bands A1, B1 and C1 are optimised. The parameter F is adjusted to reproduce the separation A1 to A2 and finally ζ is adjusted to optimise the separations between A1, B1 and D1. The procedure is repeated until satisfactory overall agreement is obtained. For Yb^{2+} in KCl, KBr and NaBr it is also possible to adjust the separation D1 to D2, thereby contributing to a more comprehensive fit. For NaCl, where definition of the B1 band is poor, the procedure is varied slightly by using the separation B2 to C1 rather than B1 to C1 to determine G.

Generally excellent quantitative agreement between theoretical and experimental energy level positions is obtained when the above iterative procedure is adopted. In addition, the transition intensities exhibit acceptable overall agreement, largely justifying the approximations made.

Appropriate parameter values are given in figure 5.31. Δ in figure 5.31 corresponds to the energy difference between the centre of energy of the $4f^{13}5d$ configuration and the $4f^{14}$ ground state. The centre of energy is defined as the position to which all the states within the configuration would converge if all of the adjustable parameters were set equal to zero. Also included in the figure is the lattice parameter d and the nephelauxetic ratios for each parameter. Precise theoretical level positions and transition intensities are given in figure 5.32 together with the corresponding experimental values.

5.4.4 Discussion

The study by Tsuboi et al [13] on $NaCl:Yb^{2+}$ may be compared with the results presented here. Unfortunately, without the benefit of data from a range of alkali halides, they based their analysis on free-ion values with the result that agreement is not particularly accurate. A point of interest concerns the two bands designated by them as H and I which occur at 50505 cm^{-1} (198 nm) and 51813 cm^{-1} (193 nm) respectively. These bands correspond to D1 and D2 respectively in the present analysis, although they are not resolved in figure 5.20 due to a strong underlying absorption associated with the nominally-pure crystal. Nevertheless, the theory developed in the present work predicts (figure 5.32) that D1 and D2 occur respectively at 50278 cm^{-1} and 51635 cm^{-1}. In addition, it correctly predicts that D1 is less intense than D2.

Although the general agreement presented above is very good, there still exist certain discrepancies. In particular, the theoretical intensity of the band A2 is in rather poor agreement with that observed experimentally. It should be noted however that the general trend of increasing intensity for A2 in accordance with the familiar sequence $I^- - Br^- - Cl^- - F^-$ is still obeyed. Discrepancies of this nature are always likely to occur due to the difficulty

LATTICE	Dq(cm^{-1})	Δ(cm^{-1})	F(cm^{-1})	G(cm^{-1})	ζ(cm^{-1})	β(F)	β(G)	β(ζ)	d(Å)
KI	900	34341	104.4	111.5	2802.7	0.559	0.577	0.950	3.533
NaI	1030	34256	105.7	101.4	2861.7	0.566	0.525	0.970	3.238
KBr	1080	35915	117.7	116.9	2861.7	0.630	0.605	0.970	3.300
NaBr	1180	35815	121.0	119.6	2905.9	0.648	0.619	0.985	2.987
KCl	1240	36676	116.4	110.3	2920.7	0.623	0.571	0.990	3.146
NaCl	1360	36856	127.0	117.9	2950.2	0.680	0.610	1.000	2.820
KF	1635	39661	170.5	165.0	2950.2	0.913	0.854	1.000	2.672

Figure 5.31 Optimum parameter values obtained using the iterative fitting procedure described in the text.

EXPERIMENTAL			THEORETICAL	
BAND	ENERGY	INTENSITY	ENERGY	INTENSITY
			46473	4
			46211	591
			44972	126
C1	38462	542	38462	1342
			38298	11
			37920	42
			37296	10
			36668	0
			36530	1
B2	35587	5	35795	2
			35325	0
B1	34435	21	34441	27
A2	28736	57	28733	147
			27967	28
			26851	2
			26101	60
A1	25873	100	25871	93
			25366	2

(a) KI

EXPERIMENTAL			THEORETICAL	
BAND	ENERGY	INTENSITY	ENERGY	INTENSITY
			49316	5
			48934	565
D2	48900	198	47615	141
D1	47619	29	40279	1179
C1	40274	460	40214	52
			39520	19
			39236	6
			38681	26
			38322	5
			37647	1
B2	36630	28	36525	66
B1	35562	35	35637	90
A2	29621	48	29620	128
			28853	34
			27729	1
			26854	65
A1	26596	100	26593	114
			26085	2

(b) KBr

EXPERIMENTAL			THEORETICAL	
BAND	ENERGY	INTENSITY	ENERGY	INTENSITY
			51100	3
D2	50684	254	50652	514
D1	49383	34	49395	140
			41738	0
C1	41322	400	41320	1060
			40848	38
			40109	0
			39520	19
B3	39062	40	38972	20
			37889	5
B2	36969	83	36960	203
B1	35971	54	35995	118
A2	29656	39	29659	133
			28885	38
			27765	1
			26888	79
A1	26624	100	26627	127
			26111	3

(c) KCl

EXPERIMENTAL			THEORETICAL	
BAND	ENERGY	INTENSITY	ENERGY	INTENSITY
			57052	13
			56565	698
			54577	147
			47779	2
C1	46729	400	46717	596
			46490	208
			45382	9
			41766	23
			40986	27
			39538	14
B1	38835	203	38871	377
			37298	112
A2	31596	43	31654	51
			30722	36
			29551	0
			28131	68
A1	27816	100	27804	117
			27370	2

(d) KF

EXPERIMENTAL			THEORETICAL	
BAND	ENERGY	INTENSITY	ENERGY	INTENSITY
			47234	3
			46828	490
			45703	142
C1	38168	407	38186	806
			38102	422
			37866	77
			37261	33
			37056	19
			36379	3
			36111	1
B2	35026	33	35008	41
B1	34188	49	34201	86
A2	28050	58	28046	154
			27293	35
			26183	1
			25402	64
A1	25157	100	25150	128
			24643	1

(e) NaI

EXPERIMENTAL			THEORETICAL	
BAND	ENERGY	INTENSITY	ENERGY	INTENSITY
			49926	5
			49528	568
D2	49505	212	48164	138
D1	48077	34	40647	0
			40479	1144
C1	40486	313	39740	23
			39196	2
			38640	11
B3	38910	40	38346	21
			37268	3
B2	36311	73	36250	138
B1	35298	39	35285	102
A2	29112	50	29109	123
			28330	36
			27195	1
			26288	73
A1	26028	100	26026	113
			25513	2

(f) NaBr

EXPERIMENTAL			THEORETICAL	
BAND	ENERGY	INTENSITY	ENERGY	INTENSITY
			52140	3
			51635	522
			50278	147
			42716	0
C1	42017	520	42044	914
			41745	82
			40889	1
			39495	19
B3	38910	65	38839	19
			37687	8
B2	36832	148	36807	279
B1	35778	71	35719	130
A2	29394	36	29424	116
			28635	41
			27507	1
			26527	77
A1	28219	100	26248	135
			25735	3

(g) NaCl

Figure 5.32 Precise theoretical and experimental energy level positions and intensities for Yb^{2+} in (a) KI, (b) KBr, (c) KCl, (d) KF, (e) NaI, (f) NaBr and (g) NaCl. Theoretical intensities are equal to $(50a_1)^2$; experimental intensities are normalised to A1 = 100. All experimental values refer to measurements made at LNT.

of obtaining a sufficiently accurate total system wavefunction. Nevertheless the agreement obtained is still sufficient to establish the identity of the bands A, B, C and D without any reasonable doubt. They are due to transitions from the $4f^{14}$ ground state of the Yb^{2+} ion to the $4f^{13}5d$ excited state configuration in a crystal field of octahedral symmetry.

Another area of interest is the observation of extra structure in the bands A1 and A2 observed for $KF:Yb^{2+}$ and to a lesser extent for $NaCl:Yb^{2+}$. This is almost certainly related to a systematic breakdown in the assumption of a high symmetry octahedral crystal field. As the lattice spacing decreases it is to be expected that the relative contribution from the off-axis cation vacancy increases. The resultant reduction in symmetry toward a proper C_{2v} crystal field leads to a partial splitting of the bands derived from an assumed O_h crystal field and to the observation of additional structure within the absorption bands.

Some interesting trends become apparent on considering further the parameter values in figure 5.31. If Δ is plotted against d as in figure 5.33, the chlorides, bromides and iodides each form pairs of almost equal Δ (to within 1%). The value of Δ appears to be independent of both the character of the lattice cation and the lattice parameter. According to the nephelauxetic effect, the parameter Δ will depend quite strongly on the degree of overlap between the 5d electron and the surrounding anions. For the chlorides, bromides and iodides, it is concluded that the degree of overlap is determined primarily by the nature of the anion and not by the Yb^{2+}-anion separation. Δ is expected to differ more between the alkali fluorides as, for this most electronegative anion, variations in the Yb^{2+}-anion separation become more significant. The plotted values in figure 5.33 may be regarded as two distinct and closely parallel linear dependencies; one for the potassium halides and the other for the sodium halides. This behaviour is represented by the empirical formula

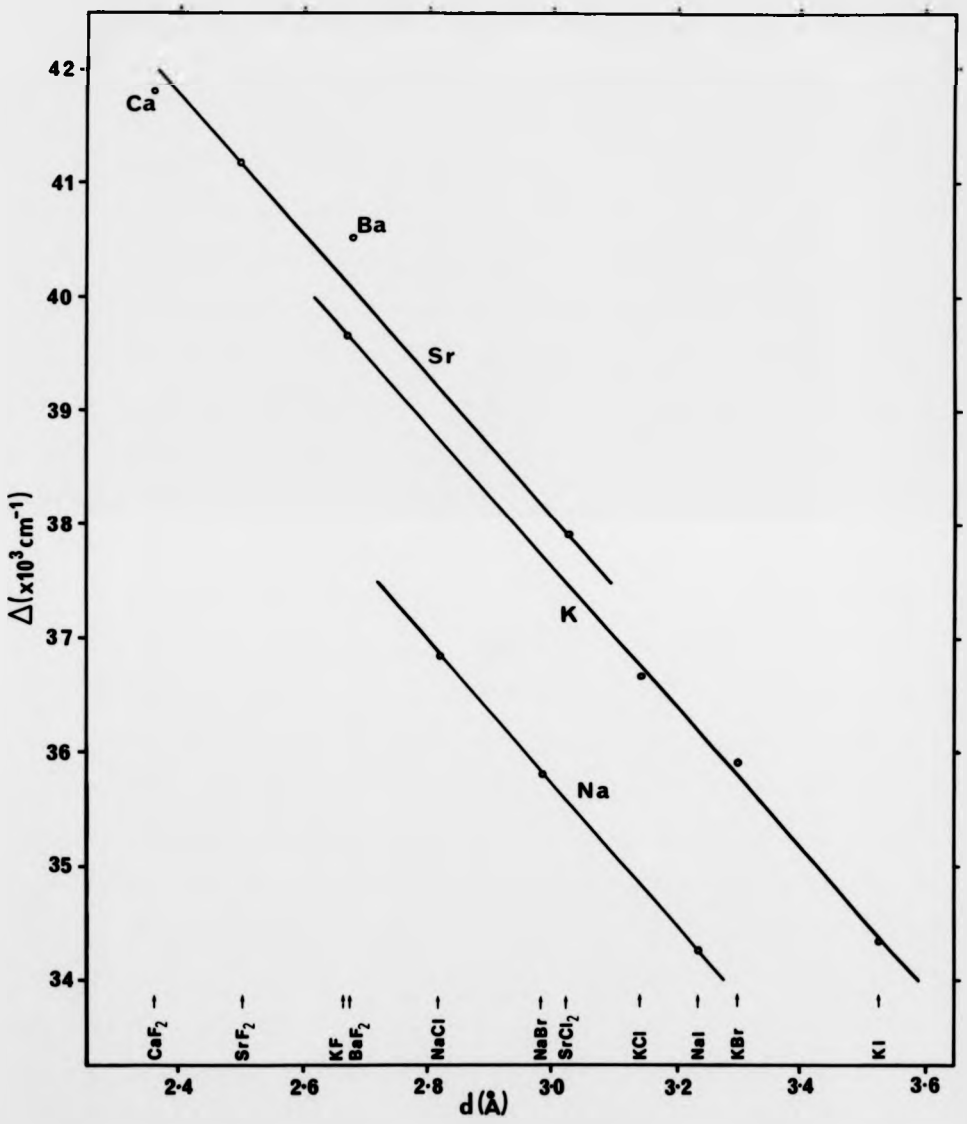

Figure 5.33 Variation of the parameter Δ with lattice parameter d. Equivalent values for Yb^{2+} in CaF_2, SrF_2, BaF_2 and $SrCl_2$ (see text) are included.

$$\Delta = -k_m d + l_m \qquad (m = K, Na) \qquad 5.27$$

Appropriate values for the coefficients in equation 5.27 are given in figure 5.34.

Also included in figure 5.33 are equivalent experimental points for Yb^{2+} in CaF_2, SrF_2 and BaF_2 [5]. Similarly a value is given for $SrCl_2$ which has been obtained based on the experimental results of Piper et al [4] but using the fitting procedure described earlier in this section. The details of how this revised value is obtained are given in a later section (section 5.7). It is interesting to note that the values for the (two) strontium halides lie on a line parallel to the lines obtained for the sodium and potassium halides. Appropriate values for the strontium coefficients in equation 5.27 are given in figure 5.34.

The comparatively large spread in Δ for the three alkaline earth fluorides in figure 5.33 is in agreement with the earlier prediction of a similar comparative spread for the fluorides of the alkali halide system. Ivoilova and Leushin [25] have analysed this configurational shift theoretically. They associate it primarily with metal-ligand exchange effects, implying a certain degree of covalence. In performing their calculations however they used values of Δ which neglected covalency effects. Their analysis predicts a more pronounced shift as the degree of covalence increases. For the alkali halide system the shift is actually reduced with increasing covalency, becoming slightly negative for the alkali bromides and iodides.

To the author's knowledge the linear dependence of Δ on d has not been observed previously. Indeed he is unaware of any comparable systematic study of this parameter encompassing such a large range of crystals. It would be interesting to obtain equivalent information from the spectrum of Yb^{2+} in the rubidium halides to check this trend further.

Another key parameter is the crystal field splitting Dq which is shown

m	k_m	l_m	p_m	q_m
Na	6219	54394	774.2	3524.3
K	6130	56036	860.6	3935.6
Sr	6134	56505	-773.6	3334.0

Figure 5.34 Values of the coefficients in equations 5.27 and 5.28. k_m and p_m are in units of $cm^{-1}Å^{-1}$. l_m and q_m are in units of cm^{-1}.

plotted against lattice parameter d in figure 5.35. Once again this rather unexpected linear dependence is observed although in this case it is less well defined. Two separate and parallel curves may be drawn through the individual sets of sodium halide and potassium halide values. This behaviour is represented in an analagous way by the empirical formula

$$Dq = -p_m d + q_m \qquad (m = K, Na) \qquad 5.28$$

Appropriate values for the coefficients in equation 5.28 are given in figure 5.34. The strontium halides ($Dq = -1400\ cm^{-1}$ for SrF_2 [5]) may also be fitted to equation 5.28. The value obtained for the gradient coefficient $p_{Sr} = -773.6\ cm^{-1}Å^{-1}$ is close (allowing for the sign reversal) to that for the potassium and sodium halides.

The nephelauxetic ratios $\beta(F)$, $\beta(Cl)$ and $\beta(I)$ are plotted against lattice parameter in figure 5.36. The reduction over the free ion value is observed to increase in general (ratio decreases) as the lattice parameter increases. If, as anticipated, the reduction is related to the covalency of the host crystal anion, then it will increase in the sequence $F^- - Cl^- - Br^- - I^-$. This trend is indeed observed.

5.5 Sodium and lithium fluorides containing Yb^{2+}

The optical absorption spectra associated with Yb^{2+} in NaF and LiF are presented in figures 5.22 and 5.23 respectively. In both cases the spectra were recorded directly after quenching to room temperature following impurity diffusion. It should be noted that for $LiF:Yb^{2+}$ a weak spectrum was observed at all times. Numerous attempts were made to produce a stronger spectrum, involving the use of a wide variety of diffusion conditions (temperature/time), however it proved impossible to improve significantly on this situation. The seemingly very low solubility

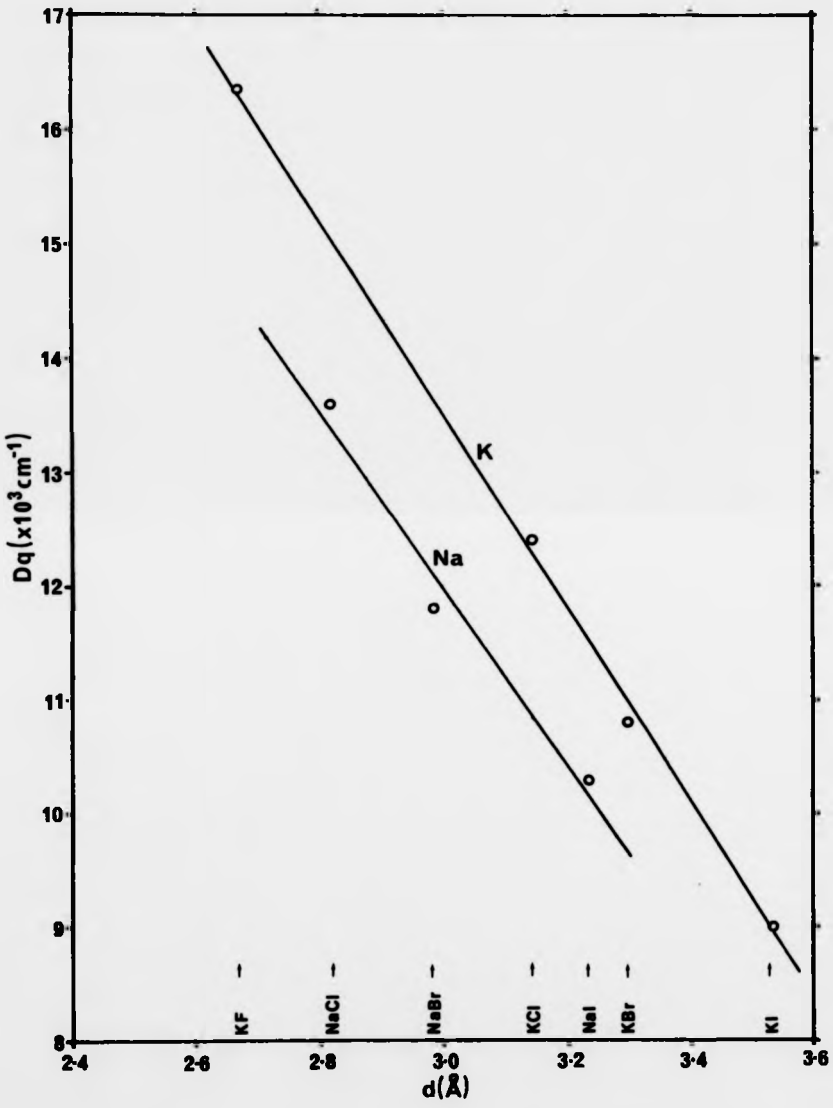

Figure 5.35 Variation of the parameter Dq with lattice parameter d.

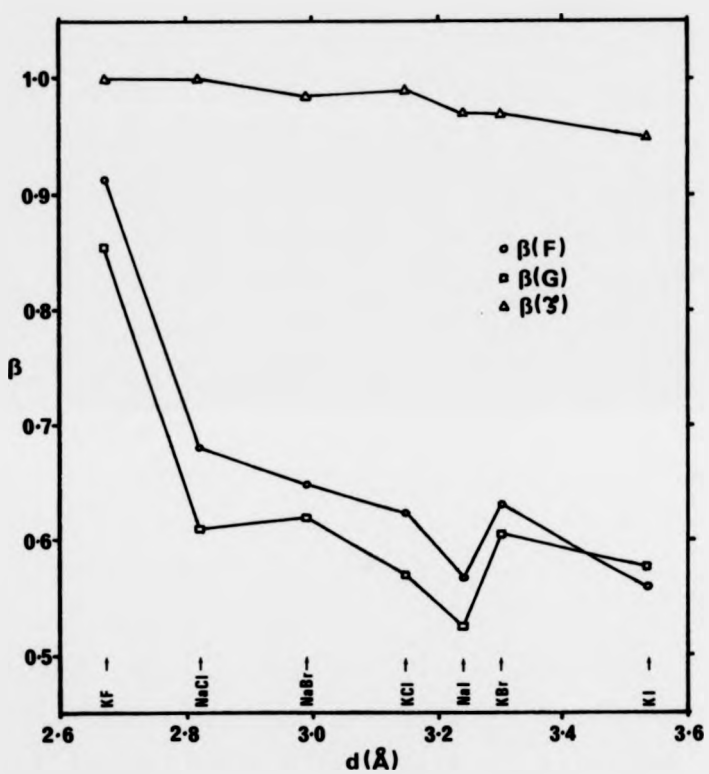

Figure 5.36 Variation of the main nephelauxetic ratios β(F), β(G) and β(ζ) with lattice parameter d.

of ytterbium in LiF was not unexpected due to the improbable substitution of a Yb^{2+} ion with a radius of 0.93 Å for a Li^{+} ion with radius 0.68 Å [26]. Nevertheless, a comparison of figures 5.22 and 5.23 does indicate that these two spectra exhibit the same overall features. The only difference is in the absolute positions of the individual absorption bands. The discussion presented here concentrates primarily on NaF but it is expected to be as equally valid for LiF.

The spectrum obtained for NaF containing ytterbium differs from the spectra obtained earlier for the majority of the alkali halides. The most obvious discrepancy is the appearance in NaF of only one strong band at low energies in place of the two bands A1 and A2. Accordingly, it is impossible to reconcile this spectrum with a 6-fold (octahedrally) coordinated Yb^{2+} ion. It does, however, correspond quite well with the type of spectrum expected for an 8-fold (cubically) coordinated Yb^{2+} ion (figure 5.14(b)). Here the low energy band A1 is quite strong and is the only significant band within the lower group of levels. It is well separated from the next pair of bands B1 and B2 which are of similar intensity. A solitary strong band designated C1 is expected at still higher energy. This is precisely the situation observed for $NaF:Yb^{2+}$ corresponding respectively to the bands at 27360, 36324, 38052 and 43535 cm^{-1}. The best fit between theory and experiment requires the use of reduced Slater-Condon and spin-orbit parameters. The relevant values are Dq = -1530 cm^{-1}, Δ = 41255 cm^{-1}, $\beta(F)$ = 0.769, $\beta(G)$ = 0.84 and $\beta(g)$ = 0.98. The excellent correlation is illustrated in figure 5.37(a).

An approximate correlation was attempted for $LiF:Yb^{2+}$ using the free-ion values. At room temperature a value of Dq = -1500 cm^{-1} was obtained. The separation of B1 and B2 in this case similarly suggests the use of slightly reduced free-ion parameters. This would probably lead to a slightly increased value for Dq. An evaluation of the reduced parameters was not attempted, however, due to the limited definition of the absorption

EXPERIMENTAL			THEORETICAL	
BAND	ENERGY	INTENSITY	ENERGY	INTENSITY
			55973	261
			55462	0
			54636	1081
			53893	20
			51888	35
C2	46512	34	46512	280
			45392	4
			43970	46
C1	43535	318	43535	369
			43090	0
			42580	3
			39314	14
B2	38052	87	38135	130
B1	36324	61	36324	56
			29399	2
			28506	12
			28142	41
A1	27360	100	27360	146

(a) NaF (cubic)

EXPERIMENTAL		THEORETICAL	
BAND	ENERGY	ENERGY	INTENSITY
		59229	53
		58976	810
		56516	128
		49973	5
C1	48900	48943	654
		48598	89
		47345	10
		43274	26
		42450	32
		40909	24
B2	40161	40410	360
	39370	38567	85
B1	33003	33053	34
		32146	30
		30956	0
A2	30581	29371	66
A1	29412	29038	92
		28656	3

(b) NaF (octahedral)

Figure 5.37 Precise theoretical and experimental energy level positions and intensities for Yb^{2+} in (a) NaF (cubic) and (b) NaF (octahedral). Energy level positions are given in units of cm^{-1}. Theoretical intensities are equal to $(50a_1)^2$; experimental intensities are given for the cubic case only and are normalised to A1 = 100.

bands.

Evidence to support the above classification derives from studies made elsewhere of the spectra obtained for Yb^{2+} in the alkaline earth fluorides [5,27-29]. The alkaline earth halide crystals possess the fluorite structure MX_2 with the metal ion present in a doubly ionized state. As a result, the substitution of a divalent impurity ion does not require charge compensation and the full cubic 8-fold symmetry of the site is maintained. The spectrum of $CaF_2{:}Yb^{2+}$ is reproduced in figure 5.38. It is clearly identical in form to that obtained for $NaF{:}Yb^{2+}$ and $LiF{:}Yb^{2+}$.

The spectrum for NaF discussed thus far was obtained following quenching to room temperature directly after ytterbium diffusion. On annealing samples prepared in this way at 800°C in a vacuum, a new set of absorption bands appeared at the expense of the original set. The evolution of these bands with the period of annealing is illustrated by spectra (a), (b) and (c) of figure 5.39. The difference between spectra (a) and (c) of figure 5.39 is shown in figure 5.40. The difference has been determined by subtracting (a) from (c) and represents an attempt to distinguish the new absorption bands from the original spectra. The new set of absorption bands share a number of similarities with the spectrum observed for Yb^{2+} in KF (see figure 5.21). Complete agreement is not obtained and the most significant difference concerns the apparent splitting of the large band in the vicinity of 40000 cm^{-1} which corresponds to B2 in $KF{:}Yb^{2+}$. New bands that cannot be directly accounted for are found at 32787 and 33557 cm^{-1}. In addition, there is a considerable increase in the structure observed in the lower energy bands.

It is proposed here that this new spectrum is characteristic of Yb^{2+} on a substitutional cation site in common with the majority of the alkali halides. The discrepancies noted above are probably the result of the continuing breakdown of the high symmetry octahedral crystal field

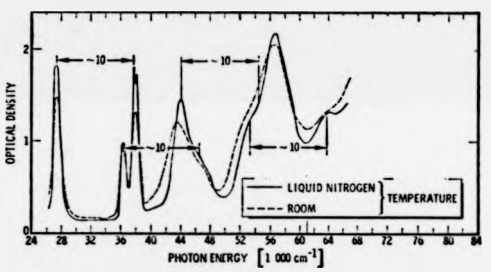

Figure 5.38 The optical absorption spectrum of Yb^{2+} in CaF_2 at RT and LNT (after Loh [29]).

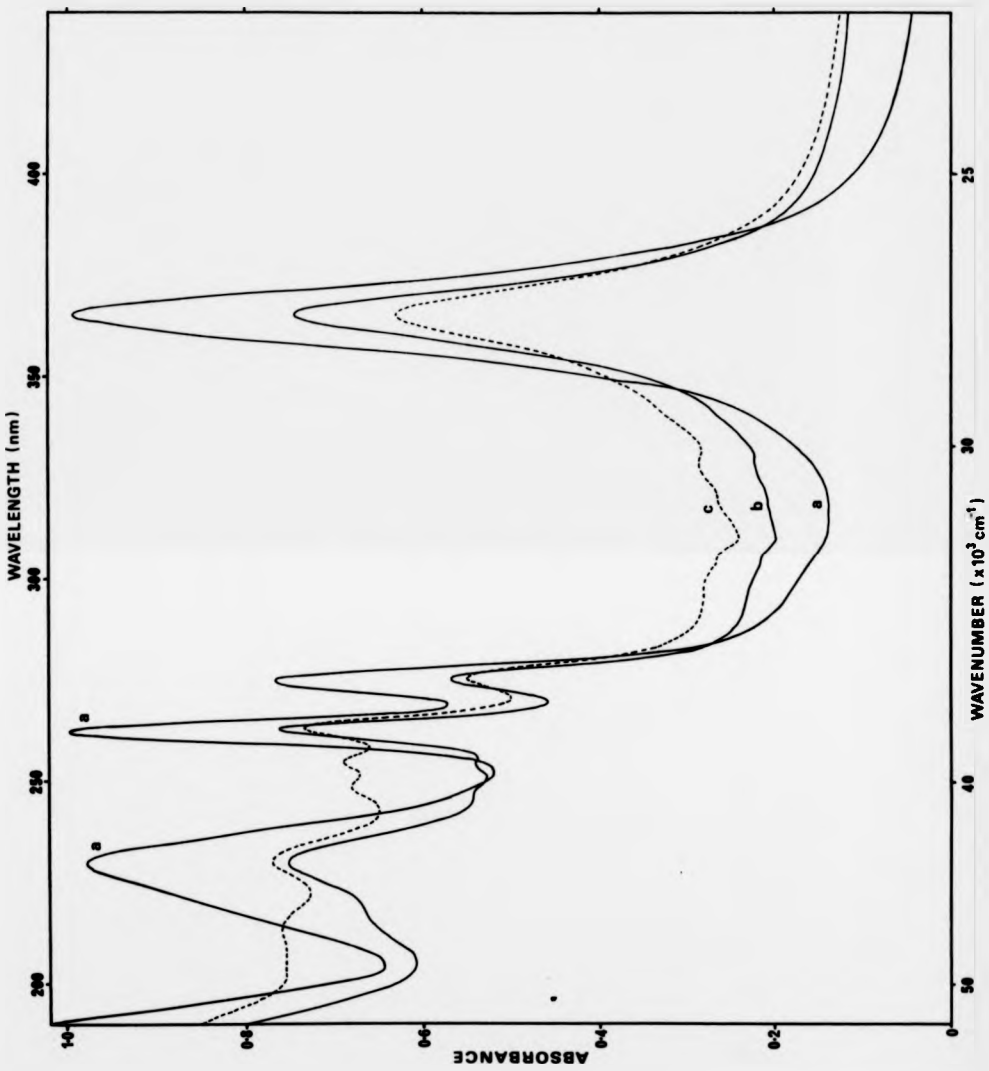

Figure 5.39 The effect of annealing at 800°C in vacuum on the optical absorption spectrum of NaF:Yb^{2+}. Samples were quenched to RT following anneal and spectra were recorded at LNT; (a) as produced, (b) after 1 hour and (c) after 2 hours.

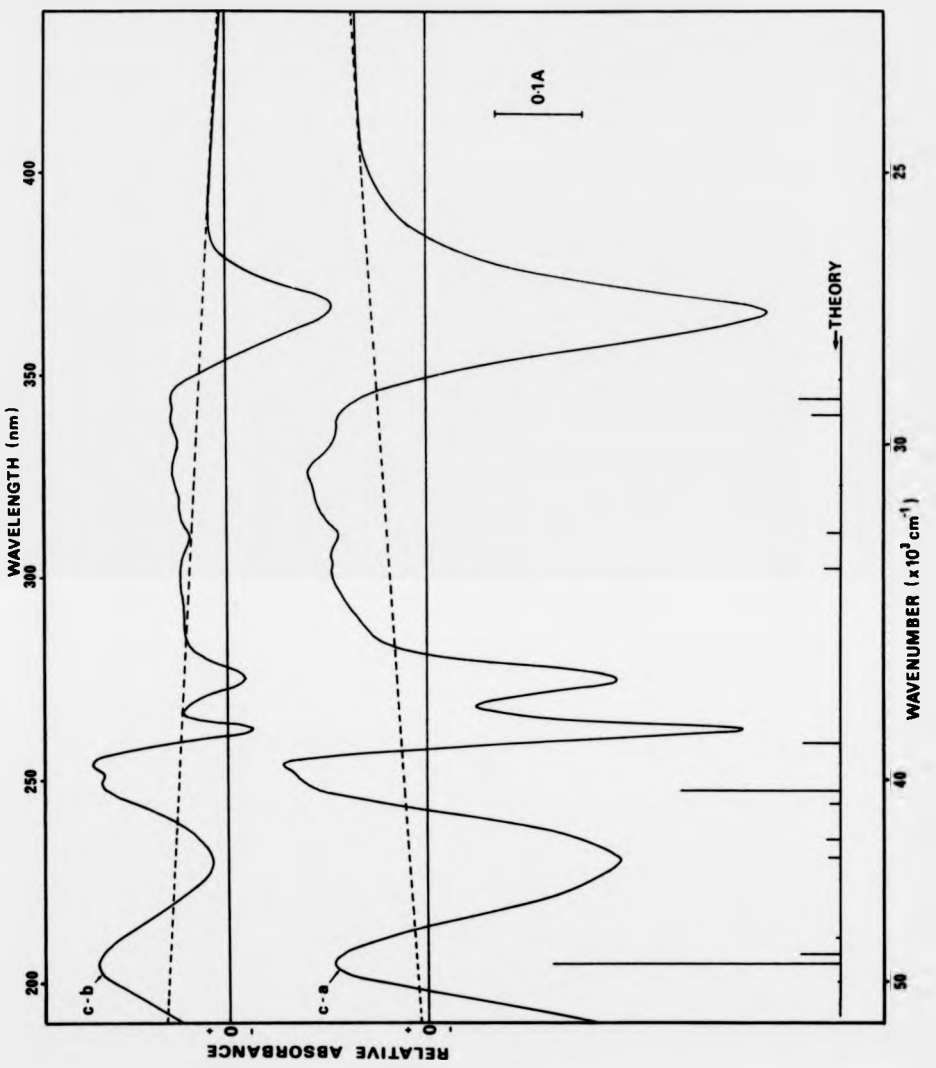

Figure 5.40 The difference spectra between traces (b) and (c) and also (a) and (c) of figure 5.39. The dashed lines indicate approximate zero levels allowing for systematic baseline shifts. Also included is a schematic representation of the best fit theoretical energy level positions and intensities for the new spectrum.

model, the beginnings of which have already been noted for $KF:Yb^{2+}$ (section 5.44). Assuming this hypothesis is correct, then a reasonable fit to the observed bands is obtained with Δ = 41700 cm^{-1} and Dq = 1700 cm^{-1}. The agreement is illustrated in figure 5.37(b). The free ion values have in this case been employed in accordance with the trends observed in figure 5.36. A more detailed analysis is not justified considering the limited accuracy of the subtraction process. It is interesting to note that the use of equations 5.27 and 5.28, which describe linear dependencies in Δ and Dq for the potassium and sodium halides, predicts values of Δ = 40003 cm^{-1} and Dq = 1733 cm^{-1} for NaF (d = 2.314 Å). These values are in very good agreement with the approximate fitted values and strongly support the above hypothesis.

The question why Yb^{2+} should be found initially to occupy a site of cubic symmetry in NaF and LiF is interesting. One possible explanation could be the incorporation of Yb^{2+} on an interstitial site. This would give rise to a true 4-fold (tetrahedral) coordination which can also be regarded as effectively cubic coordination with only half the 8 neighbouring sites occupied. This situation is shown schematically in figure 5.41. To first order, therefore, the symmetry might be expected to be similar. If it is assumed that the constituent ions act as rigid spheres in a close-packed arrangement then, using the relevant ionic radii [26], the largest sphere which can be accommodated in an interstitial position in NaF will have a radius of about 0.68 Å. The ionic radius of the Yb^{2+} ion is 0.93 Å indicating that such a situation is unlikely to occur in practice. It is interesting to note that this is the same degree of misfit as was described earlier for substitutional Yb^{2+} in LiF. In addition, a divalent ion present on a normally neutral site ($Yb_i^{\cdot\cdot}$) would require two charge compensating vacancies. This is equivalent to a trivalent ion on a substitutional lattice site which is known to be extremely rare in the alkali halides where radical departures from the host

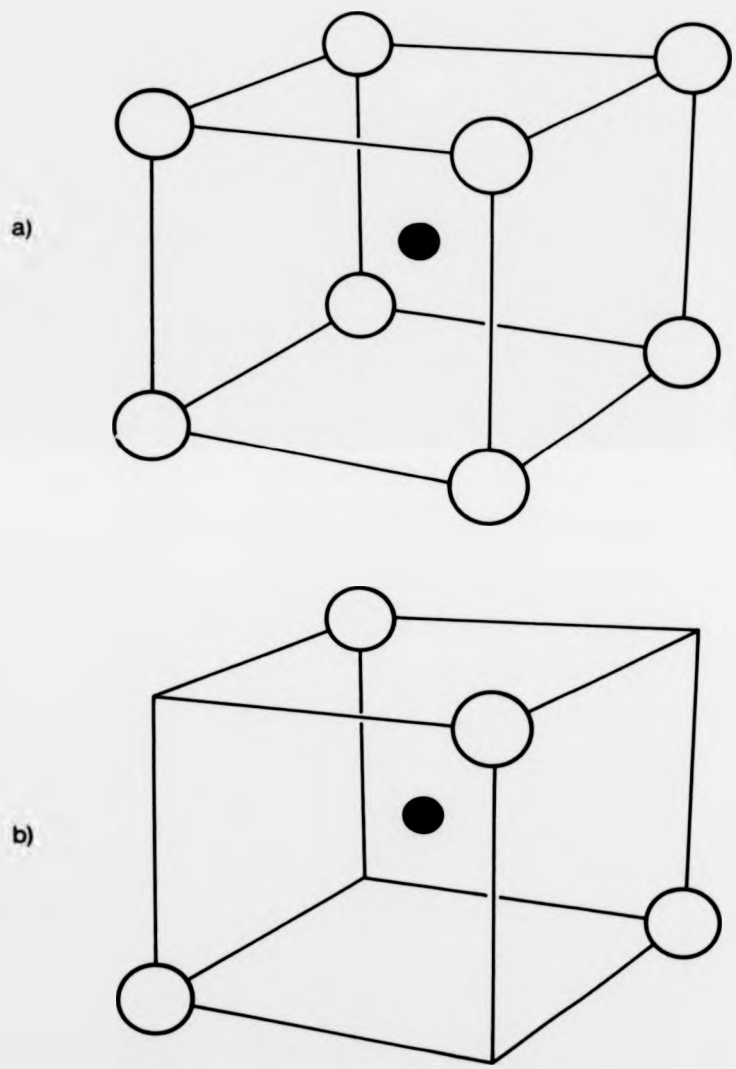

Figure 5.41 A schematic representation of a) 8-fold (cubic) and b) 4-fold (tetrahedral) co-ordination of a central ion.

ionic charge states are strongly discouraged [30]. Therefore, this hypothesis is discounted.

A second and more reasonable possibility is that the ytterbium is present as part of a separate crystalline phase. The structure of this phase is such that a Yb^{2+} ion is contained on a site of cubic symmetry. The most obvious candidate in this respect is the formation of a separate phase of YbF_2 possessing a structure of the fluorite type. The optical absorption spectrum associated with the Yb^{2+} ion in this case might be expected to be somewhat similar to that observed for a substitutional ion in CaF_2. Such a similarity was noted earlier in this section. The slight energy shifts observed between these two cases could easily be attributed to slight differences in the lattice constant.

The melting point of YbF_2 is at 1052°C [26] and suggests that it is a stable entity at the diffusion temperatures employed. Quenching quickly to room temperature effectively freezes in this separate phase. The changes which occur in the optical absorption spectrum on prolonged annealing of the quenched $NaF:Yb^{2+}$ sample may then be attributed to dissociation of the YbF_2 phase with the Yb^{2+} ion moving onto a conventional substitutional lattice site. It is significant that the YbF_2 phase does not appear to dissociate completely thus suggesting that some form of equilibrium exists between the amount of YbF_2 and substitutional Yb^{2+} present in the NaF lattice. This may be related to the solubility limit of YbF_2 in the NaF lattice which, if exceeded at these lower annealing temperatures, would provide the necessary driving force. Dissociation would continue until the solubility limit, which is likely to be a function of the annealing temperature, was no longer exceeded.

5.6 The absorption bands E1 and E2

The two absorption bands E1 and E2 were earlier distinguished from the bands A to D by their fundamentally different behaviour with respect to changes in temperature. Both bands were found to sharpen noticeably and simultaneously to exhibit a significant shift to higher energy as a result of cooling of the sample. Accordingly, it became clear that these two sets of bands belonged to two quite different classes of optical transitions. However, one very important conclusion arose after studying the spectra obtained for numerous different samples of the same type but containing widely different impurity concentrations. The relative concentration of each centre, as determined by the total transition strength for both sets of transitions, always remained fixed. Therefore, both sets of transitions arise from the same impurity centre, namely the Yb^{2+} ion.

The bands E1 and E2 are observed in the majority of the alkali halide crystals, the notable exception being the alkali fluorides. For NaCl:Yb^{2+} the E1 band is so weak or broad as to be indeterminate and for NaI:Yb^{2+} the E2 band occurs too close to a much stronger absorption band to allow it to be accurately resolved. The band positions at RT and LNT are indicated in figure 5.42. Also included in this figure is a value denoting the absorption strength of each band expressed as a function of the combined A1 plus A2 absorption band strengths. The bands A1 and A2 were chosen for this purpose since their total combined absorption strength is expected to remain relatively constant throughout the complete range of host crystals. This follows from the theory derived earlier since A1 and A2 represent the total absorption strength contained in the lowest lying $^2F_{7/2}d_{e/2}$ set of levels. Figure 5.14 shows that this absorption strength remains virtually constant due to the fairly large energy separation between this set of levels and the rest. It should also be noted that, although E1 and E2 are clearly non-Gaussian in shape, they were approximated as such in order to simplify the calculations. This

Crystal	E1 band			E2 band			Δ E1, E2 (cm^{-1})
	Energies		Relative intensity (LNT)	Energies		Relative intensity (LNT)	
	LNT(cm^{-1})	RT (cm^{-1})		LNT (cm^{-1})	RT (cm^{-1})		
KI	32,154	32,468	0.40	—	42,373	2.41	9,905
NaI	32,841	33,389	0.36	—	—	—	—
KBr	32,103	32,468	0.29	42,194	42,589	0.87	10,121
NaBr	32,949	33,557	0.26	42,974	43,630	0.96	10,073
KCl	32,680	33,167	0.18	—	43,197	0.67	10,030
NaCl	—	—	—	44,248	44,934	0.76	—

Figure 5.42 Energy level positions of the E-bands at RT and LNT. Also included are the relative intensities and the overall energy separation between the bands E1 and E2 (ΔE1, E2) at LNT.

approximation is not expected to compromise the relative values between bands in different crystals since the error is expected to be consistent.

Consideration of figure 5.42 suggests certain notable trends. The overall energy separation between E1 and E2 varies in a systematic way with host crystal. It is smallest for the alkali iodides and increases slightly according to the anion-based sequence $I^- - Br^- - Cl^-$. Similarly, the intensities of the E bands with respect to the A to D bands are strongly anion dependent, decreasing in the same sequence. The band positions are shown plotted against lattice parameter in figure 5.43 with the positions of mean energy for each pair also labelled. The anion-dependent behaviour of the E bands is superimposed on a general rise in overall energy as the lattice parameter is decreased.

Included in figure 5.43 are the free ion levels associated with the $4f^{13}6s$ configuration of Yb^{2+}. Certain similarities are found to exist. The overall splitting between the two pairs of levels is comparable with the separation between E1 and E2, and the mean energy position lies at a similar absolute value. It is extremely unlikely that these levels actually correspond to the transitions $4f^{14} - 4f^{13}6s$ since such transitions are forbidden. Nevertheless, the possibility of a relaxation of these selection rules due to certain types of interaction should be considered.

An important interaction mechanism encountered in the study of optical absorption spectra is that of configurational interaction. This interaction has been found to be of importance in the free ion spectra of Pb^{2+} [31] and Mn^{1+} [32]. Certain conditions must be satisfied in order that two configurations may interact. The configurations must both possess the same parity and they should contain certain states of the same total angular momentum. Both the $4f^{13}5d$ and $4f^{13}6s$ configurations possess odd parity and there exist three angular momentum states common to both, namely J = 2, 3 and 4. The magnitude of the interaction is dependent on matrix elements of the form [33]

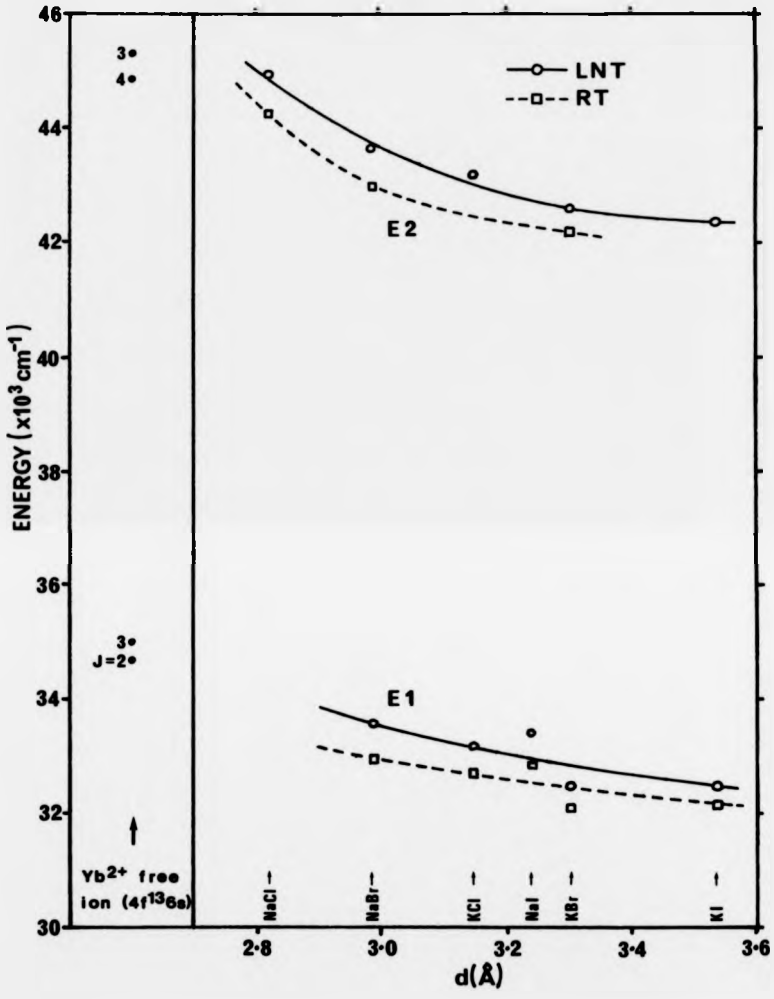

Figure 5.43 Variation in the energy level positions of the bands E1 and E2 with lattice parameter d. Also included for comparison are the positions of the free ion energy levels of the $4f^{13}6s$ configuration of Yb^{2+}.

$$(1/\Delta E)\langle(4f^{13}5d)J_1|\ U^k\ |(4f^{13}6s)J_2\rangle\ \delta(J_1,J_2) \qquad 5.29$$

where ΔE is the difference in energy between the centres of the two configurations. Consequently the interaction increases in magnitude as the overlap between the two configurations increases. The only operators producing non-zero matrix elements when equation 5.29 is evaluated are those able to simultaneously satisfy the 3-j symbols $\begin{pmatrix} 3 & k & 3 \\ 0 & 0 & 0 \end{pmatrix}$ and $\begin{pmatrix} 2 & k & 0 \\ 0 & 0 & 0 \end{pmatrix}$. The only value of k meeting this requirement is k=2, thus limiting the discussion to second order tensor operators.

For a Yb^{2+} free ion the inclusion of this type of interaction is unnecessary, however in the presence of a crystal field, configurational interaction should be considered more carefully. This aspect has been studied in detail by Rajnak and Wybourne [34]. According to their results it is only the second order tensor operators in the crystal field expansion which yield non-zero matrix elements. Now, since the true site symmetry of a divalent ion in the alkali halides is C_{2v}, there exists a second order crystal field component. The magnitude of this axial component for each of the alkali halides is unfortunately not readily available from any previous optical absorption studies. It is to be expected, however, that its magnitude will increase as the distance between the vacancy and the impurity ion decreases. This phenomenon is observed for the ESR of paramagnetic divalent impurity ions in the alkali halides. The ESR technique is far more sensitive to the precise symmetry of the site occupied by the ion and it is possible to determine very accurately the magnitude of the second order crystal field terms. The relevant parameter in this instance is b_2^0 which is directly proportional to B_2^0. The Yb^{2+} ion is not paramagnetic and therefore this information is not directly obtainable. The Eu^{2+} ion behaves in many respects in a similar way to the Yb^{2+} ion except that it is paramagnetic. A

simplified ESR analysis is presented for the Eu^{2+} ion in the following chapter (for a more detailed analysis consult the references contained therein). The simplified treatment is sufficiently detailed to demonstrate that b_2^0 increases as the lattice parameter decreases. Therefore, it is concluded that the bands E1 and E2 cannot be due to a configurational interaction of this nature since their intensities decrease as the lattice parameter decreases.

Asano [35] and Asano and Nakao [36] have considered the general case of configurational interaction between the $4f^n5d$ and $4f^n6s$ configurations in a cubic crystal field. The theory is applied to the specific case of the Eu^{2+} ion in MgS to explain the appearance of new bands in the excitation spectrum as the concentration of Eu^{2+} ions is increased. The new bands are ascribed to transitions of the type $4f^7 - 4f^6 6s$, although their analysis considers only the electrostatic interaction between the two configurations which alone does not give rise to any intensity for such transitions. Two possible mechanisms are described to account for their appearance. The first is based on the creation of a quasicubic crystal field as a (Mg,Eu)S solid solution is formed, and the second is based on a lowering of the crystal field symmetry about the Eu^{2+} ion by means of electronic interaction with surrounding Eu^{2+} ions. Both models rely on the presence of second order ($k = 2$) crystal field terms. It should be noted however that the intensity of the E bands in the alkali halides is not concentration dependent and therefore neither of the models are applicable in the present case.

The observed similarity between the E band positions and the $4f^{13}6s$ level positions implies the following situation. An electron from the $4f^{14}$ ground state is excited into an orbital of predominantly s-like character which still interacts strongly with the $4f^{13}$ core state. According to this model, the spin-orbit splitting of the $4f^{13}$ core remains a common feature. Any proposed model should, in addition, be able to account for the marked dependence exhibited by the transition

strengths of the E bands on the respective anions. There is a similarity between this observation and the earlier trend observed for the reduction of the nephelauxetic ratios corresponding to the $4f^{13}5d$ configuration (figure 5.36). If indeed the relative polarisability or covalency of the respective anion is of importance here, then it is instructive to consider in what way this might alter the energy level scheme. This problem is best approached using the molecular orbital (MO) theory of which a rather simplified treatment is presented below concentrating on the high lying normally unoccupied orbitals.

Consider initially the energy position of the outer orbitals of the negatively charged halide ions. These are shown schematically in figure 5.44 based on the configuration $ns^2np^6(n+1)s$. Notice how the separation between the normally filled ns and np orbitals and the normally unoccupied (n+1)s orbital decrease as the principal quantum number n increases. Consider now the case of a central impurity ion surrounded by an octahedral array of such halide ions. The overall symmetry classification of this octahedral anion complex is formed by combining the individual symmetry states. These combined states are broadly divisible into σ and π orbitals. The maximum electron density for a σ-bonding orbital is found along the line joining the centres of the bonded atoms. For π-bonding orbitals, the electron density lies concentrated as two "streamer orbitals", with opposite sign of wavefunction, one on each side of the line joining the atom centres, and with that line as node. This situation is illustrated schematically in figure 5.45.

An impurity ion situated within this complex interacts with the surrounding anions according to the degree of orbital overlap. Overlapping orbitals belonging to the same irreducible representation are able to interact and this gives rise to the formation of bonding and antibonding orbitals. The antibonding state lies to higher energy and is distinguished from the bonding state by a star superscript. Consider Yb^{2+} as the

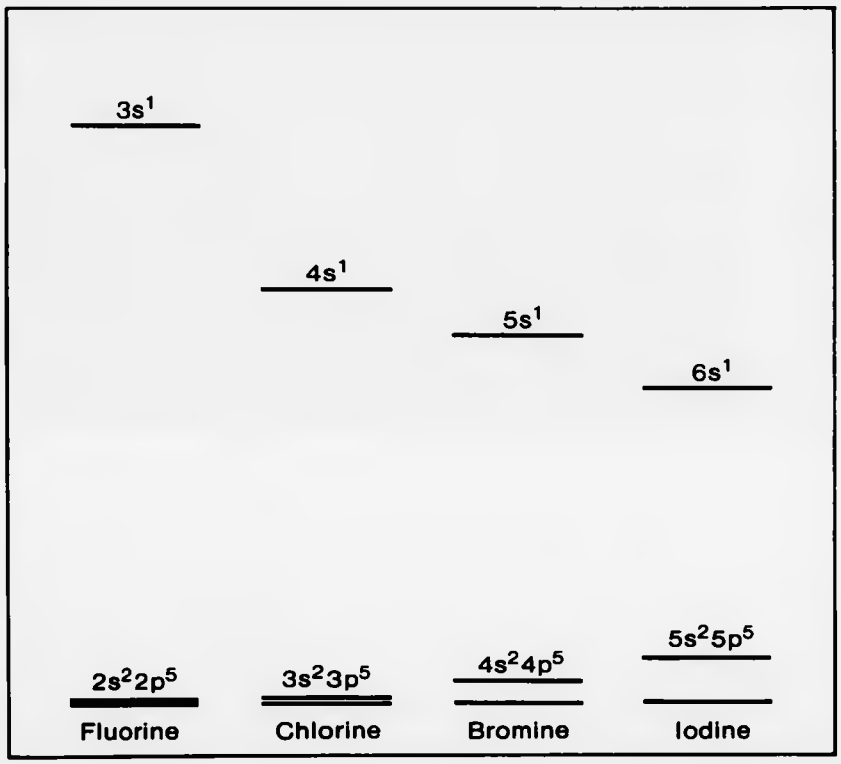

Figure 5.44 Energy levels for the configuration $ns^2np^5(n+1)s^1$ of the halogens.

Figure 5.45 The different symmetry classifications of an isolated halogen ion and of an octahedral array of such ions.

central ion. It is unlikely that there will be any significant overlap between the deep lying and shielded 4f electron orbitals and the surrounding anion complex orbitals. This situation will be true for any of the rare earth ions. The 5d and 6s orbitals possess a much larger extension in space and, as a result, are more likely to form an overlap with the anion orbitals. This is certainly the case for the 5d orbitals as was shown earlier by the necessity to adjust the free ion radial integrals (section 5.4). The likely effect on the 6s orbital is considered next.

In figure 5.46 the energy level structure of each of the halide ion octahedral complexes is included alongside the Yb^{2+} ground state orbitals. The relative separation between the centre of gravity of the Yb^{2+} ion levels and the halide complex levels is unknown but is likely to be similar to that shown in figure 5.46. In any case, since only a qualitative indication of a trend is required, this approximation should prove adequate. The 6s orbital of Yb^{2+} transforms according to the irreducible representation A_{1g} of the group O_h and, therefore, will only interact with the A_{1g} component of the σ-orbitals of the anion complex. The levels situated closest in energy are the normally unoccupied (n+1)s orbital set. An overlap of these orbitals might be expected to lead to the formation of bonding and antibonding states as indicated in figure 5.46. The depression of the bonding orbital below the 6s level of the Yb^{2+} ion is denoted by Δ'. The magnitude of Δ' will be largely determined by two factors; the energy separation between the 6s level of the Yb^{2+} ion and the (n+1)s σ-anion complex level, and the degree of covalency of the anion complex. Δ' will increase as the energy separation decreases and/or the degree of covalency increases. This model predicts that Δ' will increase quite strongly in the sequence $F^- - Cl^- - Br^- - I^-$ which is in agreement with earlier observations.

Judging by the small but gradual reduction in the separation between E1 and E2 according to the sequence $F^- - Cl^- - Br^- - I^-$, an earlier assumption that the overlap between the 4f orbital and the anion orbitals is insignificant,

central ion. It is unlikely that there will be any significant overlap between the deep lying and shielded 4f electron orbitals and the surrounding anion complex orbitals. This situation will be true for any of the rare earth ions. The 5d and 6s orbitals possess a much larger extension in space and, as a result, are more likely to form an overlap with the anion orbitals. This is certainly the case for the 5d orbitals as was shown earlier by the necessity to adjust the free ion radial integrals (section 5.4). The likely effect on the 6s orbital is considered next.

In figure 5.46 the energy level structure of each of the halide ion octahedral complexes is included alongside the Yb^{2+} ground state orbitals. The relative separation between the centre of gravity of the Yb^{2+} ion levels and the halide complex levels is unknown but is likely to be similar to that shown in figure 5.46. In any case, since only a qualitative indication of a trend is required, this approximation should prove adequate. The 6s orbital of Yb^{2+} transforms according to the irreducible representation A_{1g} of the group O_h and, therefore, will only interact with the A_{1g} component of the σ-orbitals of the anion complex. The levels situated closest in energy are the normally unoccupied (n+1)s orbital set. An overlap of these orbitals might be expected to lead to the formation of bonding and antibonding states as indicated in figure 5.46. The depression of the bonding orbital below the 6s level of the Yb^{2+} ion is denoted by Δ'. The magnitude of Δ' will be largely determined by two factors; the energy separation between the 6s level of the Yb^{2+} ion and the (n+1)s σ-anion complex level, and the degree of covalency of the anion complex. Δ' will increase as the energy separation decreases and/or the degree of covalency increases. This model predicts that Δ' will increase quite strongly in the sequence $F^- - Cl^- - Br^- - I^-$ which is in agreement with earlier observations.

Judging by the small but gradual reduction in the separation between E1 and E2 according to the sequence $F^- - Cl^- - Br^- - I^-$, an earlier assumption that the overlap between the 4f orbital and the anion orbitals is insignificant,

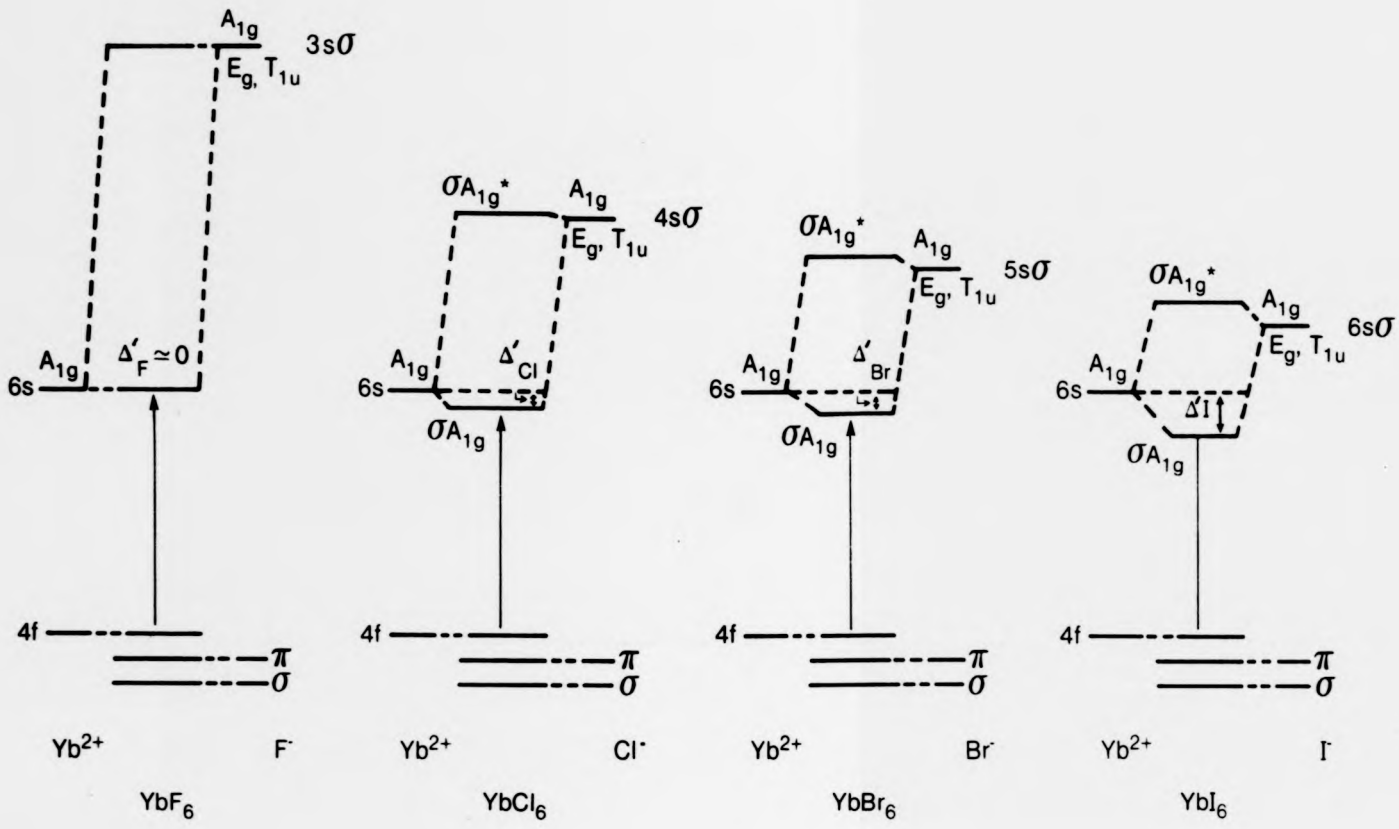

Figure 5.46 A schematic representation of the formation of bonding and antibonding orbitals for the Yb^{2+} ion in various octahedral halogen ion complexes.

is not entirely accurate. This separation between E1 and E2 is based totally on the $4f^{13}$ spin-orbit splitting parameter ζ_{4f}. Consequently a reduction in the separation between E1 and E2 implies a reduction in the free ion value for ζ_{4f} which in turn implies some degree of overlap. The observed dependence on anion is consistent with this explanation.

Mixing of the anion and impurity ion wavefunctions appears to lead to a relaxation of the optical transition selection rules, which in turn implies that the intensity of the transition will be dependent on the degree of mixing. The strongest transitions will therefore occur in the iodides and the weakest in the fluorides, with the familiar sequence obeyed. The transition described by this model cannot be classed as an ordinary charge transfer transition since the excited electron remains mainly centred on the $4f^{13}$ core. It is more exciton like in its behaviour with the transition localised within the octahedral complex. Since the final configuration is formed from a coupling of the $4f^{13}$ core to a less localised s-bonding orbital of A_{1g} symmetry, it is designated $4f^{13}s(A_{1g})$.

In the light of the above assignment for the transitions responsible for the bands E1 and E2, it is interesting to speculate on the absorption spectrum for the ytterbium monochalcogenides. Thin films of YbTe [37], which have the rocksalt structure, exhibit two sharp absorption peaks at 10 K superimposed on a broader less distinct background absorption (see figure 5.47). The peaks are separated by about 8527 cm^{-1} (1.06 eV) and their centre lies at about 20111 cm^{-1}. The underlying spectrum has features in common with the $4f^{13}5d$ absorption spectrum of Yb^{2+} while the intense pair of absorption bands resemble the $4f^{13}s(A_{1g})$ absorption spectrum. The $4f^{13}s(A_{1g})$ spectrum is shifted considerably in energy with respect to the $4f^{13}5d$ absorption. The shift is toward lower energy and is entirely consistent with the increase in covalency expected for the chalcogenides. The large increase in transition strength with increasing covalency is similarly

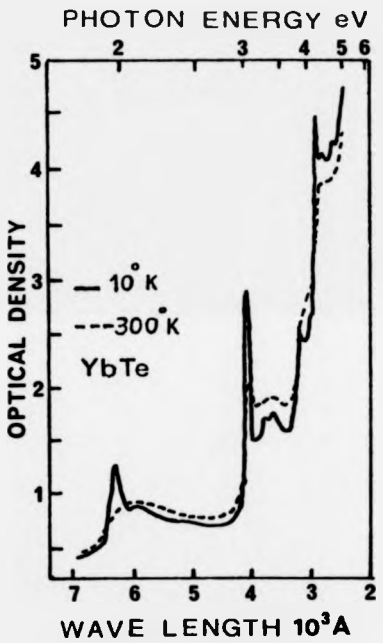

Figure 5.47 The optical absorption spectrum of YbTe at 10 K and 300 K (after Suryanarayanan et al [37]).

expected.

A similar situation is observed for thin films of YbSe [38], although in this case the corresponding absorption band pair is less prominent. This result is based on observations made on films of YbTe and YbSe of equal thicknesses [39]. The separation between the two bands is also greater in the latter case at about 9654 cm^{-1} (1.2 eV), which is much closer to the free ion $4f^{13}$ spin-orbit splitting. The differences are consistent with the fact that the selenides are less covalent than the tellurides. In addition, it is expected that the higher-lying normally-unoccupied (n+1)s levels will be closer energetically to the Yb^{2+} 6s level in the tellurides than in the selenides. If this trend is continued for YbS and YbO ($Te^{2-} - Se^{2-} - S^{2-} - O^{2-}$) then it is anticipated that the pair of bands will be very weak or even undetectable. They are certainly absent from the spectra reported to date [40,41].

Further evidence for the above absorption band assignments in the ytterbium chalcogenides is the occurrence of photoconductivity in the vicinity of the lower energy band of the $4f^{13}e(A_{1g})$ system [40,42]. The excited electron is relatively weakly bound and is only poorly localised, consequently, it may be fairly easily released into the conduction band. The photoresponse is found to be about three orders of magnitude less for YbSe than for YbTe [42]. Since the photoresponse is likely to be strongly dependent on the absorption coefficient of the photosensitive bands, then the difference is consistent with the optical absorption spectra results described earlier.

5.7 Some remarks on the optical absorption spectrum of Yb^{2+} in $SrCl_2$

The optical absorption spectrum of Yb^{2+} in $SrCl_2$ has been obtained by Piper et al [4]. It is reproduced in figure 5.48. In their paper the authors describe the spectrum as being due to transitions of the type $4f^{14} - 4f^{13}5d$.

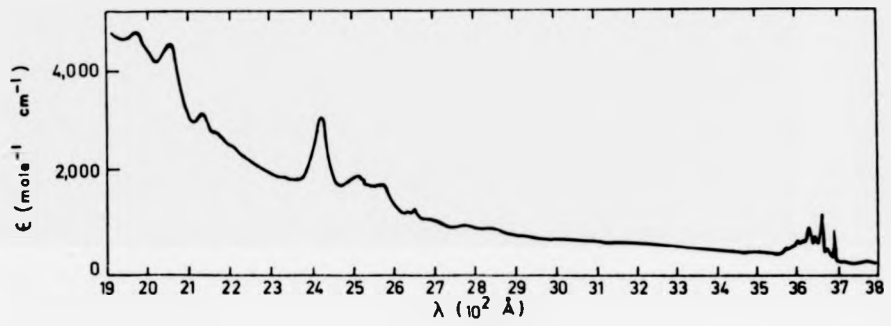

Figure 5.48 The optical absorption spectrum of Yb^{2+} in $SrCl_2$ at 4.2 K (after Piper et al [4]).

A theoretical calculation was presented and follows similar lines to that presented here, although they chose to use the earlier less elegant atomic structure calculation methods derived by Condon and Shortly [2]. The agreement between theory and experiment was not entirely accurate but was nevertheless sufficiently good to enable them to make their assignment.

Loh [43] has reconsidered the origins of the spectrum given in figure 5.48 based on an earlier analysis of the spectrum of Yb^{2+} in CaF_2 [29]. The four absorption bands observed for Yb^{2+} in CaF_2 were described as being constructed from the two components of a crystal-field-split 5d electron (e_g and t_{2g}) each coupled to the two spin-orbit split $4f^{13}$ core states ($^2F_{7/2}$ and $^2F_{5/2}$). In the later paper on $SrCl_2$:Yb^{2+} [43] he attempted to demonstrate that the seemingly complicated spectrum of figure 5.48 could still be interpreted using the same basic model derived for CaF_2. For this purpose he devised a modified model consisting of three types of "isolated" Yb^{2+} ions and attempted to subdivide the spectrum into perturbed sets of four basic levels.

Just prior to publication of the paper by Loh [43], Weakliem [44] had occasion to comment briefly on the spectrum of Yb^{2+} in $SrCl_2$. He had just presented a quite detailed study of the $4f^{n}5d$ configuration of Eu^{2+} and had concluded that a significant reduction in the values for the free ion parameters was necessary to achieve good agreement between theory and experiment. This accords with observations made earlier in this chapter for the alkali halides containing Yb^{2+}. He suggested that improved agreement between theory and experiment for Yb^{2+} in $SrCl_2$ might be achieved on using reduced values for the electrostatic f-d parameters and a larger value of Dq. It was possible to test this hypothesis using the computer program developed earlier for the alkali halides with the result that a much improved fit was obtained between the theoretical and experimental energy levels. The improved correlation is shown in figure 5.49. The value for Dq is altered significantly (from -800 cm^{-1} to -990 cm^{-1}), although only a slight correction

EXPERIMENTAL			THEORETICAL	
BAND	ENERGY	INTENSITY	ENERGY	INTENSITY
D2	50403	120	49877	91
			49632	4
D1	48575	440	48575	1014
			48137	86
C3	46649	110	46649	30
C2	41089	340	41087	728
			39611	1
C1	39749 38748	190	38878	258
			38705	68
			38226	17
B4	37625	10	37678	0
B3	37219	7	37371	4
			37107	0
B2	35028	15	35856	0
B1	29272	4	28740	3
			28098	26
			27855	23
A1	27262	100	27262	145

Figure 5.49 Precise theoretical and experimental energy level positions for Yb^{2+} in $SrCl_2$ illustrating improved agreement using reduced parameter values. Experimental values are taken from reference 4. Energy level positions are given in units of cm^{-1}. Theoretical intensities are equal to $(50a_1)^2$; experimental intensities are normalised to A1 = 100.

to the configurational energy Δ is neccesary (from 37971 cm^{-1} to 37919 cm^{-1}). The related nephelauxetic ratios are given by $\beta(F) = 0.572$, $\beta(B) = 0.633$ and $\beta(g) = 0.978$. Alig has also performed this calculation and has obtained a similar improvement in correlation between theory and experiment [45]. A value of $Dq = -1032\ cm^{-1}$ is obtained which is in good agreement with the value given above.

The need for reduced parameter values in the case of the alkaline earth halides implies that covalency effects are important in these crystals as well as in the alkali halides. For the alkaline earth fluorides the optical absorption spectra are well represented using the free ion values [5]. This is in agreement with the situation encountered earlier for the alkali fluorides. The agreement obtained between theory and experiment for the alkaline earth fluorides is in fact likely to be somewhat better than for the alkali fluorides, although in both cases covalency effects are negligible. This is because any discrepancies encountered for the alkali fluorides (and to a lesser extent for NaCl) which can be associated with a breakdown of the high symmetry crystal field approximation, will be completely absent for the alkaline earth fluorides where a true cubic symmetry is retained.

In conclusion, it would appear that the model proposed by Loh [43] is incorrect. The optical absorption spectrum of Yb^{2+} in $SrCl_2$ is in fact due to transitions of the type $4f^{14} - 4f^{13}5d$ in a cubic crystal field and is influenced by the nephelauxetic effect. The deviations caused by the nephelauxetic effect are expected to increase in the sequence $F^- - Cl^- - Br^- - I^-$. Unfortunately very little information exists on this system of crystals containing Yb^{2+}. Only the fluorides and $SrCl_2$ have been studied to date. Until a systematic study of this system is performed, it is impossible to substantiate this latter claim.

5.8 Conclusions

When ytterbium is diffused into crystals of KI, NaI, KBr, NaBr, KCl, NaCl and KF at high temperatures it enters the lattice in a doubly ionised state. It is found to reside on a substitutional cation site in association with a cation vacancy situated along the <110> direction for charge neutrality. The associated optical absorption spectra arise primarily from allowed transitions within the Yb^{2+} ion of the type $4f^{14} - 4f^{13}5d$. The agreement between experiment and a theory developed for a Yb^{2+} ion in an octahedral crystal field is excellent provided that a correction based on the relative covalency (polarisability) of the anion constituent is included. This correction increases in the sequence $F^- - Cl^- - Br^- - I^-$ and takes the form of a reduction, by up to 50%, in the values for the free ion parameters. These reductions are attributed to the nephelauxetic effect. In crystals of KF and NaCl containing Yb^{2+} some additional structure is observed in a number of the absorption bands. This additional structure is attributed to a breakdown in the assumption of an octahedral crystal field due to increases in the second order crystal field terms as the lattice parameter decreases.

When ytterbium is diffused into LiF and NaF at high temperatures it enters the lattice in a doubly ionised state. In this case, however, it resides initially on a site of cubic symmetry. Optical absorption transitions are still of the type $4f^{14} - 4f^{13}5d$ and excellent agreement is obtained between experiment and theory provided that a cubic crystal field model is used. On annealing NaF:Yb^{2+} at an elevated temperature, a new set of absorption bands appear and grow at the expense of the original set. The new spectrum is attributed to Yb^{2+} on a conventional substitutional cation site. Values that are obtained for the parameters Dq and Δ using the specially developed theoretical fitting procedure are in good agreement with extrapolated values obtained under the assumption of linear dependencies for these parameters with alkali halide lattice

parameter. A model is proposed whereby Yb^{2+} initially enters the crystal in the form of a separate phase of YbF_2. Quenching of the crystal from the diffusion temperature to room temperature effectively freezes in this cubic phase. Subsequent annealing causes the separate YbF_2 phase to dissociate to a certain extent with the Yb^{2+} ions moving onto conventional substitutional cation sites.

Two distinct and closely parallel linear dependencies, one for the potassium halides and the other for the sodium halides, are observed when the parameter Δ (the energy difference between the centre of energy of the excited $4f^{13}5d$ configuration and the $4f^{14}$ ground state) is plotted against the lattice parameter. The near equality of Δ within a pair is attributed to the degree of covalence between the Yb^{2+} ion and the surrounding anions. Similar linear dependencies with lattice parameter are observed for Dq but without the equality of parameter value. There is evidence to suggest that closely comparable dependencies exist for the alkaline earth halides.

In addition to the $4f^{13}5d$ absorption bands there is a pair of sharp absorption bands present in the spectra obtained for the alkali iodides, bromides and chlorides. These bands are associated with the Yb^{2+} ion and are assigned to transitions of the type $4f^{14} - 4f^{13}s(A_{1g})$. The excited state configuration $4f^{13}s(A_{1g})$ consists of an s-like ($s(A_{1g})$) bonding orbital coupled to the $4f^{13}$ core. The bonding orbital, along with the associated antibonding orbital at higher energy, occurs via an overlapping of the 6s orbital of the Yb^{2+} ion with a s-orbital formed from a linear combination of s orbitals on the surrounding octahedral anion complex. The transition intensity depends on the degree of overlap which, in turn, is related to the degree of covalency. The intensity increases according to the familiar sequence $Cl^- - Br^- - I^-$.

As a proposal for further study an interesting system is likely to be the silver halides containing Yb^{2+}. Of particular interest in this

system is the higher overall degree of covalency of the host crystals as compared to the alkali halides. As a result the E bands are expected to be quite prominent. One intrinsic drawback, however, is that the optical band edge in these crystals occurs at an energy of around 3.0 eV (approximately 24000 cm^{-1}) [46,47]. A large proportion of the absorption bands will therefore be masked by the very strong valence band to conduction band transitions. An additional problem arises since the absorption edge is not sharply defined as it is in the alkali halides but possesses an absorption tail to long wavelengths. This tail is a direct consequence of phonon-assisted band gap transitions due to the indirect band gap structure possessed by the silver halides. Cooling of the sample will be important since this action would not only reduce the long wavelength absorption tail but also shift the band edge to higher energy. Nevertheless, it is quite possible that the increased degree of covalency could lead to a sizeable depression in the energy of the $4f^{13}5d$ and $4f^{13}6(A_{1g})$ configurations. A shift in this direction would place them increasingly into a region of normal optical transparancy. The possibilty of photoconductivity via illumination into the E bands is also noted.

5.9 References

1. J.Hernandez A. et al, Journal of Physical Society Japan, 50, p225 (1981)

2. E.U.Condon and G.H.Shortly, "The Theory of Atomic Spectra", Cambridge University Press (1935)

3. B.W.Bryant, Journal of Optical Society America, 55, p771 (1965)

4. T.S.Piper et al, Journal of Chemical Physics, 46, p1353 (1967)

5. M.V.Eremin, Optical Spectroscopy, 29, p53 (1970)

6. M.V.Eremin, Optical Spectroscopy, 26, p317 (1969)

7. Z.J.Kiss, Physical Review A, 137, p1749 (1965)

8. H.A.Weakliem and Z.J.Kiss, Physical Review, 157, p277 (1967)

9. M.J.Weber and R.W.Bierig, Physical Review A, 134, p1492 (1964)

10. W.Low, Physical Review A, 134, p1479 (1964)

11. N.S.Altshuler et al, Soviet Physics Solid State, 7, p2023 (1966)

12. E.S.Sabisky and C.H.Anderson, Physical Review, 148, p194 (1966)

13. T.Tsuboi et al, Journal of Luminescence, 24/25, p305 (1981)

14. D.L.Dexter, Physical Review, 101, p48 (1956)

15. J.Hernandez A. et al, Journal of Chemical Physics, 72, p198 (1980)

16. C.K.Jørgensen, Progress in Inorganic Chemistry, 4, p73 (1962)

17. C.K.Jørgensen, Solid State Physics, 13, p375 (1962)

18. C.E.Schaffer and C.K.Jorgensen, Journal of Inorganic Nuclear Chemistry, 8, p143 (1958)

19. D.S.McClure, Solid State Physics, 9, p399 (1959)

20. R.C.Alig, Journal of Chemical Physics, 59, p5837 (1973)

21. E.Y.Wong and I.Richman, Journal of Chemical Physics, 36, p1889 (1962) [note also Errata, Journal of Chemical Physics, 37, p2498 (1962)]

22. E.Y.Wong et al, Journal of Chemical Physics, 39, p786 (1963)

23. R.D.McLaughlin and J.G.Conway, Journal of Chemical Physics, 38, p1037 (1963)

24. I.Richman and E.Y.Wong, Journal of Chemical Physics, 37, p2270 (1962)

25. E.Kh.Ivoilova and A.M.Leushin, Soviet Physics Solid State, 22, p601 (1980)

26. R.C.Weast Editor, "CRC Handbook of Chemistry and Physics", 62nd Edition, CRC Press Inc., Florida (1981-1982)

27. A.A.Kaplyanskii and P.P.Feofilov, Optics and Spectroscopy, 13, p129 (1962)

28. P.P.Feofilov, Optics and Spectroscopy, 1, p992 (1956)

29. E.Loh, Physical Review, 184, p348 (1969)

30. F.A.Kröger, "The Chemistry of Imperfect Crystals", 2, 2nd Edition, North Holland Publishing Co., Amsterdam (1974)

31. J.N.P.Hume and M.F.Crawford, Physical Review, 84, p486 (1951)

32. R.E.Trees, Physical Review, 83, p756 (1951)

33. R.F.Bacher, Physical Review, 43, p264 (1933)

34. K.Rajnak and B.G.Wybourne, Journal of Chemical Physics, 41, p565 (1964)

35. S.Asano, Journal of Physics C, 12, p4081 (1979)

36. S.Asano and Y.Nakao, Journal of Physics C, 12, p4095 (1979)

37. R.Suryanarayanan et al, Physical Review B, 9, p554 (1974)

38. R.Suryanarayanan and C.Paparoditis, Solid State Communications, 8, p1853 (1970)

39. C.C.Wong and C.Wood, Physics Letters, 34A, p125 (1971)

40. L.N.Glurdzhidze et al, Soviet Physics Solid State, 22, p388 (1980)

41. B.M.Angelov, Journal of Physics C, 13, pL433 (1980)

42. Z.Hurych et al, Physics Letters, 34A, p291 (1971)

43. E.Loh, Physical Review B, 7, p1846 (1973)

44. H.A.Weakliem, Physical Review B, 6, p2743 (1972)

45. R.C.Alig, RCA Review, 36, p125 (1975)

46. M.Cardona, Physical Review, 129, p69 (1963)

47. F.C.Brown, "The Physics of Solids", W.A.Benjamin Inc., N.Y. (1967)

COMMENT ADDED IN PROOF

The explanation given at the beginning of the chapter to justify the use of an octahedral crystal field ignores the possibility of an electrostatic deformation of the anion sub-lattice. Deviations of the effective charges of the divalent impurity and the cation vacancy over the host crystal charges can result in strong additional electrostatic interactions. If these interactions are taken into account then it is expected that the anions will be attracted toward the effectively positively charged divalent impurity but repelled from the effectively negatively charged cation vacancy. The first of these two distortions has no effect on the octahedral symmetry of the anion sub-lattice. The second distortion results in a lowering of the symmetry toward C_{2v} and according to C.Ruiz-Mejia et al (Journal of Chemical Physics, 73, p60 (1980)) can account for a movement of the anions by between 5 to 10 % of the cation-anion separation. It should be noted that whereas the eigenfunctions are particularly sensitive to such perturbations, the eigenvalues are much less affected. Consequently the approximation of an octahedral crystal field will be valid for calculations of the energy level structure but is expected to lead to much less accurate transition strengths.

As a final note, the increase in structure within the optical absorption bands of Yb^{2+} in NaCl and KF was described in section 5.4.4 as being a direct result of the increasing influence of the cation vacancy as the lattice parameter decreased. The electrostatic distortion described above has been shown by Ruiz-Mejia et al to increase as the lattice parameter decreases and is therefore able to account qualitatively for these observations.

6. DIVALENT EUROPIUM

6.1 Introduction

The subject of divalent europium in the alkali halides and other crystalline hosts has attracted rather more interest than the corresponding situation for divalent ytterbium. This interest is due in part to the possibility of utilising the associated broadband optical absorption and luminescence characteristics in certain lasing applications. Utilisation of these properties could conceivably lead to a tunable laser operating in the near ultraviolet spectral region [1]. Also of interest is the use of Eu^{2+} as a phosphor [2-4]. For many of the proposed applications the alkali halides provide ideal host materials due to their broad spectral range of optical transparency.

Apart from the above interest in its optical properties, Eu^{2+} possesses another rather important property which has probably contributed more to its popularity for scientific study. Eu^{2+} is paramagnetic and gives rise to a rich and detailed ESR spectrum even at room temperature. A vast amount of data has been compiled on this subject with the Eu^{2+} ion present in numerous different host materials. The ESR spectrum has now been fully characterised for most of these host crystals, including the majority of the alkali halides. A great strength of this technique lies in its ability to identify with great precision the symmetry of the site occupied by the impurity ion. Evidence for the formation of complexes with other impurities or lattice defects is readily available.

Interest in the optical properties of Eu^{2+} in crystalline environments, and in particular the optical absorption spectrum, has developed despite the fact that theoretically it represents an enormously complicated system. The situation is so complex that a detailed treatment such as was presented in chapter 5 for Yb^{2+} becomes totally impractical. Transitions are of the type $4f^7 - 4f^6 5d$ and are in principle similar to the $4f^{14} - 4f^{13} 5d$ transitions

observed for Yb^{2+}. Information obtained from the Yb^{2+} study is therefore of direct relevance. This similarity will be exploited wherever possible in the following analysis in an attempt to achieve improved understanding of the Eu^{2+} optical absorption spectrum.

The limited information provided by a study of the optical absorption spectrum of the Eu^{2+} ion is balanced to a large extent by detailed information arising from its ESR spectrum. Despite the numerous similarities between the behaviour of europium and ytterbium, they nevertheless differ significantly in their magnetic properties. The Yb^{2+} ion is diamagnetic and does not exhibit ESR. Information obtained from an ESR study of the paramagnetic Eu^{2+} ion is consequently not only interesting in its own right but also of direct relevance to achieving a deeper understanding of the behaviour of Yb^{2+} in the same host crystals.

Three important aspects of Eu^{2+} in the alkali halides will be discussed in this chapter. Firstly, the optical absorption spectra is considered. This will consist of a description of the theoretical methods applicable to the free ion, including the effect of an octahedral crystal field, and will be followed by a presentation of the experimental results. Secondly, the ESR spectra will be described and analysed. The way in which such a study is capable of indicating the Eu^{2+} ion site symmetry will be emphasised. Finally, the effect of thermal aging on the optical and ESR spectra is described. Wherever possible similarities with the behaviour of the Yb^{2+} ion will be exploited.

6.2 The free ion spectrum of Eu^{2+}

Divalent europium possesses the electronic configuration $(Xe)4f^{7}5s^{2}5p^{6}$. The presence of 7 electrons in the 4f shell results in a formidable theoretical problem. The techniques derived in chapter 3 are only applicable to two electron configurations. Special techniques are required

to handle large numbers of equivalent electrons. These methods involve the use of tensor operators in the theory of continuous groups and incorporate the concept of fractional parentage [5,6]. They were not developed in the earlier chapter since, even with them, it would still be impractical to undertake a detailed theoretical description of the Eu^{2+} ion. Instead a simplified treatment is presented.

The ground state of Eu^{2+} consists of 119 Russel-Saunders terms [7] giving a total of 327 levels [8]. The lowest in energy is an s-like term. This situation is implied by the half-filled nature of the 4f shell. The complete term energy level structure is shown in figure 6.1. It should be noted that the lowest $^8S_{7/2}$ term is separated by about 28000 cm^{-1} from the next higher $^6P_{7/2}$ term [9]. Due to the size of the separation, the lowest term is often considered in isolation. The approximation depends on this lowest term being the only occupied level at normal temperatures.

The first excited state configuration of Eu^{2+} is the $4f^65d$. A thorough theoretical treatment of this configuration involves the calculation of direct and exchange electrostatic interactions for a set of six indistinguishable 4f electrons with a solitary 5d electron. In total there are 2725 levels [8]. Such a large number of levels prohibits an "exact" calculation since it would involve the solution of a matrix of order 2725. Some manner of approximation is required.

In the previous chapter the $4f^{13}$ configuration of Yb^{2+} was considered to be basically equivalent to a $4f^1$ configuration. This situation was also expressed as being represented by a single hole in a filled 4f shell. Such an approach circumvented the problems associated with describing the interaction of 13 indistinguishable electrons. In an analagous way the $4f^6$ configuration may be considered as a single hole in a half-filled $4f^7$ shell. The latter approximation is considerably less accurate but it does allow the $4f^65d$ configuration to be treated more straightforwardly as a two electron system. Restrictions on the

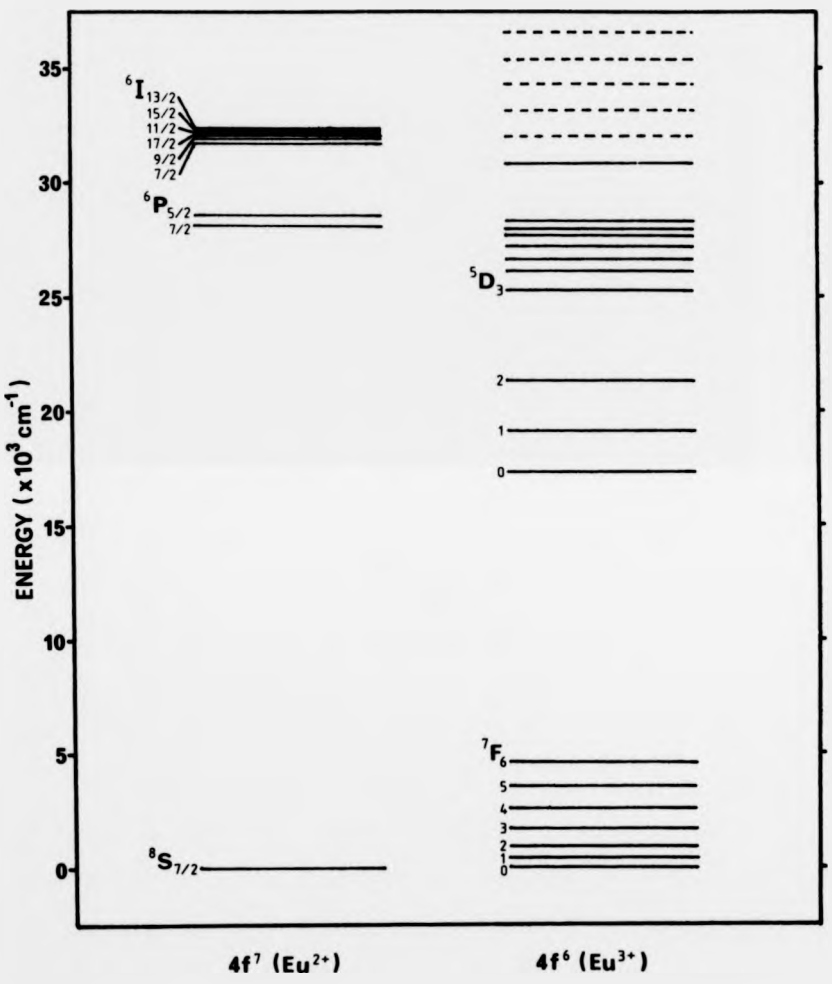

Figure 6.1 The lower energy levels of the $4f^7$ and $4f^6$ configurations of the europium ion [4,9].

electrostatic exchange interaction matrix elements are more involved in this case [10]. The above method has been used by Sugar and Spector [9] to achieve a reasonable fit to the free ion levels.

The approximation described above is equivalent to considering only the core term ^7F_J of the $4f^6$ configuration. The total angular momentum J takes values in the range 0 to 6 corresponding to L = 3 and S = 3. The next term in the energy level structure (see figure 6.1) lies about 17500 cm^{-1} higher. By analogy with the approximation made earlier for the $4f^7$ configuration it appears reasonable to neglect all higher terms. Even allowing for the simplifications described, the $4f^65d$ configuration still consists of a total of 57 levels. These arise from 10 Russel-Saunders terms, namely $^{6,8}H$, $^{6,8}G$, $^{6,8}F$, $^{6,8}D$ and $^{6,8}P$.

It should be noted that all spin-orbit effects have been neglected in the above analysis. For the well confined $4f^7$ ground state this omission is justified. For the excited state configurations the justification is not so obvious. In general, as progressively higher excited state configurations are considered the LS-coupling scheme becomes increasingly vague. Spin-orbit effects begin to dominate and a jj-coupling scheme is required. As the rare earth ions become heavier, the point of transition occurs earlier. For Yb^{2+} this situation is already applicable to the lowest excited state configuration. For Eu^{2+} the lowest-lying excited state configuration still retains a dominant LS-character.

6.3 The optical absorption spectrum of Eu^{2+} in an octahedral crystal field

The extreme complexity of the complete theoretical treatment will become apparent in this section. Consider the way in which the 57 free ion levels decompose under the influence of a high symmetry octahedral crystal field. For the Dq matrix alone it is easily shown that the 57x57 matrix

decomposes into a 40x40 Γ_6 matrix, a 41x41 Γ_7 matrix and a 81x81 Γ_8 matrix. Unfortunately group theory is unable to assist in reducing the complexity of the calculation. The ground state ($^8S_{7/2}$) transforms according to $\Gamma_6 \oplus \Gamma_7 \oplus \Gamma_8$ implying that transitions are allowed to excited states formed from a combination of all three such double valued representations. The B_4^4 and B_6^4 matrices are of equivalent complexity.

The theoretical treatment depends on the calculation of an extremely large number of matrix elements even allowing for the simplifications described earlier. The calculation will not be attempted here and it is debatable whether it is ever likely to be attempted in the present form. It may be possible with the aid of additional simplifications to achieve some form of approximate solution. The question of whether or not such approximations are possible will be considered following a study of the experimental results. The next section describes the optical absorption spectra obtained for Eu^{2+} in a broad range of alkali halide crystals. It is hoped that by using a broad range of basically similar but subtley different crystalline hosts it might be possible to uncover the existence of any simplifying trends.

6.4 The optical absorption spectrum of Eu^{2+} in the alkali halides

6.4.1 Introduction

A large amount of work has been performed to date on the optical absorption spectrum of Eu^{2+} in various crystalline hosts. Most of the work concerns the alkaline earth halides [11,12] but other crystals have been studied including the perovskites such as $RbMgF_3$ [1] and $KMgF_3$ [13,14]. Numerous studies have also been performed on the alkali halides. The optical absorption spectrum of Eu^{2+} in most of the crystals in this category has already been reported [15-19]. The only notable exception is KF.

The study presented here, although essentially running in parallel with the studies referenced above, is justified for the following reasons. All of the above studies describe samples which have been prepared by crystal growth from an europium doped melt. Normally either the Kyropoulos, Czochralski or Bridgman-Stockberger methods were employed. The present work concerns specimens prepared via vapour phase diffusion of europium at elevated temperatures. It is the first time that a study has been undertaken using crystals prepared using this technique. A comparison of the spectra obtained for Eu^{2+}-doped alkali halide crystals prepared by these two fundamentally different methods should prove interesting. In addition, the optical absorption spectrum of $KF:Eu^{2+}$ will be described for the first time.

6.4.2 Experimental results

The optical absorption spectra of europium in KI, NaI, KBr, NaBr, KCl, NaCl, KF and NaF obtained at both RT and LNT are shown in figures 6.2 to 6.9. The spectra are essentially identical to those described in previous studies on melt grown europium-doped crystals (see references contained in previous section). For $KF:Eu^{2+}$, the spectrum is reported for the first time. In all cases the familiar two broad bands are observed confirming that the europium ion is present in the divalent state. Both of the broad bands show significant structure. The fine structure becomes more apparant at LNT and is particularly prominent for the alkali iodides. The large number of partially resolved absorption bands serves to illustrate the complexity of the crystal field energy level structure. Unfortunately, the lack of detailed resolution precluded any attempt at a thorough theoretical analysis such as was presented for Yb^{2+}.

Based on a simplistic approach, the two broad bands may be attributed to the splitting of the 5d electron level in the octahedral crystal field.

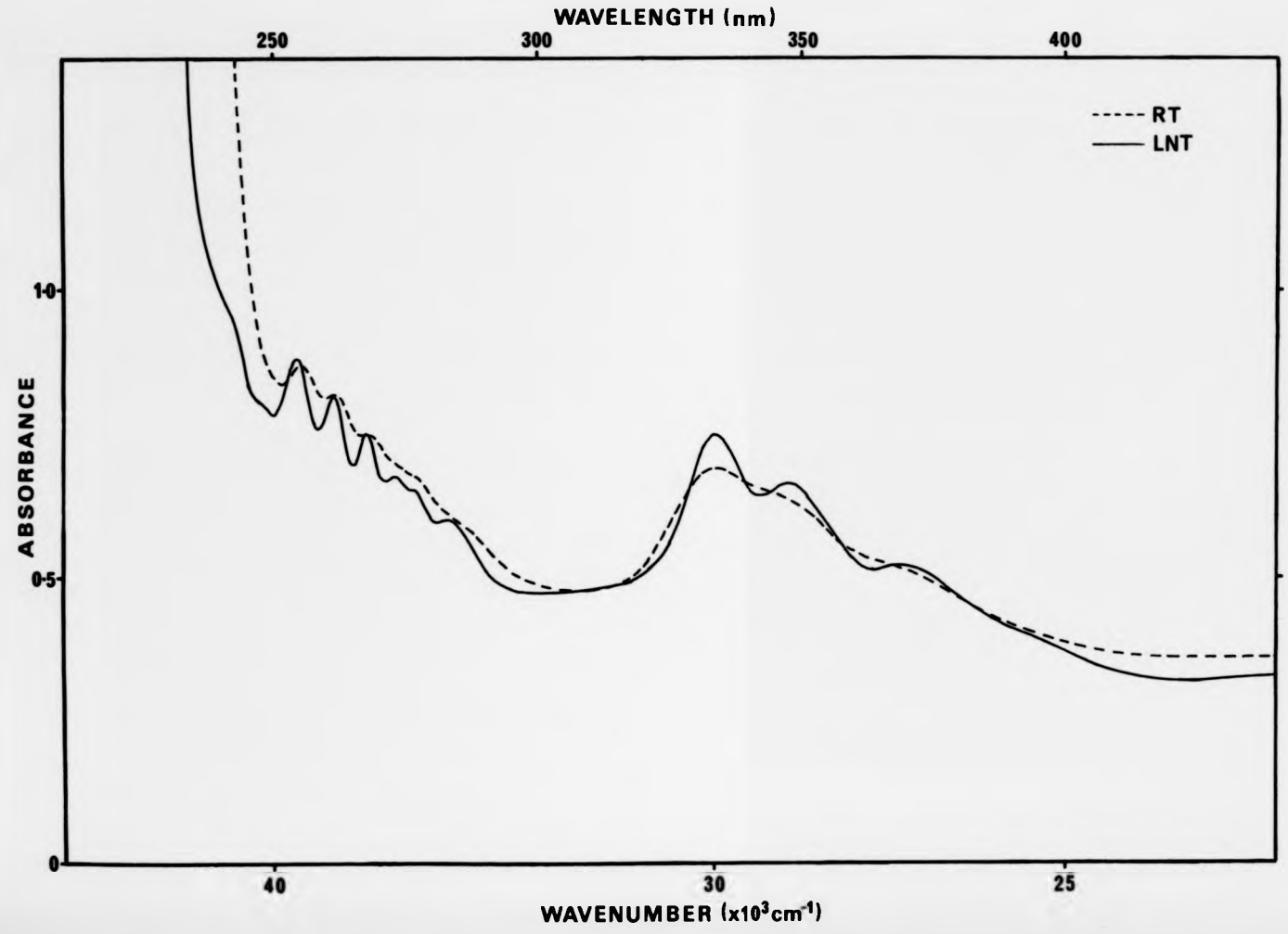

Figure 6.2 The optical absorption spectrum of Eu^{2+} in KI at RT and LNT.

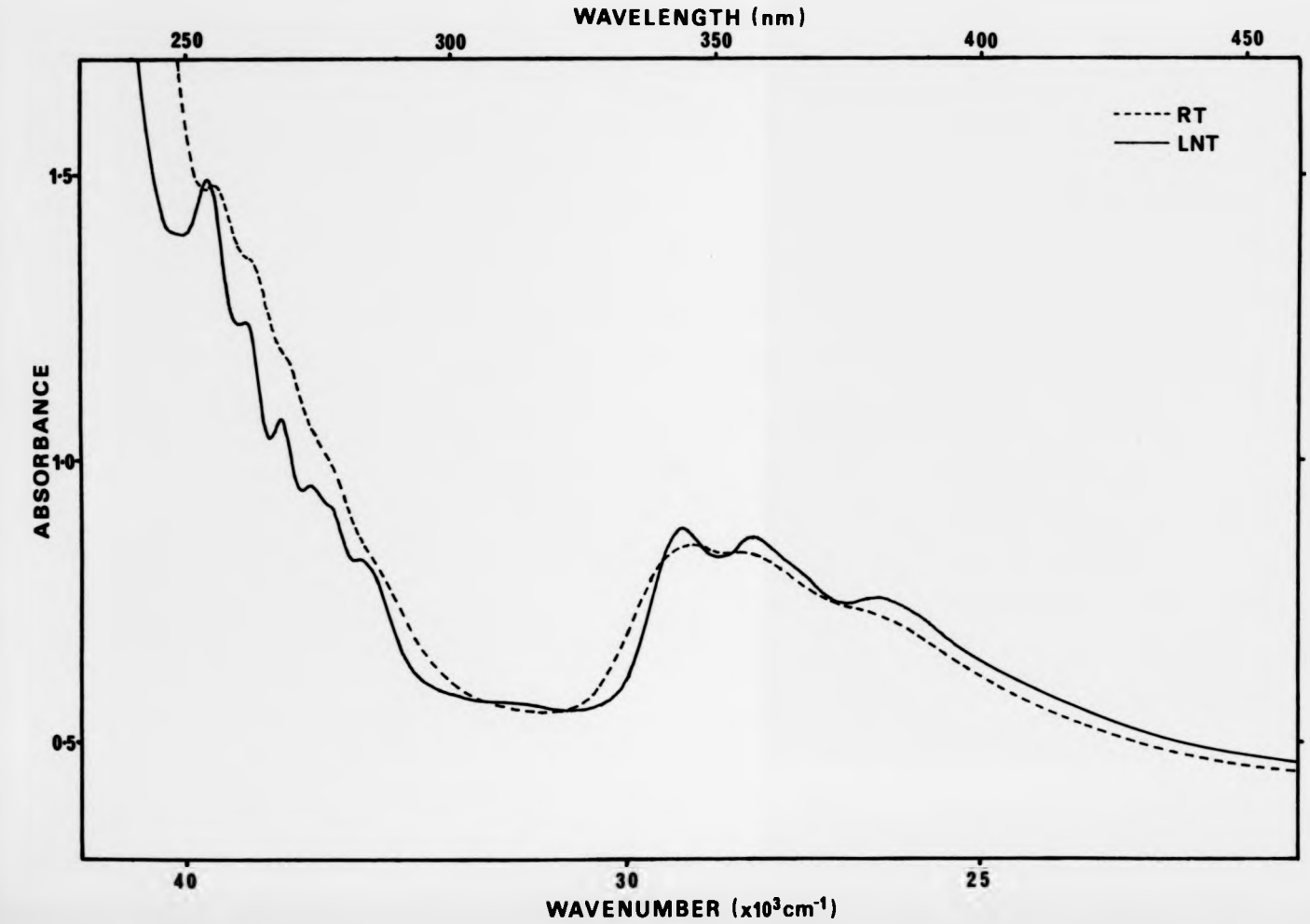

Figure 6.3 The optical absorption spectrum of Eu^{2+} in NaI at RT and LNT.

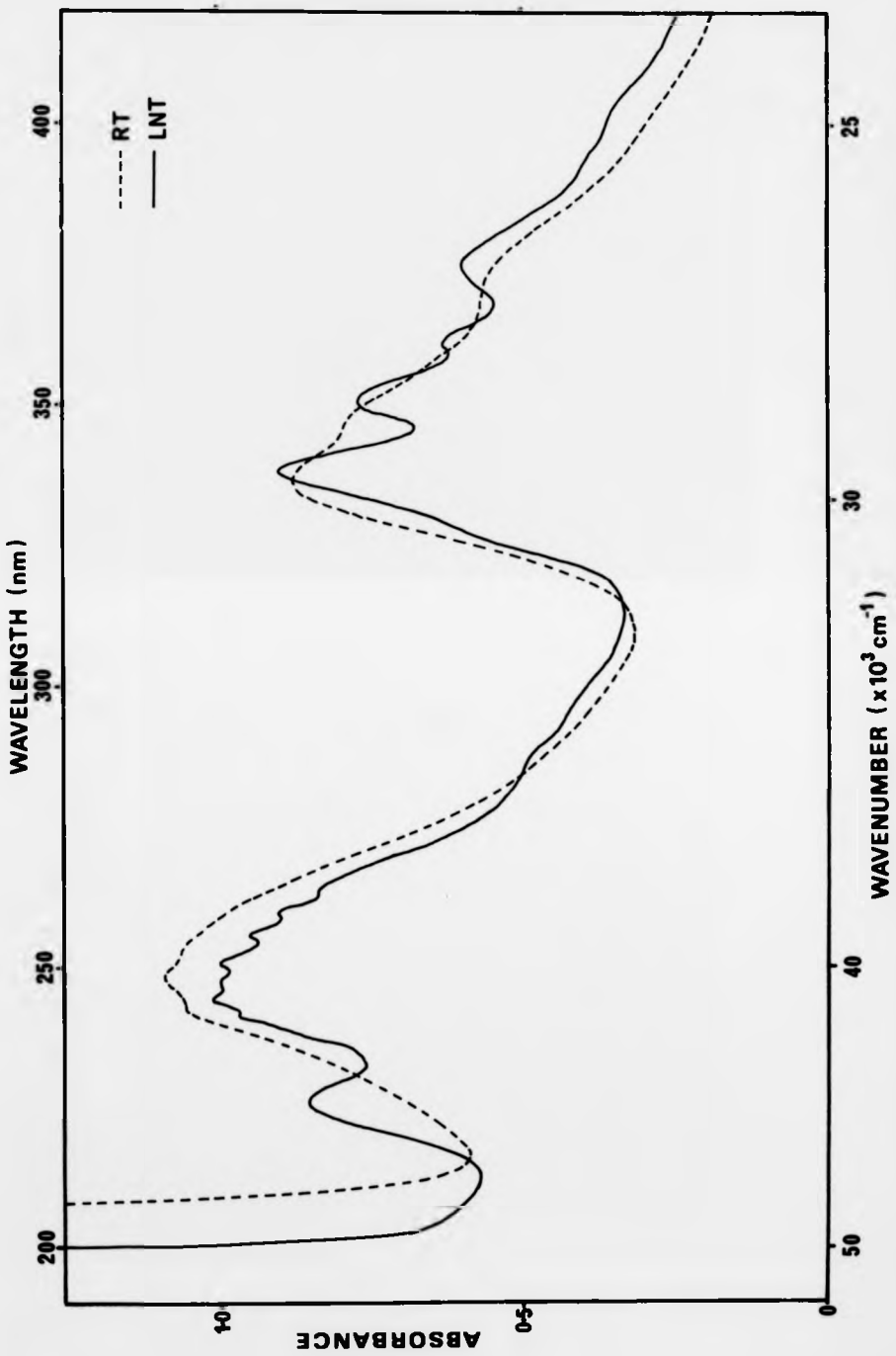

Figure 6.4 The optical absorption spectrum of Eu^{2+} in KBr at RT and LNT.

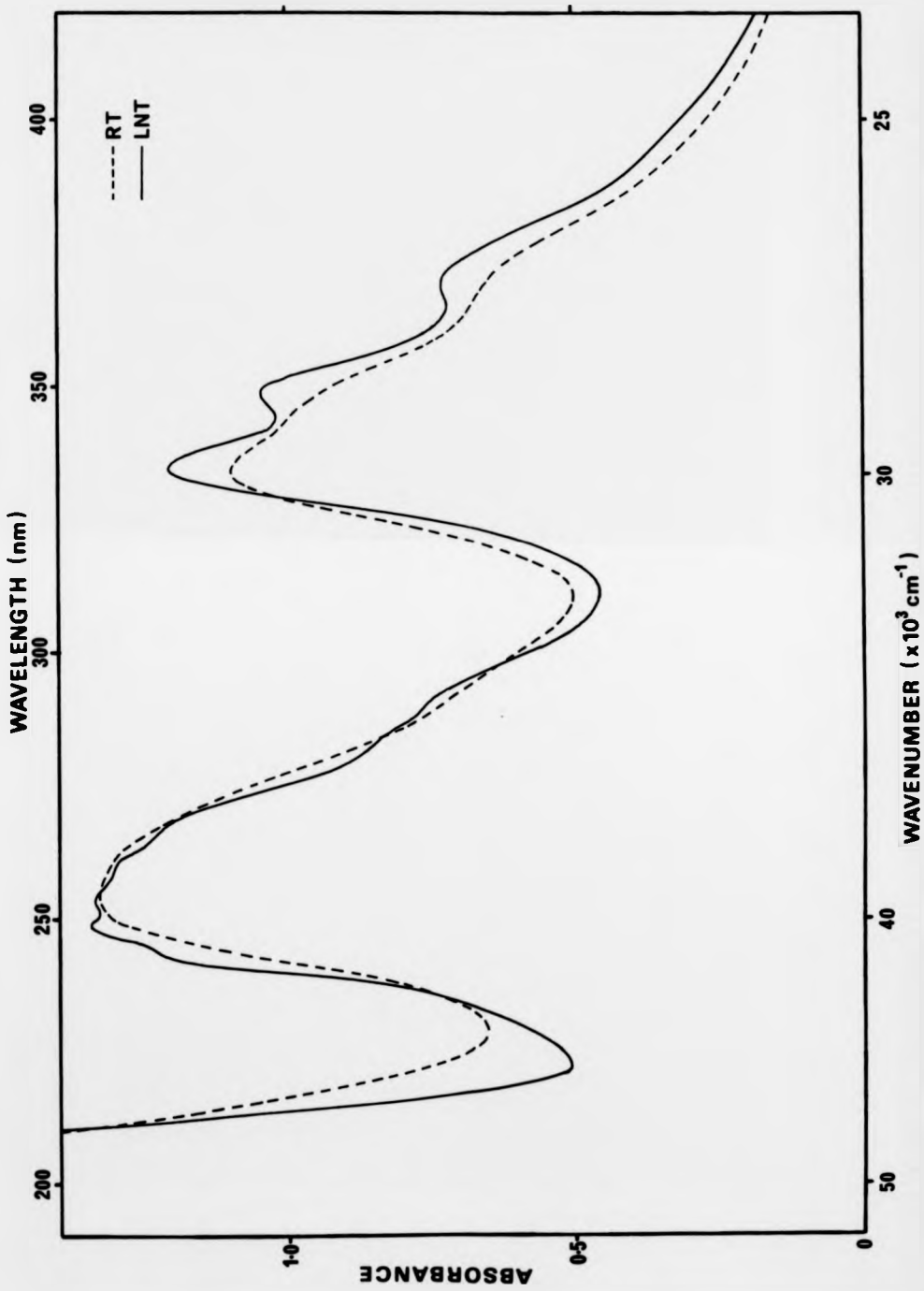

Figure 6.5 The optical absorption spectrum of Eu^{2+} in NaBr at RT and LNT.

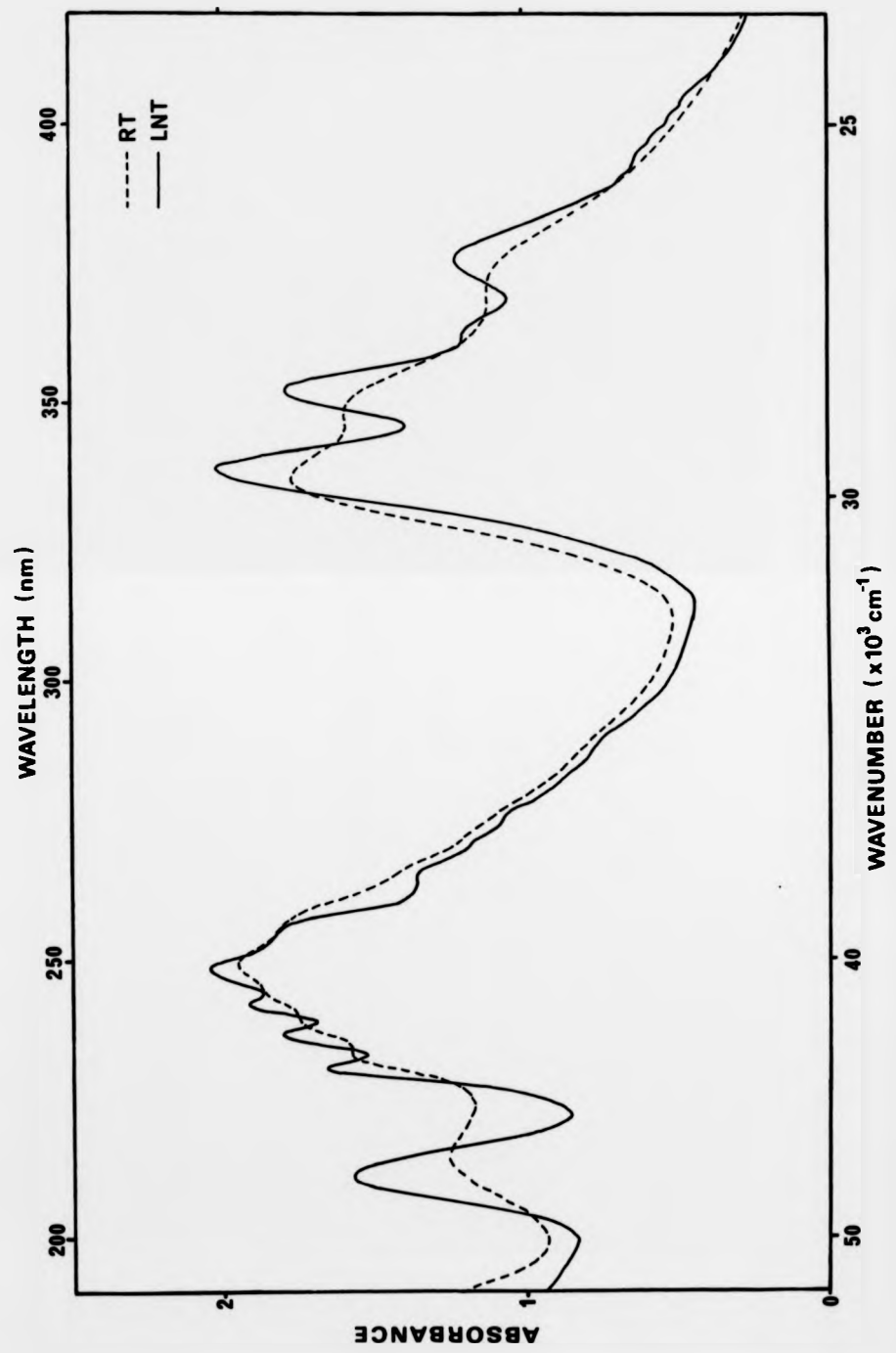

Figure 6.6 The optical absorption spectrum of Eu^{2+} in KCl at RT and LNT.

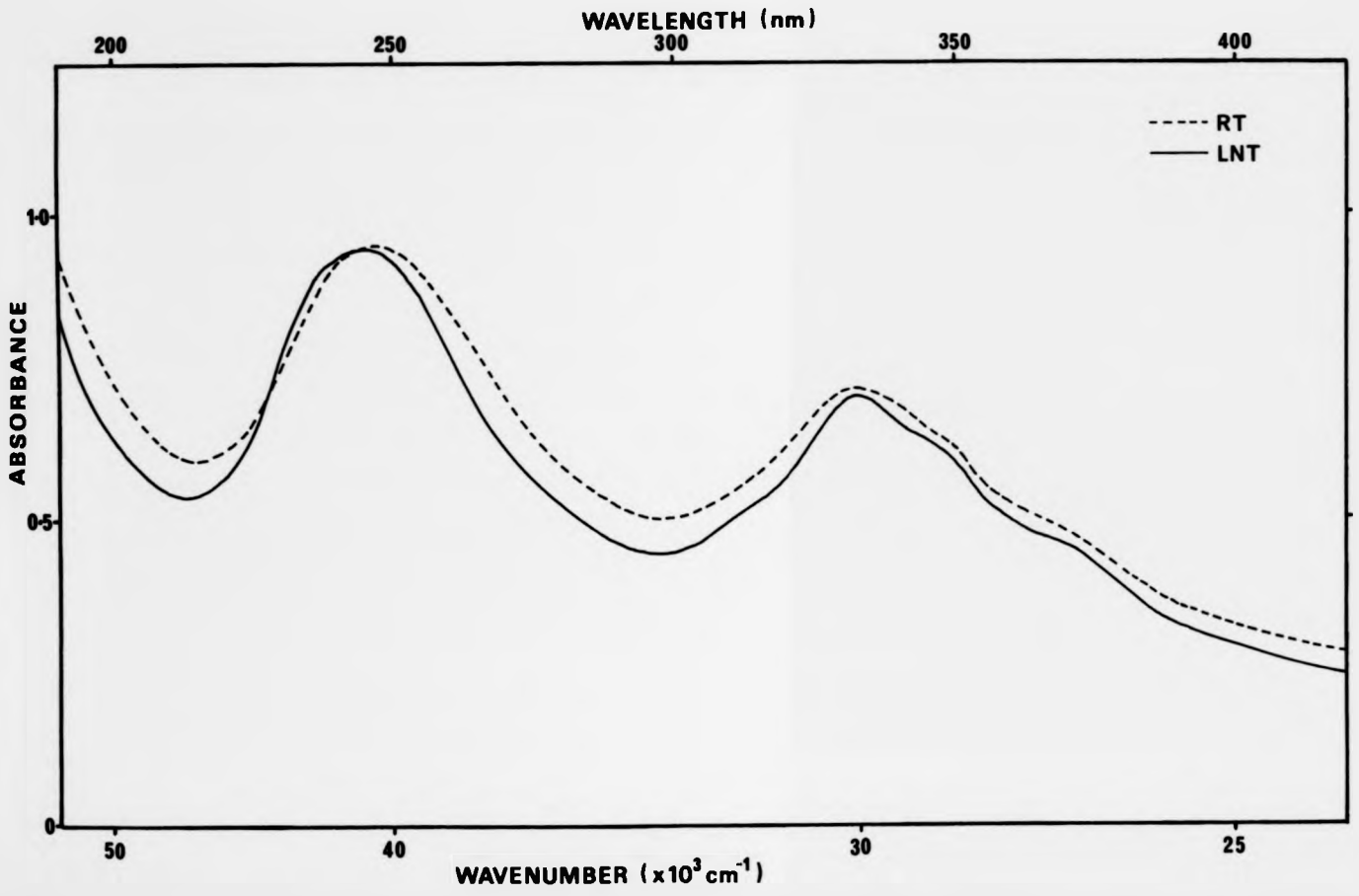

Figure 6.7 The optical absorption spectrum of Eu^{2+} in NaCl at RT and LNT.

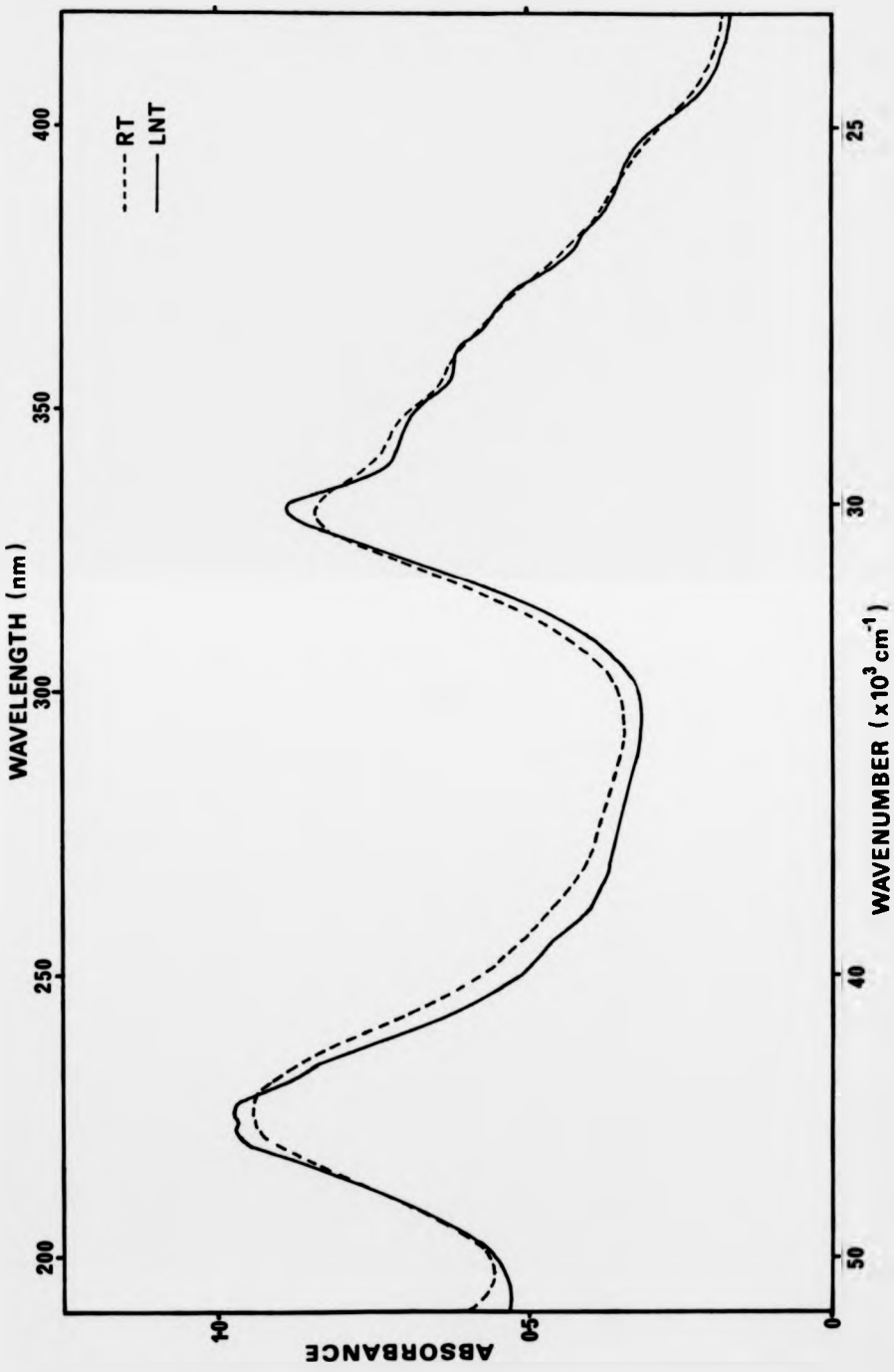

Figure 6.8 The optical absorption spectrum of Eu^{2+} in KF at RT and LNT.

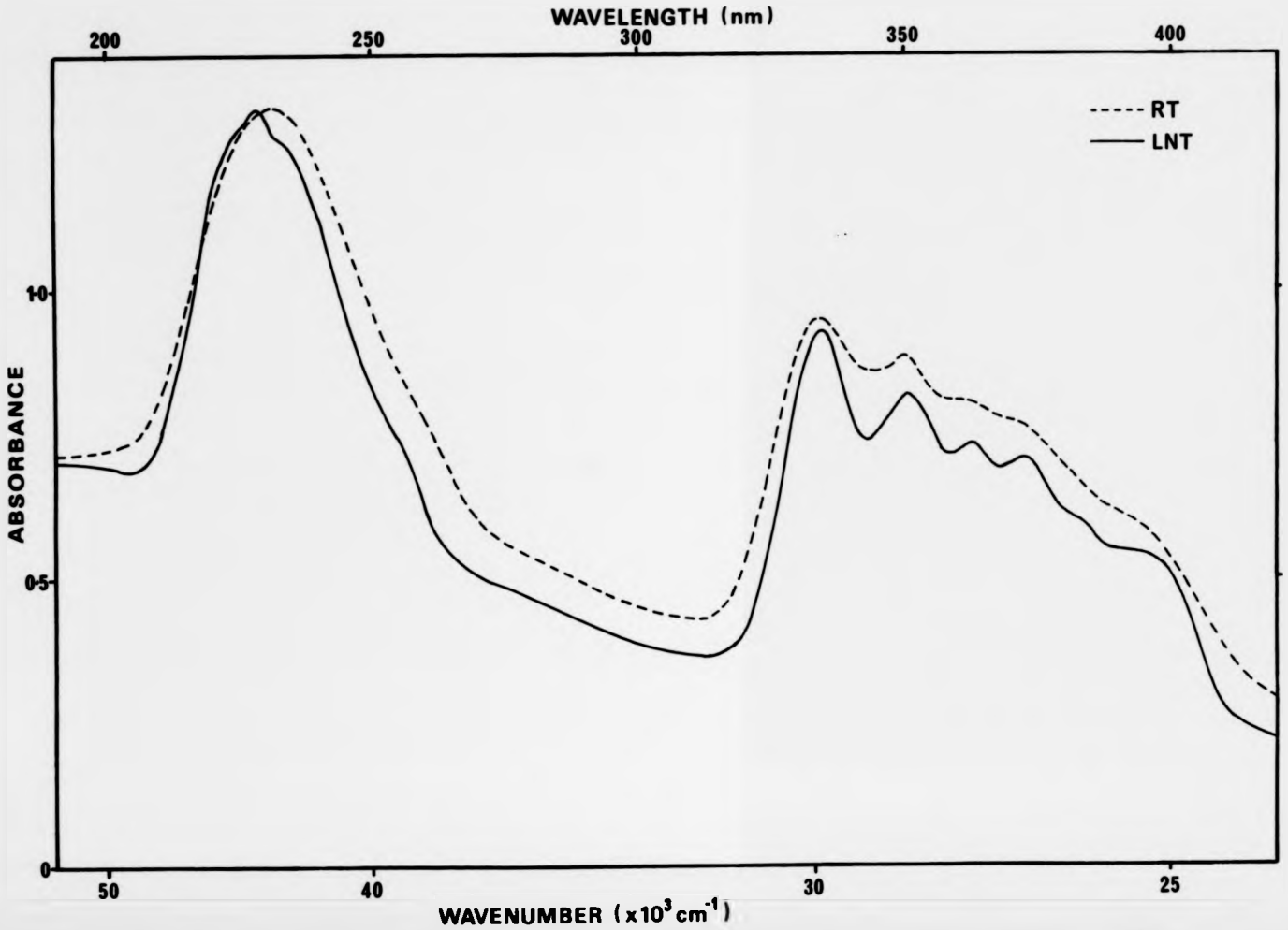

Figure 6.9 The optical absorption spectrum of Eu^{2+} in NaF at RT and LNT.

The additional structure is then accounted for by the coupling between this d-type state and the $4f^6$ core states. According to the approximations discussed earlier, this model corresponds to a 5d electron interacting with the ^7F_J core term. The situation is illustrated schematically in figure 6.10.

If one assumes that the simple model described above is applicable, then it should be possible to decompose each broad band into its six individual component bands. In general there is relatively good agreement with this model. This result is interesting in view of the findings of the previous chapter, where an entirely analagous model was considered for the $4f^{13}5d$ configuration of Yb^{2+}. The model in that instance predicted a total of four levels whereas in reality the total number of bands exceeded this number for all of the crystals studied. The difference between the two cases is attributed to the different relative magnitudes of the electrostatic and spin-orbit interactions. For divalent europium, the electrostatic interaction dominates for the low lying states and the spin-orbit contribution can be neglected. Furthermore, the large separation between the lower ^7F term and the next higher term results in a reasonably sound basis for the simple model. The situation for divalent ytterbium is more complex since a similar domination of the spin-orbit interaction over the electrostatic does not occur. Consequently both must be taken into account in this case and the simple model, which neglects the electrostatic term, is likely to be in error.

Consider further the parallel between the $4f^{13}5d$ configuration of Yb^{2+} and the $4f^6 5d$ configuration of Eu^{2+}. According to the detailed analysis, the final value obtained for the crystal field strength parameter Dq for the Yb^{2+} ion is not the same as that obtained by simply taking the energy separation between the two groups of absorption bands. It is a difficult matter to separate the bands into their individual 5d crystal field components and, even if this can be achieved, it is not easy to see how the centre of energy of each "pair" of bands is to be defined, let alone

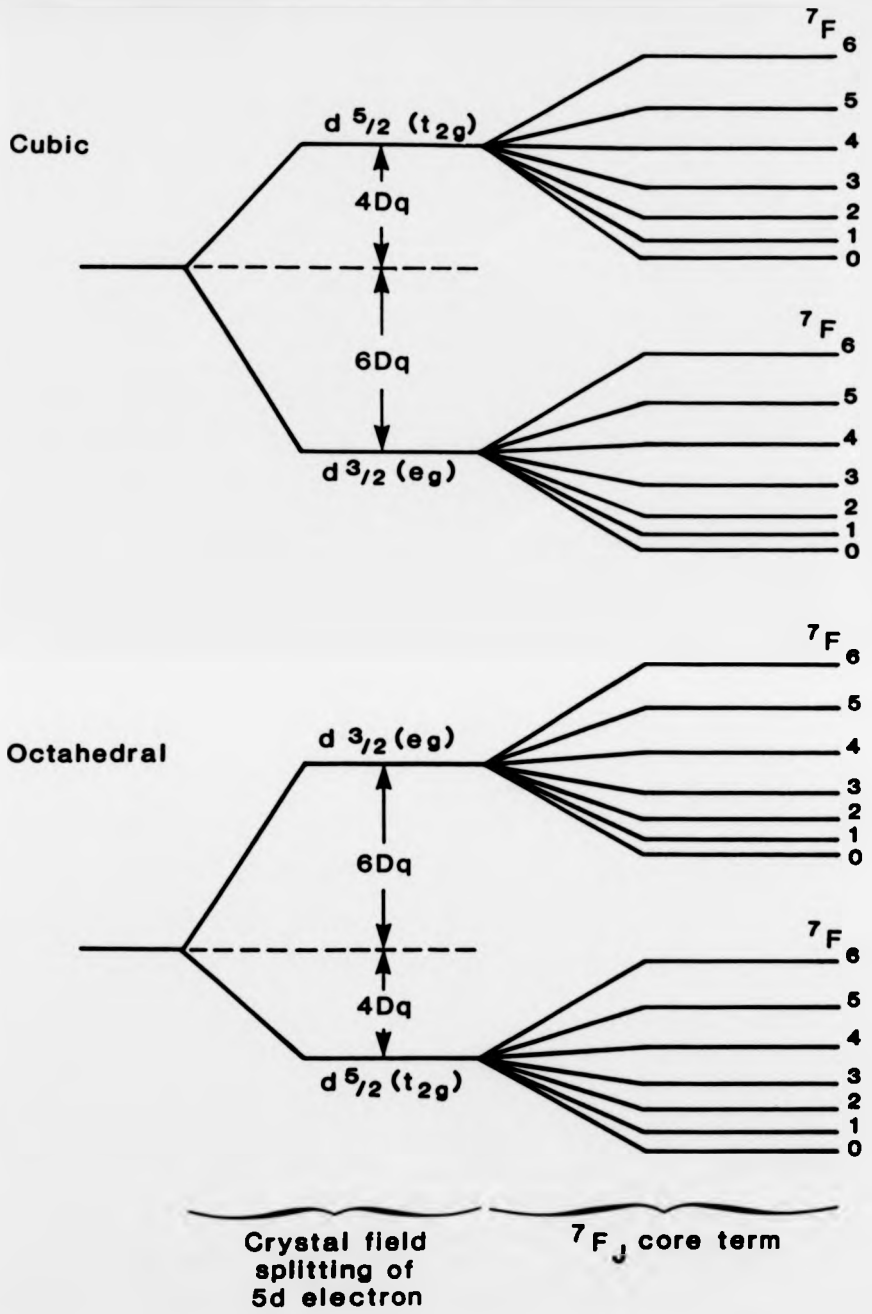

Fig.6.10 Schematic representation of the ^7F_J core levels of the $4f^6$ configuration coupled to a crystal field split 5d electron

measured to any degree of accuracy. The situation for the Eu^{2+} ion should be treated in a similar way. Consequently, although the numerous individual absorption bands separate into two broad structured bands, it is questionable as to whether Dq can be measured simply as the separation between the positions of peak absorption for each band. In making such an assumption proper account is not taken of the detailed nature of the complete optical absorption spectrum. All of the earlier studies of Eu^{2+} in the alkali halides make this assumption. A possible consequence of neglecting such considerations is an underestimation of Dq for the more covalent crystals such as KI and NaI. The reason for this is that nephelauxetic reductions in the electrostatic parameters are greater than for the spin-orbit parameters and therefore the relative importance of the spin-orbit term increases .

The fine structure observed in the Eu^{2+} optical absorption spectra is found to be rather sensitive to thermal treatment. A later section (section 6.6) will deal with this behaviour in some detail. In order to attempt an understanding of the relaxation processes involved, it proved extremely useful to characterise the Eu^{2+} impurity ion in terms of its ESR spectrum. This technique will be considered in more detail in the following section.

6.5 The electron spin resonance spectrum of Eu^{2+}

6.5.1 Introduction and basic theory

Divalent europium is paramagnetic due to an odd number of electrons in the 4f shell ($4f^7$). The ground state is described by the term $^8S_{7/2}$ and transforms according to the irreducible representation $D^{(7/2,+)}$ of the rotation-inversion group O(3). The free ion ground state level is 7-fold degenerate and the application of a lower symmetry perturbation will in principle lift this degeneracy. For example, under the influence of an

octahedral (O_h) symmetry perturbation, the ground state representation decomposes into a sum of double valued representations given by $\Gamma_{6g} \oplus \Gamma_{7g} \oplus \Gamma_{8g}$ (equation 3.72). Therefore introducing the Eu^{2+} ion into an octahedral/cubic crystal field splits the ground state level into three new levels. The mechanism involved in removing the degeneracy associated with a spherically symmetric atomic shell is less well understood. It has been suggested [20] that it is due to high-order perturbations involving simultaneously the crystal field and spin-orbit coupling. Spin-orbit effects are certainly not negligible for the rare earth ions. The ground state splitting is expected to be small because of the high-order nature of the perturbation involved.

The detailed nature of the relative splittings will depend intimately on the crystal field symmetry and magnitude. The ESR technique depends on further reducing the symmetry of the system via the application of a magnetic field. Most, if not all, of the remaining degeneracy may be lifted in this way. The additional splittings depend not only on the magnitude of the magnetic field but also on the orientation of the field with respect to the principal axes of the crystal. A correlation between the absorption energies for allowed transitions amongst the various energy levels and the orientation and strength of the magnetic field yields detailed information on the site symmetry of the paramagnetic impurity.

The magnetic field interaction described above is also known as the Zeeman interaction and the various transitions are termed the fine structure components. The number of fine structure components depends on the detailed manner in which the levels split. For example, a two-fold degenerate orbital (Kramers doublet) is split into two levels in a magnetic field. Consequently there can be at most only one transition. In general, for an ion of half integral spin S in an octahedral crystal field, there are a total of 2S fine structure components. For lower symmetry environments there will be in general a set of fine structure components

for each inequivalent symmetry axis. In addition to the fine structure there is a secondary interaction involving the nuclear spin angular momentum I. This is known as the hyperfine interaction and results in each of the 2S fine structure components being further split into (2I+1) hyperfine components.

In general it is necessary to cool the samples in order to resolve sufficiently the fine structure and hyperfine structure components. The linewidth of the absorption bands depends on the interaction between the paramagnetic ion and its surroundings. The principal interaction is usually the spin-lattice relaxation effect, where the ion spin system energy is transferred with a characteristic time constant τ_{s1} to the crystal lattice. Time constants range widely depending on the details of the interaction. A number of other broadening mechanisms may be operative, such as spin-spin relaxation (dipolar broadening), exchange interactions and even inhomogeneities in the crystal lattice and/or magnetic field. The first two of these latter interactions are only really of importance when the paramagnetic ion is present in high concentrations. Careful design of the electromagnet minimises the effects of inhomogeneous broadening.

In general τ_{s1} is small, resulting in significant broadening of the resonance lines at room temperature. In many cases this effect renders the spectrum so broad that it cannot be distinguished at all. For s-state ions such as Eu^{2+}, Gd^{3+}, Mn^{2+} and Pb^{2+}, the spin-lattice interaction is weak and consequently τ_{s1} is large. For these ions therefore the ESR spectrum is generally well resolved at room temperature.

6.5.2 A theoretical treatment of the ESR spectrum of Eu^{2+} in an octahedral crystal field

The Hamiltonian describing the interaction of an Eu^{2+} ion in an octahedral crystal field with an applied magnetic field $\underline{B}$ is given by

$$H = H_0 + H_1 + H_2 + H_3 + H_4 + H_5 \qquad 6.1$$

where $$H_4 = \beta \underline{B}.(\underline{L} + 2\underline{S}) \qquad 6.2$$

and $$H_5 = A\underline{I}.\underline{S} \qquad 6.3$$

where β is the Bohr magneton, A is the hyperfine structure constant and $\underline{I}$ is the nuclear spin. The terms H_1, H_2 and H_3 represent respectively the electrostatic, spin-orbit and crystal field interactions. The terms H_4 and H_5 are the Zeeman and hyperfine interactions respectively. Only the ground state of the ion is involved in the ESR spectrum and, as discussed earlier, LS-coupling is appropriate. As a result the term H_2 may be neglected. The crystal field and magnetic field interactions are both of similar magnitude but represent relatively small effects. The electrostatic interaction dominates and it is possible to consider the contributions H_3 and H_4 as first order perturbations with H_5 as a second order perturbation.

For most practical cases, the lowest occupied level is sufficiently removed in energy from the next higher level that the influence of that level may be neglected. It is now possible to equate the number of experimentally observed fine structure components to the multiplicity 2S' associated with an effective spin $\underline{S}'$. This is equivalent to representing the matrix elements of $\beta\underline{B}.(\underline{L} + 2\underline{S})$ by $g'\beta\underline{B}.\underline{S}'$ [6]. The symbol g' is a constant known as the spectroscopic splitting factor and depends on the detailed nature of the states involved [21]. The value of g' may differ considerably from the lande g-factor. Deviations from the orbital singlet spin-only value of g'

= 2.0023 are due to the admixture of higher lying states.

The above form for the Hamiltonian utilising the effective spin S' is known as the spin Hamiltonian H_s. The spin Hamiltonian is a convenient intermediate formulation connecting theory and experiment. For Eu^{2+} in an octahedral crystal field, the spin Hamiltonian takes the form

$$H_s = g\beta \underline{B}.\underline{S}' + B_4^0(O_4^0 + 5O_4^4) + B_6^0(O_6^0 - 21O_6^4) + A\underline{I}.\underline{S}' \qquad 6.4$$

where the spin operators O_k^q are basically equivalent to the crystal field parameters V_k^q.

Consider the case where the magnetic field is applied parallel to the <100> axis. For this particular orientation, the Hamiltonian is diagonal in both the Zeeman and hyperfine terms. The perturbation matrix for the crystal field plus Zeeman terms decomposes into a series of 2x2 matrices. A solution of these matrices yields eight energy levels, between which there are seven allowed transitions ($\Delta M_s = \pm 1$). These transitions are given to second order by [22]

$$\begin{aligned}
E(5/2,7/2) &= X + 20b_4^4 + 6b_6^4 - 40(b_4^4)^2/4X \\
E(3/2,5/2) &= X - 10b_4^4 - 14b_6^4 \\
E(1/2,5/2) &= X - 12b_4^4 + 14b_6^4 + 40(b_4^4)^2/4X \\
E(-1/2,1/2) &= X + 70(b_4^4 - 3b_6^4)^2/4X \\
E(-3/2,-1/2) &= X + 12b_4^4 - 14b_6^4 + 40(b_4^4)^2/4X \\
E(-5/2,-3/2) &= X + 10b_4^4 + 14b_6^4 \\
E(-7/2,-5/2) &= X - 20b_4^4 - 6b_6^4 - 40(b_4^4)^2/4X
\end{aligned} \qquad 6.5$$

where $X = g'\beta B$, $b_4^4 = 60B_4^4$ and $b_6^4 = 1260B_6^4$.

The second order terms are observed to introduce a little asymmetry. To first order, the spectrum is symmetrical about the 1/2 ↔ -1/2 transition with the relative intensity of each line given by 7:15:12:16:12:15:7 [23].

Each of the seven fine structure components are further split into (2I+1) hyperfine components. For europium there are two isotopes Eu^{151} (47.86%) and Eu^{153} (52.14%), both with I = 5/2. Therefore there will be two sets of six lines associated with each fine structure component corresponding to the two different isotopes. The separations between the individual absorption lines for each hyperfine set yield values for the parameters A^{151} and A^{153}. The A parameter is a sensitive indicator of the nature of the bonding between the impurity and its surroundings.

6.5.3 A theoretical treatment of the ESR spectrum of Eu^{2+} in an orthorhombic crystal field

It is well known that the true site symmetry for an Eu^{2+} ion in an alkali halide crystal is C_{2v}. The lowering of symmetry is attributed to the presence of a charge compensating cation vacancy along the <110> direction [24]. The spin Hamiltonian for a crystal field of orthorhombic symmetry is given by

$$H_s = g\beta \underline{B}.\underline{S}' + B_2^0 O_2^0 + B_2^2 O_2^2 + B_4^0 O_4^0 + B_4^2 O_4^2 + B_4^4 O_4^4 + B_4^{-2} O_4^{-2} + B_4^{-4} O_4^{-4} + \underline{A}\underline{I}.\underline{S}' \qquad 6.6$$

In general there are six inequivalent positions for the <110> vacancy about the Eu^{2+} ion resulting in a maximum of six sets of fine structure lines. When the magnetic field is applied parallel to the <100> direction, there are two sets of equivalent orientations. One set corresponds to $\theta = 90°$ (two components) and the other set corresponds to $\theta = 45°$ (four components), where θ is the angle between the symmetry axis of the crystal (direction of the orthorhombic crystal field) and the direction of the applied magnetic field. The corresponding spectrum is therefore expected to consist of two sets of seven fine structure lines each of which is

further split into its twelve (2(2I+1)) hyperfine components.

When the magnetic field is applied parallel to the <110> direction, there are three sets of equivalent orientations; $\theta = 0°$ (one component), $\theta = 90°$ (one component) and $\theta = 60°$ (four components). The spectrum in this case will consist of three sets of seven fine structure lines. If the magnetic field is rotated between the two extreme orientations of $\underline{B}$ parallel to the <100> and <110> directions, then a smooth variation between the different sets of spectra is observed. The detailed behaviour of the individual fine structure components with variations in the magnetic field orientation is a characteristic of the site symmetry of the impurity ion.

When the magnetic field is parallel to the <100> direction the spectrum is at its simplest. For this orientation, the spectrum becomes symmetrical and attains its maximum magnetic field spread. This is equivalent to stating that only the first four crystal field terms in the spin Hamiltonian (equation 6.6) are required to describe the resulting spectrum (the off-diagonal terms are small). The allowed transitions are to first order given by [25]

$$\begin{aligned}
E(5/2,7/2) &= X - 6b_2^0 - 20b_4^0 - 6b_4^4 \\
E(3/2,5/2) &= X - 4b_2^0 + 10b_4^0 + 14b_4^4 \\
E(1/2,3/2) &= X - 2b_2^0 + 12b_4^0 - 14b_4^4 \\
E(-1/2,1/2) &= X \\
E(-3/2,-1/2) &= X + 2b_2^0 - 12b_4^0 + 14b_4^4 \\
E(-5/2,-3/2) &= X + 4b_2^0 - 10b_4^0 - 14b_4^4 \\
E(-7/2,-5/2) &= X + 6b_2^0 + 20b_4^0 + 6b_4^4
\end{aligned} \qquad 6.7$$

The fine structure components are shown schematically in figure 6.11. The separations between individual fine structure components (as defined in figure 6.11) can be easily determined. They are given by

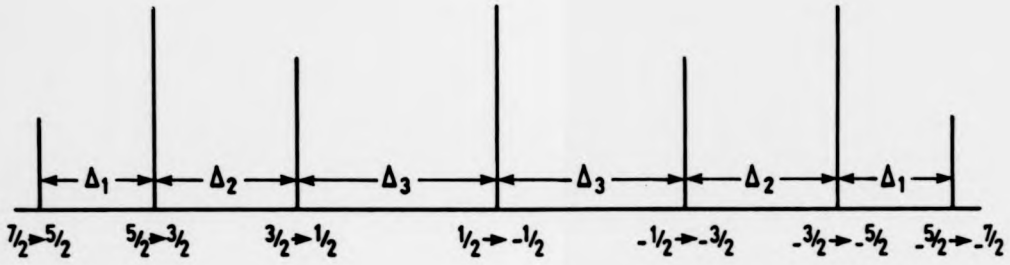

Fig.6.11 A schematic representation of the major first order ESR fine structure components for the Eu^{2+} in an orthorhombic crystal field. The magnetic field is parallel to the ⟨100⟩ direction. The height of each line represents its relative intensity.

$$\Delta_1 = 2b_2^2 + 30b_4^2 + 20b_6^2 \qquad 6.8$$

$$\Delta_2 = 2b_2^2 + 2b_4^2 - 28b_6^2 \qquad 6.9$$

$$\Delta_3 = 2b_2^2 - 12b_4^2 + 14b_6^2 \qquad 6.10$$

The orthorhombic symmetry case described above is most generally encountered for divalent ions in the alkali halides. In principle there is another possible arrangement with the cation vacancy situated on a next nearest site along the <100> direction. The symmetry in this case is tetragonal (C_{4v}). The ESR spectra can be used to distinguish between these two cases.

When the magnetic field is applied parallel to the <100> direction, for the tetragonal case, there are two sets of equivalent orientations. One set corresponds to $\theta = 0°$ (two components) and the other set corresponds to $\theta = 90°$ (four components). When the magnetic field is applied parallel to the <110> direction there are still only two sets of equivalent orientations; $\theta = 45°$ (four components) and $\theta = 90°$ (two components). In theory it is possible to distinguish between tetragonal and orthorhombic symmetries by observing the <110> spectrum since in the orthorhombic case there are three sets of equivalent orientations ($\theta = 0°$, 90° and 60°). However, in practice the 60° component is broadened beyond recognition [26] and therefore only two sets of fine structure lines appear for both cases. In order to distinguish between the two cases it is necessary to investigate the behaviour of the fine structure components as the magnetic field is rotated between the <100> and <110> directions. The tetragonal case is characterised by the presence of an angularly invariant component corresponding to $\theta = 90°$; no such component exists for the orthorhombic case.

6.5.4 The ESR spectrum of Eu^{2+} in the alkali halides

The ESR spectra obtained for Eu^{2+} in KI, NaI, KBr, NaBr, KCl, NaCl and KF are shown in figures 6.12 to 6.18 respectively. No ESR was observed for Eu^{2+} in NaF. All spectra were obtained at room temperature with the magnetic field parallel to the <100> axis of the crystal. With the exception of KF:Eu^{2+}, the spectra are in excellent agreement with those already presented by other workers [26-31]. For comparison the ESR spectrum obtained by Aguilar S. et al [27] for NaCl:Eu^{2+} is included in figure 6.19. The only noticeable difference is the occurrence of a broad underlying resonance around g = 2 in the present work. A similar resonance is observed for a number of the crystals studied. The intensity of this broad resonance is not fixed in relation to the basic fine line Eu^{2+} spectrum and is therefore not due to dispersed substitutional Eu^{2+} ions.

Figure 6.20 shows the angular variation of the major fine structure components for the Eu^{2+} spectrum in KCl. The magnetic field was rotated in the (100) plane. The behavior of the various components is typical of that expected for an orthorhombic symmetry due to a cation vacancy situated along the <110> direction [31]. No angularly invariant components were discovered, thus ruling out the possibility of tetragonal symmetry.

Only one other study of KF:Eu^{2+} has been presented to date [32]. The ESR spectrum described in this reference is reproduced in figure 6.21. It can be easily seen that there is no obvious correlation between this figure and the spectrum obtained in the present work (figure 6.18). The line structure is considerably more complex and rather different in form to that expected for the more typical substitutional Eu^{2+} case. The simple analysis presented below will provide evidence to suggest that the spectrum obtained in the present work represents the true spectrum expected for a substitutional Eu^{2+} ion associated with a <110> vacancy.

The excellent agreement between the spectra presented in figures 6.12

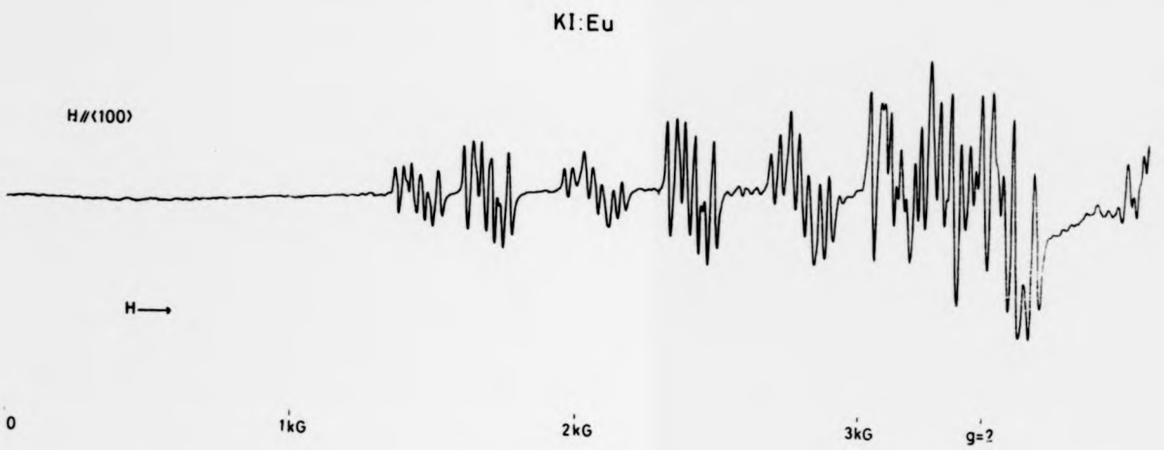

Fig. 6.12 The ESR spectrum of Eu^{2+} in KI at RT. The magnetic field is applied parallel to the <100> axis.

Fig. 6.13 The ESR spectrum of Eu^{2+} in NaI at RT. The magnetic field is applied parallel to the <100> axis.

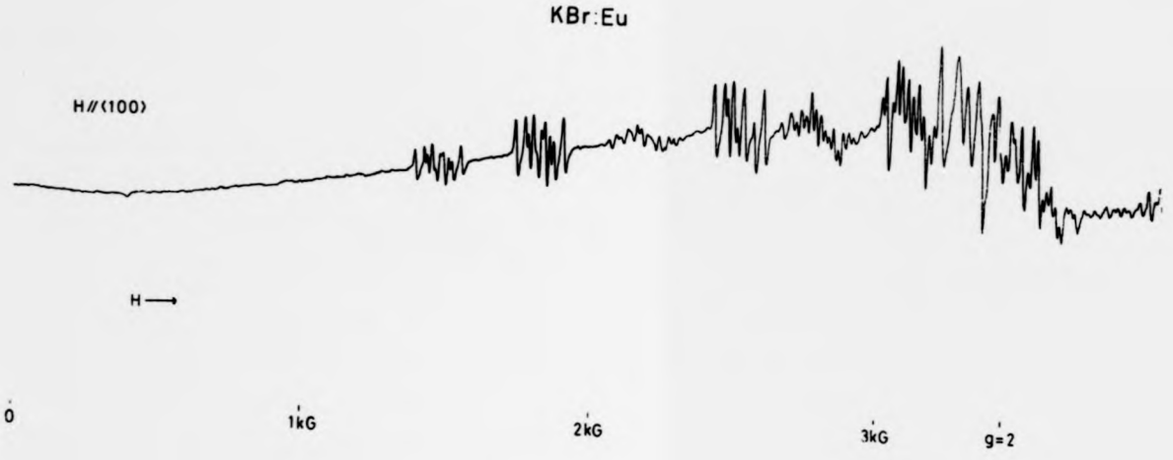

Fig. 6.14 The ESR spectrum of Eu^{2+} in KBr at RT. The magnetic field is applied parallel to the <100> axis.

Fig. 6.15 The ESR spectrum of Eu^{2+} in NaBr at RT. The magnetic field is applied parallel to the <100> axis.

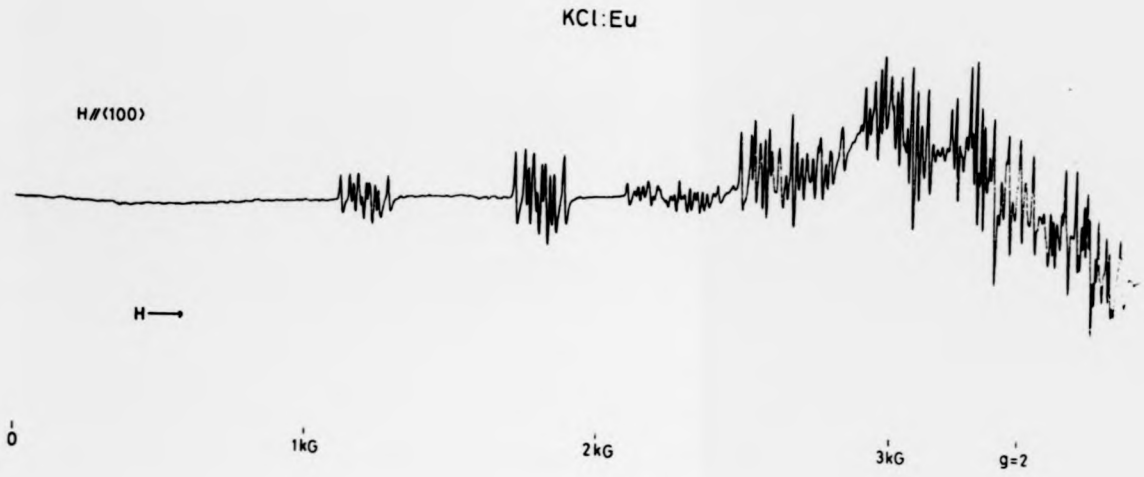

Fig. 6.16 The ESR spectrum of Eu^{2+} in KCl at RT. The magnetic field is applied parallel to the <100> axis.

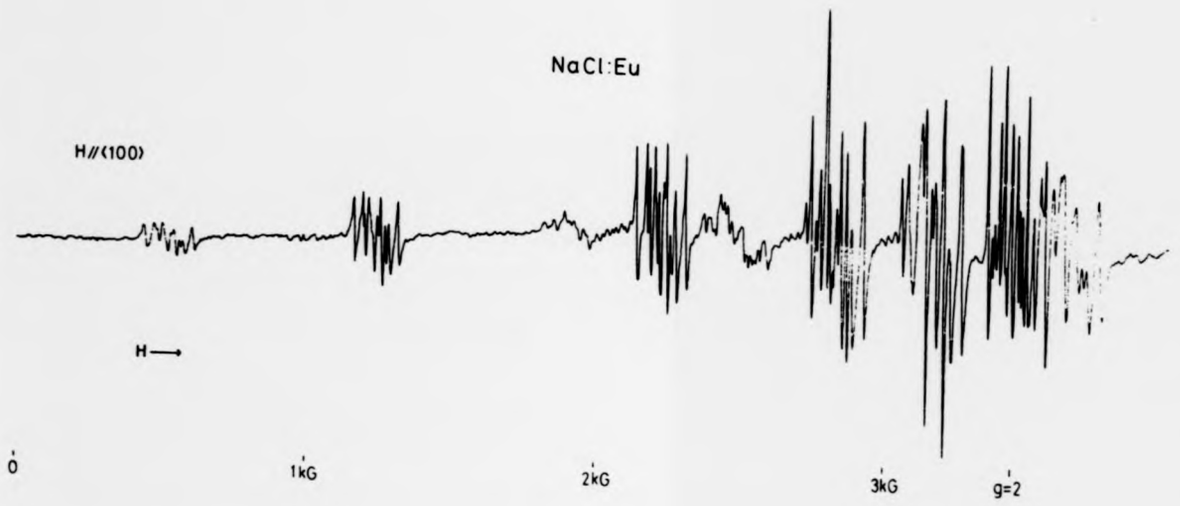

Fig 6.17 The ESR spectrum of Eu^{2+} in NaCl at RT. The magnetic field is applied parallel to the <100> axis.

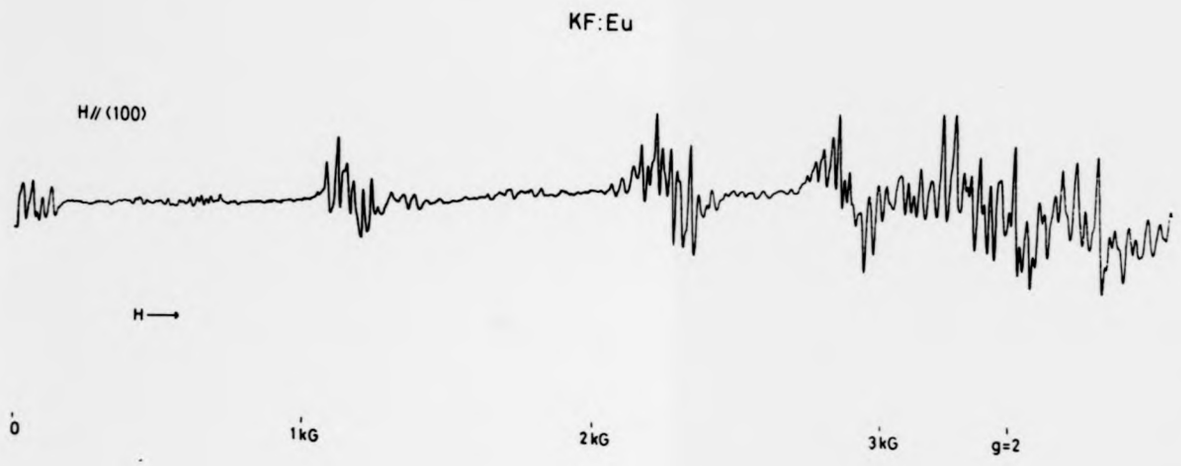

Fig. 6.18 The ESR spectrum of Eu^{2+} in KF at RT. The magnetic field is applied parallel to the <100> axis.

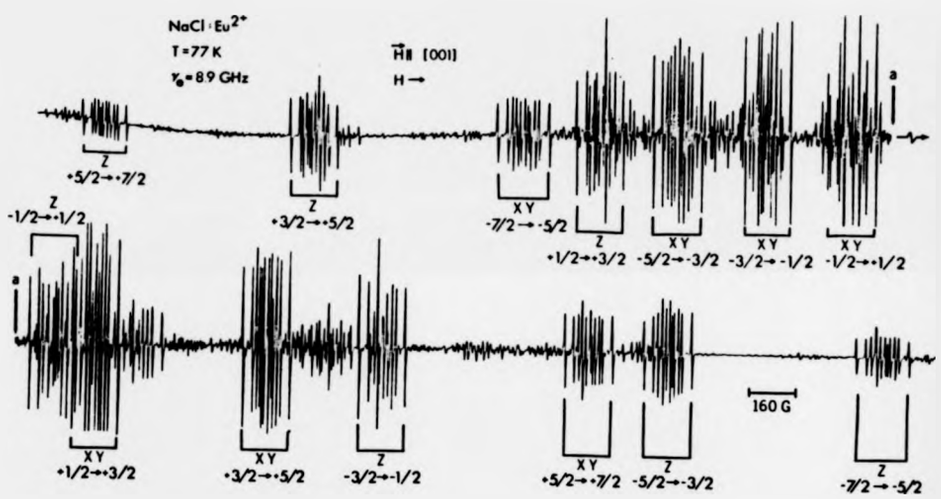

Figure 6.19 The ESR spectrum of Eu^{2+} in NaCl at 77 K, as obtained by Aguilar S et al [26].

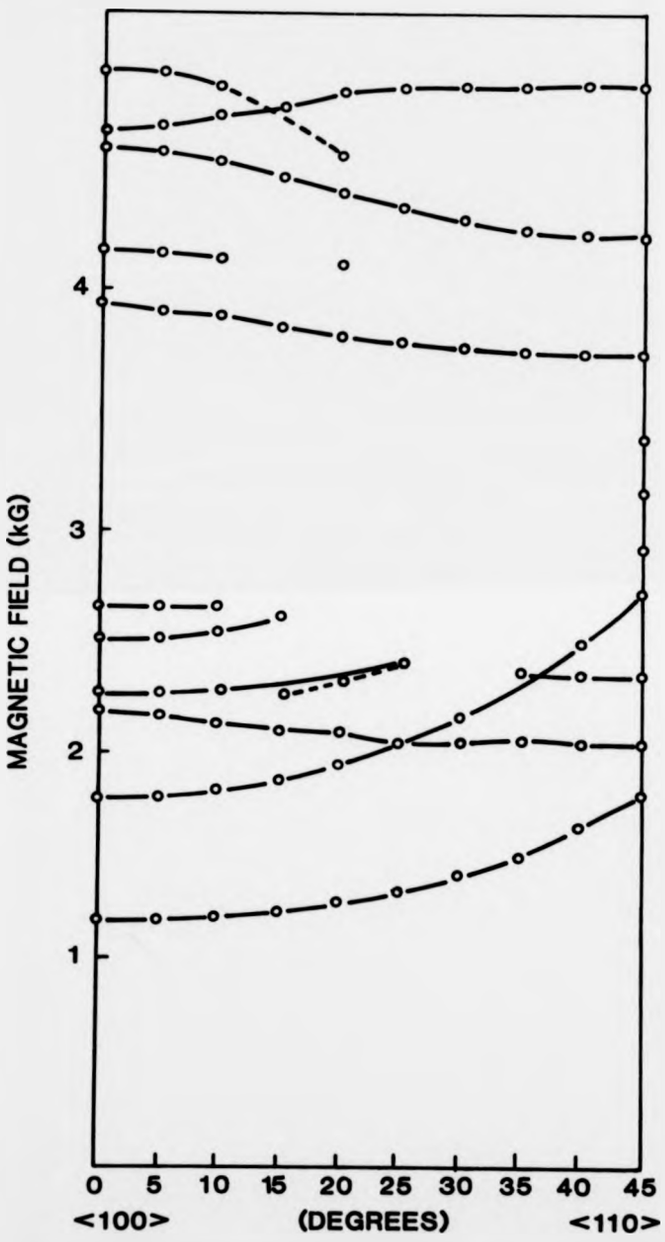

Fig. 6.20 Angular variation of the major fine structure components for the ESR spectrum of Eu^{2+} in KCl. The magnetic field has been rotated in the {100}plane

Figure 6.21 Low field part of the ESR spectrum of Eu^{2+} in KF, as obtained by Rubio O et al [31]. Three different orthorhombic sites are indicated, with type I being closest to the spectrum reported in the present work.

to 6.17 and earlier published work is very encouraging. The good correlation serves to confirm that the europium ion enters the crystal lattice in an identical form independent of the way in which the specimen was prepared. The information obtained from ESR measurements is a much more comprehensive proof of this statement than the optical absorption spectra presented earlier.

The position of the seven fine structure components for each of the host crystals are shown schematically against lattice parameter d in figure 6.22. A reasonably smooth and regular variation is observed with lattice parameter. In particular, the values obtained for KF in the present work are in good agreement with this trend. The position of the outermost $7/2 - 5/2$ transition given by Rubio O. et al [32] is also included (corrected for different frequency). The same smooth correspondance is not observed, with a maximum field spread that places it somewhere between NaBr and NaCl.

The crystal field parameters have been calculated according to equations 6.8 to 6.10, using the fine structure field positions shown in figure 6.22. The values are tabulated in figure 6.23. Also included in figure 6.23 are values obtained elsewhere using more accurate methods. The relatively good agreement for the main parameters b_2^0 and b_4^0 tends to validate the approximations described in section 6.5.3. As lattice parameter decreases, there is a systematic increase in the value for b_2^0. This behaviour is expected since the smaller the distance between the <110> cation vacancy and the Eu^{2+} ion, the greater is its perturbing effect.

The hyperfine structure parameters A^{151} and A^{153} are also of interest. Unfortunately it is difficult to obtain both values accurately since there is a considerable degree of overlap between the two corresponding sets of absorption lines. The more intense Eu^{151} line structure is the easiest to evaluate and the parameter A^{151} is found to remain relatively constant at a value of around 31.2×10^{-4} cm^{-1} for all of the crystals studied. This result is significant because the hyperfine parameter is particularly sensitive to

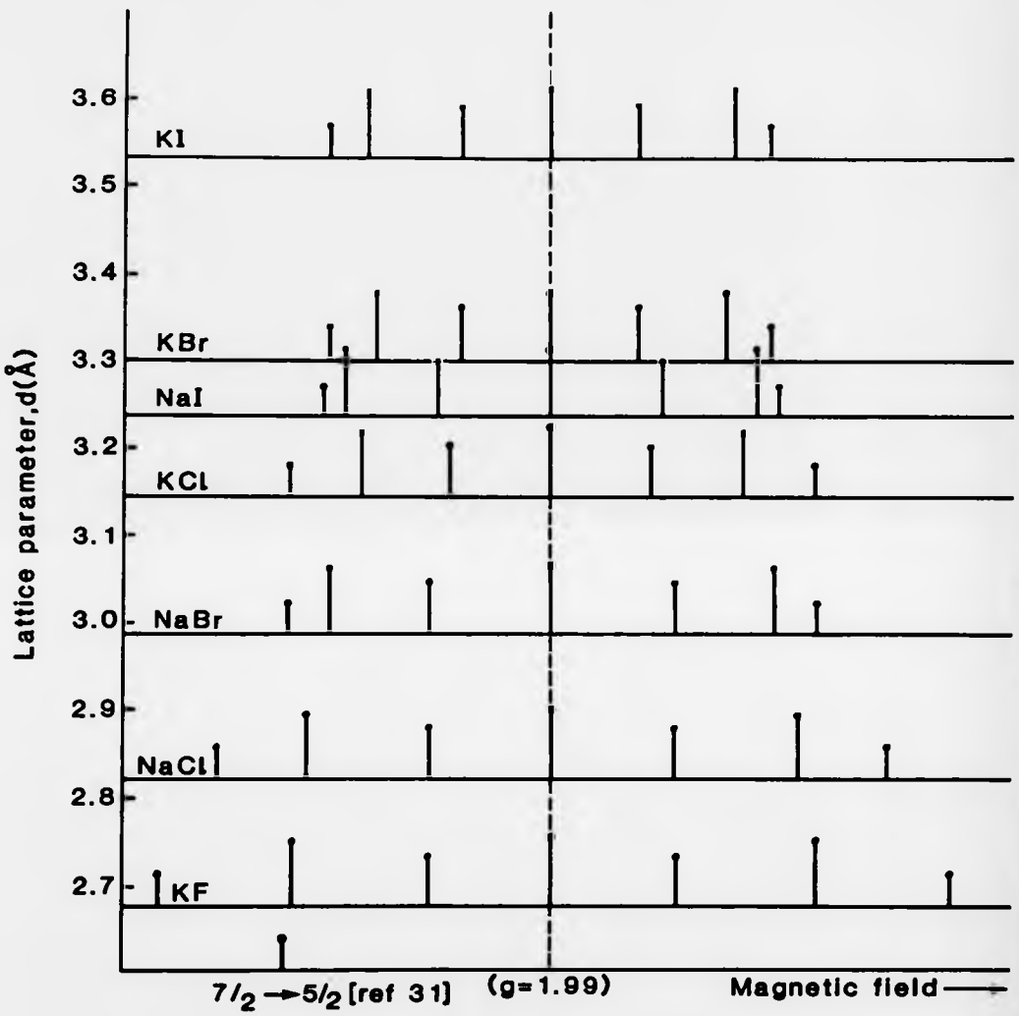

Fig.6.22 A schematic representation of the Eu^{2+} ESR fine structure component magnetic field positions versus host crystal lattice parameter d. The position of the outermost $7/2 \rightarrow 5/2$ transition of $KF:Eu^{2+}$ obtained by Rubio O et al [31] is included for comparison.

Crystal	Present work			Values obtained elsewhere			
	b_2° ($\times 10^{-4}cm^{-1}$)	b_4° ($\times 10^{-4}cm^{-1}$)	b_6° ($\times 10^{-4}cm^{-1}$)	b_2° ($\times 10^{-4}cm^{-1}$)	b_4° ($\times 10^{-4}cm^{-1}$)	b_6° ($\times 10^{-4}cm^{-1}$)	Reference
KI	326.0	-10.9	-3.1	336.8	-15.2	0.4	[30]
NaI	351.7	-17.3	-1.8	352.8	-19.2	1.3	[30]
KBr	308.2	-7.3	-1.9	319.3	-11.1	0.5	[28]
NaBr	389.0	-14.9	-0.44	384.7	-15.1	0.4	[28]
KCl	353.3	-5.9	0.01	342.5	-4.9	0.3	[25]
NaCl	458.6	-7.1	-1.3	457.7	-8.3	0.5	[26]
KF	499.5	-2.6	-2.1	271.7	21.6	2.0	[31]

Fig 6.23 Crystal field parameter values for Eu^{2+} as determined from the room temperature ESR spectra. Also included are values obtained by more accurate treatments.

the nature of the charge compensation mechanism. For example, deviations have been observed for Eu^{2+}-O^{2-} [33] and Eu^{2+}-OH^{-} [34] complexes giving values for A^{151} of 28.0 $x10^{-4}$ and 30.2 $x10^{-4}$ cm^{-1} respectively. The value of A^{151} = 30.3 $x10^{-4}$ cm^{-1} reported by Boldu O. et al [32] for $KF:Eu^{2+}$ deviates from the value expected for a substitutional ion with cation vacancy compensation. It would appear therefore that, in their study, the Eu^{2+} ion may be complexed with another impurity/defect probably situated on a neighbouring anion site. In the present work, a Eu^{2+}-vacancy pair is indicated both by the value of A^{151} and by the position of the fine structure components compared with the remaining alkali halides.

A broad resonance centred around g = 2 is observed for some of the crystals. The origins of this resonance will be considerered later. Also of interest is the complete lack of ESR for crystals of $NaF:Eu^{2+}$ especially since the same crystals show a well developed optical absorption spectrum seemingly characteristic of the Eu^{2+} ion (figure 6.9). The reason for this behaviour will become clear following an investigation of the thermal stability of the active Eu^{2+} centres to be presented in the following section.

6.6 The effect of thermal aging on the optical and ESR absorption spectrum of Eu^{2+} in the alkali halides

6.6.1 Introduction

One of the more interesting aspects of the absorption spectra of Eu^{2+} in the alkali halides is the effect of low temperature annealing. Both the optical and ESR spectra are affected in a curious way. In general the effects are rather subtle but in some cases, and for the ESR spectrum in particular, the effects can be quite dramatic.

The annealing experiments were normally carried out at a temperature of 130°C with the crystal in air. An exception to this treatment was the

heating of deliquescent crystals such as NaBr and NaI in a dry nitrogen atmosphere. The potassium and sodium halides tended to behave slightly differently and are therefore discussed separately below.

6.6.2 The potassium halides

The optical absorption spectrum of KCl:Eu^{2+} before and after annealing at 130°C for a total of 520 hours is shown in figure 6.24. The absorption band at around 215 nm (46512 cm^{-1}) is attributed to the U-centre. The annealing results in a slight increase in the overall splitting between the two main bands with, in addition, the formation (or perhaps better resolution) of some additional structure within these bands. For example, the long wavelength tails of the two main bands may be resolved at LNT into many underlying constituent bands. The inset of figure 6.24 illustrates this behaviour for the 350 nm (28571 cm^{-1}) band. The ESR spectrum appears to be unaffected by the annealing process.

The increased detail which can be resolved in the optical spectrum may result from a relaxation of the lattice strain originally created by the rapid quench to RT following diffusion. A similar sharpening and slight shift of the individual absorption bands following annealing was observed earlier for Yb^{2+}. The constancy of the ESR spectrum indicates that the Eu^{2+} ion remains on a substitutional lattice site coupled to a cation vacancy. Therefore it is proposed that the absorption spectrum obtained after prolonged low temperature annealing represents the true spectrum for substitutional Eu^{2+} in KCl. The large number of individual absorption bands, most of which are only partially resolved, is consistent with the large number of available optical transitions. This observation serves to illustrate the limitations of the simplified "two-band" model discussed earlier (section 6.4.2).

The effect which annealing has on KBr:Eu^{2+} is much the same as

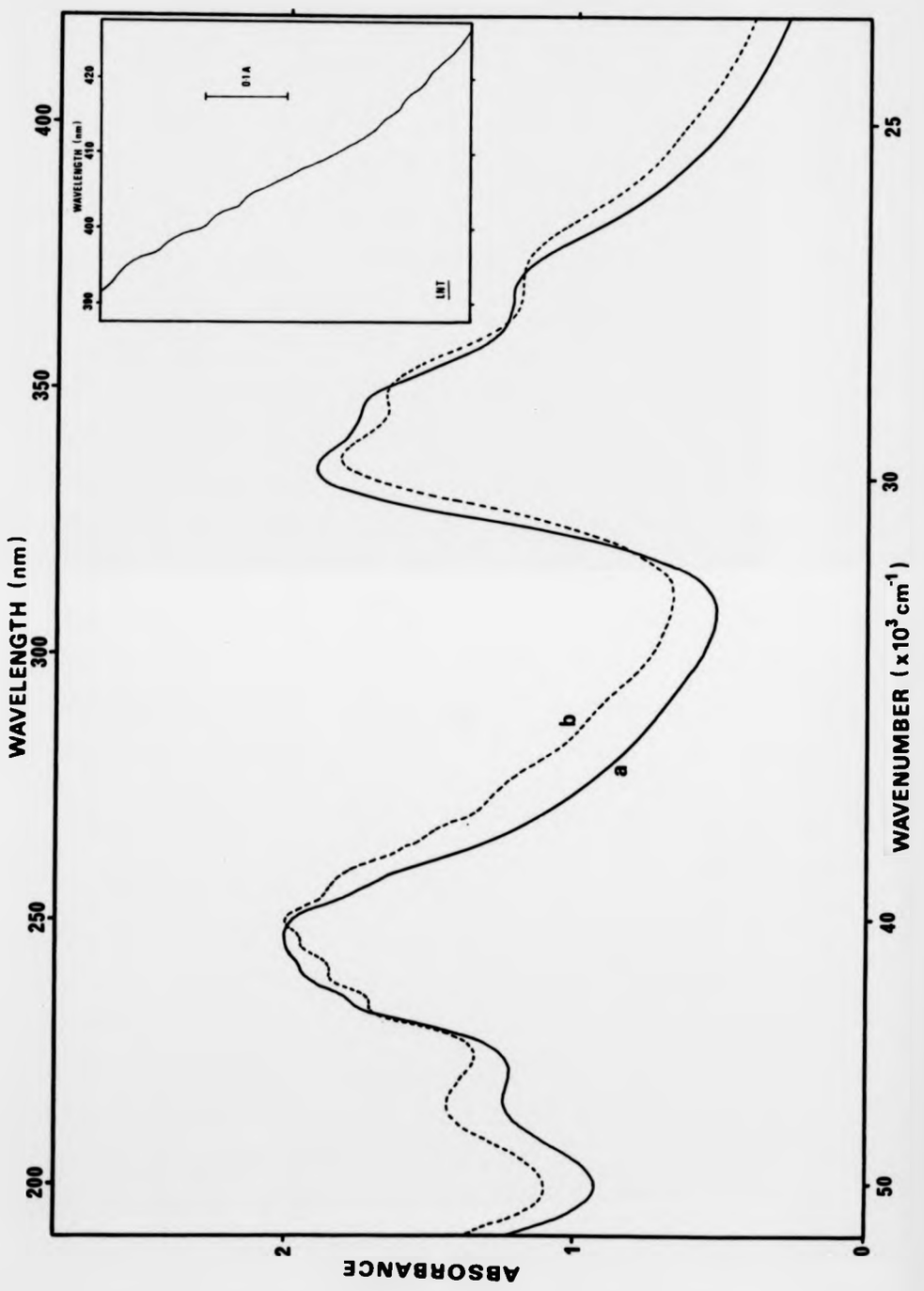

Figure 6.24 The effect of annealing at 130°C on the optical absorption spectrum of KCl:Eu^{2+}; (a) as produced and (b) after 520 hours. The inset illustrates some of the additional detail observed at LNT after annealing.

for KCl. After a total of 502 hours, additional structure is observed within the absorption bands. Spectra obtained after various different time intervals are reproduced in figure 6.25. The corresponding ESR spectra remained unchanged throughout. For one sample of KBr:Eu^{2+} however a different form of behaviour was observed. The basic two band spectrum remained but the high energy band became shifted toward lower energies and the low energy band became shifted slighty toward higher energies. This behaviour is illustrated in figure 6.26. It is not understood why this one sample should behave differently and it is only included due to its similarity with the behaviour exhibited by the sodium halides (see the following section). Unfortunately ESR measurements were not made on this sample.

The optical absorption spectrum of KI:Eu^{2+} is rich in detail immediately after sample preparation (see figure 6.2). No significant change could be induced in either the optical or ESR spectra by extended low temperature annealing.

6.6.3 The sodium halides

Thermal aging of NaCl:Eu^{2+} produces a marked change in both optical and ESR absorption spectra. Figure 6.27 illustrates the way in which the optical spectrum changes during annealing at 130°C. The high energy band increases in amplitude, while the low energy band decreases in amplitude. Simultaneously, the separation between the two bands decreases and a certain amount of additional structure appears. Prolonged annealing results in continued growth of the high energy band and further spectral compression. Specimens of NaCl:Eu^{2+} stored for an extended period at RT exhibit precisely the same changes. A two year old specimen, which is shown in figure 6.28 (trace (a)), illustrates the full extent of this spectral compression effect. A considerable departure from the

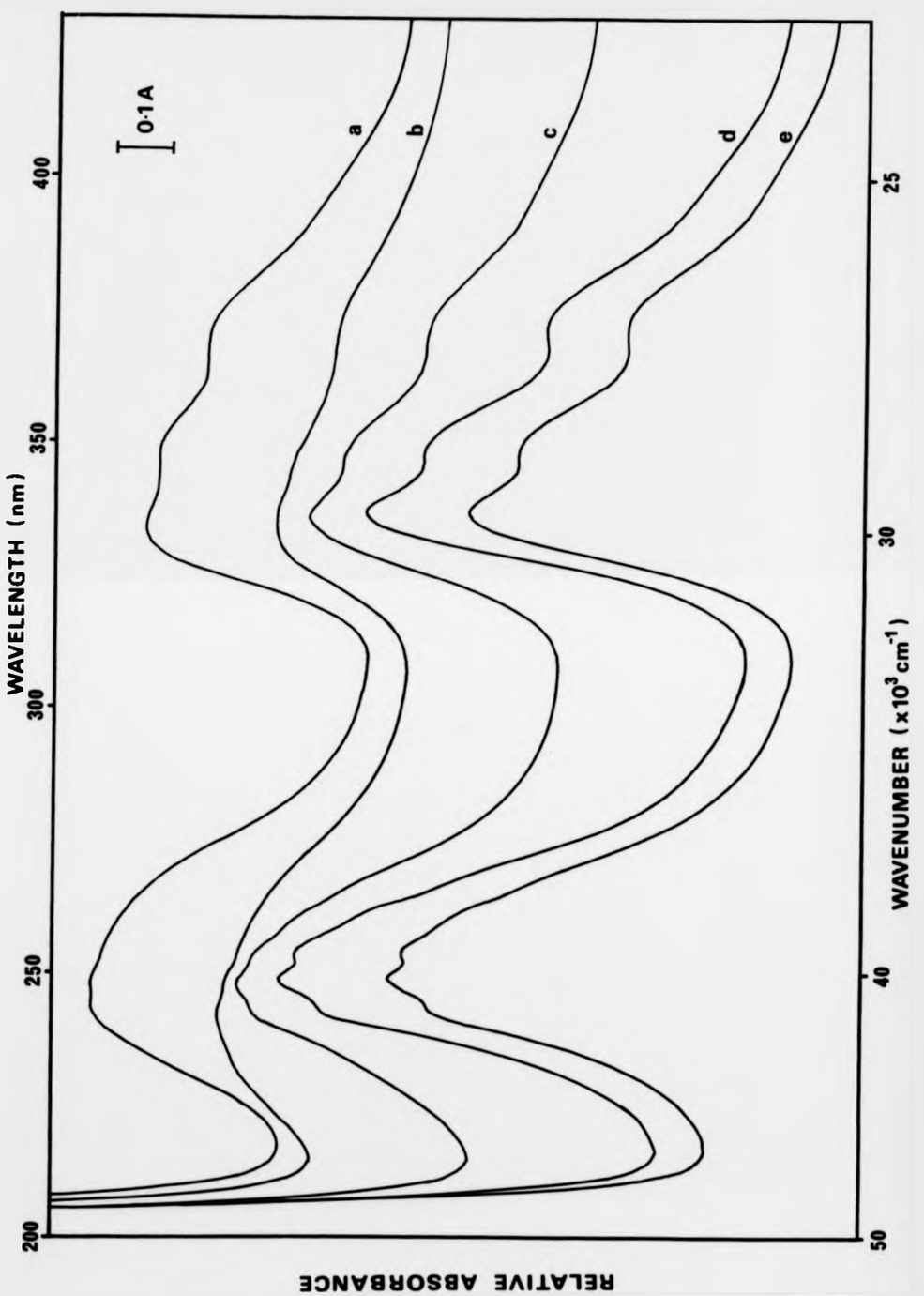

Figure 6.25 The effect of annealing at 130°C on the optical absorption spectrum of KBr:Eu^{2+}; (a) as produced, (b) after 20 hours, (c) after 48 hours, (d) after 266 hours and (e) after 502 hours.

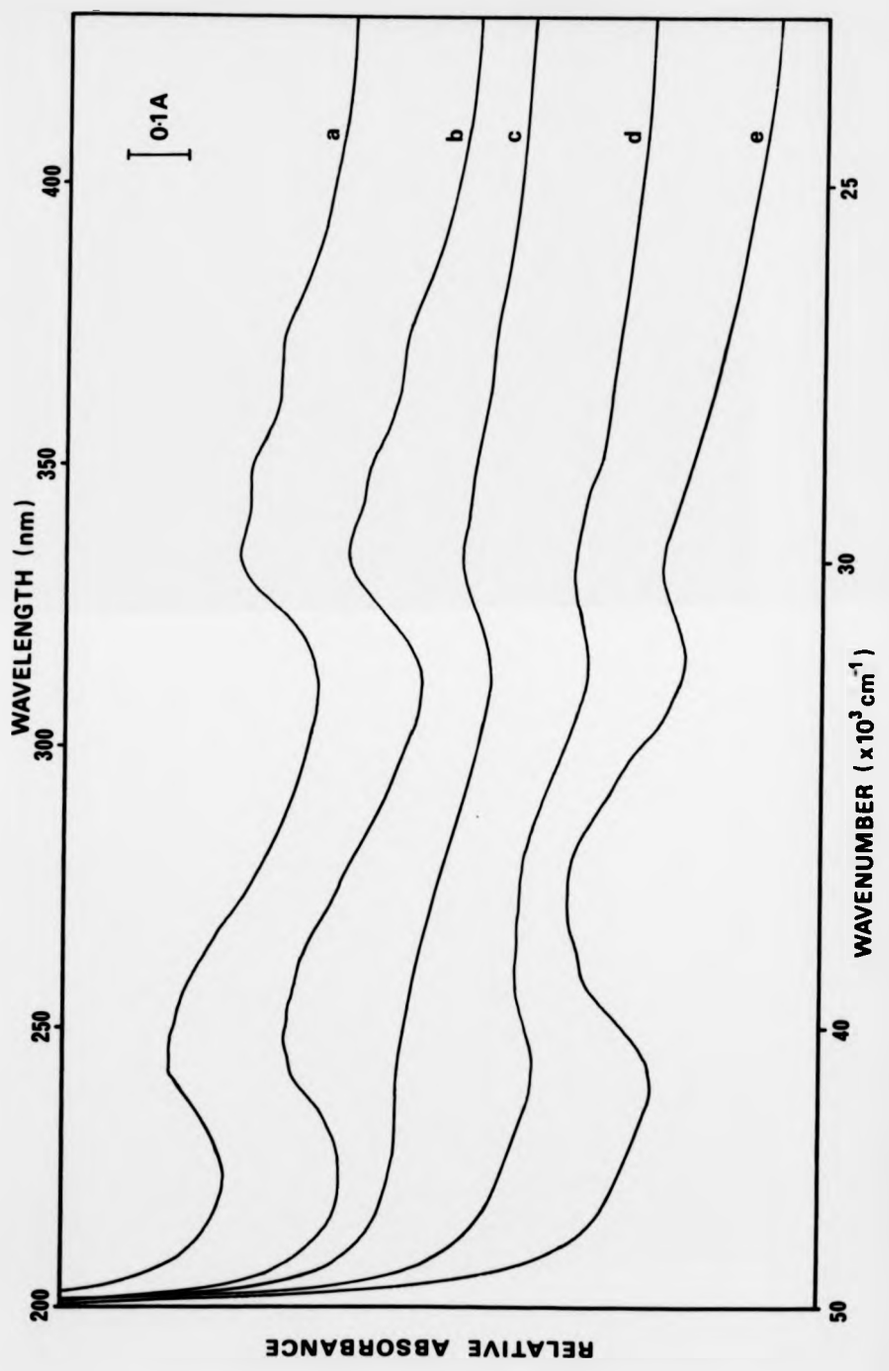

Figure 6.26 The anomalous low temperature (130°C) annealing behaviour of one sample of KBr:Eu^{2+}; (a) as produced, (b) after 20 hours, (c) after 48 hours, (d) after 266 hours and (e) after 502 hours.

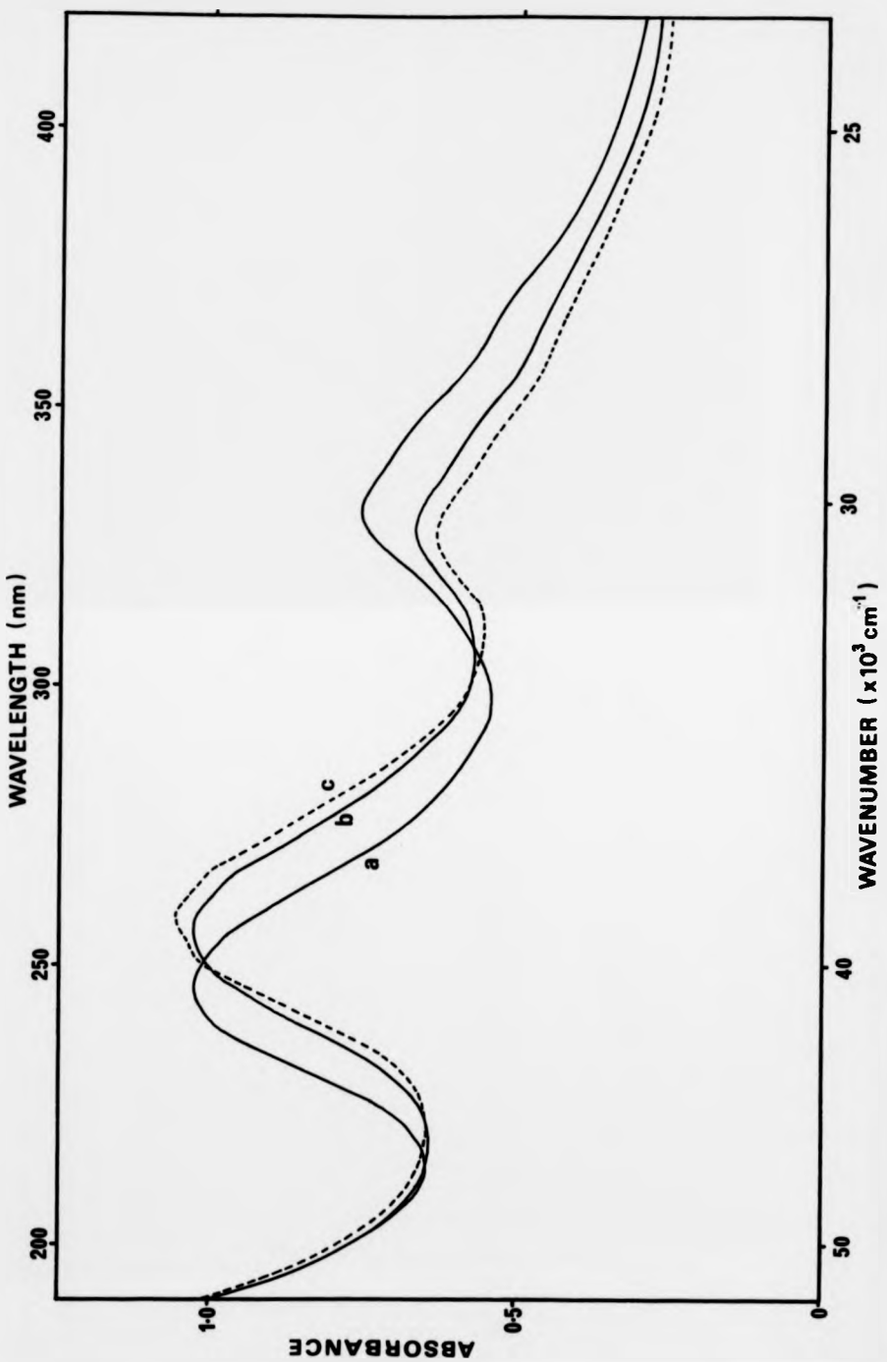

Figure 6.27 The effect of annealing at 130°C on the optical absorption spectrum of NaCl:Eu^{2+}; (a) as produced, (b) after 15 hours and (c) after 520 hours.

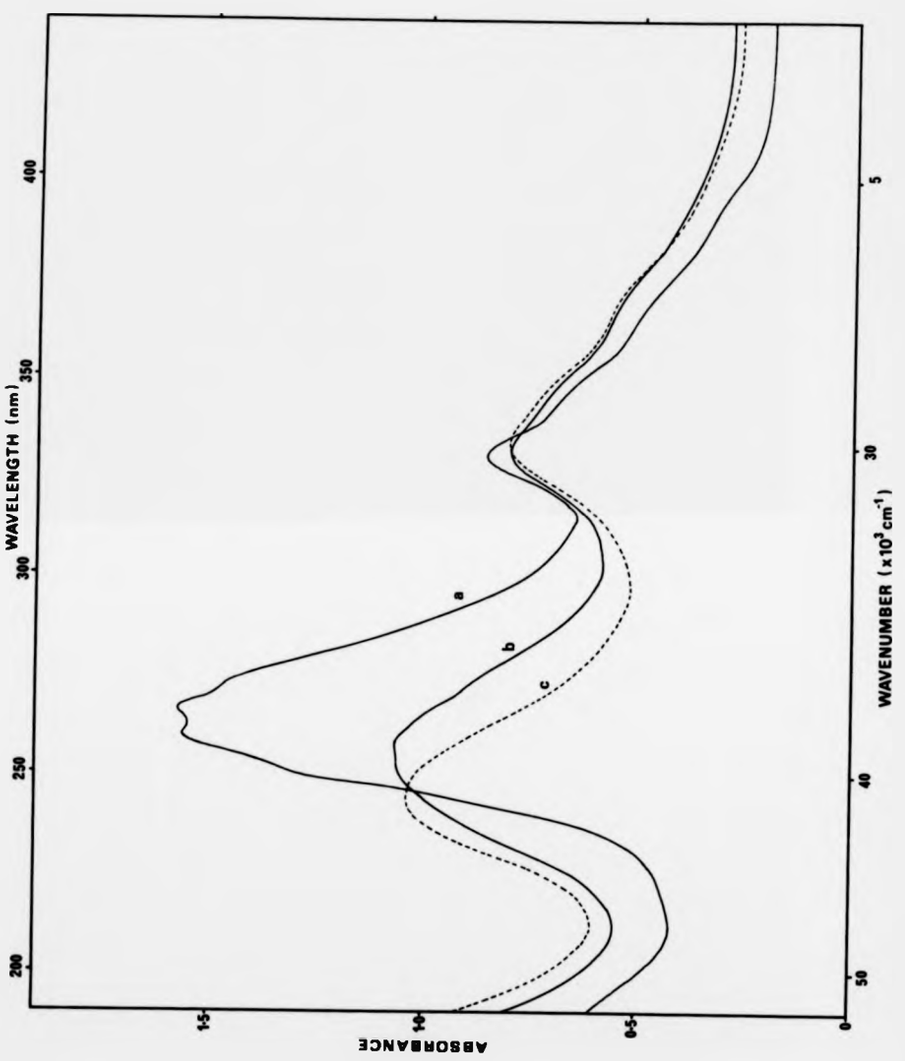

Figure 6.28 The effect of annealing at 600°C on the optical absorption spectrum of a thermally aged sample of NaCl:Eu^{2+}; (a) a two year old specimen, (b) after 30 minutes and after 90 minutes.

conventional Eu^{2+} optical absorption spectrum is observed, however the original spectrum may be recovered by simply heating the crystal to a high temperature for a short time and then quenching to RT. Traces (b) and (c) of figure 6.28 show the spectra obtained after annealing at a temperature of 600°C for a total of 30 minutes and 90 minutes respectively.

The behaviour of the ESR spectrum on thermal aging is interesting and also very suprising. For a specimen of NaCl:Eu^{2+} freshly quenched after a high temperature anneal, the spectrum is identical with that described earlier for a newly produced crystal. The Eu^{2+} ion is therefore present on a substitutional site of C_{2v} symmetry. As the specimen is thermally aged, the ESR spectrum begins to reduce in amplitude. There is no shift in the position of any of the lines and no new spectral lines occur. When the crystal is well aged, corresponding to the "cramped" optical spectrum (see figure 6.28, trace (a)), the ESR spectrum disappears completely. This behaviour is illustrated in figure 6.29 where trace (a) corresponds to the as-produced and trace (b) to the thermally aged crystal.

The effects of thermal aging on the optical and ESR spectra of crystals of NaBr:Eu^{2+} are identical to that observed for NaCl. Trace (a) of figure 6.30 shows the optical absorption spectrum recorded for a NaBr:Eu^{2+} crystal obtained about 30 minutes after initial preparation. Traces (b), (c) and (d) in the same figure illustrate the changes caused by aging at both RT and 130°C up to a total of 40 days. The ESR spectra corresponding to traces (a) and (d) of figure 6.30 are shown as traces (a) and (b) of figure 6.31 respectively. The ESR intensity is significantly reduced for the 40 day old crystal. Annealing of this same specimen at 600°C for 10 minutes followed by a rapid quench to RT fully restores both the ESR spectrum and the original optical absorption spectrum.

The same behaviour was sought in specimens of NaI:Eu^{2+} but was not observed. This might be related to the fact that the Eu^{2+} concentration in these crystals, as determined from the optical spectrum, was much lower

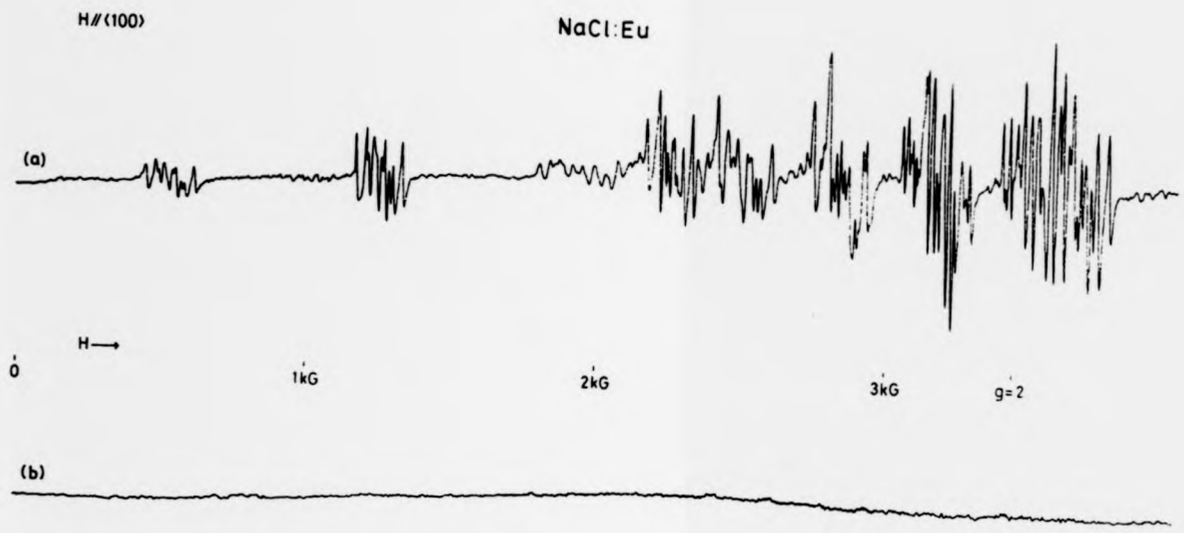

Fig. 6.29 The effect of thermal aging on the ESR spectrum of NaCl:Eu^{2+}; (a) as produced and (b) following extended aging.

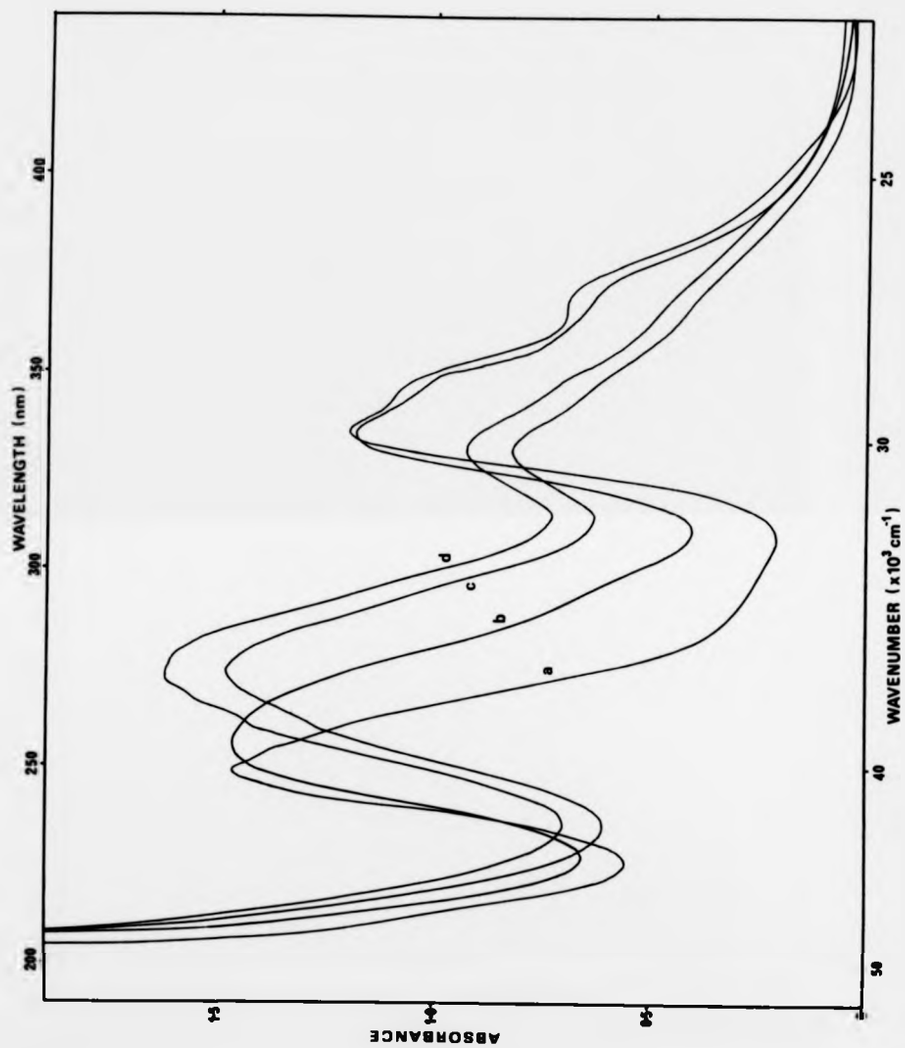

Figure 6.30 The effect of annealing at 130°C on the optical absorption spectrum of NaBr:Eu^{2+}; (a) as produced, (b) after 24 hours, (c) after 336 hours and (d) after 768 hours.

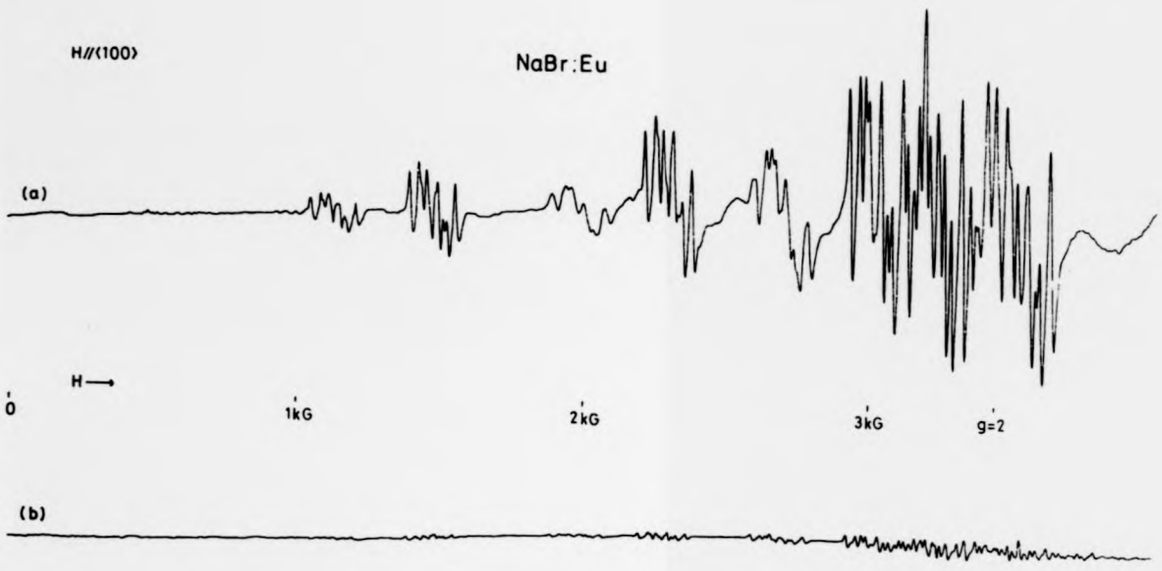

Fig. 6.31 The effect of thermal aging on the ESR spectrum of NaBr:Eu^{2+} ; (a) as produced and (b) after 768 hours at 130°C.

than that obtained for the NaCl and NaBr crystals.

NaF:Eu^{2+} crystals behaved rather differently to the other sodium halides. The optical absorption spectrum remained basically unchanged whatever the treatment and appeared to indicate convential substitutional Eu^{2+} ions. It is therefore interesting that no ESR spectrum was observed. Various different heat treatment cycles were performed on these crystals in an attempt to generate an ESR signal. Changes were made to the annealing temperatures (up to 900°C), the anneal times (up to 20 hours) and the cooling procedure all without success.

6.6.4 Discussion

The optical absorption spectrum of EuF_2 is reproduced in figure 6.32 [35]. EuF_2 possesses the fluorite structure and therefore the Eu^{2+} ion experiences a cubic (8-fold coordinated) crystal field. The basic double band structure is still observed since it is due primarily to the 5d electron orbital splitting which remains operative. The 5d orbital does not itself take part in the bonding process. There is a high degree of similarity between the EuF_2 spectrum and the spectrum described earlier for NaF:Eu^{2+} (figure 6.9). The natural implication of this observation is that the europium in NaF is present in the form of a separate phase of EuF_2. The complete lack of ESR is consistent with this assumption because the paramagnetism associated with the free Eu^{2+} ion is lost when the ion becomes bonded into a crystalline form such as EuF_2. The inability of all the various heat treatments to disperse the EuF_2 phase once formed, may be attributed to its high melting point of 1380°C [36].

The model proposed above for divalent europium in NaF agrees entirely with the conclusions of chapter 5 for divalent ytterbium. Direct evidence was provided in that chapter for the presence of a YbF_2 phase in NaF:Yb^{2+}.

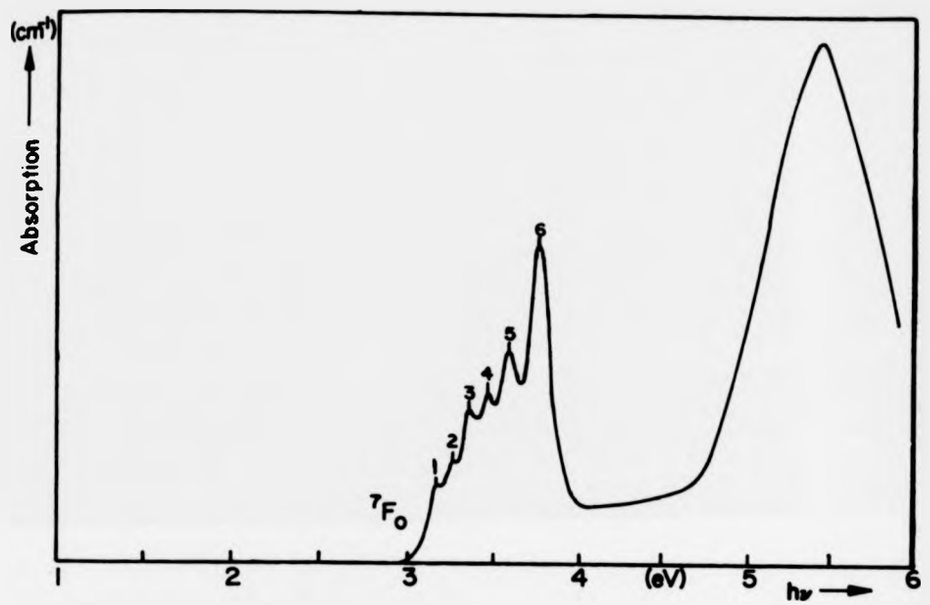

Figure 6.32 The optical absorption spectrum of EuF_2 at 20 K (after Freiser et al [34]).

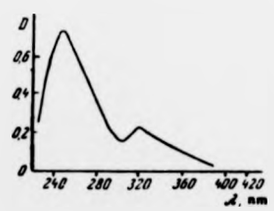

Figure 6.33 The optical absorption spectrum of a solution of $EuCl_2$ (after Gromova et al [36]).

At that time the description was based completely on a detailed study of the optical absorption spectrum. For NaF:Eu^{2+} the optical information is not sufficiently characterised to allow such a detailed conclusion to be drawn. However, the ESR information is extremely detailed and by its very absence provides direct evidence for the presence of an EuF_2 phase.

The same model proposed above may also be applied to the behaviour of NaCl and NaBr containing Eu^{2+}. After prolonged thermal aging both crystals exhibit a modified Eu^{2+} optical absorption spectrum and no ESR signal. It is interesting to compare the modified optical absorption spectrum of Eu^{2+} in NaCl (figure 6.27, trace (a)) with the optical absorption spectrum of a solution of $EuCl_2$ [37] which is reproduced in figure 6.33. Both spectra appear essentially the same. It is proposed therefore that a separate phase of EuX_2 (X = Cl, Br) is formed during the prolonged anneal. For NaCl and NaBr these separate phases may be dispersed by heating the sample to a high enough temperature; for NaF the phase remained stable. This situation is understandable since $EuCl_2$ and $EuBr_2$ possess much lower melting points (727°C and 677°C respectively [36]) than EuF_2 (1380°C).

If the changes noted above were due to the aggregation of Eu^{2+} ions then the appearance of a broad ESR signal centered around g = 2 might be expected. No such resonance was observed. Unfortunately due to the theoretical complexity of the Eu^{2+} system, it was not possible to understand or account for the interesting changes observed in the optical absorption spectra. Nevertheless based on the previous study of the Yb^{2+} ion, it is possible that the shifting together of the two major absorption bands may indicate an increase in the degree of overlap between the impurity ion and the surrounding anions.

The presence of a broad ESR resonance centred around g = 2 for the potassium halides implies some aggregation of Eu^{2+} ions. The aggregates were present immediately after sample preparation and it was not possible to increase or reduce their numbers subsequently. It would seem that they are

produced at the diffusion temperature and frozen-in on quenching. In general the potassium halides do not appear to exhibit a tendency to form a separate phase of EuX_2. The optical absorption changes are in general more subtle than for the sodium halides and no changes could be observed in the ESR spectrum. An exception to this rule was observed for one specimen of $KBr:Eu^{2+}$. For this specimen only, the optical absorption spectrum after thermal aging resembled the "cramped" spectrum normally associated with the $EuBr_2$ phase. Unfortunately an ESR spectrum was not recorded for this sample. The more general situation for the potassium halides is that of a straightforward stress relief in the vicinity of the impurity. The optical absorption spectrum obtained after the prolonged aging process therefore corresponds to the true spectrum of substitutional Eu^{2+} ions in the alkali halides.

6.7 Conclusions

Europium-doped alkali halide single crystals may be produced by vapour phase diffusion. The europium ion enters the crystals in the divalent charge state and generally resides on a substitutional cation site with a charge compensating vacancy present along the <110> direction. In some of the crystals a proportion of the Eu^{2+} ions are present in the form of an aggregate immediately after production. These aggregates give rise to a broad ESR resonance around $g = 2$. The majority of the europium ions are in a dispersed state and give rise to a richly detailed ESR spectrum which is characteristic of an Eu^{2+} ion on a site of orthorhombic (C_{2v}) symmetry. The corresponding optical absorption spectra are characterised by two broad bands in the near ultraviolet spectral region. These bands are attributed to optical transitions of the type $4f^7 - 4f^6 5d$.

Crystals of NaF containing europium behave differently from the majority of the alkali halides. The optical absorption spectrum obtained for $NaF:Eu^{2+}$

produced at the diffusion temperature and frozen-in on quenching. In general the potassium halides do not appear to exhibit a tendency to form a separate phase of EuX_2. The optical absorption changes are in general more subtle than for the sodium halides and no changes could be observed in the ESR spectrum. An exception to this rule was observed for one specimen of $KBr:Eu^{2+}$. For this specimen only, the optical absorption spectrum after thermal aging resembled the "cramped" spectrum normally associated with the $EuBr_2$ phase. Unfortunately an ESR spectrum was not recorded for this sample. The more general situation for the potassium halides is that of a straightforward stress relief in the vicinity of the impurity. The optical absorption spectrum obtained after the prolonged aging process therefore corresponds to the true spectrum of substitutional Eu^{2+} ions in the alkali halides.

6.7 Conclusions

Europium-doped alkali halide single crystals may be produced by vapour phase diffusion. The europium ion enters the crystals in the divalent charge state and generally resides on a substitutional cation site with a charge compensating vacancy present along the <110> direction. In some of the crystals a proportion of the Eu^{2+} ions are present in the form of an aggregate immediately after production. These aggregates give rise to a broad ESR resonance around $g = 2$. The majority of the europium ions are in a dispersed state and give rise to a richly detailed ESR spectrum which is characteristic of an Eu^{2+} ion on a site of orthorhombic (C_{2v}) symmetry. The corresponding optical absorption spectra are characterised by two broad bands in the near ultraviolet spectral region. These bands are attributed to optical transitions of the type $4f^7 - 4f^6 5d$.

Crystals of NaF containing europium behave differently from the majority of the alkali halides. The optical absorption spectrum obtained for $NaF:Eu^{2+}$

is the same as that obtained for EuF_2 and implies that the Eu^{2+} ions are present in the form of a separate phase of EuF_2. The lack of an ESR signal supports this model. Thermal aging of crystals of $NaCl:Eu^{2+}$ and $NaBr:Eu^{2+}$ leads similarly to the production of separate phases of $EuCl_2$ and $EuBr_2$ respectively. Changes are observed in both the optical and ESR spectra as the aging process proceeds. The optical absorption spectrum becomes increasingly "cramped" with the two major absorption bands moving closer together while the ESR spectrum decreases in intensity and finally disappears completely. The optical absorption spectrum for $NaCl:Eu^{2+}$ after aging is essentially the same as that observed for $EuCl_2$. A similar phenomenon was searched for in $NaI:Eu^{2+}$ crystals but was not found, presumably due to the lower concentrations of Eu^{2+} ions involved. The phenomenon was also observed for one sample of $KBr:Eu^{2+}$ and is not therefore exclusive to the sodium halides although it appears to be more favourable for such hosts. The most important factor in this respect appears to be the difference in radius between the divalent impurity ion and the host cation. The activation energy for impurity-vacancy pair clustering increases as the ratio M^{2+}/M^{+} increases [38]. Consequently the formation of the dihalide phase is more likely for Eu^{2+} (r = 1.09 Å) in the sodium halides (r_{Na} = 0.97 Å) than in the potassium halides (r_K = 1.33 Å) [36].

In general the potassium halides are only slightly affected by the thermal aging treatment. The more subtle changes observed in the optical spectrum are associated with a reduction in the lattice strain in the vicinity of the Eu^{2+} ion. This relaxation effect leads to a sharpening of the individual optical absorption bands resulting in an increase in the resolved detail. The observation of no change in the ESR spectrum is in agreement with this description.

6.8 A comparison with other published work

6.8.1 Introduction

Towards the latter stages of compiling this chapter the findings of a large group of workers at the University of Mexico came to my attention. During the past two or three years they have pursued a parallel study on the precipitation effects in europium-doped alkali halides. A series of papers have now been published [39-43]. Three earlier papers by the same group of workers on the optical absorption spectrum of Eu^{2+} ions in the alkali halides [15,16,19] were already in my possession but their later papers on the more specific topic of precipitation phenomena completely escaped my attention. As a result, the study of these precipitaion and separate-phase formation effects was performed simultaneously, though totally independently, by both the group at Mexico and myself. There is an important difference between the two studies however and this concerns the method of sample preparation. The work of the Mexico group centred on specimens grown from an europium-doped crystal melt whereas this work reports measurements made on samples prepared by vapour phase diffusion of europium. It is encouraging nevertheless to find that both sets of results and general conclusions are in agreement. A brief synopsis of their relevant work is now given.

6.8.2 Brief history

Changes in the optical absorption spectrum of an aged crystal of $NaCl:Eu^{2+}$ compared with a freshly prepared specimen were first noted in March 1979 [19]. More detailed work followed using both optical absorption and luminescence spectroscopy. In particular the luminescence information proved extremely useful in identifying the various different types of precipitated centre present in the aged crystal. It should be noted that this information was not available in the present work.

Controlled aging of NaCl, KCl, NaBr, KBr and NaI crystals containing europium was performed using temperatures between 25°C and 600°C. Basically two different forms of behaviour were observed; one for the sodium halides and the other for the potassium halides. These two cases are now described separately.

6.8.3 The sodium halides

Freshly quenched crystals of NaCl, NaBr and NaI exhibit conventional optical absorption spectra with one emission band at 427 nm (23419 cm^{-1}), 428 nm (23364 cm^{-1}) and 439 nm (22779 cm^{-1}) respectively. This result is associated with an Eu^{2+}-cation vacancy complex. Annealing of the crystals at temperatures between 25°C and 200°C resulted in a marked change in the optical absorption spectra with a large reduction in the separation between the low and high energy bands. Simultaneously, three new emission bands appeared at the expense of the original single band. These occured at 410, 439 and 485 nm (24390, 22779 and 20619 cm^{-1} respectively) for NaCl, at 428, 453 and 487 nm (23364, 22075 and 20534 cm^{-1} respectively) for NaBr and at 415, 461 and 488 nm (24096, 21692 and 20492 cm^{-1} respectively) for NaI. Based on X-ray diffraction data obtained for NaCl [39], the three emission bands are ascribed to a stable phase of $EuCl_2$ (428 nm emission) plus two metastable $EuCl_2$-like plate zones lying parallel to the {111} plane (439 nm emission) and {310} plane (485 nm emission).

Annealing of the crystals also resulted in changes in their ESR spectra. In all cases the resonance was observed to disappear entirely but at a rate much faster than the decay of the emission band associated with the Eu^{2+}-cation vacancy complex. This apparent anomaly was reconciled by assuming that the products of the first stages of aggregation to be dimers and trimers for which optical results would, to first order, remain relatively unaffected. The ESR spectrum is more sensitive to slight

changes in the site symmetry of the Eu^{2+} ion and is significantly affected by the above changes.

Heating of the aged crystals to progressively higher temperatures resulted in all cases in a dissolution of the metastable phases and a strengthening of the EuX_2 phase. Similarly it was observed that the various phases described above were formed at low temperatures in the reverse order of their high temperature dissolution.

The above results indicate that at low temperatures two processes occur:

i) The formation of simple aggregates.

ii) The nucleation and growth of precipitates of the metastable and stable phases.

6.8.4 The potassium halides

Aging of $KCl:Eu^{2+}$ at temperatures less than 150°C and $KBr:Eu^{2+}$ at temperatures less than 130°C resulted in only small changes to their optical absorption spectra, namely a slightly increased separation between high and low energy bands. A slight reduction in the ESR intensity was similarly observed along with a movement of the single emission band from 419 nm (23867 cm^{-1}) to 427 nm (23419 cm^{-1}) for KCl, and from 423 nm (23641 cm^{-1}) to 433 nm (23695 cm^{-1}) for KBr. The new emission bands are ascribed to the formation of a Suzuki phase.

Annealing at higher temperatures (greater than 200°C) resulted in the formation of additional emission bands and a gradual reduction in the separation between the high and low energy absorption bands. The overall form of the optical absorption spectra tends towards that expected for a separate EuX_2 phase. For KCl the new emission bands occur at 410, 439 and 478 nm (24390, 22779 and 20921 cm^{-1} respectively); for KBr there are only two such bands and these occur at 427 and 459 nm (23419 and 21786 cm^{-1}

respectively). The band positions for KCl are very similar to those given earlier for annealed NaCl and therefore exactly the same designations are applicable. For KBr, the lower wavelength band agrees very well with the emission band associated with the stable $EuBr_2$ phase in NaBr. The second emission band at 459 nm corresponds to metastable aggregates.

The above results indicate that the potassium halides behave in an identical way to the sodium halides for annealing temperatures greater than around 130°C. Annealing at lower temperatures results in the formation of Suzuki phases.

6.8.5 A comparison between the two parallel studies

It is important to note that in the present work the maximum annealing temperature that was used was only 130°C. This particular temperature, according to the work just described, marks a transition between two different types of behaviour for the potassium halides containing Eu^{2+}. Generally speaking the behaviour observed in the present work is that to be associated with the formation of Suzuki phases. The seemingly anomalous result which was described earlier for one particular sample of $KBr:Eu^{2+}$ and which appeared to indicate the formation of a separate phase of $EuBr_2$, is now understandable. Clearly with the annealing experiments being performed at around the transition temperature of 130°C, it is not suprising to discover at least one specimen which exhibits the nominally slightly higher anneal temperature behaviour.

All of the remaining results described in the present work are in excellent agreement with the work presented by the group at Mexico University. One small area of disagreement is in the inability of the present study to observe the formation of a separate phase of EuI_2 in crystals of $NaI:Eu^{2+}$. At the time this slightly anomalous behaviour was attributed to the low concentrations of europium in the NaI crystals

studied. According to the results described in this closing section, this behaviour is in fact to be expected.

6.9 References

1. R.Alcala et al, Journal of Luminescence, 27, p273 (1982)

2. M.S.Waite, Journal of the Electrochemical Society, 121, p1122 (1974)

3. G.Blasse et al, Philips Research Reports, 23, p189 (1968)

4. G.Blasse and A.Bril, Philips Technical Review, 31, p304 (1970)

5. G.Racah, Physical Review, 63, p367 (1943)

6. B.R.Judd, "Operator Techniques in Atomic Spectroscopy", McGraw-Hill, N.Y. (1963)

7. E.U.Condon and G.H.Shortly, "The Theory of Atomic Spectra", Cambridge University Press (1935)

8. G.H.Dieke, "Spectra and Energy Levels of Rare Earth Ions in Crystals", Ed. H.M.Crosswhite and H.Crosswhite, Interscience, J.Wiley and Sons, NY (1968)

9. J.Sugar and N.Spector, Journal of the Optical Society of America, 64, p1484 (1974)

10. H.A.Weakliem, Physical Review B, 6, p2743 (1972)

11. A.A.Kaplyanskii and P.P.Feofilov, Optics and Spectroscopy, 13, p129 (1962)

12. E.Loh, Physical Review, 184, p348 (1969)

13. S.N.Bodrug et al, Optics and Spectroscopy, 34, p176 (1973)

14. M.A.Dubinskii et al, Soviet Physics Solid State, 22, p711 (1980)

15. J.Hernandez A. et al, Journal of Chemical Physics, 72, p198 (1980)

16. J.Hernandez A. et al, Journal of the Physical Society of Japan, 50, p225 (1981)

17. R.Reisfield and A.Glasner, Journal of the Optical Society of America, 54, p331 (1964)

18. A.K.Mehra, Journal of the Optical Society of America, 58, p853 (1968)

19. J.Hernandez A. et al, Japanese Journal of Applied Physics, 18, p533 (1979)

20. J.H.van Vleck and W.G.Penney, Philosophical Magazine, 17, p961 (1934)

21. W.Low, "Paramagnetic Resonance in Solids", Solid State Physics (supplement 2), Academic Press (1960)

22. G.B.Bacskay et al, Journal of the Physics and Chemistry of Solids, 29, p1213 (1968)

23. W.Low, Physical Review, 109, p265 (1958)

24. R.Röhrig, Physics Letters, 16, p20 (1965)

25. G.B.Singh et al, Journal of Chemical Physics, 46, p2885 (1967)

26. P.G.Nair et al, Journal of the Physics and Chemistry of Solids, 29, p2183 (1968)

27. G.Aguilar S. et al, Journal of Chemical Physics, 60, p4665 (1974)

28. J.Rubio O. et al, Journal of Chemical Physics, 61, p5273 (1974)

29. G.Aguilar S. et al, Journal of Chemical Physics, 62, p1197 (1975)

30. E.Munoz P. et al, Journal of Chemical Physics, 62, p3416 (1975)

31. J.Rubio O. et al, Journal of Chemical Physics, 63, p4222 (1975)

32. J.Boldu O. et al, Journal of Chemical Physics, 67, p2391 (1977)

33. R.Nakata et al, Journal of the Physical Society of Japan, 41, p1996 (1976)

34. M.Sumita et al, Solid State Communications, 24, p655 (1977)

35. M.J.Freiser et al, Journal of Applied Physics, 39, p900 (1968)

36. R.C.Weast Editor, "CRC Handbook of Chemistry and Physics", 62nd Edition, CRC Press Inc, Florida (1981-1982)

37. M.I.Gromova et al, Vestnik Moskovskogo Universiteta Khimiya, 24,

p30 (1969)

38. J.S.Cook and J.S.Dryden, Journal of Physics C, 14, p1133 (1981)

39. J.Garcia M. et al, Physical Review B, 21, p5012 (1980)

40. F.J.Lopez et al, Physical Review B, 22, p6428 (1980)

41. F.J.Lopez et al, Journal of Luminescence, 26, p129 (1981)

42. J.Rubio O. et al, Physical Review B, 24, p4847 (1981)

43. M.Aguilar G. et al, Solid State Communications, 44, p141 (1982)

7. IMPURITY DIFFUSION AND COLOUR CENTRE FORMATION

7.1 Introduction

An interesting consequence of the use of vapour phase diffusion to introduce ytterbium and europium into the alkali halides is the formation simultaneously of colour centres within the crystal. The coloration is observed after the diffusion of either type of impurity but it is probably slightly more marked for ytterbium. Coloration is only observed in crystals which have been quenched rapidly to room temperature following diffusion. Slow cooling appears to result in thermal bleaching of any coloration produced.

The doped crystals generally exhibit a distribution of colour centres both of type and spatial arrangement. The differently coloured regions are arranged into a number of concentric zones about the centre of the crystal. The first part of this chapter is concerned with identifying the defect centres responsible for the differently coloured regions via a study of their characteristic optical absorption spectra. A detailed description of the spatial distribution of the colour centres is shown to be possible using the traversing slit (TS) assembly. The use of optical and thermal bleaching techniques enables the stability of the various defects and their distributions to be assessed.

A number of additional experiments were devised in an attempt to further elucidate the coloration mechanism. These experiments are described in section 7.4. Also included in this section is the discussion of a possible model to describe the coloration process. Throughout the chapter the new method of colour centre formation will be referred to as aliovalent coloration. This name is intended to convey the notable similarity with the additive coloration process whilst indicating the use of an impurity with a valency greater than one.

7.2 An optical analysis of the nature and distribution of colour centres

7.2.1 The potassium halides

The potassium halides colour readily using the aliovalent coloration technique. Immediately after quenching, the coloration consists almost entirely of F-centres. The only deviation from a pure F-centre concentration is the formation, in the more highly coloured crystals, of a small concentration of F-aggregate centres. In general the coloured crystals exhibit two distinct zones; the outer zone is clear to the eye and extends inwards from the crystal surface to a depth of 0.5 to 1 mm, the inner zone contains a roughly uniform concentration of colour centres. The boundary between these zones is extremely sharp and appears instantaneous to the eye. It is interesting to note that the clear outer zone also appears where a fissure extends into the crystal. The inner surfaces of the fissure appear, therefore, to behave in an identical manner to the outer crystal surfaces. For crystals of KF, the zone structure is in many ways similar to the arrangement observed for the other potassium halides except for the appearance of a number of additional zones. These extra zones contain new types of impurity-related colour centres. A separate section (section 7.3) is devoted to a study of the new colour centres in KF and their rather interesting behaviour.

The optical absorption spectrum obtained for a cross-sectional slice taken from a typical sample of KCl:Yb^{2+} is shown in figure 7.1. A number of different curves are shown corresponding to spectra recorded using the TS assembly. The crystal is progressively sampled, starting at a position parallel with the outer edge of the crystal and moving inwards towards the crystal centre. It should be noted that the individual spectra have been corrected for differing background absorbance levels. The spectra indicate an outer zone characterised by an absorption typical of the Yb^{2+} ion. As the slit moves towards the centre of the crystal, the Yb^{2+} spectrum disappears and there is a rapid growth of the

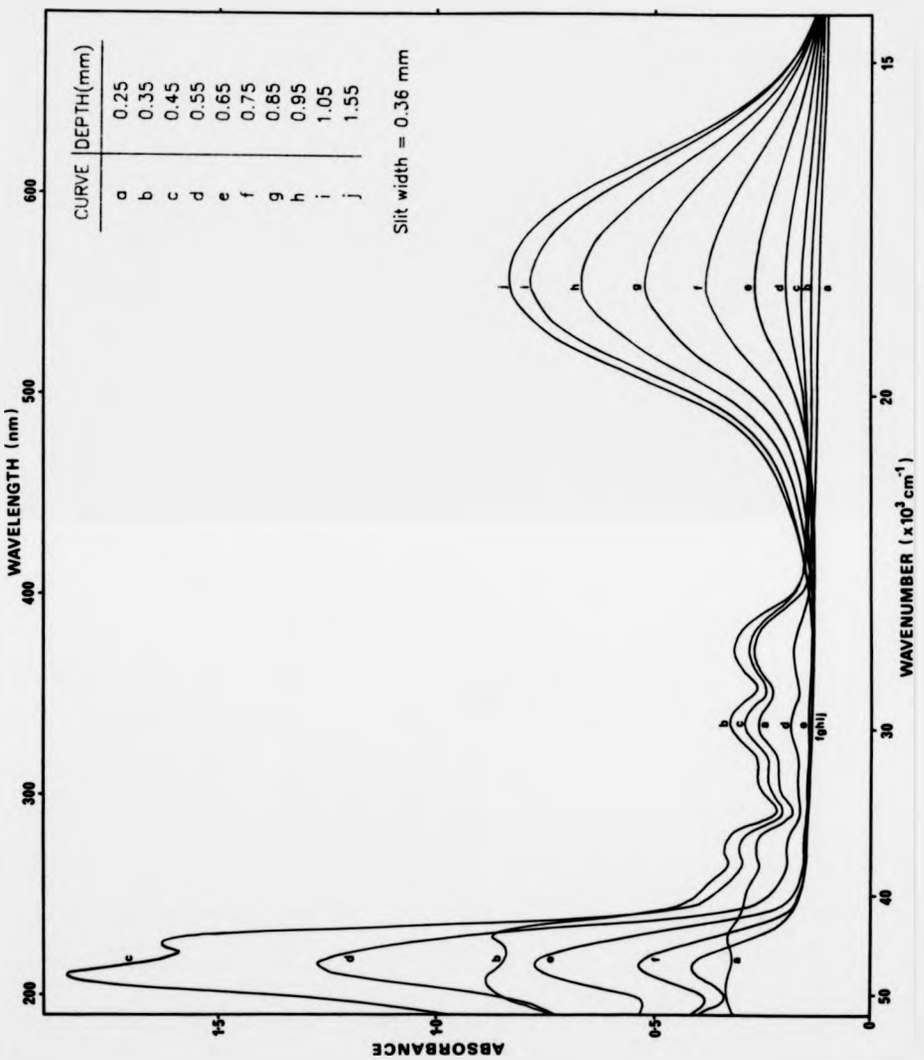

Figure 7.1 Optical absorption spectra obtained using the TS assembly for an aliovalently coloured crystal of KCl:Yb^{2+}. The crystal has been sampled at the depths indicated below its surface (total depth of crystal is 5 mm).

F-centre absorption band at 558 nm (17921 cm^{-1}).

The information obtained in figure 7.1 is replotted in figure 7.2 in terms of a variation in the concentration of each defect centre versus depth measured into the crystal. Concentration information has been obtained assuming a proportionality between the peak absorbance value for the characteristic absorption band associated with a particular defect and its concentration. Note that the A1 absorption band was used in the case of the Yb^{2+} impurity ion. The coefficient of proportionality for each centre has not been determined and therefore only qualitative variations are described. The distribution shown in figure 7.2 appears to indicate a region of overlap between the F-centre and Yb^{2+} zones. Care is necessary in the interpretation of such a distribution due to the smearing effect associated with a sampling slit of finite width. The slit width is 0.36 ± 0.01 mm and is roughly comparable with the width of the actual distributions being sampled. Examples of the relationship between the measured concentration distribution and the actual defect centre distribution were described earlier (see figure 4.8). An approximate defect distribution which is consistent with the curves shown in figure 7.2 is shown schematically in figure 7.3. According to figure 7.3 there is in fact zero overlap between the F-centre and Yb^{2+} zones, which is in agreement with the lack of observation of any Z-centre absorption bands.

Figure 7.4 shows the TS spectra obtained for a sample of $KCl:Eu^{2+}$. The derived defect distribution is reproduced in figure 7.5. It should be noted that both $KCl:Yb^{2+}$ and $KCl:Eu^{2+}$ behave in a completely analagous way. The small differences in total impurity diffusion depth are thought to be due primarily to slight differences in the diffusion times and temperatures.

The TS derived spectra for a sample of $KBr:Yb^{2+}$ are shown in figure 7.6. The equivalent spectra for a sample of $KBr:Eu^{2+}$ are identical in form and are not reproduced here in the interests of brevity. The overall distribution of defect centres obtained from an analysis of figure 7.6 is essentially

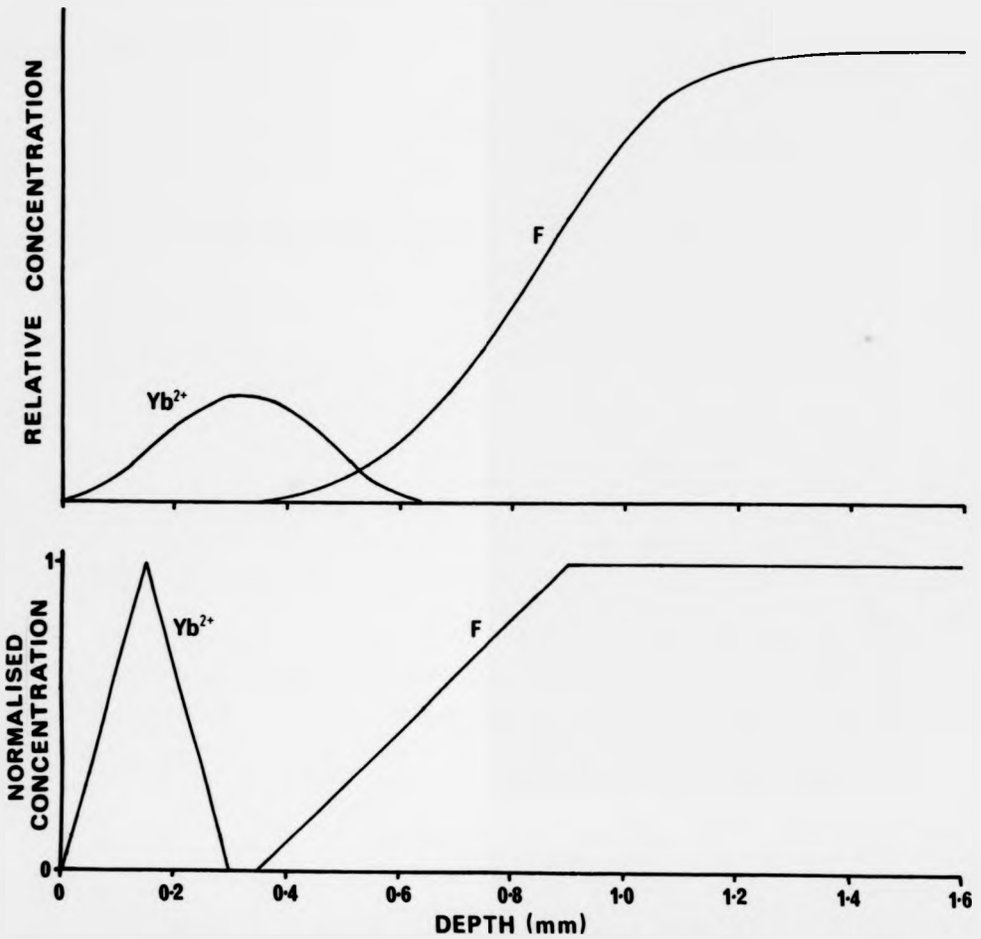

Figure 7.2 Defect centre concentration variations with depth for KCl:Yb^{2+}, as obtained from an analysis of figure 7.1.

Figure 7.3 Deconvolution of the curves in figure 7.2 to obtain approximate defect centre distributions.

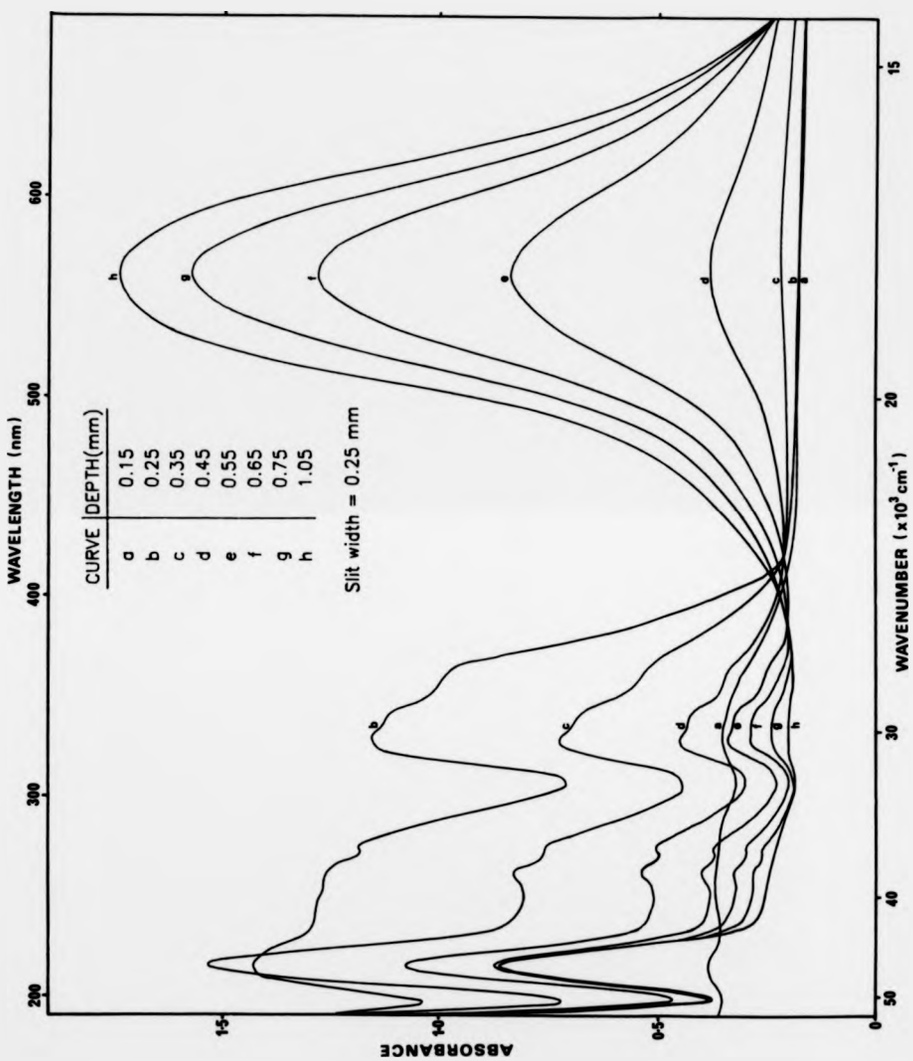

Figure 7.4 Optical absorption spectra obtained using the TS assembly for an aliovalently coloured crystal of KCl:Eu^{2+}. The crystal has been sampled at the depths indicated below its surface (total depth of crystal is 4 mm).

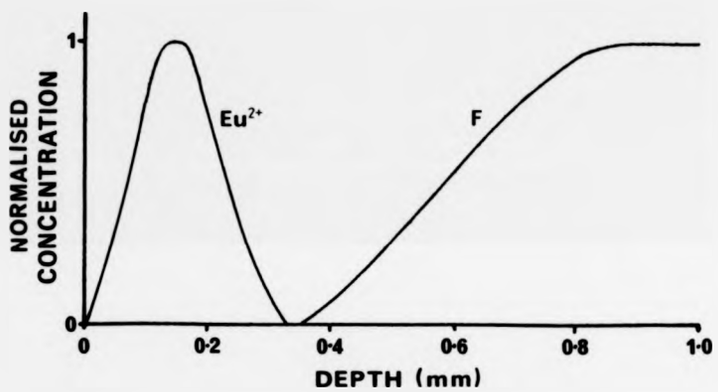

Figure 7.5 Approximate defect centre distributions for a crystal of KCl:Eu^{2+}, as obtained from an analysis of figure 7.4.

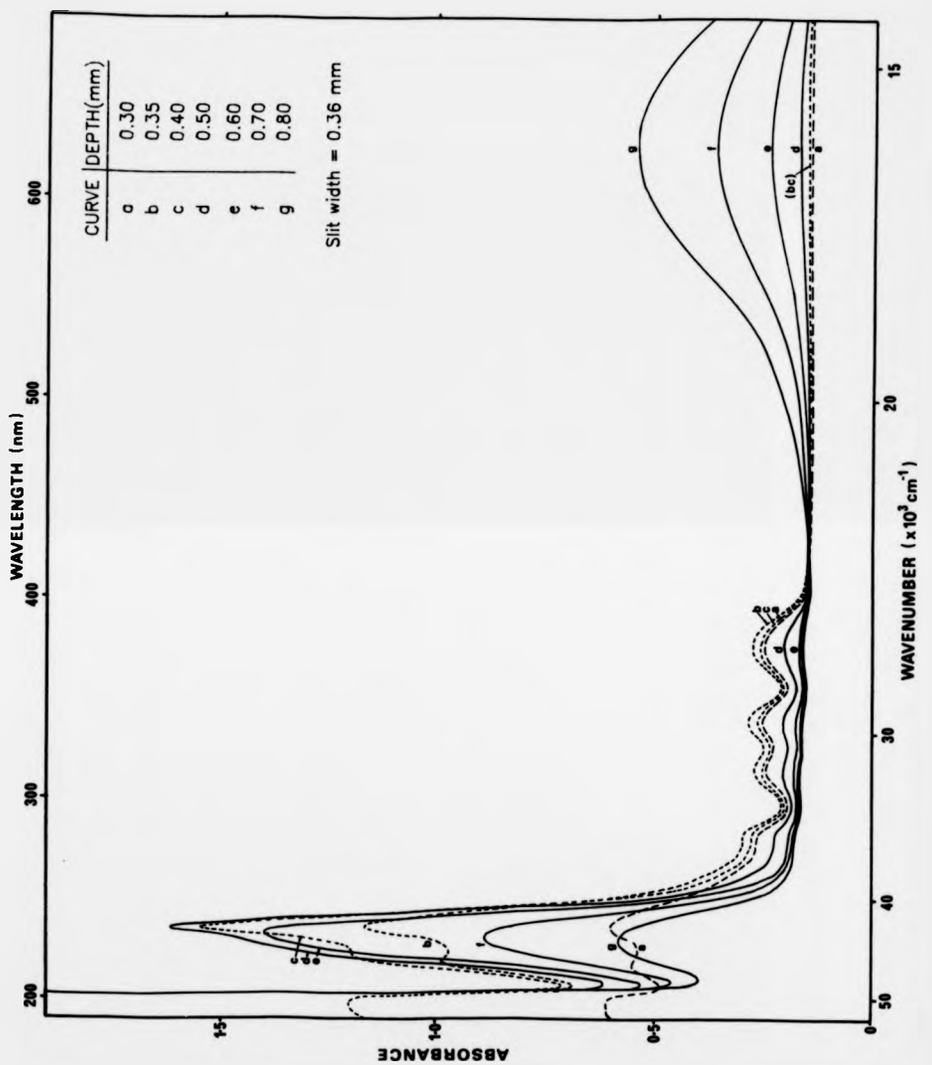

Figure 7.6 Optical absorption spectra obtained using the TS assembly for an aliovalently coloured crystal of KBr:Yb^{2+}. The crystal has been sampled at the depths indicated below its surface (total depth of crystal is 5 mm).

identical to that described earlier for KCl crystals doped with ytterbium and europium. Once again no absorption bands characteristic of Z-centres are observed implying zero overlap of rare earth impurities and F-centres. Crystals of KI containing both ytterbium and europium were observed to colour in an identical manner to crystals of KCl and KBr.

Optical bleaching experiments were performed on coloured crystals of KCl, KBr and KI. In all cases F-band illumination resulted in the formation of F-aggregate centres. Initially the M-band is obtained, to be followed a short time later by the R-bands. This behaviour is identical to that observed for the optical bleaching of F-centres produced by more conventional coloration techniques. No changes occurred in the rare earth impurity absorption bands nor were any changes observed at the interface. In particular no Z-bands were formed, thereby confirming the presence of a spatial separation between the impurities and the F-centres.

7.2.2 The sodium halides

The sodium halides were observed to colour readily following quenching of the crystals after rare earth impurity diffusion. The dominant type of colour centres were not in this case the F and F-aggregate centres but the X-centre and small colloids. The existence of colloidal particles was evident from the observation of strong Tyndall scattering.

The colour centres were distributed throughout the crystals in the form of a number of concentric zones. Crystals of NaBr and NaI produced the simplest situation with only two zones. The inner zone contained X-centres and other colloid centres, but no F-centres, whereas the outer zone, which extended to a depth of about 1 mm, remained clear to the eye. The behaviour of these crystals is very similar to that observed for the potassium halides apart from the formation of colloidal centres in preference to isolated electron excess centres.

The situation for crystals of NaCl and NaF is slightly more complex with at least three different zones to consider. For both crystals the nature of the rare earth impurity appears to be of little consequence to the overall distribution of the colour centres. For NaCl crystals there are three basic zones; a very thin outer clear edge (zone 1), a broad blue-grey region of around 2 mm width (zone 2) and a central region of predominantly brown coloration but with a hint of grey (zone 3). Although the three zones have well defined boundaries, the coloration within each zone is not in general as uniform as was observed for the potassium halides. Sometimes "splashes" of colour from one zone are observed within an adjacent zone. For example there were often irregular regions of yellow coloration present within zones 1 and 2. In certain cases, and particularly where ytterbium had been used to colour the crystal, the yellow regions became more extensive and formed a zone of their own (denoted by zone 2').

The relative broadness of the major zones in NaCl enabled an optical absorption spectrum to be recorded individually for each zone. The various spectra obtained for a typical sample of NaCl:Yb^{2+} are shown in figure 7.7. Zones 2 and 3 are characterised by the presence of two broad absorption bands, one centred around 468 nm (21370 cm^{-1}) and the other at between 600 nm (16667 cm^{-1}) and 700 nm (14286 cm^{-1}). The shorter wavelength band is attributed to the F-band, even allowing for a small shift from the expected position of 465 nm (21505 cm^{-1}) [1]. The longer wavelength band is due to absorption by colloidal particles. The position of this band is more variable, with the shift towards longer wavelengths being associated with colloids of increasing size. Cooling of the same crystal to LNT resulted in a shift of the 468 nm band to shorter wavelength (459 nm (21786 cm^{-1})). This observation agrees well with the behaviour expected of the F-band. The bands between 600 nm and 700 nm display negligible change in position on cooling which is to be expected for colloids.

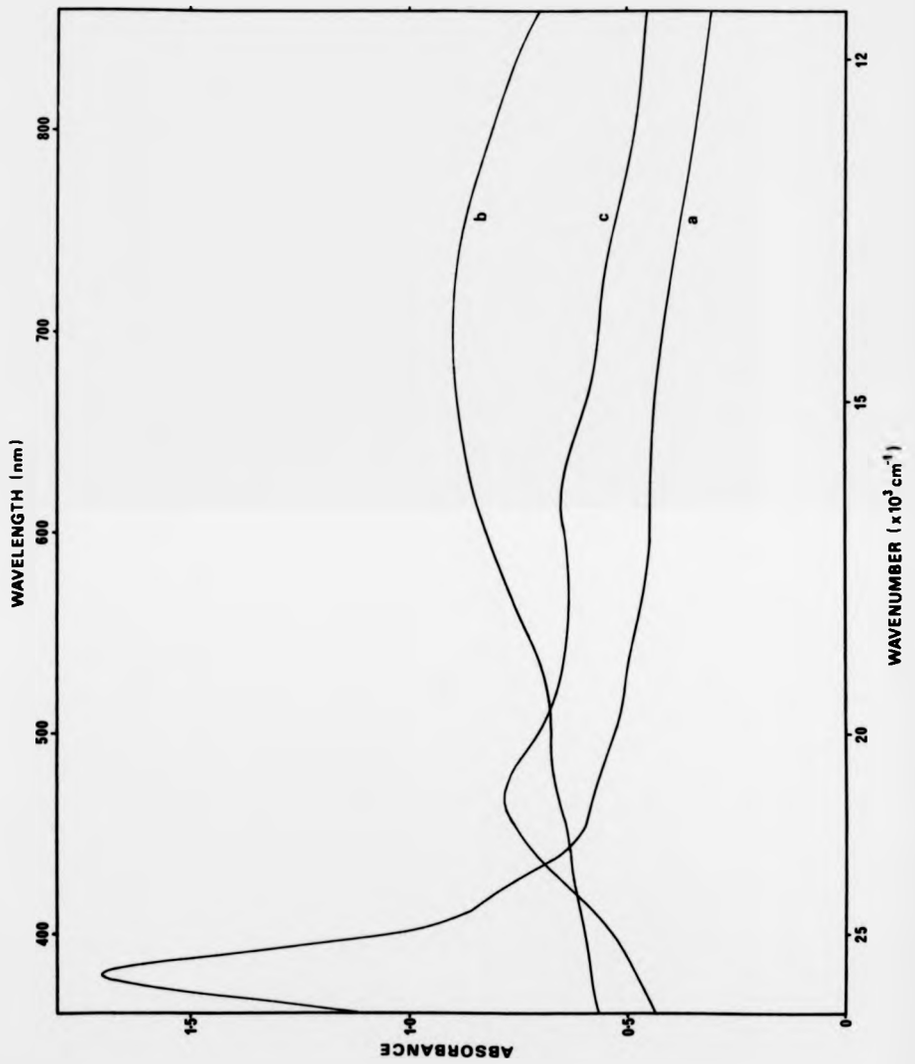

Figure 7.7 Characteristic optical absorption spectra for the various different zones in an aliovalently coloured crystal of NaCl:Yb^{2+}; (a) zone 1, (b) zone 2 and (c) zone 3.

The different perceived coloration associated with zones 2 and 3 depends basically on the relative intensity of the F-band and the colloid band. The F-band dominates in zone 3 resulting in the brown coloration; the colloid band dominates in zone 2 giving rise to the blue-grey coloration. Zone 1 is characterised by the presence of the rare earth impurity ion absorption bands in the ultraviolet and with negligible features in the visible. In addition to the rare earth bands there is an underlying absorption at around 420 nm (23810 cm^{-1}). The intensity of this new absorption band is variable within zone 1 and is responsible for the observation of irregular areas of yellow coloration. The yellow coloration that characterises zone 2′ is similarly attributed. Unfortunately it was not possible to study this band in detail due to a strong overlap with either the A1 band of the Yb^{2+} impurity or the lower wavelength band of the Eu^{2+} impurity. The close proximity of zones 1 and 2′ prevented either region being observed in isolation.

Crystals of NaF containing either ytterbium or europium behave in a very similar manner to crystals of NaCl. Three distinct coloured zones are observed of which the outer region (zone 1) did not appear clear to the eye but took on a grey-blue appearance. The adjacent region (zone 2) varies from a vivid orange colour next to the boundary with zone 3 to a more red-orange colour at the boundary with zone 1. Even though there is a smooth variation of coloration within this region, it is still registered as a single zone since it possesses sharp boundaries with the adjacent regions. The inner region (zone 3) is characterised by a pink-orange coloration.

Using the TS attachment it was possible to determine the characteristic absorption bands for each of the three zones present in NaF crystals. The relevant spectra for $NaF:Yb^{2+}$ are shown in figure 7.8. Zone 1 is characterised by the Yb^{2+} absorption bands in the ultraviolet, a broad weak band in the visible centred around 510 nm (19608 cm^{-1}) and a weak underlying

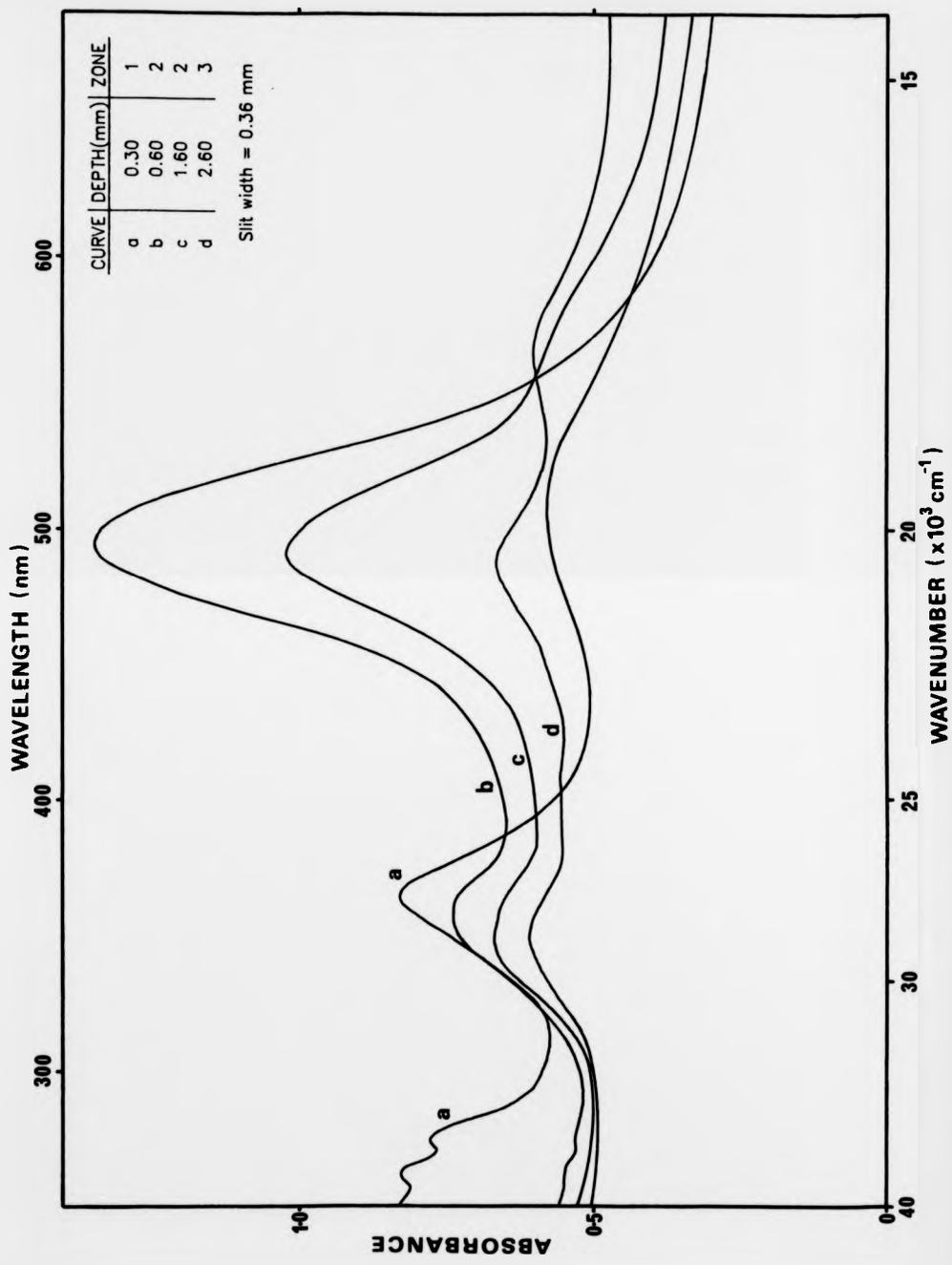

Figure 7.8 Optical absorption spectra obtained using the TS assembly for an aliovalently coloured crystal of NaF:Yb^{2+}. The crystal has been sampled at the depths indicated below its surface (total depth of crystal is 6.5 mm). The zones to which the different curves correspond are also indicated.

band at 353 nm (28329 cm^{-1}). Zone 2 is characterised by a strengthening of the band at 353 nm, which is identified as the F-band, and the appearance of a very strong X-band absorption at 480 nm (20833 cm^{-1}). The intensity of the X-band absorption varies from one edge of zone 2 to the other, resulting in the observed colour change from strong red-orange to orange. Finally, zone 3 is characterised by the appearance of a new band at approximately 568 nm (17606 cm^{-1}) in addition to the F-band and X-band. This new band is attributed to large colloid formation.

The relatively broad zones encountered for crystals of NaF meant that a single zone could be isolated for further more detailed study. Figure 7.9 shows the optical absorption spectrum for zone 2 at both RT and LNT. The F-band is observed to sharpen and shift from 353 nm to 345 nm (28986 cm^{-1}) on cooling. The X-band similarly sharpens and shifts from 480 nm to 475 nm (21053 cm^{-1}). The X-band shift is less pronounced and appears to be associated to a large extent with a general reduction of the long wavelength tail. Figure 7.10 illustrates the effect on the optical absorption spectrum of annealing the specimen at 630°C for various time periods. The X-band disappears and is replaced by the colloid band which shifts gradually toward longer wavelength as the colloidal particle size increases. The F-band is reduced significantly in intensity but any F-aggregate bands which may have been formed are completely masked by the broad and intense colloid absorption.

7.2.3 The identification of perturbed U-centres

The TS spectra shown earlier for crystals of KCl and KBr containing ytterbium (figures 7.1 and 7.6 respectively) exhibit curious behaviour in the vicinity of the standard U-centre absorption band. The U-centre normally gives rise to a single absorption band of approximately Gaussian shape positioned at 214 nm (46729 cm^{-1}) for KCl and 228 nm (43860 cm^{-1}) for

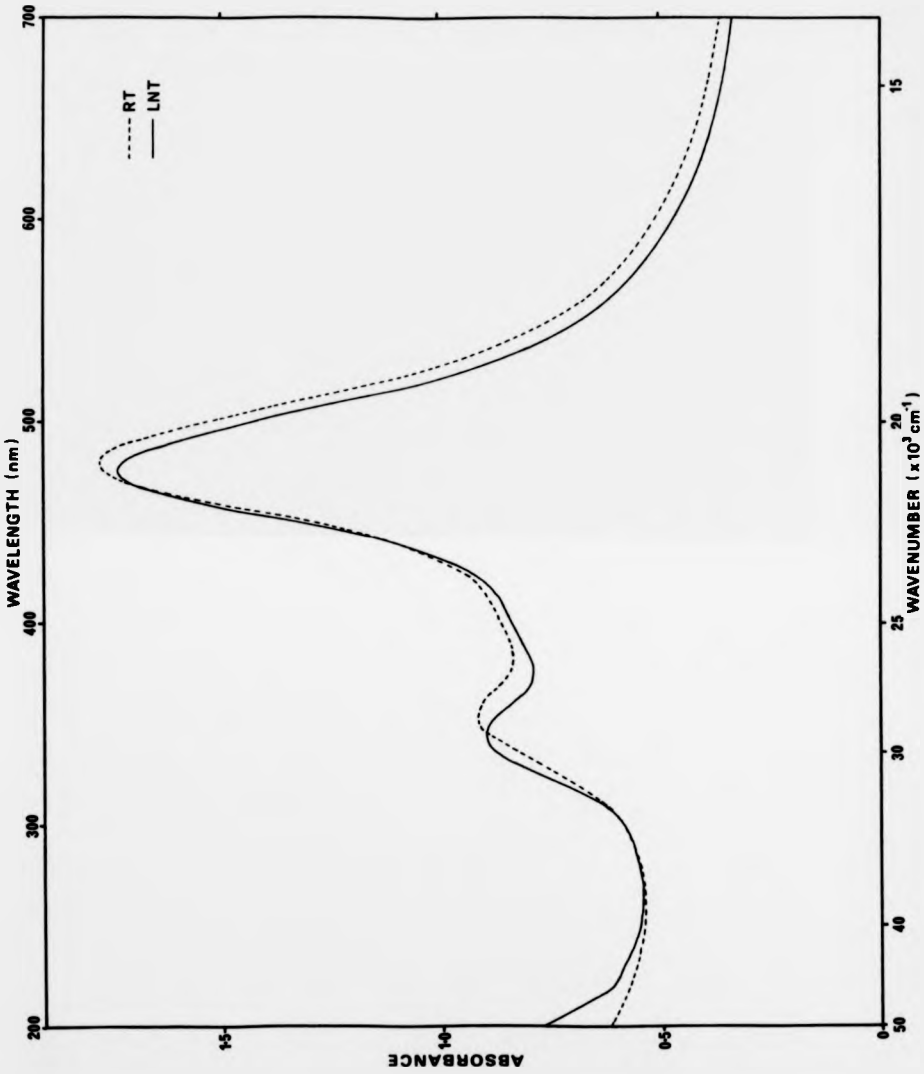

Figure 7.9 The optical absorption spectrum for zone 2 of a coloured NaF:Yb^{2+} crystal at RT and LNT.

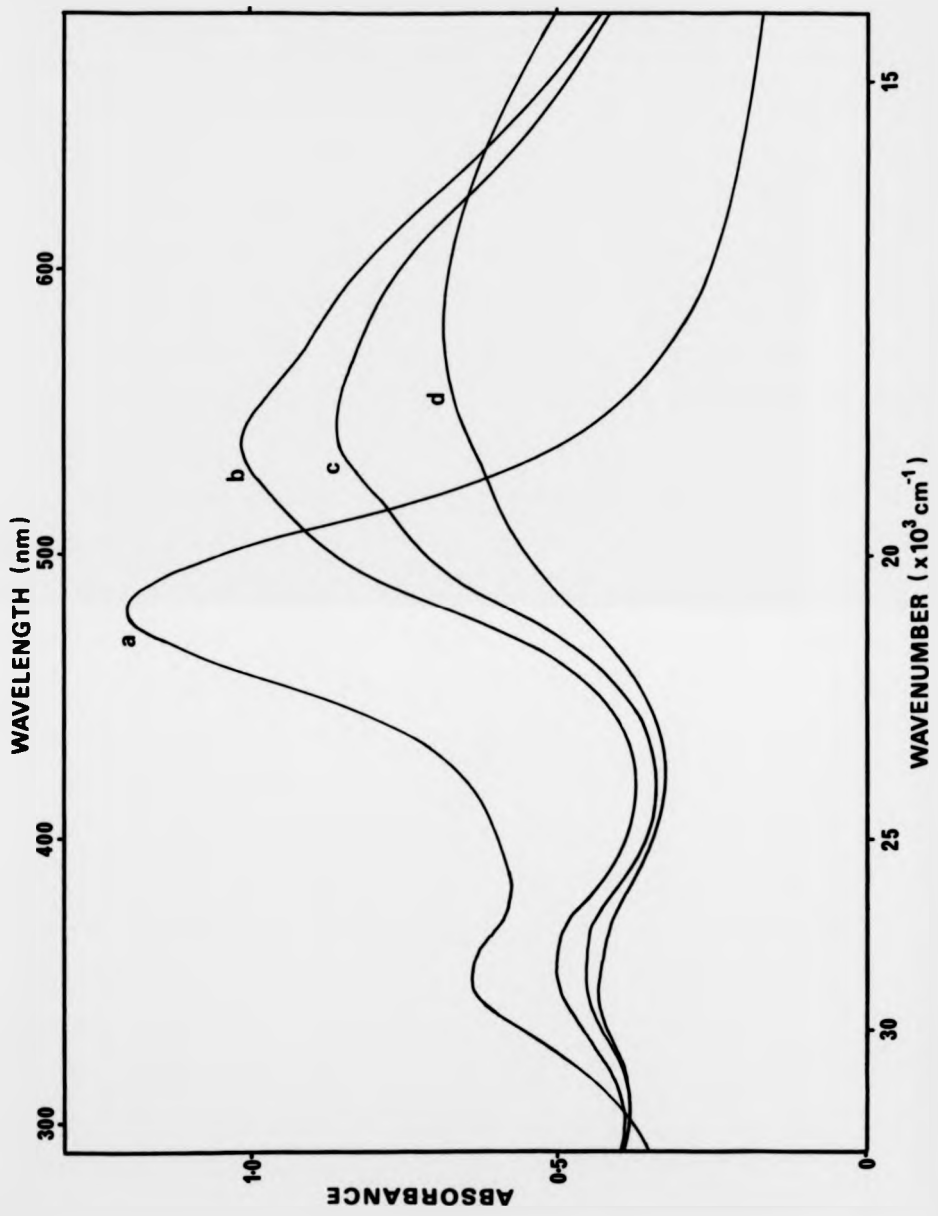

Figure 7.10 The effect of annealing at 630°C on the optical absorption spectrum associated with zone 2 of a coloured crystal of NaF:Yb^{2+}; (a) as produced, (b) after 20 minutes, (c) after 40 minutes and (d) after 120 minutes.

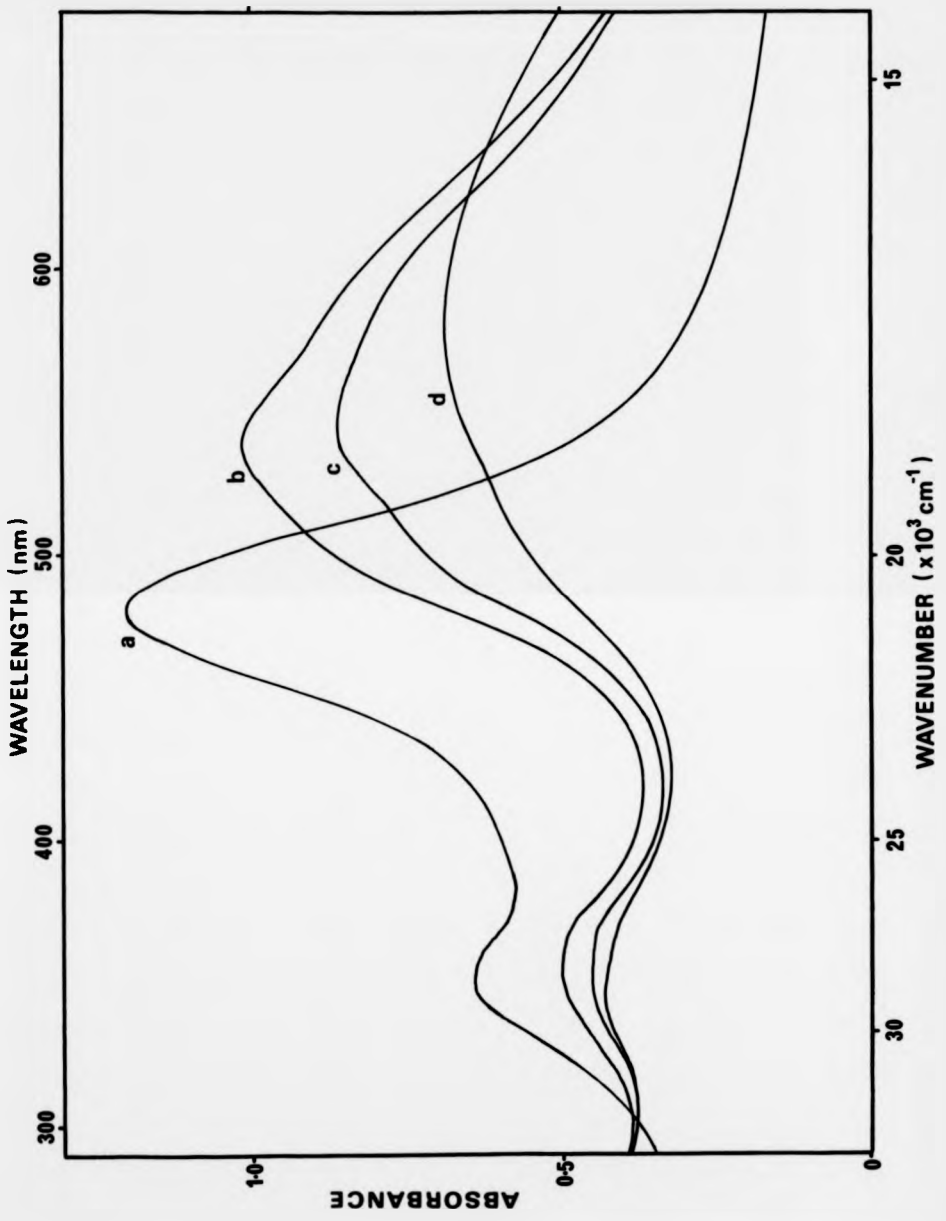

Figure 7.10 The effect of annealing at 630°C on the optical absorption spectrum associated with zone 2 of a coloured crystal of NaF:Yb^{2+}; (a) as produced, (b) after 20 minutes, (c) after 40 minutes and (d) after 120 minutes.

KBr. In the outer regions of these ytterbium-doped crystals the intense U-band appears to be split into two separate bands. These bands occur at 205 nm (48780 cm^{-1}) and 226.5 nm (44150 cm^{-1}) for KCl and at 216 nm (46297 cm^{-1}) and 236 nm (42373 cm^{-1}) for KBr. They are of different intensity with the most intense band being situated towards higher energy for KCl and towards lower energy for KBr. The splitting only occurs at the surface where the Yb^{2+} concentration is at its highest. Deeper into the crystal the two bands gradually weaken and simultaneously merge to reform the single U-band.

A similar behaviour has not been directly observed for europium doped crystals. A distinct broadening of the U-band occurs for some samples and, therefore, the difference is probably due to the lack of suitable specimens rather than to any intrinsic difference between the two rare earth impurities. A second possible reason for the difference is the fact that the U-centre concentration in crystals doped with europium was usually less than for crystals doped with ytterbium.

An experiment was performed to test the thermal stability of the new absorption bands. A crystal of $KCl:Yb^{2+}$ displaying the double band structure was heated to 600°C in air for 10 minutes. No change was observed in the absorption bands following this treatment, indicating excellent stability.

It is interesting to note a resemblance between the relationship of the new bands to the standard U-band and the relationship of the F_A-bands to the F-band. There is certainly a close resemblance for KCl, although for KBr the two bands are reversed in intensity. The U-centre is very similar in structure to the F-centre. The F-centre consists of an electron trapped in the potential well created by an anion vacancy whereas the U-centre consists of an electron trapped in the potential well created by a substitutional hydrogen ion (H_X^-). As a consequence of the similarity between the two defect centres, the allowed

optical transitions will be of the same form in each case. Differences in the central potential field give rise to the observed differences in the energy of the main s – p transition. F_A-bands are observed when the F-centre is perturbed by an univalent impurity which is present on a nearest neighbour cation site along the <100> direction. The single triply degenerate p-like excited state is split into two states (one of which is doubly degenerate) by the reduction in symmetry. The doubly degenerate band is the most intense and is situated at a higher energy than the singly degenerate band.

The two new bands observed in the vicinity of the U-band behave as if some symmetry lowering mechanism is operative. If the cause were a univalent impurity ion situated along the <100> direction, then the resulting bands (U_A-bands) would certainly resemble the F_A-bands. It is known, however, that the new bands are associated with the presence of a divalent impurity ion, plus presumably the charge compensating cation vacancy. Therefore, although it is rather difficult to reconcile the observed reversal in intensity of the perturbed bands between KCl and KBr using a U_A-type model, it may be possible to describe the behaviour based on a U-centre perturbed by a divalent impurity-cation vacancy pair, that is a type of U_2-centre.

There are a number of possible arrangements for the U-centre plus a divalent impurity-cation vacancy complex. Four of the most probable arrangements are shown schematically in figure 7.11. Configurations (a), (b), and (c) represent to first order the same overall reduction in symmetry at the U-centre (toward C_{4v}); configuration (d) represents an altogether lower symmetry (only single fold rotations and reflection in (100) plane). The observation of only two absorption bands for KCl and KBr is consistent with a reduction to C_{4v} in both cases. As a lower symmetry would result in three bands, arrangement (d) is rejected. The intensity distribution observed for KCl is consistent with a model similar

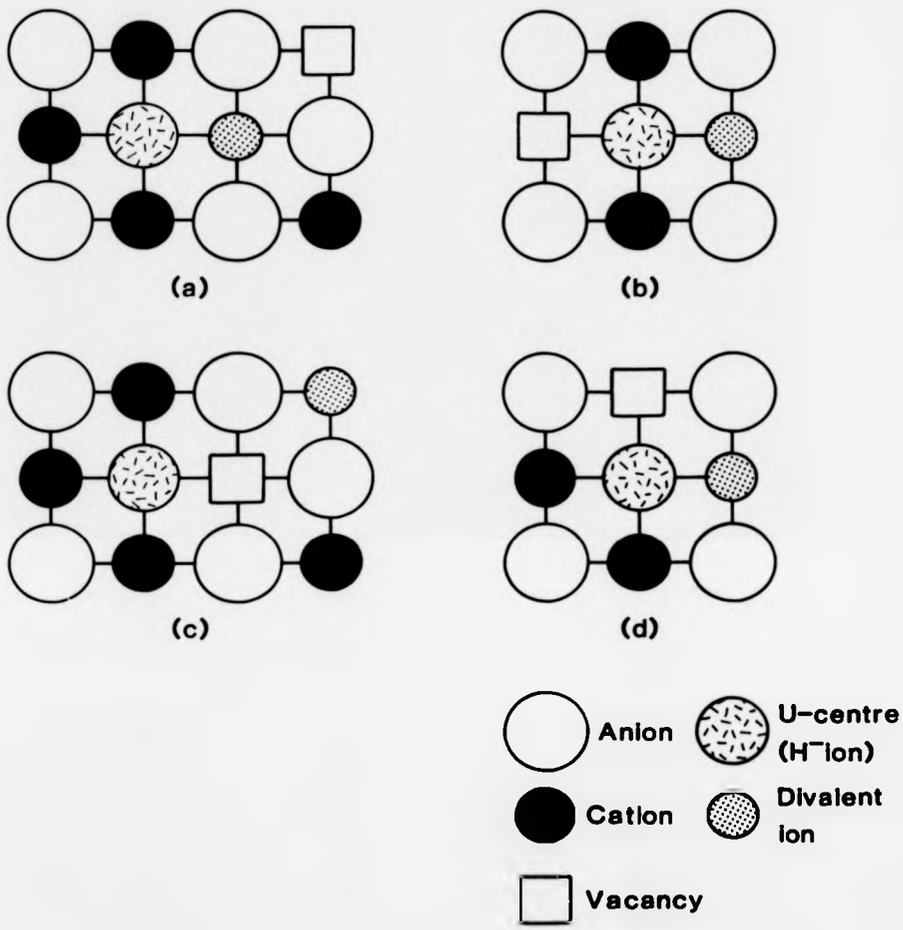

Fig. 7.11 A schematic representation of the four most probable arrangements of a U-centre combined with a divalent impurity-cation vacancy complex

in form to the Z_1-centre. The most probable candidate for KCl is therefore arrangement (c) in figure 7.11. This configuration is equivalent to a Z_1-centre with the F-centre replaced by a U-centre.

The reversal of intensity distribution for the two bands in KBr indicates a different type of arrangement in this case. Both arrangements (a) and (b) of figure 7.11 have the divalent impurity ion situated next to the U-centre. The impurity ion possesses an effective positive charge and consequently the crystal field strength is increased along that direction. A configuration of this type would give rise to a shift of the singly degenerate (less intense) band to a higher energy than the doubly degenerate band. An arrangement of type (b), although giving the correct symmetry, has not been previously reported in the alkali halides at RT due presumably to the relative stability of the impurity-vacancy complex [2]. Arrangement (a) is not normally observed for an F-centre since the centre becomes more stable by the addition of a second electron to form a Z_2-centre. Note that the F'-centre acts as an intermediary in the Z_2-centre formation process. The trapping of a second electron does not occur for the U-centre and therefore arrangement (a) is more likely in this instance to be the stable configuration. Consequently it is thought to be the most suitable model for the perturbed U-centre in KBr.

The author is unaware of any mechanism which could render arrangement (a) the most favourable for KBr but arrangement (c) most favourable for KCl. The two models are proposed solely as possible explanations for the different splittings observed for the perturbed U-centre in two seemingly equivalent hosts. It is not possible, based on the limited information currently available, to offer anything more than a speculative preliminary judgement.

It is unfortunate that ESR measurements were not made on these samples since such information would, in principle, allow the correct model to be identified. This information would be especially interesting for the case

of a Eu^{2+} perturbed U-centre where both entities are paramagnetic. A comparison could then be made with the case of a Yb^{2+} perturbed U-centre, where only the U-centre resonance would be observed. The strong spatial localisation of these defect centres in an area which is free of F-centres will allow the spectra to be studied without any attendent problems of overlap.

7.3 The aliovalent coloration of potassium fluoride

7.3.1 Introduction

Potassium fluoride crystals coloured readily using the aliovalent coloration technique. This observation is in itself very interesting since it is generally regarded as difficult or even impossible to colour KF crystals by any other technique except high energy electron or X-ray irradiation [3-6]. Both ytterbium and europium have been used with seemingly identical results. The coloration is similar in form (two zone) to that described earlier for crystals of KCl and KBr. The only significant difference is that the yellow coloration associated with the presence of F-centres extends much closer to the crystal surface. The outer clear zone is still present but it is very thin and difficult to resolve by eye. Experiments performed using the TS assembly suggest a width for this zone of approximately 0.2 mm.

On some occasions when the F-centre concentration was particularly high, a blue-green coloration appeared in the central region of the crystal. An optical absorption spectrum obtained for this region indicates the presence of M-centres at 650 nm (15385 cm^{-1}) and colloid centres at 685 nm (14599 cm^{-1}).

7.3.2 Optical bleaching experiments

Coloured crystals of KF behaved differently from the other potassium halides during optical bleaching. Exposing a coloured crystal to white light, even very briefly, resulted in the yellow coloration associated with the F-band (448 nm (22321 cm^{-1})) changing to an orange-brown colour in the outer regions. The width of this outer region for KF appeared to be of a similar order to the width of the outer clear zone observed for the other potassium halides. The central region remained yellow in colour. This same behaviour occurred regardless of whether the crystal was doped with ytterbium or europium. Due to the sensitivity of the coloured crystals to light, they were always handled under filtered light to prevent F-band bleaching.

Figure 7.12 illustrates the effect of F-band illumination at RT using 450 nm (22222 cm^{-1}) light applied in relatively short duration bursts. Initially the F-band assumes an asymmetrical shape with the peak shifting towards slighly higher energies. As the bleaching continues, the peak gradually shifts back towards the normal F-band position and the absorption band finally assumes the usual Gaussian shape. The M-band at 650 nm (15385 cm^{-1}) appears during the bleaching process along with a new band at around 530 nm (18868 cm^{-1}) for longer bleaching times. The new band occurs alone and it is well removed from the expected positions of the R-bands, for example the R_1-band occurs at 570 nm (17544 cm^{-1}) [7]. It is the simultaneous presence of the F-band and the 530 nm band that is responsible for the observed orange-brown coloration following optical bleaching. The 530 nm band will be referred to as the Q-band in subsequent discussions. The origins of the asymmetry and the identity of the Q-band are now considered.

An optically bleached $KF:Yb^{2+}$ crystal was investigated using the TS assembly. A typical colour centre distribution is shown in figure 7.13. It can be seen that the centre responsible for the Q-band is confined to a region ranging between approximately 0.2 mm and 0.5 mm beneath the crystal

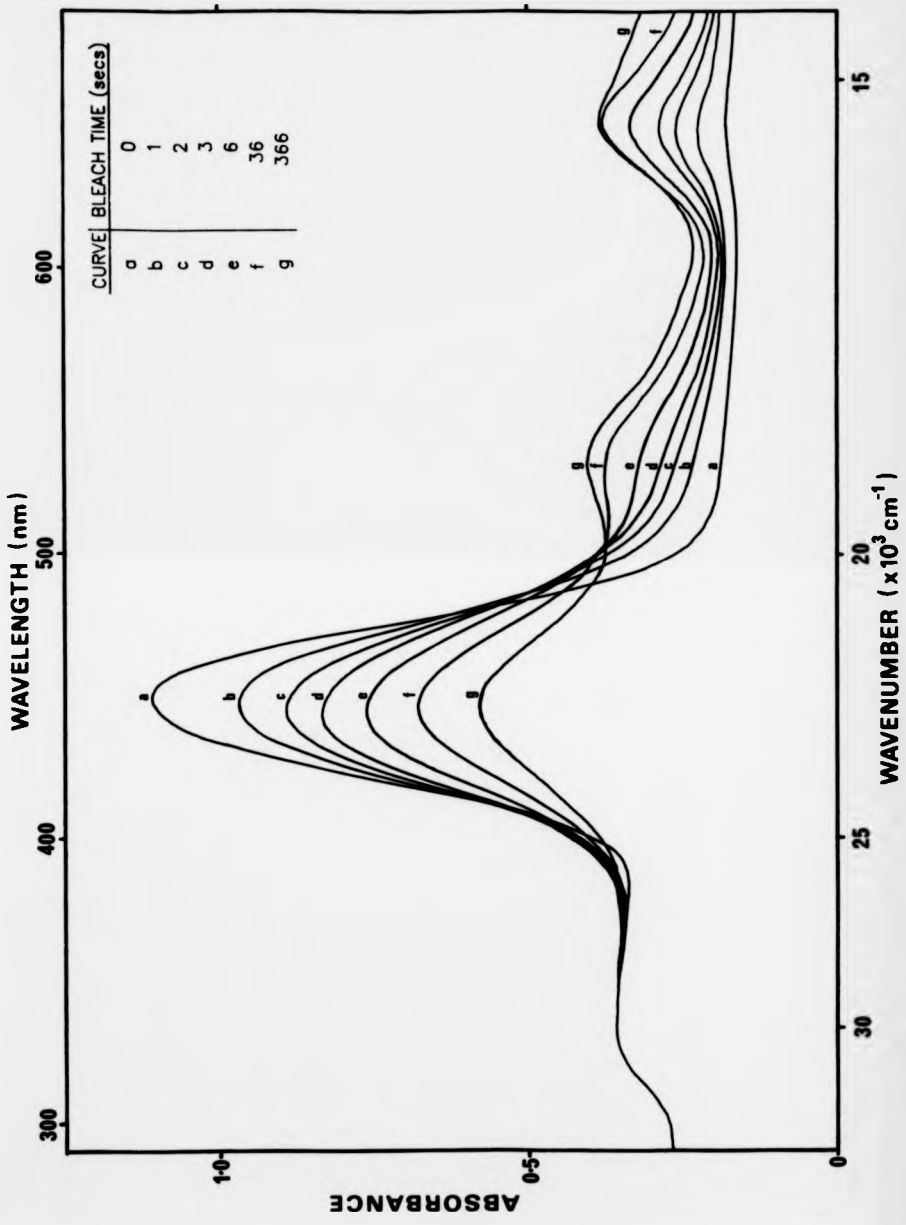

Figure 7.12 The effect of F—band (450 nm) illumination at RT on the optical absorption spectrum of aliovalently coloured KF:Eu^{2+}. The total bleaching times for each curve are indicated in the figure.

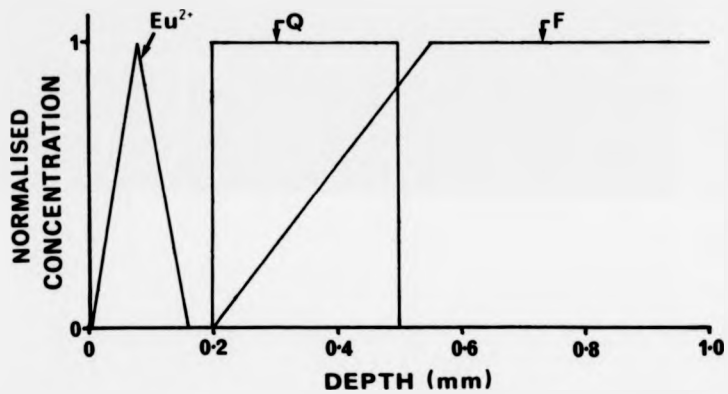

Figure 7.13 Approximate defect centre distributions for a typical aliovalently coloured crystal of KF:Eu^{2+}.

surface. As there is zero overlap of the region containing the Q-band with the extreme outer zone containing ytterbium, the Q-band is not associated with a Z-centre.

KF crystals containing europium behaved in an identical manner to the ytterbium doped specimens. Optical bleaching similarly resulted in the formation of the Q-band at 530 nm. In general the Q-band is slightly more prominent in crystals of $KF:Eu^{2+}$. This observation is thought to be related to the shorter times and slightly lower temperatures normally employed for the diffusion of europium. It implies that the Q-band is associated with a defect centre which is present only in the outer regions of the crystal and to an extent determined by the previous heat treatment.

A study was made of the origins of the asymmetry observed in the F-band during the initial stages of bleaching. The sample was exposed to low intensity F-band illumination at RT and then cooled immediately to LNT. The optical absorption spectrum was recorded at LNT in order to resolve individual bands. The process was repeated a number of times and a detailed record of the changes was obtained. The result is shown in figure 7.14. The initial F-band illumination leads to the rapid increase of a pair of bands underlying the F-band with peaks at around 426 nm (23474 cm^{-1}) and 472 nm (21186 cm^{-1}). These two bands always appear together and will be referred to as the S-bands. The observed asymmetry of the F-band at RT is due to the simultaneous presence of these bands. The Q-band, which is situated at 522 nm (19157 cm^{-1}) at LNT, is weak at this stage. As bleaching is continued, the intensity of both F-band and S-bands decreases. At the same time, the intensity of the Q-band and M-band increases. There is some evidence to suggest that, if during this stage the Q-band is optically bleached, there is a regrowth of both the F-band and the underlying S-bands. Further F-band illumination results in a saturation of the Q-band, the disappearance of the S-bands and the formation of additional F-aggregate bands.

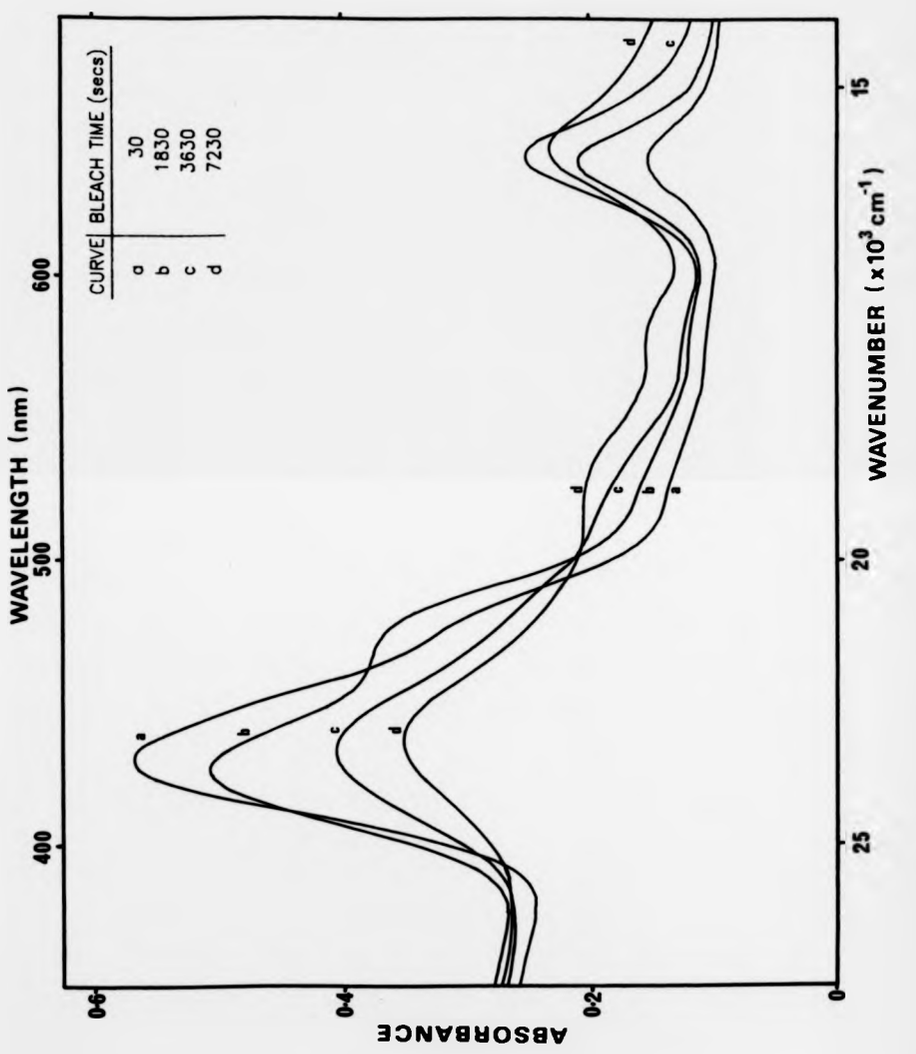

Figure 7.14 The effect of F—band (450 nm) illumination at RT on the optical absorption spectrum of aliovalently coloured KF:Eu^{2+}. Spectra have been recorded at LNT. The total bleaching times for each curve are indicated in the figure.

If a crystal is cooled to LNT directly after impurity diffusion, then only the F-band (plus in some cases a small M-band) is observed. Prolonged F-band illumination at this temperature results in very inefficient bleaching of the F-band. There is only a very small conversion of F-centres into the centres responsible for the S-bands and the Q-band. This observation implies the need for ionic motion during the formation process. Once the Q-band has been formed by F-band bleaching at RT however, then the subsequent bleaching behaviour at LNT is quite interesting. Illumination into the Q-band results in a regrowth of the F-band. Subsequent F-band illumination leads to a regrowth of the Q-band. The conversion process appears remarkably efficient and can be performed repeatedly without producing any new bands or affecting any existing bands (for example the M-band). Figure 7.15 illustrates this behaviour.

The ability to isolate the process of interchange between the F-centres and Q-centres by selective optical bleaching at LNT is able to provide some useful information. The following simple relationship exists between the observed changes in the concentration of F-centres (ΔN_F) and Q-centres (ΔN_Q)

$$\Delta N_F + x\,\Delta N_Q = 0 \qquad 7.1$$

where x represents the number of F-centres that need to be destroyed to produce one Q-centre. Since at LNT only electron interchange is able to take place, x indicates the number of electrons contained in the Q-centre. Equation 7.1 can be rewritten using Smakula's equation as

$$\frac{W_F \Delta A_F}{f_F} + x\,\frac{W_Q \Delta A_Q}{f_Q} = 0$$

or

$$x = -\frac{W_F \Delta A_F}{W_Q \Delta A_Q} \cdot \frac{f_Q}{f_F} \qquad 7.2$$

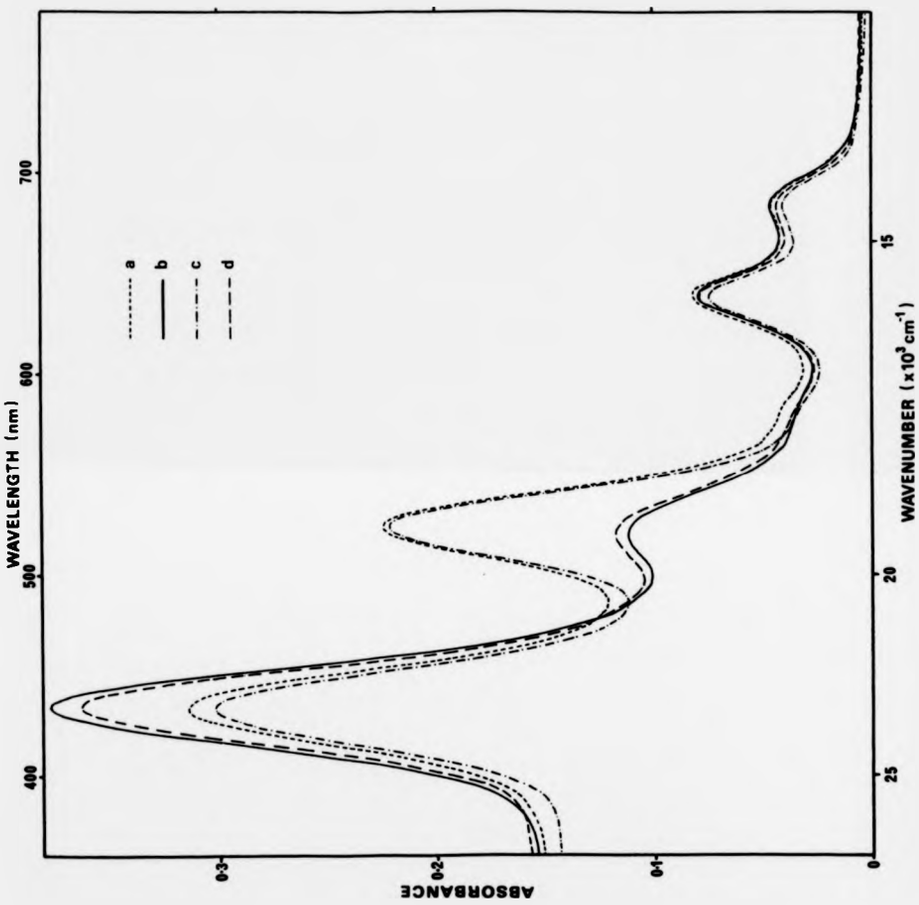

Figure 7.15 Repeated optical conversion between F–centres and Q–centres at LNT. The following sequence is indicated; (a) after Q–band formation at RT, (b) after Q–band (550 nm) illumination at LNT for 5 minutes, (c) after F–band (450 nm) illumination at LNT for 5 minutes and (d) after Q–band illumination at LNT for 5 minutes. The apparent changes in intensity of the M–band and colloid band for this sample are due to systematic baseline shifts.

where the symbols W, f and ΔA represent the half-width, oscillator strength and change in peak absorbance value for each centre. The analysis of spectra such as that given in figure 7.15 yields the following

$$\frac{W_F \Delta A_F}{W_Q \Delta A_Q} \simeq -1 \qquad 7.3$$

and therefore

$$x \simeq \frac{f_Q}{f_F} \qquad 7.4$$

The F-centre oscillator strength in KF is 0.85 [8] and, in order to satisfy $f_Q \leq 1$ with $x = 1, 2, \ldots$, the Q-centre has to be a one electron centre with an oscillator strength about the same as that of the F-centre.

Bleaching of the M-band at RT, once formed, does not appear to affect either the F-band or the Q-band specifically but seems to allow the two distributions to achieve an equilibrium. In fact the intensity of the Q-band soon saturates against illumination of either the F-band or the M-band implying that the Q-centre is to be associated with an impurity or defect which is present in a limited concentration.

In order to check that the new bands are indeed associated with only the outer regions of the inner zone, these outer regions were removed from a typical sample. When the remaining inner section was optically bleached using F-band illumination, only the standard F-aggregate and colloid bands were formed as expected.

7.3.3 Discussion

One of the important discoveries made about the nature of the new colour centres in KF crystals is the need for ionic motion in their formation. At LNT ionic mobility is insufficient to enable either the S-centre or the Q-centre to be formed. The S-centre is the first product of optical bleaching of the F-band. The twin band structure associated

with this defect centre suggests a low symmetry perturbation such as is observed for the F_A-type centre. The S-centre is not too stable at RT and, as it decomposes, a new centre, designated the Q-centre, is formed. The Q-centre gives rise to a single absorption band situated at a longer wavelength than either the F-band or S-bands. A unique one-to-one relationship exists between the F-centre and the Q-centre with respect to optical bleaching. Optical bleaching measurements also show that the Q-centre is a one electron centre.

The new colour centres occur within the outer regions of the crystal but at a depth much larger than the rare earth impurity diffusion depth. They are not therefore to be associated directly with the rare earth impurities. It is most likely that they are associated with impurities which are already present in the as-received crystal. Heating the crystal at a high temperature in the presence of a vapour of ytterbium or europium produces some modification in the distribution and nature of the native impurities. The observation of a more pronounced region containing the new colour centres for europium-doped compared with ytterbium-doped crystals is consistent with such a dependence on previous heat treatment. Shorter diffusion times and slightly lower temperatures were used for the diffusion of europium, a procedure which appears to create a larger concentration of impurities in the required state.

It is well known that a common impurity in the alkali halides is water and its many derivatives, such as the hydroxyl ion OH^-, various hydrogen-based centres (for example the U-centre) and numerous oxygen-based centres (for example O^-, O^{2-}, O_2^- and O_2^{2-}). It is also known that the presence of many of these centres has a profound effect on the colourability of the alkali halides. For example, the OH^- ion is thought to be responsible for the difficulty observed in colouring the alkali fluorides [9]. Similarly, the introduction of a high concentration of OH^- ions into KCl crystals creates a similar situation of

non-colourability [10].

A number of workers have shown that heating alkali halide crystals in various different atmospheres has a dramatic effect on the nature and distribution of these water-related centres. Matsumura and Kuczynski [11] and Kuczynski et al [12] have studied colour centres formed by ultraviolet irradiation of KCl crystals heated at 600°C both in vacuum and in a gettering atmosphere. There are a number of similarities between the spectra they present and the spectra described earlier for an optically bleached KF crystal (figures 7.14 and 7.15). For example, the absorption band at 625 nm (16000 cm^{-1}) in KCl, which they designate the Y'-band, behaves in an analagous way to the Q-band in KF. In addition there is an underlying band in the vicinity of the F-band in KCl, although this does not exhibit the same F_A-like twin-band structure. A paper by Dumke [13] has described an absorption band in KCl which also resembles the Q-band in KF. In this case the band is associated with the centre FU_2, which is an F-centre next to an interstitial hydrogen atom (H_i^+). This particular centre is only stable below 120 K and is therefore unlikely to be the Q-centre in KF. Rusch and Seidel [14,15] have studied in detail the $(H_2O)^-$ centre in KCl, which is an F-centre containing an H_2O molecule (that is $(H_2O)^{\times}_{C_l}$). The optical absorption associated with this centre reflects the reduction in symmetry created by the presence of the water molecule. The F-band is split into two absorption bands at 523 nm (19130 cm^{-1}) and 595 nm (16800 cm^{-1}). A strong resemblance is apparant between the shape of these F_A-like bands in KCl and the S-bands in KF. In addition it is interesting that the separation between the two bands is 2330 cm^{-1} (0.29 eV) for both KCl and KF. There is evidence to suggest that the $(H_2O)^-$ centre is only stable up to about 220 K in KCl. The situation in KF is likely to be slightly different. Smaller interstitial sites are available for the H_2O molecule to move into and stability will be further aided by the greater ionicity of the KF lattice. Consequently the H_2O^- centre could be stable in KF up to around

room temperature.

Based on the above observations, a possible process by which the S-centre and Q-centre are produced in KF is now be described. Both ytterbium and europium are excellent getters and heating the KF crystal in a gettering atmosphere results in the formation of $(H_2O)_i$ centres. Quenching the crystal to RT serves to prevent these centres from dissociating. The interstitial water molecule is free to move at RT and can interact with an anion vacancy and an electron freed from an F-centre to form an $(H_2O)^-$ centre. The S-centre is therefore an electron trapped at a substitutional water molecule. Continued optical bleaching results in the destruction of the S-centre and the formation of the Q-centre. The Q-centre must therefore be associated with some decomposition product of the S-centre. The Y'-centre in KCl [11,12], which behaves in a similar way to the Q-centre, has been attributed to an F'-centre situated next to a substitutional O^- ion. In the present study it has already been established that the Q-centre is a one electron centre so this particular model is not applicable. Possible products of the direct decomposition of H_2O are O^-, OH^- and H_i. However it is difficult to account for the formation of the Q-centre involving these entities. Although it is impossible to determine the precise structure of the Q-centre from the limited available information, it is likely that it is caused by the interaction of the water molecule with a second water related impurity. For example the interaction of $(H_2O)_i$ and O^- centres is likely to produce the OH_i centre. If the OH_i centre were present next to an F-centre then it could conceivably produce an absorption band similar to that described for the FU_2-centre [13] but would also be more thermally stable due to its greater size.

It is once again unfortunate that ESR spectra were not obtained for these crystals, since it might then have been possible to investigate the validity of the models proposed.

7.4 The aliovalent coloration mechanism

7.4.1 Introduction

The aim of this section is to develop a model to describe the observed coloration of the alkali halides following aliovalent impurity diffusion. The description is centred on the results obtained for the potassium halides, since for the sodium halides the presence of strong colloid bands tends to mask many of the important absorption bands. The basic coloration mechanism is in any case essentially the same in both types of crystal. The various results described earlier in this chapter will be reassessed in an attempt to gather all of the relevant facts. A number of additional experiments will be described. These experiments were devised in an attempt to yield further information on the coloration process.

7.4.2 Additional coloration experiments

The first of the additional experiments assessed the effect of ultraviolet irradiation on the various defect centres present following aliovalent coloration. The absorption of ultraviolet light can lead to the destruction of certain defect centres and the production of others. The commonest reactions are given by [10,16,17]

$$h\nu(OH^-): \quad OH_x^x + V_x^{\cdot} \longrightarrow V_x^x + OH_i^x \qquad 7.5$$

$$h\nu(U): \quad H_x^x + V_x^{\cdot} \longrightarrow V_x^x + H_i^x \qquad 7.6$$

$$h\nu(O^{2-}): \quad O_x^{\prime} + V_x^{\cdot} \longrightarrow V_x^x + O_x^x \qquad 7.7$$

where the illumination is directed into the impurity band indicated. Most alkali halide crystals contain variously OH^- impurities, U-centres or O^{2-} impurities and therefore the normal result of ultraviolet irradiation is

the production of F-centres. Of the three reactions above, the bleaching of U-centres is the most efficient. The behaviour of a crystal under ultraviolet irradiation can therefore provide evidence of the presence of certain defects and also their position within the crystal.

Crystals of KCl:Yb^{2+}, coloured by the aliovalent coloration technique and consisting of an outer clear zone and an inner F-coloured zone, were subjected to the light from a high pressure Hg lamp. The extreme outer edge became lightly coloured while the main part of the outer zone remained clear. Optical absorption measurements made on this extreme outer edge revealed the presence of the Yb^{2+} impurity, the F-band and a new absorption band around 590 to 600 nm (16949 to 16667 cm^{-1}) measured at LNT. This new band agrees well in position with the Z_1-band [18]. Heating the specimen at 100°C for 15 minutes resulted in the destruction of the Z_1-band and a reduction in the overall F-centre concentration. Simultaneously a new weak absorption band appeared at around 670 nm (14925 cm^{-1}) at LNT, which agrees well in position with the Z_2-band [18].

From the TS measurements on coloured crystals made earlier, there is a large U-centre concentration at the very surface of the crystal. The results described above are therefore consistent with the creation of F-centres through the destruction of U-centres. The observation of Z-centres following this treatment confirms that the Yb^{2+} impurity ions and the newly formed F-centres are contained within the same region of the crystal.

A check was also made on the behaviour of the perturbed U-centres described earlier (section 7.2.3) under ultraviolet irradiation. Even prolonged exposure to ultraviolet radiation was unable to produce any change in the absorption band structure. Therefore it must be those U-centres which are not complexed with the impurity ion which are destroyed by ultraviolet light to produce the F-centres. Once the U-centre is complexed with the impurity, then apparently it becomes a very stable and

effective electron trapping centre.

The following experiment was devised in an attempt to observe the coloration process directly. A small hole (1 mm diameter) was drilled to a depth of about 2 mm into a KCl crystal. A sliver of ytterbium metal was placed into the hole and the crystal was held under vacuum inside a quartz tube. The tube was then inserted into a furnace preheated to 700°C. Immediately on insertion, a cloud of coloration appeared around the hole and continued to spread outwards into the bulk of the crystal. This behaviour is illustrated schematically in figure 7.16. The evolution of the colour cloud from the point of contact of the ytterbium metal resembles very strongly the process of electron injection from the pointed cathode during electrolytic coloration [1,19]. The implication is that electron injection is an important part of the aliovalent coloration process.

A KCl crystal coloured using the above technique was removed from the heated tube after approximately 30 seconds and quenched to RT. The crystal was cleaved into a number of thin slices perpendicular to the drilled hole. The thin slices clearly show that the coloured region is circular in cross-section with the hole at the centre and consists of F-centres. It is important to note that there is a thin clear outer zone situated about the inner surfaces of the hole which is in agreement with the behaviour observed for crystals heated in an ytterbium or europium vapour. Thus it appears that the coloration mechanism is identical in both cases.

7.4.3 Discussion

An analysis of the above results suggests that there are two separate mechanisms involved in the coloration process. The first relates to the formation of distinct zones within the alkali halide crystal as a result of subjecting the crystal to high temperatures. The second mechanism is concerned with the formation of colour centres via the injection of

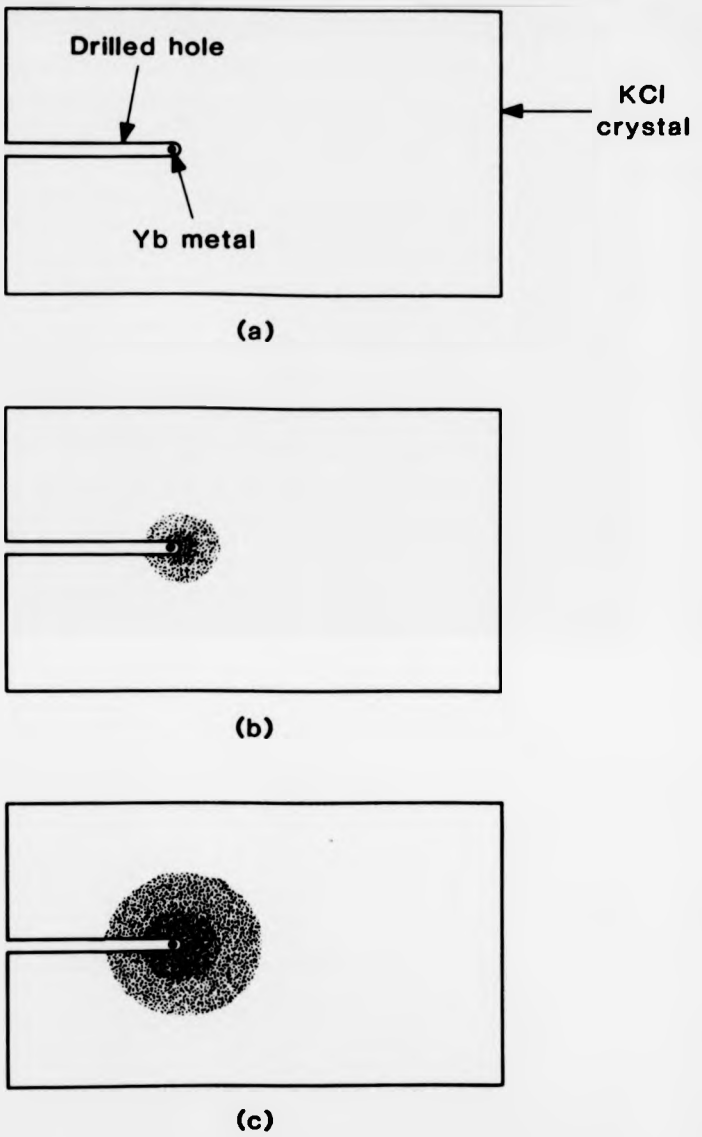

Fig. 7.16 A cross-sectional view of the evolution of an F-centre colour cloud from a small piece of Yb metal situated within a hole drilled in a KCl crystal. The different stages depicted are; (a) before heating, (b) after about 1 minute at 700°C and (c) after about 4 minutes at 700°C

electrons. Electron injection appears to be associated with the simultaneous presence of the rare earth impurity. Quenching of the crystal to RT is a necessary procedure for the observation of colour centres since slow cooling allows them to thermally bleach out.

Ikeda [20], Matsumura and Kuczynski [11] and Kuczynski et al [12], have all observed the formation of concentric zones of differing properties for alkali halide crystals heated under different conditions. Ikeda has shown that for crystals of KCl heated in vacuum at 600°C, there is a desorption of OH^- ions from the surface. The width of the desorbed region is inversely related to the initial OH^- ion concentration. In addition, he observed that heating the crystal in a Cl_2 atmosphere results in a significant increase in the width of the desorbed region. In general the desorbed widths are of the same order (0.3 mm to 1 mm) as the width of the clear outer zone created during aliovalent coloration. A new absorption band at 240 nm (41667 cm^{-1}) was observed at the interface between the outer and inner regions following desorption of OH^- ions in a Cl_2 atmosphere. The defect responsible has not been positively identified.

Matsumura and Kuczynski [11] and Kuczynskii et al [12] described a similar behaviour for KCl crystals heated in a vacuum at 600°C for several hours. The crystals were exposed to ultraviolet irradiation following the heat treatment and this resulted in the creation of two differently coloured concentric zones. The outer zone possessed a light blue colour while the inner zone exhibited the standard purple F-centre coloration. An optical absorption spectrum of the outer zone indicated the presence of the F-band and two new absorption bands which were associated with two new defect centres designated the Y- and Y'-centres respectively. If the crystal was heated in the presence of a gettering impurity such as tin or magnesium instead of a vacuum, then three zones were produced following ultraviolet irradiation. These zones consisted of an outer clear zone, an

intermediate zone containing the F-, Y- and Y'-centres and a central F-centre coloured zone. The thickness of the intermediate zone was dependent on both the gettering impurity and the alkali halide crystal. In many cases it was sufficiently thin to be virtually undetectable.

Both ytterbium and europium are strong gettering agents and according to the above results might be expected to create three concentric zones within the heated alkali halide crystals. These zones would be specifically an outer clear zone, an intermediate zone containing F-, Y- and Y'-type centres and an inner F-coloured zone. A behaviour of this type is observed for crystals of KF but, interestingly enough, is not apparant for crystals of KCl. It is assumed that in the present work the intermediate zone for KCl crystals is too thin to be observed. The reasons for this difference are not fully understood but are presumably related to the chemical nature of the impurity and to the details of the times and temperatures of the heat treatment/diffusion process. It should also be noted that the extreme edge of the outer clear zone of the KCl crystals prepared in the present work actually contains a high concentration of rare earth impurity ions.

There is little doubt that the different zones described above represent areas containing different combinations of oxygen and water-related centres. The changes in stoichiometry are brought about by the heating process and are affected in detail by the type of atmosphere present. A key effect appears to be the out-diffusion of water-related impurities, such as OH^- or O^- ions, from the surface of the crystal. The outer clear regions therefore correspond to areas possessing a depressed concentration of water-related impurities compared with the bulk. The use of a gettering agent accentuates this effect. At the very edge of the crystal there is the rare earth impurity plus a fairly large concentration of U-centres. The region containing the U-centres is slightly wider than the thin region containing the rare earth impurity. Wherever both U-centre

and rare earth concentrations are simultaneously high, there is a high probability of the formation of perturbed U-centres. In the regions where the U-centre concentration is higher than the rare earth impurity concentration, then the U-centres behave in the normal manner and can be destroyed by ultraviolet irradiation. The destruction of U-centres results in the production of a small concentration of Z-centres.

It is not possible, on the basis of the experimental information presently available, to determine with any degree of confidence the nature of the defects responsible for the S- and Q-bands in KF. The behaviour of these centres is certainly similar to that observed for the Y and Y'-bands in KCl [11,12] although there is evidence to suggest that the model of an F'-centre situated next to a substitutional O^- impurity for the Y'-centre is not applicable to the Q-band. The description of the Y-band as an F_A-centre agrees with the model proposed earlier for the S-centre although the impurity involved is attributed differently. For KF crystals, the S-centre is most probably an electron trapped at a substitutional water molecule $(H_2O)_F^\times$. The Q-centre is tentatively assigned to an F-centre situated next to an interstitial OH impurity $(V_F^\cdot OH_i^\cdot)^\times$.

The central region of the crystal appears to be unaffected by the impurity diffusion process. The behaviour of the colour centres in this region is entirely conventional.

Hitherto only the process by which the concentric zones are formed has been discussed. Zone formation is basically due to a redistribution of water related centres caused by heating the crystal. Zone formation is not necessarily accompanied by the introduction of colour centres. The coloration mechanism is peculiar to a heating of the crystals in the presence of ytterbium and europium. Probably the most important property that these impurities share, and that which distinguishes them from impurities such as tin and magnesium, is their low electronegativity. It would appear that this property is responsible for the preferential release

and rare earth concentrations are simultaneously high, there is a high probability of the formation of perturbed U-centres. In the regions where the U-centre concentration is higher than the rare earth impurity concentration, then the U-centres behave in the normal manner and can be destroyed by ultraviolet irradiation. The destruction of U-centres results in the production of a small concentration of Z-centres.

It is not possible, on the basis of the experimental information presently available, to determine with any degree of confidence the nature of the defects responsible for the S- and Q-bands in KF. The behaviour of these centres is certainly similar to that observed for the Y and Y'-bands in KCl [11,12] although there is evidence to suggest that the model of an F'-centre situated next to a substitutional O^- impurity for the Y'-centre is not applicable to the Q-band. The description of the Y-band as an F_A-centre agrees with the model proposed earlier for the S-centre although the impurity involved is attributed differently. For KF crystals, the S-centre is most probably an electron trapped at a substitutional water molecule $(H_2O)^{\cdot}_F$. The Q-centre is tentatively assigned to an F-centre situated next to an interstitial OH impurity $(V_F^{\cdot}OH_i^{\cdot})^{\times}$.

The central region of the crystal appears to be unaffected by the impurity diffusion process. The behaviour of the colour centres in this region is entirely conventional.

Hitherto only the process by which the concentric zones are formed has been discussed. Zone formation is basically due to a redistribution of water related centres caused by heating the crystal. Zone formation is not necessarily accompanied by the introduction of colour centres. The coloration mechanism is peculiar to a heating of the crystals in the presence of ytterbium and europium. Probably the most important property that these impurities share, and that which distinguishes them from impurities such as tin and magnesium, is their low electronegativity. It would appear that this property is responsible for the preferential release

of electrons by the impurity which then diffuse into the crystal to form colour centres. The probable reaction is

$$(Yb^{\circ})_{...} \longrightarrow Yb^{2+} + 2e^{-} \qquad 7.8$$

or the equivalent for europium. According to this reaction, two electrons are injected as the impurity becomes divalently charged on entering the crystal. Thermodynamic considerations state that the anion vacancies required for F-centre formation will be present in large concentrations at these high temperatures. It is conceivable, however, that anion vacancies are not available in the outer crystal region due to the precise nature of the zone formation process. Such nonstoichiometry could then account for the presence of an outer clear zone. Quenching the crystal causes the electrons to remain trapped at the available anion vacancies thereby creating the observed coloration.

7.5 Conclusions

When alkali halide crystals are heated at a high temperature in the presence of ytterbium or europium and then quenched to room temperature, various colour centres are produced. This new coloration method is suitable for producing colour centres in the majority of the alkali halides, including KF and NaF. It is referred to as the aliovalent coloration technique. The colour centres produced by the technique are not distributed homogeneously throughout the crystal but are segregated into a number of concentric zones. As many as four different zones are produced. They can be distinguished by their differing characteristic optical absorption spectra. The transition between adjacent zones is sharply defined.

The behaviour of potassium and sodium halide crystals with respect to

aliovalent coloration is similar. The only significant difference is the enhanced ability of the sodium halides to form colloids. The central zone of either type of crystal contains colour centres which are typical of the nominally-pure host. In the potassium halides this zone contains F-centres and F-aggregate centres; in the sodium halides, except NaF and NaCl, it contains X-centres and other colloids. For NaF and NaCl there is a mixture of F-centres and colloids of various sizes. The central zone extends to within approximately 1 mm of the surface of the crystal.

The outer regions of the crystals behave in a more complex manner. In all crystals the extreme outer edge contains the divalent rare earth impurity ion plus a quite large concentration of U-centres. For the majority of the alkali halides the remaining outer zone appears clear to the eye and is found to contain no obvious distinguishing absorption bands. For crystals of KF,NaF and NaCl the behaviour within this outer zone is more complex. For KF the outer zone consists of two separate regions in addition to the impurity-doped edge region. The outer of these is clear to the eye but in this case is very thin. The inner contains a mixture of F-centres with two new colour centres which are attributed to water related defects. These new colour centres are only observed for crystals of KF and consist of a centre characterised by an F_A-type absorption spectra and a second centre giving rise to an absorption band on the long wavelength side of the F-band. The first of these new centres is attributed to the defect centre $(H_2O)_F^x$, while the second is tentatively assigned to the defect $(V_F^x OH_i^x)^x$.

For crystals of NaF and NaCl, the clear outer zone is similarly very thin but is in this case followed by a region containing a mixture of F-centres and X-centres or small colloids. The same centres are also present in the inner zone and the different coloration associated with these two regions is determined by the relative concentration of each type of colour centre. In the central region the F-centre dominates while in

the adjoining zone the X-centre dominates. For NaCl crystals an additional yellow-coloured zone is often observed sandwiched between these two regions. The coloration in this thin intermediate zone is due to an absorption band at 420 nm (23810 cm^{-1}) which is probably associated with an oxygen-containing defect.

It is possible to separate the aliovalent coloration process into two basic mechanisms. The first mechanism involves the formation of the various concentric zones of differing properties within the crystal. The formation of zones is directly attributable to the presence of water-related defect centres in the as-received Harshaw crystals. Heating these crystals in the presence of a getter, such as ytterbium or europium, accentuates the outward diffusional motion of typical water-related impurities such as OH^-. The defect content of the outer faces of the crystals is thus altered in a complex way by this process. The second mechanism involves the injection of electrons. The rare earth impurity donates two electrons as it enters the crystal and assumes a divalent positive charge. It is thought that the low electronegativity of these particular ions promotes this process. The injected electrons become trapped at anion vacancies to form F-centres. The clarity of the outer zone could possibly indicate a lack of suitable vacancies in this region.

The basic aliovalent coloration process appears to be the same for both ytterbium and europium. It is interesting to note that no similar coloration effect has been reported for other common divalent impurities such as Ca^{2+}, Ba^{2+} and Sr^{2+}. This difference in behaviour is attributed primarily to the fact that the electronegativity values for the latter ions are much higher than for the rare earths. In addition, for the purpose of the experiments described in the present work, the crystals were only heated in the presence of the impurity for a relatively short time. This procedure probably prevents complete equilibrium from being achieved. The resulting condition is "frozen-in" by the act of quenching to room

temperature.

The simultaneous presence of a high concentration of divalent impurity ions and U-centres in crystals of KCl and KBr results in the creation of a new defect centre. This condition is often satisfied in the outer edge of some of the crystals and the outcome is a perturbation of the standard U-centre absorption. The usual single absorption band in the ultraviolet is split into two bands. The basic structure of this new centre implies a splitting of the triply degenerate excited orbital of the U-centre due to the close presence of the divalent impurity. It is interesting to note therefore that the more intense of the two absorption bands is situated at higher energy for KCl and at lower energy for KBr. A tentative model is proposed to account for this difference. For KBr the divalent impurity is assigned to a position next to the U-centre along the <100> direction with the cation vacancy along the <210> direction. For KCl the divalent impurity and cation vacancy positions are reversed.

It is clear from the preliminary nature of a number of the conclusions presented in this chapter that there is much scope for further work. In particular, the thermodynamics of the coloration process, incorporating impurity diffusion, zone formation and electron injection, are not well understood. Additional experiments are required to determine the relative importance of the various defect centres present and to understand the complex interdependence of the various mechanisms. For example, it would be interesting to repeat these experiments with crystals which are free of water related impurities in order to determine their role in the coloration process. A second experiment might consider in more detail the diffusion rates of rare earth ions and other defect centres and correlate this information with the phenomenon of zone formation.

A number of new defect centres have been observed, namely the S, Q and perturbed U-centres, however based on the available information it has only been possible to give tentative structural models. Further work is

required to accurately determine the precise structure of the defects involved. Possible experimental techniques are ESR, ENDOR and ODMR.

7.6 References

1. J.J.Markham, "F-centers in the Alkali Halides", Solid State Physics, Supplement 8, Academic Press, NY and London (1966)

2. R.Röhrig, Physics Letters, 16,p20 (1965)

3. P.Podini, Physica Status Solidi, 9, p737 (1965)

4. P.Gorlich et al., Physica Status Solidi, 3, p1629 (1963)

5. A.Chandra and M.L.Meistrich, Journal of Physics and Chemistry of Solids, 29, p1119 (1968)

6. G.H.Jirgal Jr., American Journal of Physics, 37, p963 (1968)

7. H.Ivey, Physical Review, 72, p341 (1947)

8. W.B.Fowler Editor, "Physics of Colour Centres", Academic Press, NY and London (1968)

9. W.C.Collins et al., Applied Physics Letters, 24, p403 (1974)

10. V.R.Dumke, Physica Status Solidi (a), 44, pK133 (1977)

11. G.Matsumura and G.C.Kuczynski, Physica Status Solidi (b), 55, p329 (1973)

12. G.C.Kuczynski et al., Physica Status Solidi (b), 87, p581 (1978)

13. V.R.Dumke and M.de Souza, Physical Review B, 10, p1617 (1974)

14. W.Rusch and H.Seidel, Solid State Communications, 9, p231 (1971)

15. W.Rusch and H.Seidel, Physica Status Solidi (b), 63, p183 (1974)

16. F.Fischer et al., Zeitschrift fur Physik, 189, p79 (1966)

17. F.Fischer and G.Gummer, Zeitschrift fur Physik, 189, p97 (1966)

18. S.Radhakrishna and B.V.R.Chowdari, Physica Status Solidi (a), 12, p557 (1972)

19. M.T.Montojo et al., Journal of the Electrochemical Society, 122, p1325 (1975)

20. T.Ikeda, Japan Journal of Applied Physics, 12, p1810 (1973)

8. MAIN CONCLUSIONS

This study has served to illustrate the many similarities between divalent ytterbium and europium in the alkali halides. Ytterbium and europium were already known to possess many similarities in the elemental and free-ion states. Both metals possess relatively low melting points and high vapour pressures and these properties have enabled rare earth impurity-doped alkali halide crystals to be produced for the first time by diffusion from the vapour phase. In this study the impurity is only diffused into the outer regions of the crystal. Nevertheless it is shown that, where comparison is possible, the behaviour of the dopant is the same as when the impurity is introduced into crystals by more conventional bulk growth techniques.

Both impurities enter the alkali halides in the divalent state. For the majority of the crystals the divalent ion is present on a substitutional cation site with a charge compensating vacancy situated along the <110> direction. There is evidence for some degree of aggregation of Eu^{2+} ions in a number of the crystals when the impurity concentration is very high. For crystals of NaF, the Yb^{2+} and Eu^{2+} ions are present in the form of separate phases of YbF_2 or EuF_2. This separate phase possesses the fluorite structure with the impurity ion effectively 8-fold coordinated. A similar behaviour is observed for crystals of $LiF:Yb^{2+}$. High temperature annealing of crystals of $NaF:Yb^{2+}$ results in a limited dissociation of the YbF_2 phase with the simultaneous production of dispersed Yb^{2+} ions. The EuF_2 phase remains stable at all times.

The greater stability of the EuF_2 phase leads to some rather interesting phenomena in crystals of $NaCl:Eu^{2+}$ and $NaBr:Eu^{2+}$. Initially these crystals contain only dispersed Eu^{2+} ions. However prolonged aging of the crystals at between RT and 130°C results in the formation of phases of the type EuX_2. A similar behaviour was not found for crystals of $NaI:Eu^{2+}$. This observation

is not attributed to any intrinsic difference between the sodium halides, but rather to the much lower concentration of Eu^{2+} in the iodide. Heating crystals containing the phases $EuCl_2$ and $EuBr_2$ to 600°C for a short time followed by a quench to RT results in a return to the original dispersed Eu^{2+} ion state.

The formation of separate phases of the type described above appears to be a phenomenon confined primarily to the sodium halides. The potassium halides did not in general exhibit the same behaviour, except for one anomalous sample of KBr:Eu^{2+}. The preferential formation of such phases in the sodium halides is probably related to the preferential formation of colloids in the same hosts. It is interesting to note that the same behaviour was not observed for any of the crystals containing Yb^{2+}.

The presence of Yb^{2+} or Eu^{2+} ions in the alkali halides results in the creation of strong optical absorption bands in the ultraviolet. In both cases the absorption bands are due to transitions of the type $4f^n - 4f^{n-1}5d$ which are strongly allowed. The situation for the Yb^{2+} ion can be described theoretically by considering the behaviour of the J,j-coupled $4f^{13}5d$ excited state configuration in a crystal field. The same theory can in principle be applied to the predominantly LS-coupled $4f^6 5d$ configuration of the Eu^{2+} ion, although the very much larger number of states renders the calculation impractical. The true site symmetry of the divalent impurity ion in the alkali halides is C_{2v} due to the charge compensating vacancy. For the purpose of calculating the energy levels and optical dipole transitions, it is possible to use the approximation of O_h symmetry. This approximation can be applied with excellent results for all crystals except NaCl and KF. In these crystals the perturbation caused by the <110> vacancy becomes more significant and leads to some additional structure within the absorption bands.

The agreement between theory and experiment for the optical absorption

spectrum of Yb^{2+} in the alkali halides is excellent provided that a reduction is made in the free ion Slater-Condon parameter values. The reduction is negligible for the alkali fluorides, increases in the sequence $F^- - Cl^- - Br^- - I^-$, and can be quite significant (approximately 50%) for the alkali iodides. The reduction is a consequence of the delocalisation of charge distributions in the less ionic crystals. The effective expansion of the outer electron orbitals, which is a direct result of charge overlap, is referred to as the nephelauxetic effect.

The delocalisation of charge densities implies a picture somewhere between crystal field theory and MO theory. One particularly interesting consequence of charge overlap is the observation of transitions of the type $4f^{14} - 4f^{13}6(A_{1g})$, where $6(A_{1g})$ represents a σ-bonding orbital created between the 6s orbital of the Yb^{2+} ion and a σ orbital of the surrounding octahedrally coordinated anion complex. Transition intensities are dependent in this case on the degree of overlap and are therefore strongest for the iodides and weakest for the fluorides.

The aliovalent coloration phenomenon is described by a two stage process. The first stage is the production of a number of concentric zones due to the heating of the crystal in the presence of a getter. Zone formation is attributed to an alteration of the water-related impurity centre content in the outer regions of the as-received crystal due to an out-diffusional process. The second stage is an injection of the electrons which are released as the rare earth impurity assumes divalent positive charge on entering the crystal. The low electronegativity of the rare earth ions is thought to be an important contributing factor in this process. Electrons are trapped at available sites within the crystal creating colour centres. The central region is not affected significantly by the heating process and the colour centres created within that region are typical of those observed in crystals coloured by standard techniques. The behaviour of colour centres in the outer regions depends on the

modified defect content. A number of different zones are observed in this region corresponding to the presence or absence of the various important defects required for colour centre formation.

For crystals of KF, the coloration in the outer zone indicates the presence of two new types of defect centre. The new centres only appear after optical bleaching of the standard F-centres at RT. The S-centre appears initially and is characterised by an optical absorption spectrum resembling an F_A-type centre. It is attributed to an electron trapped at a substitutional water molecule, that is $(H_2O)_F^x$. As the bleaching process is continued, the S-centre (and F-centre) is destroyed and the Q-centre is created. The absorption band associated with the Q-centre is situated on the long wavelength side of the F-centre. The Q-centre is tentatively assigned to an F-centre situated next to an interstitial OH ion, that is $(V_F^+OH_i^-)^x$.

The very outer edge of the aliovalently coloured crystals contains both the divalent rare earth impurity and also an enhanced concentration of U-centres. For crystals of KCl and KBr where the Yb^{2+} concentration and the U-centre concentration are simultaneously very high, the optical absorption spectrum associated with the U-centre is modified. The single ultraviolet absorption band of the unperturbed U-centre is split into two bands. The splitting is associated with a reduction in the site symmetry of the U-centre. The more intense of these two bands is situated to higher energy for crystals of KCl and to lower energy for crystals of KBr. The difference is presumably associated with the precise details of the relationship between the U-centre, the Yb^{2+} ion and the charge compensating cation vacancy. The following models are proposed in an attempt to account for this difference. For KBr crystals, the Yb^{2+} ion is assigned to a position next to the U-centre along the <100> direction with the cation vacancy along the <210> direction. For KCl crystals, the divalent impurity and cation vacancy positions are reversed.

APPENDIX 1

Direct sum and direct product of matrices

The direct sum of two square matrices A of order m and B of order n is a square matrix C of order m+n defined by

$$C = A \oplus B = \begin{pmatrix} A & 0 \\ 0 & B \end{pmatrix} = \begin{pmatrix} A_{11} & \cdots & A_{1m} & & & \\ \vdots & & \vdots & & 0 & \\ A_{m1} & \cdots & A_{mm} & & & \\ & & & B_{11} & \cdots & B_{1n} \\ & 0 & & \vdots & & \vdots \\ & & & B_{n1} & \cdots & B_{nn} \end{pmatrix}$$

where 0 denotes null matrices.

The direct product of two matrices A of order LxM and B of order PxQ is a matrix C of order IxJ, where I = LP and J = MQ, defined by

$$C = A \otimes B = \begin{pmatrix} A_{11}B & A_{12}B & \cdots & A_{1M}B \\ A_{21}B & A_{22}B & \cdots & A_{2M}B \\ \vdots & \vdots & & \vdots \\ A_{L1}B & A_{L2}B & \cdots & A_{LM}B \end{pmatrix}$$

where each $A_{lm}B = \begin{pmatrix} A_{lm}B_{11} & A_{lm}B_{12} & \cdots & A_{lm}B_{1Q} \\ A_{lm}B_{21} & A_{lm}B_{22} & \cdots & A_{lm}B_{2Q} \\ \vdots & \vdots & & \vdots \\ A_{lm}B_{P1} & A_{lm}B_{P2} & \cdots & A_{lm}B_{PQ} \end{pmatrix}$

APPENDIX 2

Matrix elements of the crystal field interactions $H_3(d)$ and $H_3(f)$ for the $4f^{13}5d$ configuration

The matrix elements of the most important crystal field interactions are given below for the $4f^{13}5d$ configuration in terms of J,j-coupled states. Three matrices are given corresponding to:

(a) The fourth order d electron crystal field interaction.

(b) The fourth order f electron crystal field interaction.

(c) The sixth order f electron crystal field interaction

Note that all of the matrices are symmetric and only the lower major is therefore given.

	J	$^7/_2,\ ^5/_2$						$^7/_2,\ ^3/_2$				$^5/_2,\ ^5/_2$					$^5/_2,\ ^3/_2$		
		6	5	5	4	3	1	5	5	4	3	5	5	4	3	1	4	3	1
$^7/_2$ $^5/_2$	6	$-32\sqrt{7}$																	
	5	$-7\sqrt{385}$	$-44\sqrt{7}$																
	5	$7\sqrt{11}$	$-44\sqrt{5}$	$44\sqrt{7}$															
	4	189	$-3\sqrt{55}$	$-9\sqrt{77}$	$-12\sqrt{7}$														
	3	$35\sqrt{11}$	$11\sqrt{5}$	$-11\sqrt{7}$	$-12\sqrt{77}$	$44\sqrt{7}$													
	1	○	$33\sqrt{35}$	99	$33\sqrt{11}$	33	○												
$^7/_2$ $^3/_2$	5	$-7\sqrt{165}$	$-77\sqrt{3}$	$-11\sqrt{105}$	$-2\sqrt{1155}$	$-22\sqrt{105}$	$-77\sqrt{15}$												
	5	$\sqrt{231}$	$-11\sqrt{105}$	$77\sqrt{3}$	$-42\sqrt{33}$	$154\sqrt{3}$	$-33\sqrt{21}$		○										
	4	$63\sqrt{11}$	$-33\sqrt{5}$	$-99\sqrt{7}$	$18\sqrt{77}$	$66\sqrt{7}$	-99												
	3	$35\sqrt{33}$	$-55\sqrt{15}$	$55\sqrt{21}$	$10\sqrt{231}$	$-22\sqrt{21}$	$-11\sqrt{3}$												
$^5/_2$ $^5/_2$	5											$33\sqrt{7}$							
	5											$33\sqrt{5}$	$-33\sqrt{7}$						
	4			○					○			$22\sqrt{5}$	$66\sqrt{7}$	$-33\sqrt{7}$					
	3											$66\sqrt{5}$	$-66\sqrt{7}$	$-11\sqrt{7}$	$-33\sqrt{7}$				
	1											$11\sqrt{70}$	$33\sqrt{2}$	$-132\sqrt{2}$	$-88\sqrt{2}$	○			
$^5/_2$ $^3/_2$	4											$11\sqrt{30}$	$33\sqrt{14}$	$-33\sqrt{14}$	$-55\sqrt{14}$	330			
	3			○					○			$33\sqrt{30}$	$-33\sqrt{42}$	$-33\sqrt{42}$	$33\sqrt{42}$	$66\sqrt{3}$		○	
	1											$154\sqrt{5}$	$66\sqrt{7}$	$66\sqrt{7}$	$22\sqrt{7}$	○			

$\times \frac{\sqrt{7}}{231} Dq$

(a) The fourth order d electron crystal field interaction matrix

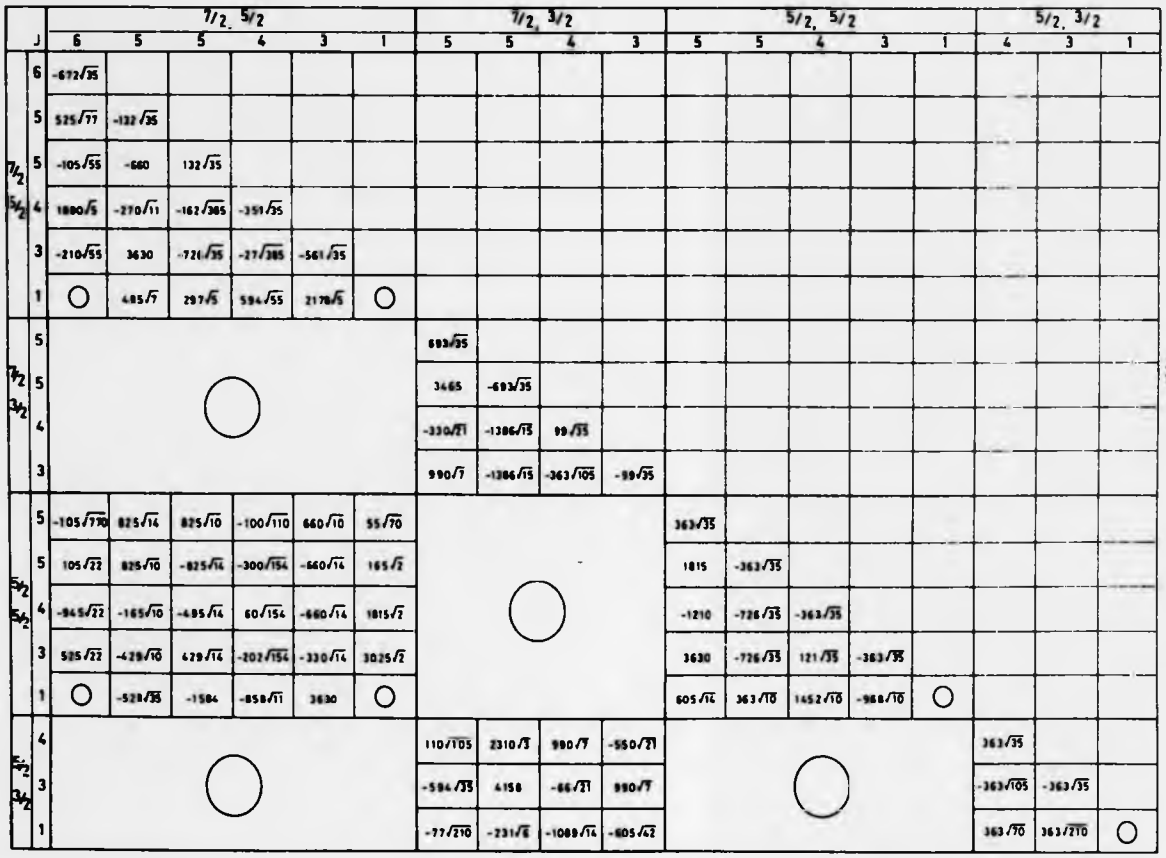

(b) The fourth order f electron crystal field interaction matrix

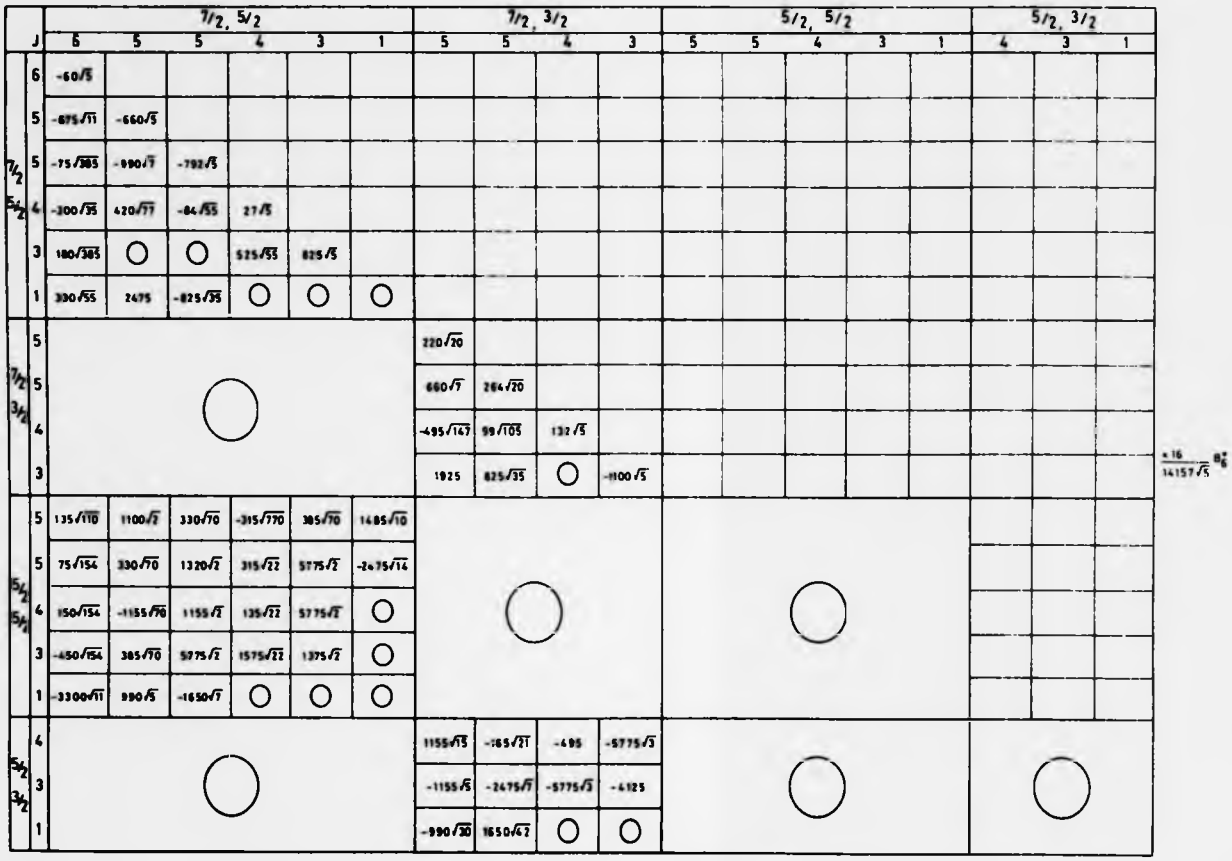

(c) The sixth order f electron crystal field interaction matrix

J. Phys. C: Solid State Phys., 18 (1985) 1525–1538. Printed in Great Britain

$4f^{14} \rightarrow 4f^{13}5d$ optical transitions of divalent ytterbium in the potassium and sodium halides

S W Bland† and M J A Smith
Department of Physics, University of Warwick, Coventry CV4 7AL, UK

Received 2 April 1984, in final form 10 September 1984

Abstract. The optical absorption spectra of Yb^{2+} in a range of potassium and sodium halide crystals are described and analysed. Attention is focused on the strongly allowed $4f^{14} \rightarrow 4f^{13}5d$ transitions. Excellent general agreement is obtained between theory and experiment provided that a correction based on the nephelauxetic effect is included. Parallel linear dependencies for the potassium and sodium halides are established between a parameter Δ, representing the energy difference between the centre of energy of the excited $4f^{13}5d$ configuration and the $4f^{14}$ ground state, and the lattice parameter d. Similar dependencies are established between the crystal-field parameter Dq and d.

1. Introduction

The optical absorption spectrum associated with divalent ytterbium in various crystalline hosts has attracted a certain amount of attention in the past. This is due primarily to the relative simplicity, for a rare-earth ion, of its electronic energy level structure. The principal electronic transitions are of the type $4f^{14} \rightarrow 4f^{13}5d$ and are, therefore, reasonably accessible to direct theoretical calculation even with the inclusion of crystal-field interactions (Eremin 1970, Piper *et al* 1967).

Previous studies of Yb^{2+} have been confined largely to the alkaline-earth halides (Feofilov 1956, Kaplyanskii and Feofilov 1962, Piper *et al* 1967, Loh 1969, Johnson and Sandoe 1969, Eremin 1970, Loh 1973), although a few early papers discuss ytterbium in the alkali halides. Wagner and Bron (1965) studied the vibonic structure found in the optical absorption bands of Yb^{2+} in NaCl, KCl, RbCl, KBr and KI at low temperature. Sootha *et al* (1971) described the presence of a single principal absorption band in NaCl and KCl situated in the ultraviolet. The simultaneous observation of electron paramagnetic resonance led them to attribute the spectra to the Yb^{3+} ion. Radhakrishna and Chowdari (1972), in their study of Z centres in alkali halides doped with rare-earth ions, reported on the optical absorption of Yb^{2+} in KBr, KCl and NaCl. Their results are, however, questionable following a more comprehensive study performed recently by Tsuboi *et al* (1981) on NaCl: Yb^{2+}. There is no agreement between the latter studies.

In the present paper we present and interpret the optical absorption spectra arising from the $4f^{14} \rightarrow 4f^{13}5d$ transitions of Yb^{2+} in KI, NaI, KBr, NaBr, KCl, NaCl and KF. We will discuss the special case provided by NaF: Yb^{2+} elsewhere. An additional set of

† Present address: Standard Telecommunication Laboratories Ltd, London Road, Harlow, Essex CM17 9NA, UK.

0022-3719/85/071525 + 14 $02.25

absorption bands associated with a new class of transitions of Yb^{2+} in the alkali halides will also receive separate treatment.

2. Experimental method

Single crystals of KI, NaI, KBr, NaBr, KCl, NaCl and KF containing ytterbium were produced by diffusion of ytterbium from its vapour into the solid crystal. This is the first time that such a method has been reported for obtaining Yb^{2+}-doped alkali halide crystals. Although Radhakrishna and Chowdari (1972) have described the use of vapour-phase diffusion, their results suggest that any ytterbium that may have entered their crystals was not in the divalent state. It should be noted that, of all the rare earths, ytterbium is the best suited to the present technique since it possesses the highest vapour pressure (Honig 1962) in the temperature range of interest (650 to 1000 °C).

The alkali halides used in this study were supplied by Harshaw Chemical Company in the form of single crystals. Ytterbium metal of 99.9% purity was supplied by Koch-Light Laboratories Ltd. Freshly cleaved crystals of approximate dimensions $8 \times 5 \times 2\ mm^3$ were placed, together with about 15 mg of ytterbium metal, in a cylindrical cavity of approximately 4 cm^3 produced by drilling an axial hole in a stainless steel rod. A finely machined dry conical joint matched to an outer stainless steel plug was provided at the open end of the cavity. A needle valve within the plug enabled the cavity to be evacuated and sealed prior to diffusion. The cavity and its plug were held under vacuum inside a heated container during diffusion.

The diffusion temperature was chosen to be about 50 °C below the melting point of the particular alkali halide. Diffusion times were kept relatively short, ranging from about 30 min to 3 h. Although melting of the crystal faces was avoided, diffusion was limited to a depth of about 0.5 mm. Such inhomogeneous doping proved advantageous since sectioning of the crystal enabled all those absorption bands associated with the nominally pure crystal to be identified. In all cases the crystals were annealed in a dry nitrogen atmosphere after diffusion in order to eliminate the effects of stress. Normally 20 min at about 50 °C below the diffusion temperature proved sufficient. After annealing, the crystal was quenched to room temperature on a copper block.

Optical absorption spectra were recorded between 190 and 900 nm using a Varian DMS-90 spectrophotometer.

3. Theory of the $4f^{14} \rightarrow 4f^{13}5d$ transitions

The general theory of an excited $4f^{13}5d$ configuration in an octahedral crystal field has been described by Piper *et al* (1967) and by Eremin (1970). In the present work the basic approach of Eremin (1970) is followed, although with some modification. In particular, the use of *LS*-coupled wavefunctions is rejected in favour of a J_1j-coupling scheme which better describes the final states (Racah 1960, Bryant 1965).

The true site symmetry of the substitutional Yb^{2+} ion in the alkali halides is expected to be C_{2v} rather than octahedral due to the bound charge-compensating cation vacancy situated along the ⟨110⟩ direction. However, it is often found (Hernandez *et al* 1981) that, for optical electric dipole transitions, the excited configuration experiences a negligible perturbation from the vacancy. Consequently, the configuration acts as if the site symmetry is effectively that of the full octahedral O_h point group. This behaviour is understandable since the excited electron orbital is expected to interact predominantly with the oppositely charged and octahedrally coordinated nearest-neighbour anions. The approximation of octahedral symmetry is adopted here.

The 20 free-ion levels associated with the excited $4f^{13}5d$ configuration of Yb^{2+} (Bryant 1965) decompose in an octahedral crystal field into a total of 58 levels. Each of these final states transforms according to one of the irreducible representations Γ_i ($1 \leqslant i \leqslant 5$) of the O_h point-symmetry group. The complete decomposition is given by

$$6\Gamma_{1u} \oplus 5\Gamma_{2u} \oplus 12\Gamma_{3u} \oplus 18\Gamma_{4u} \oplus 17\Gamma_{5u} \qquad (1)$$

where the subscript u indicates odd parity. The $4f^{14}$ ground state is simply represented by Γ_{1g}, where g indicates even parity. Electric dipole transitions are allowed only between the ground state and the 18 levels transforming according to Γ_{4u}.

The irreducible tensor operator methods developed by Racah (see, for example, Judd 1963) are used to calculate the matrix elements of the electrostatic, spin–orbit and crystal-field Hamiltonians. Each Hamiltonian is separated into an angular and a radial component. The relevant matrix elements of the angular component are calculated after first expressing the component in irreducible tensor operator form. The coefficients tabulated by Eremin (1970) are used to determine the crystal-field matrix elements. The radial component is left in the form of a radial integral and is treated as an adjustable parameter to be determined by comparison between theory and experiment. The ten adjustable parameters required to describe the $4f^{13}5d$ configuration in an octahedral field are the direct and indirect Slater–Condon (electrostatic) parameters F_2, F_4, G_1, G_3 and G_5, the spin–orbit parameters ζ_f and ζ_d and the crystal-field parameters Dq, B_4^0 and B_6^0.

Figure 1 illustrates the predicted effect of variations in the crystal-field strength parameter Dq on the levels of the $4f^{13}5d$ configuration for the case of octahedral or sixfold coordination. The Slater–Condon and spin–orbit parameters have been set equal to their free-ion values. Also included in figure 1 are the relative transition strengths of each level expressed as $(50a_i)^2$, where a_i is the coefficient of the $^1P_1$-type wavefunction contained in each level. The separation of the 18 levels into four distinct groups at high crystal fields is consistent with a model based on a crystal-field-split 5d electron ($d_{\varepsilon 2}$, $d_{\gamma 2}$) coupled to a spin–orbit-split $4f^{13}$ core ($^2F_{7/2}$, $^2F_{5/2}$). The four groups correspond to the overall states $^2F_{7/2}d_{5/2}$, $^2F_{5/2}d_{5/2}$, $^2F_{7/2}d_{3/2}$ and $^2F_{5/2}d_{3/2}$ in order of increasing energy.

In deriving figure 1 certain assumptions are made about the higher-order crystal-field parameters B_4^0 and B_6^0 which characterise the expansion of the field Hamiltonian in spherical functions. Detailed calculations show that variations of B_4^0 and B_6^0 affect only slightly the eigenvalues and, hence, the energy levels. Indeed, Piper *et al* (1967) chose to present their analysis based on the parameter Dq alone. In contrast, the eigenfunctions, which determine the transition strengths, are very sensitive to variations in any of the adjustable parameters. Eremin (1970) included both B_4^0 and B_6^0 but with values fixed relative to Dq ($Dq : B_4^0 : B_6^0 = 60 : -7 : 1$). In order to reproduce the energy level structure and the transition intensities as accurately as possible, all of the parameters are retained in the present work but with the following relationships incorporated to connect Dq, B_4^0 and B_6^0.

According to the point-ion model of the crystal field (Hutchings 1964) both Dq and B_4^0 are proportional to R^{-5}, where R is the Yb^{2+}–anion distance. B_6^0 is proportional to R^{-7}. Experimentally, the dependence for B_4^0 is found to be more like R^{-2} (Kiss 1965). It is also apparent from Weakliem and Kiss (1967) and from Kiss (1965) that the ratio B_6^0/B_4^0 remains relatively constant for a particular rare-earth ion regardless of the host

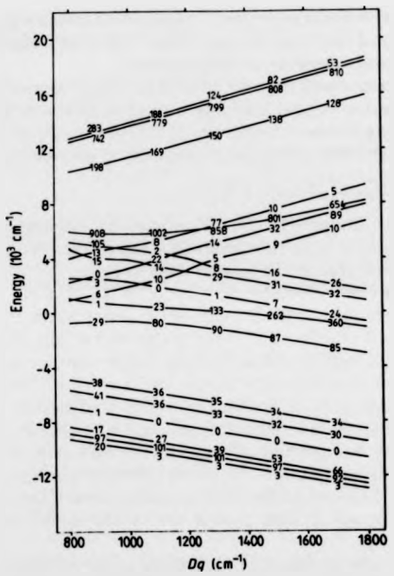

Figure 1. Theoretical energy level positions and intensities of the allowed $4f^{14} \rightarrow 4f^{13}5d$ transitions of Yb^{2+} in an octahedral crystal field as a function of field strength parameter Dq. Energy level positions are given with respect to the centre of energy of the configuration. Equations (2) and (4) are used to express B_6^0 and B_4^0 in terms of Dq. Free-ion values are employed for the Slater–Condon (electrostatic) and spin–orbit parameters.

lattice. Even for different rare-earth ions the ratio varies only slightly. For example, for Ho^{2+} ($4f^{11}$) in CaF_2 the ratio is found to equal -0.18 (Weakliem and Kiss 1967). It becomes -0.19 for Tm^{2+} ($4f^{13}$) in the same host (Weber and Bierig 1964). Extrapolating from this small, but general, trend and anticipating that the extra d electron of the $4f^{13}5d$ configuration will improve the shielding slightly, a reasonable estimate for the Yb^{2+} ion in the cubic or eightfold-coordinated field is $(B_6^0/B_4^0)_{cub} = -0.20$. According to the point-ion model, the same ratio for the octahedral crystal field is

$$B_6^0/B_4^0 = 0.075. \tag{2}$$

It is more difficult to justify connecting Dq and B_4^0 by a simple relationship of the form of equation (2). The 5d electron is strongly influenced by the surrounding lattice ions, whereas the deeper 4f electrons are well shielded and are only weakly perturbed. For Dy^{3+} in a range of alkaline-earth fluorides (Low 1964, Altshuler *et al* 1969), the dependence of B_4^0 on crystal-field strength, assuming typical values for Dq (Eremin 1970), may be closely fitted to the linear relationship

$$(B_4^0)_{cub}^D = -(150 + 0.067|Dq|) \tag{3}$$

where parameter values are in cm^{-1} and the superscript D denotes a specific value for Dy^{3+}. When a divalent rare-earth is studied in the same alkaline-earth fluorides, the magnitude of B_4^0 is found to be smaller. For example, Dy^{3+} in CaF_2 yields a value of $B_4^0 = -257.2\ cm^{-1}$ (Altshuler *et al* 1969) consistent with equation (3), whilst $B_4^0 = -180\ cm^{-1}$ (Weber and Bierig 1964) or $-189\ cm^{-1}$ (Sabisky and Anderson 1966) for the isoelectronic divalent ion Tm^{2+} in the same host. Similarly for $CaF_2:Dy^{2+}$ a value of $B_4^0 = -188\ cm^{-1}$ is obtained (Kiss 1965). We assume that a functional dependence similar to equation (3) connects B_4^0 and the magnitude of Dq for divalent ions. A direct scaling of the coefficients in equation (3) gives

$$B_4^0 = 100 + 0.05|Dq| \tag{4}$$

for the Yb^{2+} ion in an octahedral field.

The use of equations (2) and (4) to express B_6^0 and B_4^0 in terms of Dq, as in figure 1, reduces the number of adjustable parameters in the theoretical model to eight.

4. Results and discussion

The optical absorption spectra associated with Yb^{2+} in KI, NaI, KBr, NaBr, KCl, NaCl and KF were obtained at both room and liquid nitrogen temperatures. In the interest of brevity, only the spectra of the potassium salts are presented (figure 2). We note that the spectrum for $NaCl:Yb^{2+}$ agrees well with that reported by Tsuboi *et al* (1981).

A number of common features characterise the spectra. In all cases absorption starts around 25 000 cm^{-1} (400 nm) with two distinct bands, designated A1 and A2, of approximately fixed separation and relative intensity. A strong absorption band C1 occurs in the range 38 000 to 42 000 cm^{-1} (263 to 213 nm) preceded in energy by a pair of weaker bands designated B1 and B2. For NaBr, KCl and NaCl a partially resolved band B3 appears between B2 and C1. At higher energies two relatively strong bands, designated D1 and D2, are observed in KBr, NaBr and KCl. In the other crystals corresponding D bands are either obscured by a strong absorption edge associated with the nominally pure host or lie (presumably) outside the range of the spectrophotometer. All bands A to D sharpen slightly on cooling from room to liquid nitrogen temperature and generally exhibit a small shift in position, either to higher or lower energy. There is no apparent change in the total area under the absorption band envelopes and, hence, in their individual transition strengths. This observation implies that the spectra are associated with allowed transitions.

The two bands designated E1 and E2 in figure 2 behave differently from bands A to D with respect to changes in temperature. They sharpen more noticeably on cooling and exhibit a larger shift in position, always to higher energy. It will be shown in a subsequent paper that E1 and E2 are not due to $4f^{14} \rightarrow 4f^{13}5d$ transitions, although they are still to be associated with the Yb^{2+} ion. Their presence is a consequence of covalency.

Figure 3 shows the experimental energy level positions of the most intense absorption bands at liquid nitrogen temperature as a function of crystal-field strength Dq described by d^{-5}, where d is the lattice parameter. For the alkali halides, d represents the cation–anion separation which is assumed equal to the Yb^{2+}–anion separation R in our analysis. Absolute configuration energies have been chosen arbitrarily. Experimental transition strengths are indicated by numbers normalised to A1 = 100 for each crystal. A comparison of figure 3 with the theoretical field dependence for the $4f^{14} \rightarrow 4f^{13}5d$ transitions given in figure 1 shows very acceptable qualitative agreement. In particular,

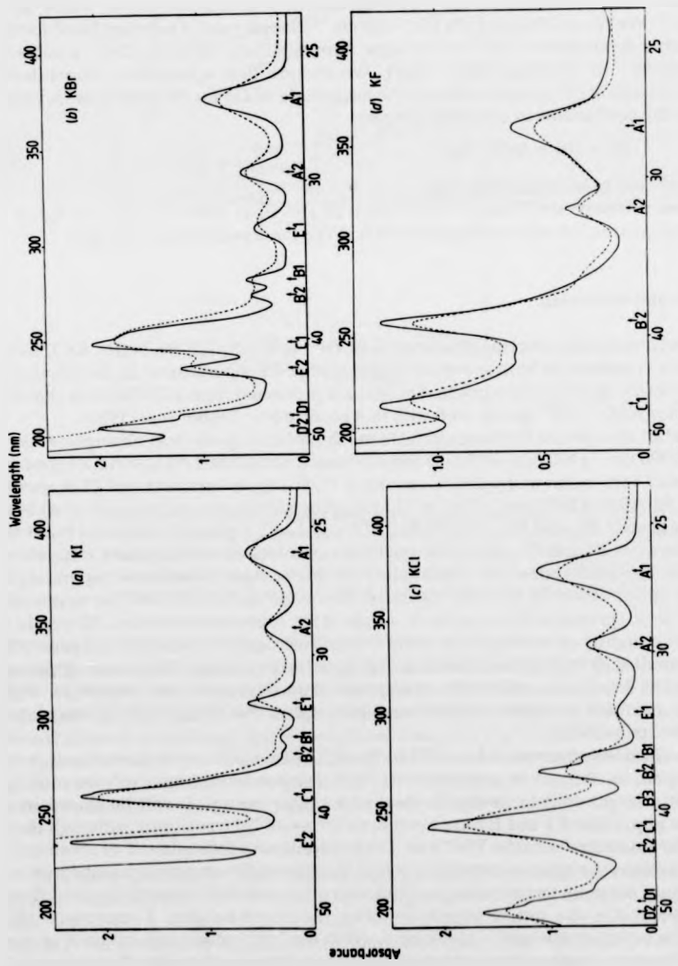

Figure 2. Experimental optical absorption spectra associated with Yb^{2+} in (*a*) KI, (*b*) KBr, (*c*) KCl and (*d*) KF. The full curves refer to liquid nitrogen temperature and the broken curves to room temperature. For KCl, the absorption band near 47 400 cm^{-1} is attributable to the well known U band.

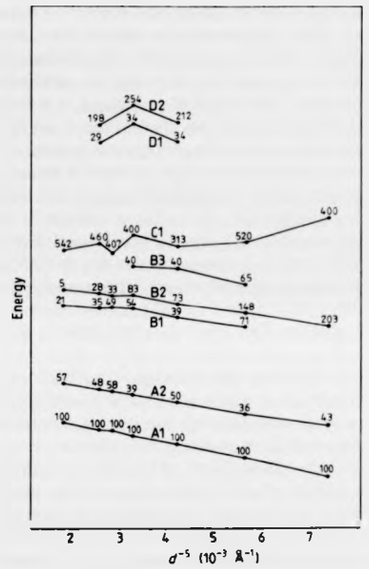

Figure 3. Experimental energy level positions and intensities (numbers normalised to A1 = 100) of the most intense absorption bands at liquid nitrogen temperature as a function of d^{-5}. Absolute configuration energies have been adjusted to illustrate qualitative agreement with figure 1.

the experimental B1 absorption band is more intense than B2 at low crystal fields whereas the reverse is true at high fields. The theory correctly predicts this reversal.

The labelling scheme adopted here to distinguish and classify individual bands is based on the predicted separation of the allowed energy levels of the $4f^{13}5d$ configuration into four distinct groups at high crystal fields. Each group is assigned a letter from A to D in order of increasing energy. A number is added in order to distinguish individual bands within a group. Evidence to support the classification is provided by the behaviour of the absorption bands with temperature. On cooling, the lattice contracts slightly leading to a decrease in d and an associated increase in Dq. According to the theory, those bands that belong to group A will shift to lower energy, while those in group D will shift to higher energy. For bands in groups B and C the behaviour is more complex with, typically, two separate cases to be considered. For $Dq \leqslant 1000\ \text{cm}^{-1}$, the theory predicts that bands C1 and B2 will both shift to lower energies, while B1 will shift to higher energy. In the contrasting case where $Dq \geqslant 1000\ \text{cm}^{-1}$, C1 will shift to higher energy while both B1 and B2 will shift to lower energies. These trends are reproduced perfectly in the experimental spectra. In particular, C1 for KI : Yb^{2+} shifts to lower energy on cooling thereby establishing a value of Dq below 1000 cm^{-1} for this lattice in agreement with other work (Hernandez *et al* 1980).

The spectrum for KF: Yb^{2+}, and to a lesser extent NaCl: Yb^{2+}, exhibits additional structure in the bands A1 and A2. This observation is almost certainly related to a systematic breakdown in the assumption of a high-symmetry octahedral crystal field. As the lattice spacing decreases, it is to be expected that the relative contribution from the off-axis ($\langle 110 \rangle$) cation vacancy increases. This gradual reduction in symmetry towards a C_{2v} crystal field leads to a partial splitting of the levels derived from the assumed O_h crystal field and, hence, to extra structure within the absorption bands.

Although satisfactory qualitative agreement has been obtained, some serious quantitative discrepancies remain. Theoretically the minimum separation between B1 and C1 is 6400 cm^{-1} at $Dq = 950\ cm^{-1}$, while for KI: Yb^{2+} ($Dq = 900\ cm^{-1}$) and NaI: Yb^{2+} ($Dq = 1030\ cm^{-1}$) the experimental separations are 4027 cm^{-1} and 3980 cm^{-1} respectively. Indeed, it is only for KF: Yb^{2+} that a single value for Dq ($=1650\ cm^{-1}$) can be found that reasonably satisfies all the energy separations simultaneously. It would appear that the free-ion values employed for the various radial parameters in the theoretical treatment are at best only meaningful for KF: Yb^{2+}. For the iodides in particular the values are totally unsuitable.

We seek improved agreement by allowing the radial parameters to vary from their free-ion values. In addition, the presence of eight adjustable parameters (F_2, F_4, G_1, G_3, G_5, ζ_f, ζ_d and Dq) in the analysis necessitates the use of a further simplifying approximation. The approximation consists of holding the ratios F_4/F_2, G_3/G_1, G_5/G_1 and ζ_f/ζ_d fixed at their free-ion values (Weakliem 1972). This particular form was adopted following a study of the effect of each parameter on the energy levels. In general, it was found that parameters of the same type (direct, indirect or spin–orbit) produced changes in the same directions. The eight original parameters become fully represented by four; that is by the Slater–Condon parameters $F(=F_2)$ and $G(=G_1)$, the spin–orbit parameter $\zeta(=\zeta_f)$ and the crystal-field parameter Dq.

The energy separations between the dominant bands A1, A2, B1, B2, C1, D1 and D2 are selective in their dependence on redefined parameter values. For example, the separations between A1 and A2 and between B1 and B2 are determined principally by F. The separations A1 to C1 and B1 to C1 are determined by G. The parameter ζ affects both the A1 to B1 and the A1 to D1 separations but the latter only weakly so. F and G control the D1 to D2 separation. Based on these dependencies the following iterative procedure was devised to fit the theoretical energy levels to the experimental levels. Initially, an approximate value of Dq is chosen by reference to figure 1 in order to satisfy the experimental separation between A1 and B1 and, if available, the separation between A1 and D1. The parameter G is next adjusted until the relative separations between the bands A1, B1 and C1 are optimised. The parameter F is adjusted to reproduce the separation A1 to A2 and finally ζ is adjusted to optimise the separations between A1, B1 and D1. The procedure is repeated until satisfactory overall agreement is obtained. For Yb^{2+} in KCl, KBr and NaBr it is also possible to adjust the separation D1 to D2, thereby contributing to a more comprehensive fit. For NaCl, where definition of the B1 band is poor, the procedure is varied slightly by using the separation B2 to C1 rather than B1 to C1 to determine G

Generally excellent quantitative agreement between theoretical and experimental energy level positions is obtained when the above iterative procedure is adopted. In addition, the transition intensities exhibit acceptable overall agreement, largely justifying the approximations made. Appropriate parameter values are given in table 1. Δ in table 1 corresponds to the energy difference between the centre of energy of the $4f^{13}5d$ configuration and the $4f^{14}$ ground state. Also included in table 1 is the lattice parameter

d and a reduction factor β for each redefined parameter equal to the reduced parameter value divided by its free-ion value. Precise theoretical level positions and transition intensities are given in table 2 together with the corresponding experimental values.

The study by Tsuboi *et al* (1981) on NaCl: Yb^{2+} may be compared with the results presented here. Unfortunately, without the benefit of data from a range of alkali halides, they based their analysis on free-ion values with the result that agreement is not particularly accurate. A point of interest concerns the two bands designated by them as H and I which occur at 50505 cm^{-1} (198 nm) and 51813 cm^{-1} (193 nm) respectively. These bands correspond to D1 and D2 respectively in the present analysis, although they are masked in our spectrum by a strong overlapping absorption band associated with an unidentified impurity present in the as-received crystal. Nevertheless, our theory predicts (table 2) that D1 and D2 occur respectively at 50278 cm^{-1} and 51635 cm^{-1}. In addition, it correctly predicts that D1 is less intense than D2.

The above results emphasise the inadequacies of the model adopted which assumes localised charge distributions and purely electrostatic forces. The limitations of the point-ion approach are well known and have been discussed by Jørgensen (1962a, b). A more realistic model should allow for the effects of overlap between the charge densities of the anions and the outer excited 5d orbital of the Yb^{2+} impurity ion. One particular consequence of overlap is a transfer of charge from the anion to the impurity ion, with the impurity ion behaving as if it possessed an effective ionic charge below its oxidation number. This effect is referred to as central-field covalency. A second effect, known as symmetry-restricted covalency, relates to the formation of molecular orbitals from the anion and impurity ion orbitals. Electron delocalisation into the molecular orbitals results in a lowering of the charge density close to the impurity ion. The outcome of these overlap effects is an expansion of the outer orbitals for which the mean extension appears to increase as the electronegativity of the anion decreases (polarisability increases). Behaviour involving orbital expansion is usually referred to as the nephelauxetic effect (Schäffer and Jørgensen 1958).

A consequence of an effective orbital expansion is a reduction in the magnitude of the radial integrals below their free-ion values, which, in turn, leads to a reduction in the associated Slater–Condon, or equivalent Racah, and spin–orbit parameters. β in our analysis is the nephelauxetic ratio and serves to quantify the extent of the reduction. The magnitude of the nephelauxetic effect, as represented by $(1 - \beta)$, increases in the sequence $F^- \rightarrow Cl^- \rightarrow Br^- \rightarrow I^-$ corresponding to a decreasing anion electronegativity (table 1). The ordering of anions is in agreement with the nephelauxetic series (Jørgensen

Table 1. Optimum parameter values obtained using the iterative fitting procedure described in the text.

Lattice	Dq (cm^{-1})	Δ (cm^{-1})	F (cm^{-1})	G (cm^{-1})	ζ (cm^{-1})	$\beta(F)$	$\beta(G)$	$\beta(\zeta)$	d (Å)
KI	900	34341	104.4	111.5	2802.7	0.559	0.577	0.950	3.533
NaI	1030	34256	105.7	101.4	2861.7	0.566	0.525	0.970	3.238
KBr	1080	35915	117.7	116.9	2861.7	0.630	0.605	0.970	3.300
NaBr	1180	35815	121.0	119.6	2905.9	0.648	0.619	0.985	2.987
KCl	1240	36676	116.4	110.3	2920.7	0.623	0.571	0.990	3.146
NaCl	1360	36856	127.0	117.9	2950.2	0.680	0.610	1.000	2.820
KF	1635	39661	170.5	165.0	2950.2	0.913	0.854	1.000	2.672

Table 2. Precise theoretical and experimental energy level positions and intensities for (*a*) KI, (*b*) KBr, (*c*) KCl, (*d*) KF, (*e*) NaI, (*f*) NaBr and (*g*) NaCl. Energy level positions are given in units of cm^{-1}. Theoretical intensities are equal to $(50a_1)^2$; experimental intensities are normalised to A1 = 100. All experimental values refer to measurements made at liquid nitrogen temperature.

Experimental			Theoretical	
Band	Energy	Intensity	Energy	Intensity
(a) KI			46473	4
			46211	591
			44972	126
C1	38462	542	38462	1342
			38298	11
			37920	42
			37296	10
			36668	0
			36530	1
B2	35587	5	35795	2
			35325	0
B1	34435	21	34441	27
A2	28736	57	28733	147
			27967	28
			26851	2
			26101	60
A1	25873	100	25871	93
			25366	2
(b) KBr			49316	5
			48934	565
			47615	141
			40279	1179
			40214	52
			39820	19
			39236	6
			38681	26
			38322	5
			37647	1
			36525	66
			35637	90
			29620	126
			28853	34
			27725	1
			26854	65
			26593	114
			26085	2
(c) KCl			51100	3
D2	50684	254	50652	514
D1	49383	34	49395	140
			41738	0
C1	41322	400	41320	1060
			40846	38
			40109	0
			39520	19
B3	39062	40	38972	20
			37889	5
B2	36969	83	36960	203
B1	35971	54	35995	118
A2	29656	39	29659	133
			28885	38
			27765	1
			26888	79
A1	26624	100	26627	127
			26111	3
(g) NaCl			52140	3
			51635	522
			50278	147
			42716	0
C1	42017	520	42044	914
			41745	82
			40889	1
			39495	19
B3	38910	65	38839	19
			37687	8
B2	36832	148	36807	279
B1	35778	71	35719	130
A2	29394	36	29424	116
			28635	41
			27507	1
			26527	77
A1	26219	100	26246	135
			25735	3
(d) KF			57052	13
			56565	698
			54577	147
			47779	2
C1	46729	400	46717	596
			46490	208
			45382	9
			41766	23
			40986	27
			39538	14
B2	38835	203	38871	377
			37298	112
A2	31596	43	31654	51
			30722	36
			29551	0
			28131	68
A1	27816	100	27804	117
			27370	2
(f) NaBr			47234	3
D2	49505	212	46828	490
D1	48077	34	45703	142
			38186	806
C1	40486	313	38102	422
			37866	77
			37261	33
			37056	19
B3	38910	40	36379	3
			36111	1
B2	36311	73	35008	41
B1	35298	39	34201	86
A2	29112	50	28046	154
			27293	35
			26183	1
			25402	64
A1	26028	100	25150	128
			24643	1
(e) NaI			49926	5
			49528	568
			48164	138
			40647	0
C1	42017	1144	40479	1144
			39740	23
			39196	2
			38640	11
			38346	21
			37268	3
B2	36832	138	36250	138
B1	35778	102	35285	102
A2	29394	123	29109	123
			28330	36
			27195	1
			26288	73
A1	26219	113	26026	113
			25513	2

1962a). For the transition-metal ions, examples of the use of a reduced Racah parameter are common with β taking a value typically between 0.6 and 0.9. Treatments of this nature are much less common for the rare-earth ions even though β is likely to be similar where d electrons are involved. Alig *et al* (1973) have studied Tm^{2+} in $SrCl_2$ and found it necessary to use a reduced value for the electrostatic interaction ($\beta \simeq 0.6$). Weakliem (1972), in his study of the $4f^{6}5d$ configuration of Eu^{2+} in CaF_2, obtained good agreement between theory and experiment provided that he used Coulomb f–d parameters equal to about one half the free-ion values.

The relative importance of the two types of covalency responsible for the nephelauxetic effect may be determined by comparing the spin–orbit and electrostatic parameter reductions (Jørgensen 1962a). Central-field covalency is associated with a greater relative reduction in the spin–orbit parameter; the reverse situation implies the operation of symmetry-restricted covalency. For the system under investigation, the small variation of $\beta(\zeta)$ below unity compared with $\beta(F)$ and $\beta(G)$ does not necessarily indicate a 5d orbital expansion due to symmetry-restricted covalency since $\beta(\zeta)$ does not define uniquely a reduction in the relevant parameter $\beta(\zeta_d)$. Theoretically, we have determined that the energy level structure is only weakly dependent on variations in ζ_d. Consequently, the parameter $\beta(\zeta)$ reflects primarily a reduction in ζ_f which is both expected and found to be small. As the reduction in ζ_d cannot be obtained directly, it is not possible on the basis of the above arguments to distinguish between the two possible covalency mechanisms.

Some interesting trends become apparent on considering further the parameter values in table 1. If Δ is plotted against d as in figure 4, the chlorides, bromides and iodides each form pairs of almost equal Δ (to within 1%). The value of Δ appears to be independent of both the character of the lattice cation and the lattice parameter. According to the nephelauxetic effect, the parameter Δ will depend quite strongly on the degree of overlap between the 5d electron and the surrounding anions. For the chlorides, bromides and iodides, we conclude that the degree of overlap is determined primarily by the nature of the anion and not by the Yb^{2+}–anion separation. Δ is expected to differ more between the alkali fluorides as, for this most electronegative anion, variations in the Yb^{2+}–anion separation become more significant. The plotted values in figure 4 may be regarded as two distinct and closely parallel linear dependencies; one for the potassium halides and the other for the sodium halides. This behaviour is represented by the empirical formula

$$\Delta = -k_m d + l_m \qquad (m = K, Na). \tag{5}$$

Appropriate values for the coefficients in equation (5) are given in table 3.

Also included in figure 4 are equivalent experimental points for Yb^{2+} in CaF_2, SrF_2 and BaF_2 obtained from Eremin (1970) and in $SrCl_2$ obtained indirectly from Piper *et al* (1967). The abscissa for these materials in figure 4 is the Yb^{2+}–anion distance which is taken to be equal to the cation–anion distance. Neither study takes account of the nephelauxetic effect which is expected to affect the accuracy of the values given for Δ, particularly in the case of the less ionic $SrCl_2$. We have repeated the theoretical calculation for $SrCl_2$: Yb^{2+} using the methods described earlier to obtain improved agreement with the experimental values given by Piper *et al* (1967). Dq is altered significantly (from -800 to $-990\ cm^{-1}$), although only a slight correction to the configurational energy Δ is necessary (from 37971 to 37919 cm^{-1}). The corrected value is used in figure 4. Alig (1975) has similarly reexamined the $SrCl_2$: Yb^{2+} system to include the nephelauxetic effect. His corrected value of $Dq = -1032\ cm^{-1}$ is in good agreement.

We note that the values of Δ for the (two) strontium halides in figure 4 lie on a line parallel to the lines obtained for the sodium and potassium halides. Appropriate values for the strontium coefficients in equation (5) are also given in table 3. The comparatively large spread in Δ for the three alkaline-earth fluorides in figure 4 is in agreement with

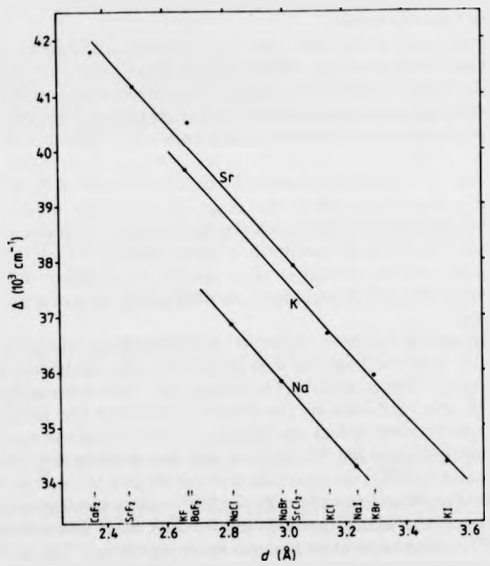

Figure 4. The variation of the parameter Δ with lattice parameter d from the data of table 1. Equivalent values for Yb^{2+} in CaF_2, SrF_2 and $SrCl_2$ (see text) are included.

our prediction of a similar comparative spread for the fluorides of the alkali halide system. Ivoilova and Leushin (1980) have analysed this configurational shift theoretically. Qualitative agreement was obtained using a model based on impurity–anion charge overlap effects but allowing for exchange between electrons of the $4f^{13}5d$ configuration and the anions. In order to achieve quantitative agreement, effects arising from anion polarisation had to be included together with changes in the Yb^{2+}–anion separation. We note that the experimental values for Δ used in their analysis were uncorrected for the same overlap effects.

The crystal-field parameter Dq may also be plotted against the lattice parameter d from the data given in table 1. Again two parallel linear dependencies are obtained for the potassium and sodium halides, although they are less well defined in this case.

Moreover, the ordinates (Dq) differ within a halide pair by about 10%, with the potassium halides (larger d) taking the lower value. Such behaviour reflects the more electrostatic character of this intermediate parameter in the theory compared with Δ. The observed linear dependencies of Dq on d may be expressed empirically as

$$Dq = -p_m d + q_m \qquad (m = K, Na) \tag{6}$$

with the coefficients given in table 3. Similarly the strontium halides (Dq = $-1400\ cm^{-1}$ for SrF_2 (Eremin 1970)) may be fitted to equation (6). The value obtained for the gradient coefficient $p_{Sr} = -773.6\ cm^{-1}\ Å^{-1}$ is close (allowing for the sign reversal) to that for the potassium and sodium halides.

Table 3. Values of the coefficients in equations (5) and (6). k_m and p_m are in units of $cm^{-1}\ Å^{-1}$. l_m and q_m are in units of cm^{-1}.

m	k_m	l_m	p_m	q_m
Na	6219	54394	774.2	3524 3
K	6130	56036	860.6	3935.6
Sr	6134	56505	−773.6	3334.0

5. Conclusions

When ytterbium is diffused into KI, NaI, KBr, NaBr, KCl, NaCl and KF at high temperatures, it enters the lattice substitutionally in a doubly ionised state in association with a cation vacancy. The observed optical aborption spectra arise principally from allowed transitions of the type $4f^{14} \rightarrow 4f^{13}5d$ associated with the Yb^{2+} ion. Generally excellent agreement is obtained between experiment and a theory utilising the J_1j-coupling scheme to describe the Yb^{2+} ion in an octahedral crystal field, provided that a correction based on the degree of overlap between the wavefunctions of the outer 5d electron and the anions is included. The correction increases in the sequence $F^- \rightarrow Cl^- \rightarrow Br^- \rightarrow I^-$ as the electronegativity of the anion decreases and takes the form of a reduction, by up to 50%, in the values for the free-ion parameters. These reductions are associated with the nephelauxetic effect.

Two distinct and closely parallel linear dependencies, one for the potassium halides and the other for the sodium halides, are observed when the parameter Δ (the energy difference between the centre of energy of the excited $4f^{13}5d$ configuration and the $4f^{14}$ ground state) is plotted against the lattice parameter. The near equality of Δ within a halide pair illustrates the importance of anion electronegativity in determining the degree of charge overlap. An additional dependence on the Yb^{2+}–anion separation is expected to gain in importance as the electronegativity of the anion increases. Similar linear dependencies with lattice parameter are observed for Dq but without the equality of parameter value. This behaviour is consistent with a greater comparative dependence on the Yb^{2+}–anion separation. There is evidence to suggest that closely comparable dependencies exist for the alkaline-earth halides. Work is in progress to investigate the possibility of linear dependencies for the rubidium halides.

Acknowledgments

One of us (SWB) would like to thank the Science and Engineering Research Council for financial support. Both of us thank Mr C F Randle for his technical support.

References

Alig R C 1975 *RCA Rev.* **36** 125
Alig R C, Duncan R C Jr and Mokross B J 1973 *J. Chem. Phys.* **59** 5837
Altshuler N S, Eremin M V, Luks R K and Stolov A L 1969 *Sov. Phys.–Solid State* **11** 2921
Bryant B W 1965 *J. Opt. Soc. Am.* **55** 771
Eremin M V 1970 *Opt. Spectrosc.* **29** 53
Feofilov P 1956 *Opt. Spectrosc.* **1** 992
Hernandez A J, Cory W K and Rubio O J 1981 *J. Chem. Phys.* **72** 198
Hernandez A J, Lopez F J, Murrieta S H and Rubio O J 1981 *J. Phys. Soc. Japan* **50** 225
Honig R E 1962 *RCA Rev.* **23** 567
Hutchings M T 1964 *Solid State Phys.* **16** 227 (New York: Academic Press)
Ivoilova E Kh and Leushin A M 1980 *Sov. Phys.–Solid State* **22** 601
Johnson K E and Sandoe J N 1969 *J. Chem. Soc.* A 1694
Jørgensen C K 1962a *Prog. Inorg. Chem.* **4** 73
—— 1962b *Solid State Phys.* **13** 375 (New York: Academic Press)
Judd B R 1963 *Operator Techniques in Atomic Spectroscopy* (New York: McGraw-Hill)
Kaplyanskii A A and Feofilov P P 1962 *Opt. Spectrosc.* **13** 129
Kiss Z J 1965 *Phys. Rev.* **137** A1749
Loh E 1969 *Phys. Rev.* **184** 184
—— 1973 *Phys. Rev.* B **7** 1846
Low W 1964 *Phys. Rev.* **134** A1479
Piper T S, Brown J P and McClure D S 1967 *J. Chem. Phys.* **46** 1353
Racah G 1960 *J. Opt. Soc. Am.* **50** 408
Radhakrishna S and Chowdari B V R 1972 *Phys. Status Solidi* a **12** 557
Sabisky E S and Anderson C H 1966 *Phys. Rev.* **148** 194
Schaffer C E and Jørgensen C K 1958 *J. Inorg. Nucl. Chem.* **8** 143
Sootha G D, Tripathi T C and Agarwal S K 1971 *Phys. Status Solidi* b **44** K61
Tsuboi T, Witzke H and McClure D S 1981 *J. Lumin.* **24/25** 305
Wagner M and Bron W E 1965 *Phys. Rev.* **139** A223
Weakliem H A 1972 *Phys. Rev.* B **6** 2743
Weakliem H A and Kiss Z J 1967 *Phys. Rev.* **157** 277
Weber M J and Bierig R W 1964 *Phys. Rev.* **134** A1492